A novel Automatic Optic Disc and Cup Image Segmentation System for Diagnosing Glaucoma using RIGA dataset

by

Ahmed Almazroa

A thesis

presented to the University of Waterloo

in fulfillment of the

thesis requirement for the degree of

Doctor of Philosophy

in

Vision Science

Waterloo, Ontario, Canada, 2016

AUTHOR'S DECLARATION

I hereby declare that I am the sole author of this thesis. This is a true copy of the thesis, including any required final revisions, as accepted by my examiners. I understand that my thesis may be made electronically available to the public.

Abstract

The optic nerve head (ONH) of the retina is a very important landmark of the fundus and is altered in optic nerve pathology especially glaucoma. Numerous imaging systems are available to capture the retinal fundus and from which some structural parameters can be inferred the retinal fundus camera is one of the most important tools used for this purpose. Currently, the ONH structure examination of the fundus images is conducted by the professionals only by observation. It should be noted that there is a shortage of highly trained professional worldwide. Therefore a reliable and efficient optic disc and cup localization and segmentation algorithms are important for automatic eye disease screening and also for monitoring the progression/remission of the disease Thus in order to develop a system, a retinal fundus image dataset is necessary to train and test the new software systems.

The methods for diagnosing glaucoma are reviewed in the first chapter. Various datasets of retinal fundus images that are publically available currently are described and discussed. In the second chapter the techniques for the optic disc and cup segmentations available in the literature is reviewed. While in the third chapter a unique retinal fundus image dataset, called RIGA (retinal images for glaucoma analysis) is presented. In the dataset, the optic disc and cup boundaries are annotated manually by 6 ophthalmologists (glaucoma professionals) independently for total of 4500 images in order to obtain a comprehensive view point as well as to see the variation and agreement between these professionals. Based upon these evaluations, some of the images were filtered based on a statistical analysis in order to increase the reliability. The new optic disc and cup segmentation methodologies are discussed in the fourth chapter. The process starts with a preprocessing step based on a reliable and precise algorithm. Here an Interval Type-II fuzzy entropy

based thresholding scheme along with Differential Evolution was applied to determine the location of the optic disc in order to determine the region of interest instead of dealing with the entire image. Then, the processing step is discussed. Two algorithms were applied: one for optic disc segmentation based on an active contour model implemented by level set approach, and the second for optic cup segmentation. For this thresholding was applied to localize the disc. The disc and cup area and centroid are then calculated in order to evaluate them based on the manual annotations of areas and centroid for the filtered images based on the statistical analysis. In the fifth chapter, after segmenting the disc and cup, the clinical parameters in diagnosis of glaucoma such as horizontal and vertical cup to disc ratio (HCDR) and (VCDR) are computed automatically as a post processing step in order to compare the results with the six ophthalmologist's manual annotations results. The thesis is concluded in chapter six with discussion of future plans.

Acknowledgements

I am grateful to Almighty Allah blessing me to finish this thesis.

I could not find a better word to say thank you, but first of all I would like to acknowledge my parents for their encouragements and support all the time.

I truly must also acknowledge my supervisor Dr. Vasudevan Lakshminarayanan for his permanent support, inspiring ideas, encouragements and instructions in my PhD study. Actually, without his support, this work would never have reached the level it did.

Moreover, I would like to express my deepest appreciation and gratitude to my co supervisor Dr. Kaamran Raahemifar for the unlimited guidance and support throughout my research study.

I also would like to thank the rest of my thesis committee Drs William Bobier and Simarjeet Saini who has been very helpful and generous.

My gratitude finally goes to my colleagues and friends and other members in school of optometry and vision science for their supports and helps.

Table of Contents

List of Figures

List of Tables

List of Abbreviations

IOP	Intraocular pressure.
RNF	Nerve fiber layer.
OCT	Optical Coherence Tomography.
POAG	Primary open angle glaucoma.
SD- OCT	Spatial domain-optical coherence tomography.
SAP	Standard automated perimetry
CDR	Cup to disc ratio
RNFL	Retinal nerve fiber layer
ISNT	Inferior (I), superior,(S) nasal (N), and temporal
OD	Optic disc
OC	Optic cup
DRIVE	Digital Retinal Images for Vessel Extraction
STARE	Structured Analysis of Retina
ONH	Optic nerve head
MESSIDOR	Methods to evaluate segmentation and indexing techniques in the field of retinal ophthalmology
ORIGA	Online Retinal Fundus Image Dataset for Glaucoma Analysis and Research
DIARETDB0	The Standard Diabetic Retinopathy Dataset Calibration level
DIARETDB1	Diabetic retinopathy dataset and evaluation protocol
SP	Specificity
SN	Sensitivity
ACC	Accuracy
PPA	Positive Predictive Accuracy
DM	Dice metric
RAD	Relative area difference
ROI	region of interest
RMIN	operator which detects the regional minima pixels
SBGFRLS	Selective Binary and Gaussian Filtering Regularized Level Set
PPA	Peripapillary atrophy
ARIA	Automatic retinal image analysis
LoG	Laplacian of Gaussian
POI	Patches of interest
SERI	Singapore eye research institute
LIBSVM	Library for support vector machine
SiMES	Singapore Malay Eye Study
SCEN	Singapore Chinese Eye Study
MCV	Chan-Vese model
CHT-ASM	Circular Hough transform combined with an active shape model
EHT	Elliptical Hough transform
MDM	Modified deformable models
KNN	K nearest neighbor classifier
BAYES	Bayes classifier
SVM	*Support vector machines*
HCDR	Horizontal cup to disc ratio
VCDR	vertical cup to disc area
SD	Standard deviation
FOU	Footprint of uncertainty
PDE	partial differential equation
GUI	graphical user interface

Chapter 1

Introduction

1.1. Background

1.1.1. Glaucoma

Glaucoma is a chronic eye disease in which the optic nerve is gradually damaged. Glaucoma is the second leading cause of blindness after cataract, with approximately 60 million cases reported worldwide in 2010 [1]. It is estimated that by 2020 about 80 million people will suffer from glaucoma [1]. If undiagnosed, glaucoma causes irreversible damage to the optic nerve leading to blindness. Therefore, diagnosing glaucoma at an early stage is extremely important for appropriate early management [2-4]. Accurate diagnosis of glaucoma requires three different sets of examinations: (1) evaluation of the intraocular pressure (IOP) using contact (Goldmann tonometry) or noncontact tonometry ("air puff test"), (2) evaluation of the visual field, and (3) evaluation of the optic nerve head [5]. Accurate diagnosis of glaucoma requires additional measurements, that is, gonioscopy and assessment of retinal nerve fiber layer (RNFL) [4]. Since both elevated-tension and normal-tension glaucoma may or may not increase the IOP, the IOP by itself is not a sufficient screening or diagnosis method [6]. On the other hand, visual field examination requires special equipment which is usually available only in tertiary care hospitals that have a fundus camera and possibly an Optical Coherence Tomography (OCT) [6]. In routine practice, patients with primary open angle glaucoma (POAG) can be manifested with inconsistent reports between SD (spatial domain)-OCT and standard automated perimetry (SAP). In the elderly, higher cup to disc (this refers to the optic nerve head) ratio, larger cup volume, and lower rim area on SD-OCT appear to be associated with detectable damage. Moreover, additional worsening in

RNFL parameters might reinforce diagnostic consistency between SD-OCT and SAP [7]. Therefore, the optic nerve head examination (cup-to-disc ratio) is a valuable method for diagnosis of glaucoma structurally [8]. The visual field test, on the other hand, diagnoses glaucoma functionally by detecting the damage done to the visual field. Determining the cup-to-disc ratio is a very expensive and time consuming task currently performed only by professionals. Therefore, automated image detection and assessment of glaucoma will be very useful.

There are two different approaches for automatic image detection of optic nerve head [6]. The first approach is based on the very challenging process of image feature extraction for binary classification of normal and abnormal conditions. The second and more common approach however is based on clinical indicators such as cup-to-disc ratio as well as inferior (I), superior(S), nasal (N), and temporal (T) zones rule in the optic disc area [6]. The optic disc is made of 1.2 million ganglion cell axons passing across the retina and exiting the eye through the scleral canal in order to transit visual information to brain [8]. Examining the optic disc helps clarify the relationship between the optic nerve cupping and loss of visual field in glaucoma [8]. The optic disc is divided into three different areas: neuroretinal rim, the cup (central area), and sometimes parapapillary atrophy [9]. The cup-to-disc ratio (CDR) is the ratio of the vertical diameter of the cup to the vertical diameter of the disc [10].

1.1.2. Retinal image processing

1.1.2.1. Fundus photography

Fundus photography is a complicated process. The fundus camera is essentially a low power microscope designed to capture the image of the posterior pole of the eye as well as the whole retina.

Fundus photography allows three types of examination: (1) color, in which white light is illuminated on the retina to examine it in full color; (2) red-free, in which the contrast among vessels and other structures is improved by removing the red color through filtering the imaging light; and (3) angiography, in which the contrast of vessels is improved by intravenous injection of a fluorescent dye [11].

1.1.2.2. Optical coherence tomography (OCT)

OCT is an optical signal acquisition method for capturing 3D images with micrometer resolution from within optical scattering media. OCT applies near infrared light and is based on the Michaelson interferometry method.

The long wavelength light has the advantage of penetrating into the scattering medium. OCT is usually used for imaging the retina due to its ability to provide high resolution cross-sectional images [12]. It is also a useful imaging technique in other areas such as dermatology and cardiology [13].

1.2. Optic disc and optic cup segmentation

The Optic Disc (OD) is one of the most important parts of a retinal fundus image [14] (Figure 1). OD detection is considered a preprocessing component in many methods of automatic image segmentation of retinal structures, which is a common step in most retinopathy screening procedures [15]. The OD has a vertical oval (elliptical) shape [16] and is divided into two separate zones: the central zone or the cup, and the peripheral zone or neuroretinal rim [6].

Figure 1.1 Optic Disc in fundus image [17]

Changes in the color, shape, or depth of OD are indications of ophthalmic pathologies such as glaucoma [18]; therefore, OD measurements have important diagnostic values [19, 20]. In automated image processing for detection of glaucoma, accurate detection of the central point of OD is important. Furthermore, correct segmentation of OD requires accurate detection of the boundary between the retina and the rim [16]. Pathological cases occurring on the OD boundaries, such as papillary atrophy, influence the segmentation accuracy. Optic Cup (OC) segmentation is further challenged by the density of blood vessels covering parts of the cup and the gradual change in color intensity between the rim and the cup. The kinks in the blood vessels sometimes facilitate detecting the cup boundaries and make it more challenging. Bad image acquisition also affects cup segmentation. Accurate disc and cup segmentation is very important in all pathological cases since errors in disc and cup segmentation may mislead the professionals and hence affect their diagnosis.

1.3. Publicly available retinal image datasets

Most of the retinal optic disc and cup segmentation methodologies presented in the Literature Review chapter were tested on various publicly available datasets, for example, DRIVE, STARE, MESSIDOR, and ORIGA. In this section we provide a brief summary of these datasets.

DRIVE Dataset

The Digital Retinal Images for Vessel Extraction (DRIVE) dataset [21] consists of 40 color fundus images. The images were acquired from a diabetic retinopathy research program in the Netherlands. Seven images of the dataset have pathology. Figure 1.2 shows an example of a normal (A) and a pathological (B) image. A Canon CR5 non-mydriatic 3CCD camera with a 45° field of view was used to obtain the images. The images were divided into two groups, a training set and a test set, with 20 images in each group. Three experts manually segmented the images in order to have reference images for evaluating the automatic segmentation techniques by comparing the manually segmented images with those segmented automatically.

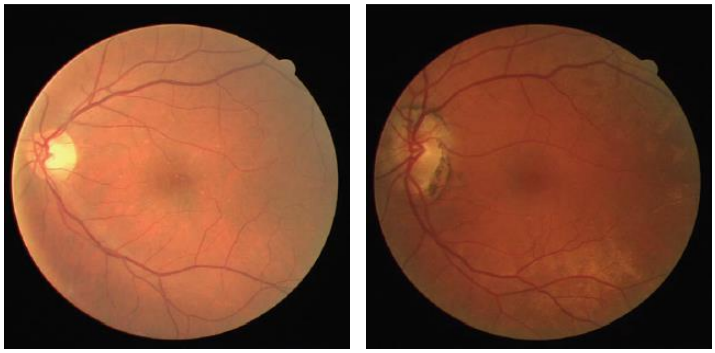

(A) (B)

Figure 1.2 Retinal images from DRIVE: (a) normal image, (b) pathological image.

STARE Dataset

The Structured Analysis of Retina (STARE) dataset [22] is funded by the US National Institutes of Health. The dataset has 400 fundus images. The blood vessels are annotated in 40 images. The optic nerve head (ONH) is localized in 80 images. A Topcon TRV-50 fundus camera with 35° field of view was used to capture the images.

MESSIDOR Dataset

MESSIDOR [23] contains 1200 images in two sets; the images were captured in three ophthalmology departments by a research program sponsored by the French Ministries of Research and Defense. Two diagnoses have been provided by the medical experts for each image, namely, retinopathy grade, and risk of macular edema. A color video 3CCD camera on a Topcon TRC NW6 non-mydriatic retinography with a 45° field of view was used to capture the images. The images are saved in uncompressed TIFF format.

ORIGA Dataset

The Online Retinal Fundus Image Dataset for Glaucoma Analysis and Research (ORIGA) [24] consists of 650 images acquired through Singapore Malay Eye Study (SiMES). Critical signs for glaucoma diagnosis are annotated. SiMES is conducted by the Singapore Eye Research Institute (SERI) [25]. The images were annotated by experts by employing "key nodes" which are imagine landmarks along the disc boundary and cup boundary and were stored in a centralized server. The dataset includes 168 glaucomatous and 482 non-glaucoma images.

DIARETDB0 Dataset

The Standard Diabetic Retinopathy Dataset Calibration level 0 DIARETDB0 [26] consists of 130 color fundus images, 20 normal images, and 110 images with signs of diabetic retinopathy, acquired from the Kuopio University Hospital in Finland. The images were captured by a digital fundus camera with 50° field of view.

DIARETDB1 Dataset

The diabetic retinopathy dataset and evaluation protocol DIARETDB1 [27] consists of 89 color fundus images acquired from the Kuopio University Hospital in Finland. The dataset consists of 84 images with diabetic retinopathy and 4 normal images. The images were captured by a digital

fundus camera with 50° field of view. Four experts annotated the microaneurysms, hemorrhages, and hard and soft exudates.

1.4. Performance Metrics

The outcome of optic disc segmentation process is pixel based. Figure 1.3 shows the three distinctive areas: (1) the true positive area representing the overlapping area between the manually annotated (ground truth) and automatically annotated (segmented image) areas, (2) the false negative area where a pixel is classified only in the manually annotated area, and (3) the false positive area where the pixel is classified only in the automatically segmented area. Sensitivity measures the proportion of the actual positives which are correctly identified. A higher sensitivity value implies a higher validity of results [28]. On the other hand, there are different measurements used in image classification of the optic disc and optic cup segmentation to determine whether an image is normal or glaucomatous. Cup-to-disc ratio is defined as the ratio of vertical distances between pixels at the highest and lowest vertical position inside the cup and disc region [29] (Figure 1.4). Table 1.1 summarizes the OD and OC segmentation algorithms performance metrics. Various methods are used for image classification which is a clinical assessment of the ISNT rule for the optic nerve. The ISNT rule is considered to be an observer to the gradual decrease or no change in rim width at the following position order: inferior (I) ≥ superior (S) ≥ nasal (N) ≥ temporal (T) (Figure 1.5).

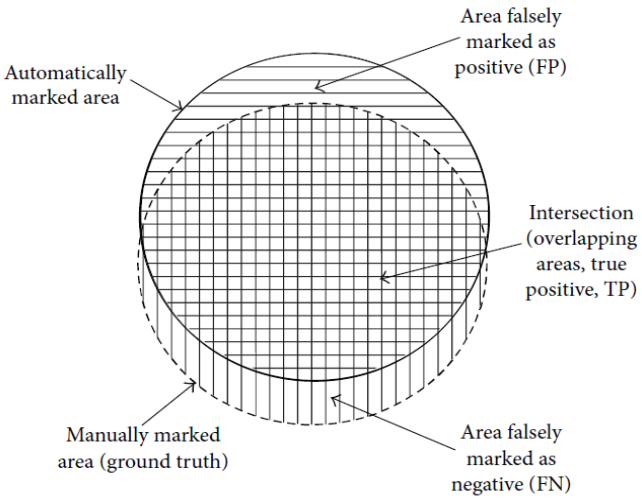

Figure 1.3 The relation between the ground truth and automatically annotated area [9].

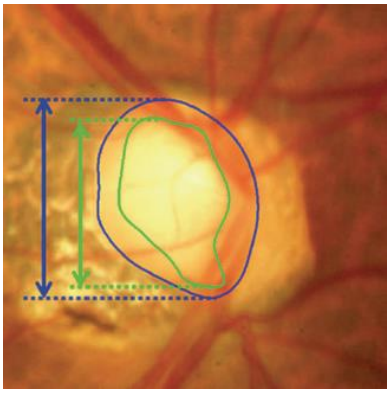

Figure 1.4 Measurement of cup-to-disc ratio for a tilted disc [30].

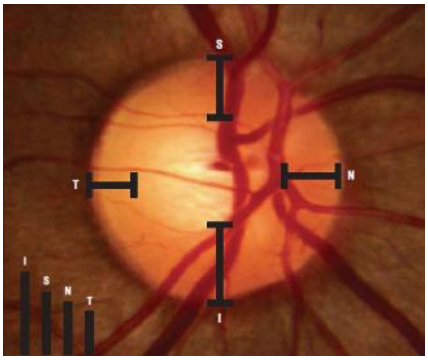

Figure 1.5 Measurement of the ISNT rule [31].

Table 1.1 Performance metrics for optic disc and optic cup segmentation.

Measurement	Description
Optic disc overlap	TP/TP+FN+FP
CDR error	CDR (GR) – CDR (PRP)
ISNT rule	Optic disc-optic cup (obtain the thickness in all the four quadrants)
Specificity (SP)	TN/TN+FP
Sensitivity (SN)	TP/TP+FN
Accuracy (Acc)	TP+TN/TP+FP+FN+TN
Positive Predictive Accuracy (PPA)	TP/TP+FP
Dice metric (DM)	2*TP/FP+TP+FN
Relative area difference (RAD)	FP+FN/GT

As mentioned before, sensitivity is the probability of an abnormal class to be identified as abnormal. Specificity however, is the probability of a normal class to be identified as normal. Accuracy represents the ability or quality of the performance. The positive predictive accuracy represents the precision in detecting normal and abnormal cases. The true negative represents the number of normal images identified as normal, while false negative represents the number of glaucoma images identified as normal. True positive represents the number of glaucoma images identified as glaucoma and false positive represents the number of normal images identified as glaucomatous [32].

In this chapter we have reviewed the methods for diagnosing glaucoma as well as the methods used to take the images of the eye fundus and various datasets of retinal fundus images that are publically available. In addition, the performance matrices used to compute the accuracy of the automatic systems have been introduced.

Chapter 2

Literature review and thesis objectives

2.1. Literature review

Different techniques have been used for optic disc (OD), optic cup (OC), or optic disc with optic cup segmentation. In this chapter, the OD and OC segmentation methodologies that automatically detect OD and OC boundaries are critically reviewed. These techniques help professionals with diagnosing and monitoring glaucoma by providing them with clear and accurate information regarding the ONH structure. The uniqueness of this literature review is in demonstrating the segmentation methodology by creating a flowchart for each technique. In this chapter the algorithms applied for OD and OC segmentation are introduced and the pros and cons of each method are discussed. Suggestions for future research are also provided.

2.1.1. Segmentation approaches

Various techniques have been used in image processing methodologies of optic disc and optic cup segmentation in the literate. These techniques for segmentation are, thresholding, edge-based methods, and region-based methods [33]. Here, three segmentation methodologies are considered: (1) optic disc segmentation approaches, (2) optic cup segmentation approaches, and (3) optic disc and optic cup segmentation together. While most algorithms are concerned with just optic disc segmentation, few are concerned with optic cup segmentation and even fewer with optic disc and optic cup segmentation together.

2.1.1.1. Optic Disc segmentation approaches

Optic disc extraction or segmentation is performed using segmented reference images called "ground truth" on which the optic disc is accurately annotated by ophthalmologists. The OD processing includes two main steps: localization (detecting the center point of OD) and segmentation (detecting the disc boundary) [34]. Different OD detection and segmentation algorithms have already been introduced; however, many of these algorithms have a number of limitations [35] such as using images with a clear color variation across OD boundary. Preprocessing methods are important steps for analyzing an image by enhancing the image and finding the region of interest (ROI). The OD segmentation approaches are summarized in Table 2.1 and their results are shown in Table 2.2.

Table 2.1 Optic disc segmentation methods.

Authors	Year	Image processing technique	Performance metrics	Dataset	Number of Images
Lupascu et al. [36]	2008	Circles passing through three noncollinear points	Success rate	DRIVE	40
Youssif et al. [16]	2008	Normalized DFI by means of a vessels' direction matched filter	Success rate	STARE	81
Zhu and Rangayyan [37]	2008	Edge detection using canny and sobel methods and through transform	Success rate	DRIVE STARE	40 82
Welfer et al. [38]	2010	Adaptive morphological approach	Overlap (Acc)	DRIVE DIARETDB1	40 89
Aquino et al. [34]	2010	Morphological, edge detecting, and feature extraction techniques	Overlap (Acc)	MESSIDOR	1200
Tjandrasa et al. [39]	2012	Hough transform and active contours	Overlap (Acc)	DRIVE	30
Yin et al. [40]	2011	Model based segmentation	Overlap (Acc)	ORIGA	650
Cheng et al. [41]	2011	Peripapillary atrophy elimination	Overlapping error	ORIGA	650
Lu [35]	2011	Circular transformation	Overlap (Acc)	MESSIDOR ARIA STARE	1200 120 81
Dehghani et al. [42]	2012	Histogram matching	Success rate	DRIVE STARE Local	40 81 237
Zhang et al. [43]	2012	Projection with vessel distribution and appearance characteristics	Success rate	DRIVE	40
Fraga et al. [44]	2012	Fuzzy convergence and Hough transform	Success rate	VARIA	120
Sinha and Babu [45]	2012	Optic disc localization using L1 minimization	Overlap (Acc)	DIARETDB0 DIARETDB1 DRIVE	130 89 40
Kumar and Sinha [28]	2013	Maximum intensity variation	Overlap (Acc) SN	MESSIDOR DIARETDB0	40 130

Table 2.2 Performance results for the optic disc segmentation.

Authors	Year	Dataset	Sensitivity	Average overlapping	Overlap error	Success rates (Acc)	Computation time (s)
Lupascu et al. [36]	2008	DRIVE				95% localization 70% identification of OD	60
Youssif et al. [16]	2008	DRIVE STARE				100% localization 98.77% localization	210
Zhu and Rangayyan [37]	2008	DRIVE STARE				92.5% 40.24%	N/A
Welfer et al. [38]	2010	DRIVE DIARETDB1				100% 97.7%	1083
Aquino et al. [34]	2010	MESSIDOR				99% localization 86% segmentation	1.67 5.69
Yin et al. [40]	2011	ORIGA			11.3%		N/A
Cheng et al. [41]	2011	ORIGA			10%		N/A
Lu [35]	2011	MESSIDOR ARIA STARE				98.77% detection 97.5% detection, 91.7% segmentation 99.75% detection, 93.4% segmentation	5
Tjandrasa et al. [39]	2012	DRIVE				75.56%	N/A
Fraga et al. [44]	2012	VARIA				100% localization 93.36% segmentation	0.6
Dehghani et al. [42]	2012	DRIVE STARE Local				100% 91% 98.9%	27.6
Zhang et al. [43]	2012	DRIVE Self-selection STARE DIARETDB0 DIARETDB1				100% 97.5% 91.4% 95.5% 92.1%	13.2
Sinha and Babu [45]	2012	DIARETDB0 DIARETDB1 DRIVE				96.9% 100% 95%	3.8
Kumar and Sinha [28]	2013	MESSIDOR DIARETDB0	93%	0.895			90

Fraga et al. [44] presented a methodology for OD segmentation containing different stages (Figure 2.1). In order to reduce contrast variability and increase process reliability, the retinal image was normalized by means of the retinex algorithm [46]. Two different techniques were used to localize the optic disc: (1) analyzing the convergence of the vessels [47] to detect the circular bright shapes, and (2) detecting the brightest circular area based on a fuzzy Hough transform [48]. After detecting the OD, the segmentation techniques were conducted using the region of interest specified by a difference of Gaussian filter. The vessel tree boundaries were segmented by Canny filter to compute the edges. The vessel edges from the Canny output were suppressed using the vessel tree

segmentation. Finally, the histogram information was included to measure the accuracy of segmentation. The methodology was evaluated on 120 images and achieved 100% of OD localization for both fuzzy convergence and Hough transform. Using brute force search, the segmentation success rates were 92.23% and 93.36% for the fuzzy convergence and Hough transform, respectively. The aforementioned OD segmentation approach did not involve pathologic retinal images affecting the OD. This is a limitation which should be addressed in the future work in order to develop a robust methodology.

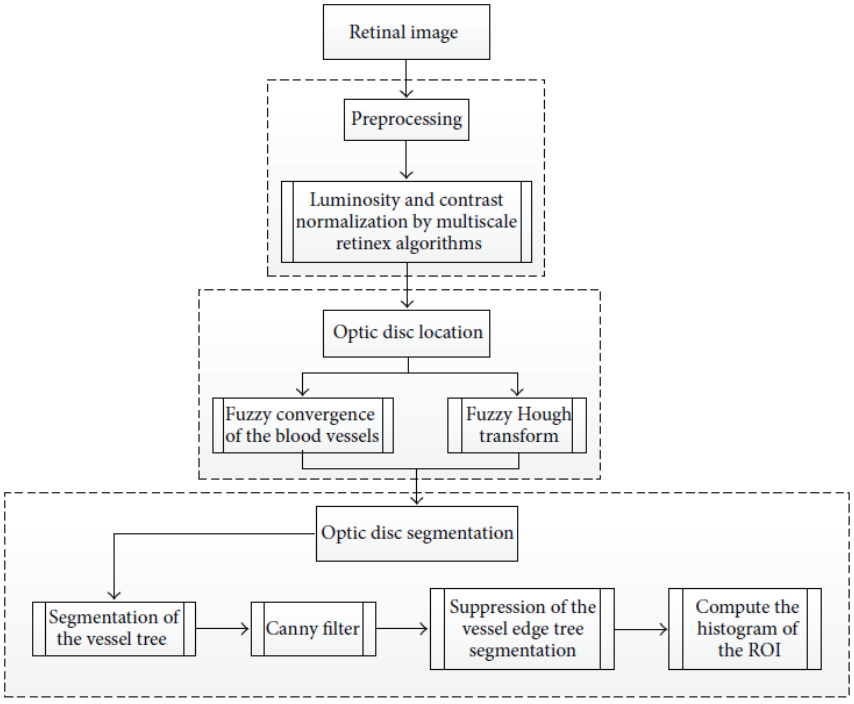

Figure 2.1 Flowchart for algorithm proposed in [44].

Welfer et al. [38] present a new adaptive method based on a model of the vascular structure using mathematical morphology for the OD automatic segmentation (Figure 2.2). This methodology has two main stages: (1) detecting OD location using the information of the main vessels arcade, where the vessels were detected to determine the foreground and background of the green channel image.

In this stage, the RMIN operator (which detects the regional minima pixels) was used to identify the background region; (2) detecting the optic disc boundary. In order to detect the OD boundary using the watershed transform, an internal point to the optic disc and other points in vicinity of the internal point were identified based on the previously detected vascular tree and using the following three steps: (1) using a specific algorithm to find the OD position and to determine whether it is on the right or left side of the image (morphological skeleton and pruning cycle are used in this step), (2) locating the optic disc by removing the less important vessels from the pruned image, (3) describing the shape of the optic disc. The methods were tested on 40 images obtained from DRIVE dataset and 89 images from DIARETDB1 dataset. The success rate in optic disc localization was 100% and 97.75% for the DRIVE and DIARETDB1 datasets, respectively. Future work should consider detecting other important retina structures, such as fovea, based on the proposed method.

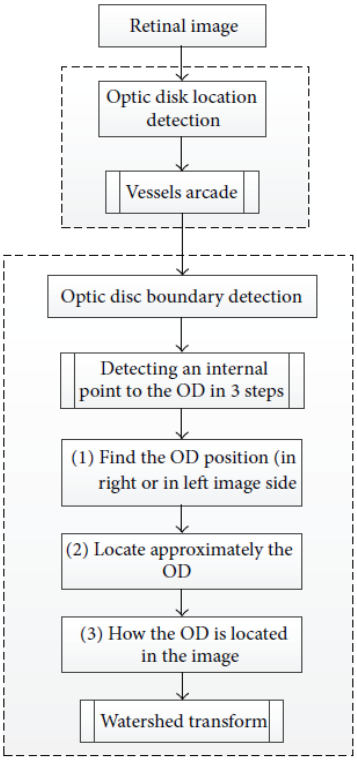

Figure 2.2 Flowchart for algorithm proposed in [38].

Aquino et al. [34] proposed a new algorithm for OD segmentation (Figure 2.3), where the localization methodology obtains a pixel from the OD called optic disc pixel. The methodology contains three different detection methods (Figure 2.4). Each method has its own OD candidate pixel, and the final pixel was chosen by a voting procedure. The green channel has been selected since it provides the best contrast. Two of the three detection methods are called maximum difference method and maximum variance method. In general the maximum variation occurs between the bright region (OD) and the dark region (blood vessels in the disc). Therefore, the maximum variation was used to select the OD pixel of those two methods. In addition, the statistical variance for every pixel was calculated in the maximum variance method and the bright pixels were obtained by blue channel thresholding via Otsu method [49]. The last method was low pass filter method, where the OD pixel was the maximum gray level pixel in the filtered image.

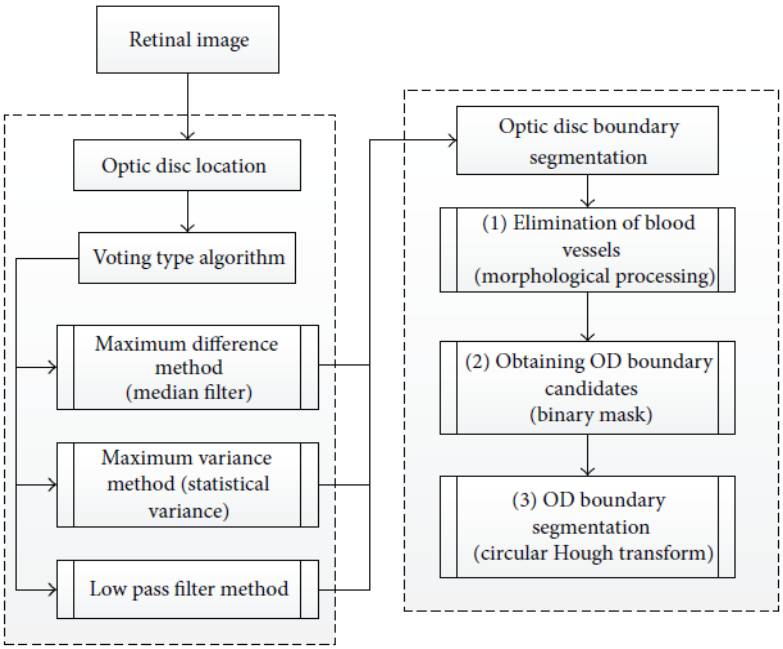

Figure 2.3 Flowchart for algorithm proposed in [34].

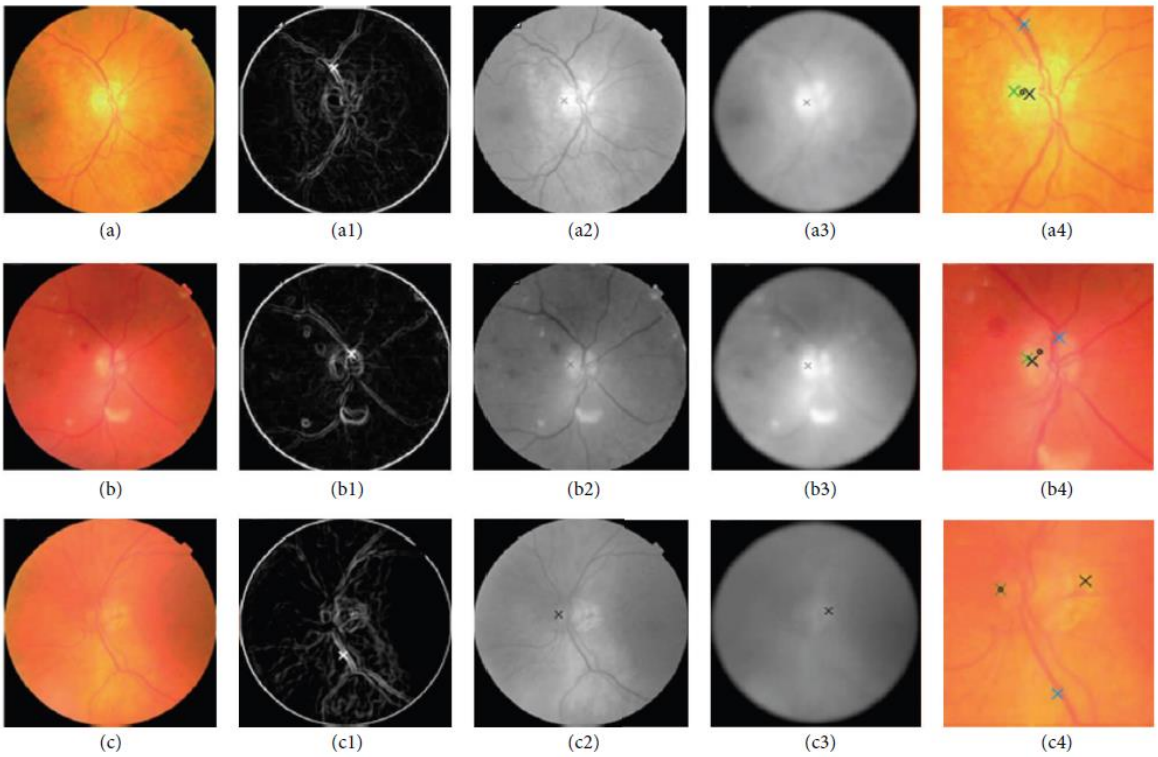

Figure 2.4 ODP determination. (a), (b), and (c): Original images; (a1), (b1), and (c1): OD pixels provided by the maximum difference method; (a2), (b2), and (c2): OD pixels provided by the maximum variance method; (a3), (b3), and (c3): OD pixels provided by the low-pass filter method; (a4), (b4), and (c4): Final ODP determination.

Finally, the maximum variance method has been chosen to have the final OD pixel according to the voting procedure. On the other hand, the OD segmentation methodology was applied on two "red" and "green" components and the better segmentation was selected (Figure 2.5). The procedure was based on removing the blood vessels by employing a special morphological processing and then applying edge detection and morphological techniques to obtain a binary mask of the OD boundary candidates. Finally, the circular approximation of the OD was computed using a circular Hough transform. The methodology was evaluated using the publicly available MESSIDOR dataset. The localization was successful in 99% and the segmentation was successful in 86%. The current research is concentrated on improving the algorithm for executing a controlled elliptical deformation of the obtained circumference.

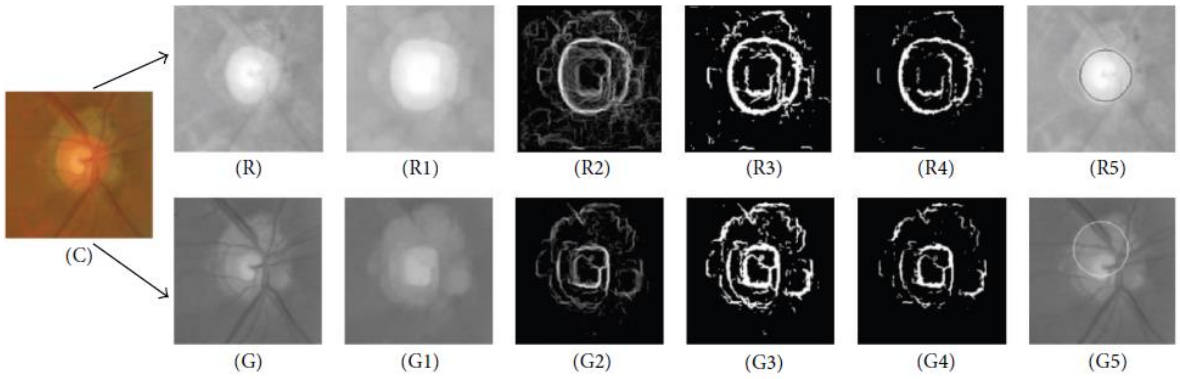

Figure 2.5 The calculation process of the circular OD boundary approximation. (R) Red channel; (G) Green channel. R1 and G1: Vessel elimination; R2 and G2: Gradient magnitude image; R3 and G3: Binary image; R4 and G4: Cleaner version of the binary image; R5 and G5: Circular OD boundary approximation.

Tjandrasa and colleagues [39] applied the Hough transform as an initial level set for the active contours for optic disc segmentation. The algorithm procedure is shown in Figure 2.6. The OD segmentation steps started by converting the image into a grayscale image and then implementing the image preprocessing (image enhancement). Therefore, homomorphic filtering was applied to reduce the effect of uneven illumination. Homomorphic filtering has two stages: (1) applying a Gaussian low pass filter, and (2) obtaining the filtered edge by performing dilation. The blood vessels are removed in the next step to facilitate the segmentation process. The threshold was applied to detect the low pixel values in the image and followed by applying the median filter to blur the blood vessels. The next step in OD segmentation was detecting a circle which matches the location of OD by performing a Hough transform. Subsequently, an active contour model was used to obtain OD boundaries that are as close to the original OD boundaries as possible. The active contour model was applied with a special processing termed Selective Binary and Gaussian Filtering Regularized Level Set (SBGFRLS) [50]. The algorithm achieved 75.56% accuracy using 30 images from DRIVE dataset. Further work can be done to segment the cup disc in order to classify the images into normal and glaucomatous.

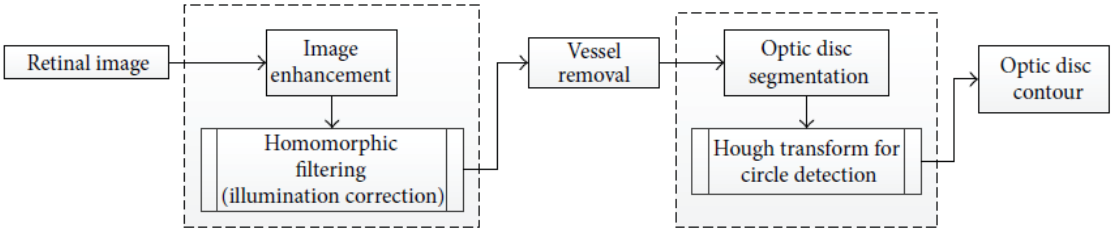

Figure 2.6 Flowchart for algorithm proposed in [39].

Lupascu and colleagues [36] presented an alternative technique (Figure 2.7) to detect the best circle that matches the OD boundary. The technique used a regression based method and texture descriptors to identify the circle which fits the OD boundary. The variation in the intensity of pixels described the appearance of the OD, and therefore this fact was utilized in the algorithm. Since the color fundus images have a dark background, the background pixels were not considered. A mask image was computed with zero values for background pixels and one for the foreground pixels. The maximum intensity pixels within the green component provide the highest contrast, and therefore were selected. The initial point was established based on the center of the mass of the region, where eight directions were considered. The directions were obtained by moving counterclockwise in steps of 45°. Each direction was based on the rapid variation of intensity. Three points were considered for each direction; thus in total there were 24 points. The Euclidean distances (the distances between the initial point and each of the 24 points of interest) were computed and their mean value was calculated. The circles were created using three non-collinear points. Hundreds of circles were obtained; however, based on their specific properties, less than twenty circles were selected as the better ones and the rest were removed. Using bilinear filtering, the selected circles were mapped into polar coordinate space. The next step was to find the maximum derivatives in y direction by applying the linear least squares fitting technique. The correlation coefficient was computed to measure the quality of the fitting. The circle with the

maximum correlation coefficient was chosen as the best circle matching the OD. The algorithm was tested on 40 images. An ophthalmologist manually annotated the ground truth of OD boundary using the standard software to select some pixels on the OD boundary. The success rate was 95% for OD localization and 70% for OD contour (circle) identification. This method caused false detection of OD in low quality images; therefore, further study is needed to improve the algorithm by refining the selection of the initial points.

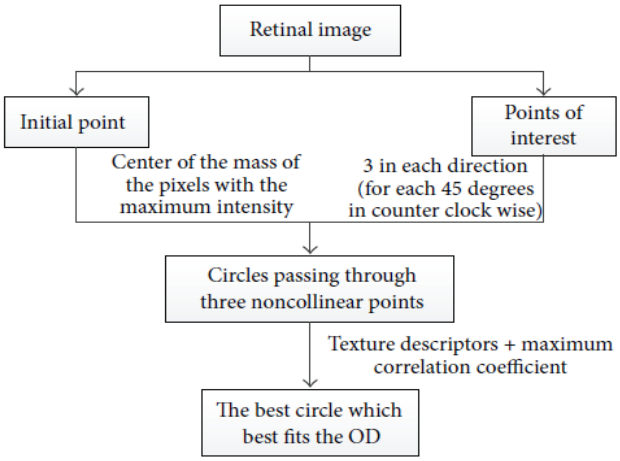

Figure 2.7 Flowchart for algorithm proposed in [36].

Yin et al. [40] have recently proposed a novel technique that consists of edge detection, circular Hough transform, and a statistical deformable model to determine OD (Figure 2.8). The Point Distribution Model was utilized to model the shape of the disc using a series of landmarks. A preprocessing step was performed to analyze the image and reduce the effect of blood vessels. The optimal channel was also selected by applying a voting scheme based on heuristics.

Subsequently, the OD was approximated by a circle using circular Hough transform to determine the optic disc center and diameter. Ultimately, the statistical deformable model was applied to fine-tune the disc boundary according to the image texture. The direct least squared ellipse fitting method was executed to smooth the OD boundary (Figure 2.9). The ORIGA dataset was used to

test the algorithm. The average error in the overlapping area was 11.3% and the average absolute area error was 10.8%.

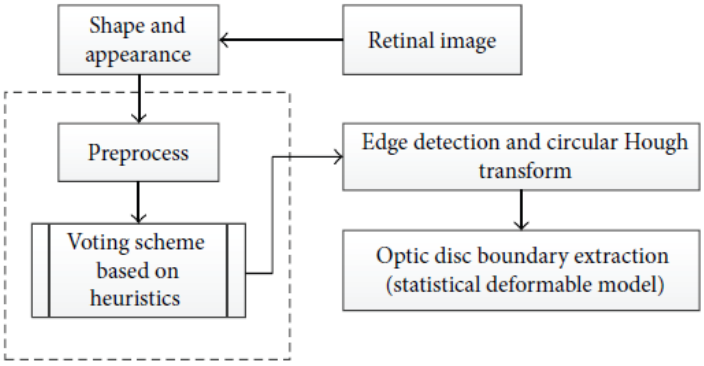

Figure 2.8 Flowchart for algorithm proposed in [40].

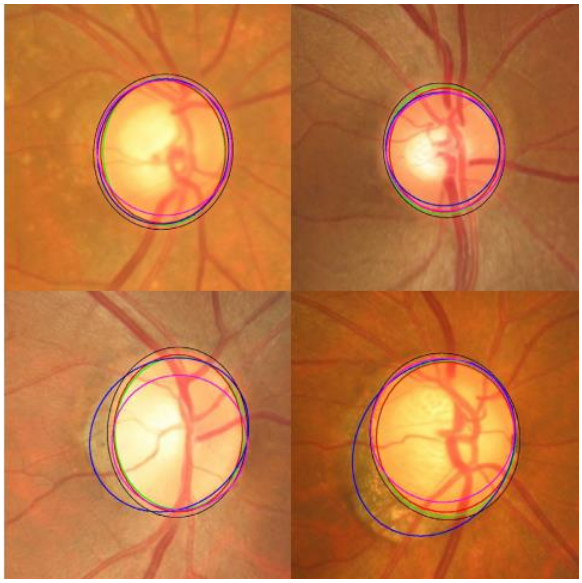

Figure 2.9 Optic disc segmentation using the proposed method (red), level set method (blue), FCM method (black), CHT method (cyan), and ground truth (green).

Cheng et al. [41] proposed an OD segmentation method based on peripapillary atrophy (PPA) elimination. The algorithm included three parts: edge filtering, constraint elliptical Hough transform, and β-PPA detection (Figure 2.10). Extracting the region of interest and detecting the edges of OD were the initial steps in this algorithm. In the aforementioned steps, a low pass filter was applied to remove the noise, and then the first derivative from each row of the region of interest

(ROI) was computed. The first PPA elimination was edge filtering (EF). There are two types of PPA: α and β. α-PPA is pigmentary and includes a structural irregularity of retinal pigment epithelial cells (darker than OD), while β-PPA is a complete loss of retinal pigment epithelial cells (similar color to OD). The α-PPA was detected simply by comparing the ROI with the threshold, i.e., the mean intensity in the ROI, followed by a morphological closing processing. Due to the elliptical shape of PPA together with OD, a second elimination of PPA was conducted by a constrained elliptical Hough transform. Finally, the third PPA elimination was conducted by β-PPA detection. β-PPA is much more difficult than α-PPA due to the similarity of its color with that of OD. To avoid false segmentation between the PPA and OD, a ring area was determined from the detected disc boundary and was divided into quarters. Inspired by the texture within β-PPA, the local maximums and minimums were extracted within the ring and were named as feature points. β-PPA was considered present in a quadrant if the number of feature points in a quadrant exceeded the threshold. The threshold level was obtained by comparing the cases with and without β-PPA. Then the edge points along the detected disc boundary were removed from the quadrant. Finally, the constrained elliptical Hough transform was reapplied to obtain the new disc boundary (Figure 2.11). The ORIGA dataset with 200 images with PPA was used to evaluate the algorithm. Results showed an average overlapping error of 10%, an average absolute area error of 7.4%, and an average vertical disc diameter error of 4.9%. In the future studies, the method should be reapplied to segment OC for diagnosis of glaucoma.

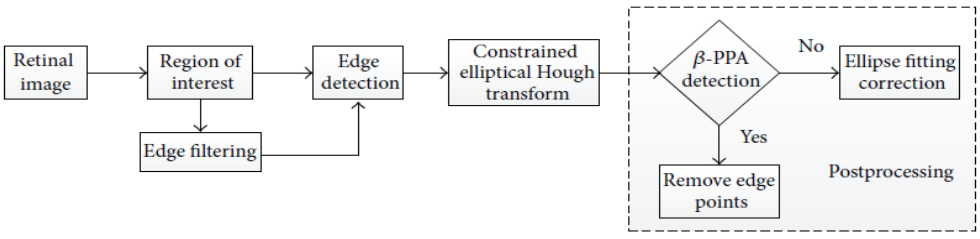

Figure 2.10 Flowchart for algorithm proposed in [41].

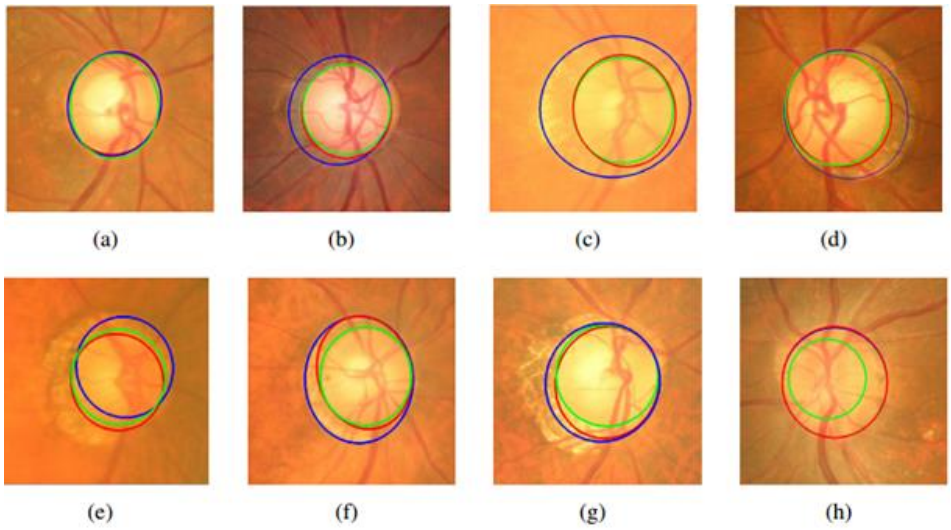

(A)

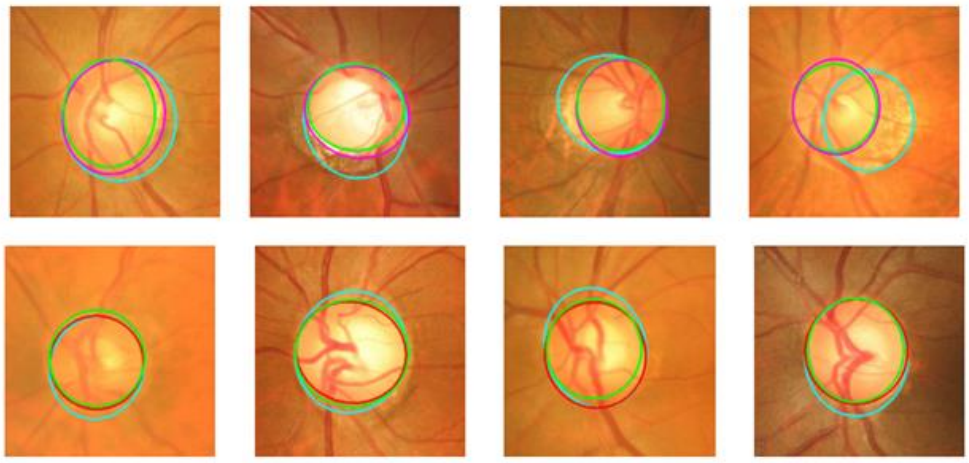

(B)

Figure 2.11 (a) The results (blue: without EF, red: with EF, and green: ground truth). (b)The results (cyan: before β-PPA detection, magenta: after β-PPA detection, red: with ellipse correction, and green: ground truth).

Zhu and Rangayyan [37] proposed an automated segmentation method based on Hough transform to detect the center as well as the radius of a circle that approximates the boundary of OD (Figure 2.12). The method has been used by Gonzalez and Woods [51] and Canny [52]. To calculate reference intensity for circle selection, a preprocessing step was conducted by normalizing the

color image components and converting them to luminance components and then thresholding the effective region of the image. Finally, morphological erosion was used to remove the artifacts from the DRIVE dataset which was used to test this algorithm. A median filter was applied to remove outliers from the image. The components of horizontal and vertical gradient of the Sobel operator were obtained by convolving the preprocessed image with specified operators. The binary edge map was obtained by a threshold applied to the gradient magnitude image. On the other hand, Canny operator was applied to detect the edges based on three criteria: multidirectional derivatives, multiscale analysis, and optimization procedures. After edge detection, Hough transform was applied to detect the center and radius of the circle. The algorithm was tested on two datasets: DRIVE and STARE. The algorithm achieved 92.5% (DRIVE) and 40.24% (STARE) success rates for Sobel method, and 80% (DRIVE) and 21.95% (STARE) success rates for Canny method. The algorithm needs to be improved by applying additional characteristics of OD.

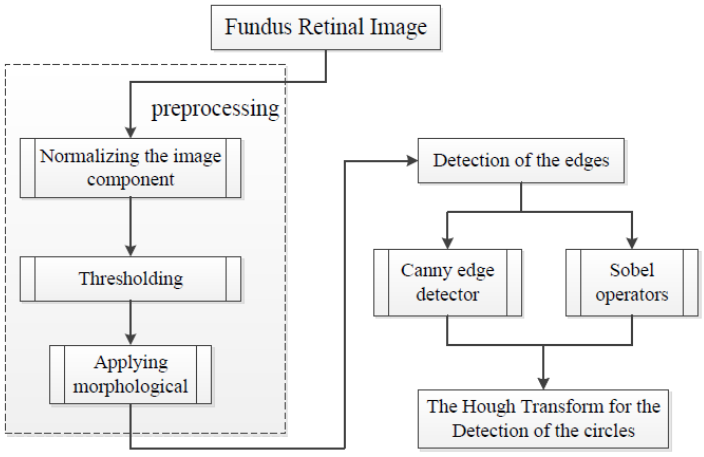

Figure 2.12 Flowchart for algorithm proposed in [37].

Dehghani and colleagues [42] proposed a novel technique that used histogram matching for localizing OD and its center in the presence of pathological regions. The methodology is summarized in Figure 2.13. Four retinal images from DRIVE dataset were used to create three

histograms from the color image components (red, blue, and green) as a template. An average filter was applied to the image to reduce noise. The next step included extracting the OD for each retinal image using a window with a typical size of OD. Then a template was created by obtaining a histogram for each color component for each OD and calculating the mean of the aforementioned histograms. To reduce the effect of pathological regions with high intensity, the histograms with intensity of less than 200 were used. The correlation between the histograms of each channel was calculated in order to gain the similarity of two histograms. Finally, thresholding was applied to the correlation function to localize the center of the OD. The methodology was applied on three datasets: 40 images from DRIVE, 273 images from a local dataset, and 81 images from STARE. The success rates were 100%, 98.9%, and 91.36%, respectively. In the future work, the OD center should be used as the first step for localizing the boundary as well as for human recognition based on the retinal image.

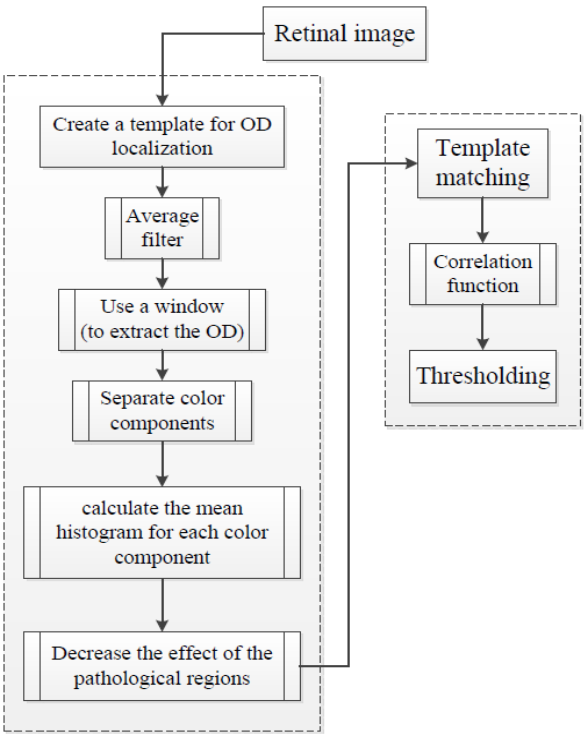

Figure 2.13 Flowchart for algorithm proposed in [42].

Zhang et al. [43] proposed a novel OD localization technique based on 1D projection (Figure 2.14). The vascular scatter degree was used to determine the horizontal location of OD. The vertical location of OD was obtained by brightness and edge gradient around OD. A preprocessing step was necessary in which a binary mask obtained by morphological erosion operation was used to identify the region of interest of the retinal image. Blood vessel extraction was then conducted using non-vessel boundary suppression based on Gabor filtering and multithresholding process [53]. The structure of the main vessels is more critical in measurement of vascular scatter degree; therefore, vessels smaller than 30 pixels were neglected. After preprocessing, a vertical window was defined and was slid over the vessels map to calculate the vascular scatter degree in order to obtain a 1D horizontal projection signal and find the horizontal location of the OD at the minimum position of horizontal projection curve. Then a rectangular window was defined, centered at horizontal location of OD, and slid over Gabor filter map and gray intensity image to obtain the 1D vertical projection signal, where the location of the maximum peak of vertical projection curve was the vertical location of the OD. The algorithm was evaluated on four publicly available and one self-marked dataset: (1) 40 images from DRIVE (achieved 100% success rate); (2) 81 images from STARE (achieved 91.4% success rate); (3) 130 images from DIARETDB0 (achieved 95.5% success rate); (4) 89 images from DIARETDB1 (achieved 92.1% success rate); and (5) 40 images from self-selection (achieved 97.5% success rate). Future studies should test the algorithm using a larger dataset.

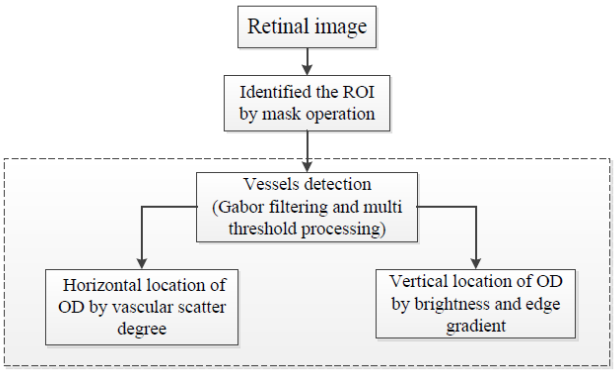

Figure 2.14 Flowchart for algorithm proposed in [43].

Lu [35] proposed an alternative technique for automatic segmentation of OD (Figure 2.15). The technique is based on a circular transformation other than Hough. The circular transformation was conducted to detect the circular boundary and color variation across the OD boundary simultaneously.

A preprocessing step was essential to improve the accuracy of OD segmentation. The intensity image was first derived from the given retinal image by combining the red and green components since these components contain most of the structural information about OD. Several operations were performed to speed up the process and to improve the accuracy. To decrease the computation cost, image size was reduced to one-third. Then the image was filtered by a median filter to suppress speckle noise as well as variation across the retinal vessels. The OD search space was minimized using the OD probability map based on Mahfouz's method [54]. Designing the circular transformation was based on observing the variation of the distance from the point within a circular area to the boundary area which reaches the minimum when the point lies exactly at the centroid region. In particular, each pixel detects maximum variation pixels (PMs) along several evenly oriented radial line segments of specific length. In the next step, the PMs were filtered and finally the OD map was obtained by converting the image. In this map, the maximum value represents

the OD center and the PMs detected for the pixels at the identified OD center lie on the OD boundary. The algorithm was evaluated on three public datasets: MESSIDOR containing 1200 image, ARIA containing 59 images from individuals with diabetes and 61 normal images, and STARE containing 31 normal and 50 pathological images. The OD detection accuracies were 98.77%, 97.5%, and 99.75%, respectively. The OD segmentation technique was applied only on STARE and ARIA datasets, and the accuracies were 93.4% and 91.7%, respectively.

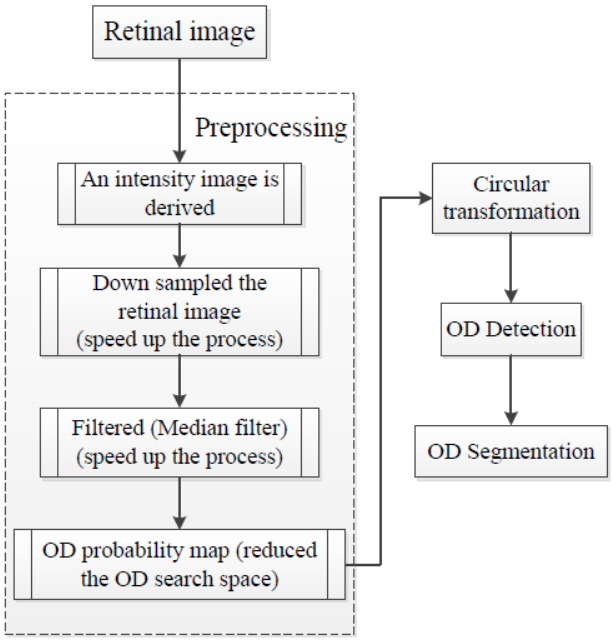

Figure 2.15 Flowchart for algorithm proposed in [35].

Another OD detection algorithm based on the matched filter inspired by means of vessel direction was introduced by Youssif et al. [16] and is summarized in Figure 2.16. In the preprocessing step a binary mask was generated by thresholding the red component image, and then a morphological operator was applied to label the pixels on the ROI. The aforementioned was followed by equalizing the illumination using the Hoover and Goldbaum equation [47] to avoid the negative effects of uneven illumination on the OD localization process [55]. The adaptive histogram

equalization was applied to improve and normalize the contrast and in turn assist in detecting the small blood vessels with low contrast levels.

The blood vessels were segmented based on an algorithm proposed by Chaudhuri et al. [56], where the similarity between the predefined 2D Gaussian template and the fundus image was maximized. To model the retinal vascular in all different orientations, twelve filters were generated to obtain the maximum response for each pixel. To detect the OD direction, match filter was used to match the direction of the vessels at the OD. The algorithm was tested on 40 images from DRIVE dataset and 81 images from STARE dataset. The success rates were 100% and 98.77%, respectively. The future work should aim to improve blood vessel segmentation by applying other pre- and post-processing techniques, using other OD parameters or vascular-related OD (e.g., vessel density and diameter), as well as using a larger dataset for testing the algorithm and employing other vessel segmentation algorithms where the vessels direction map can be obtained.

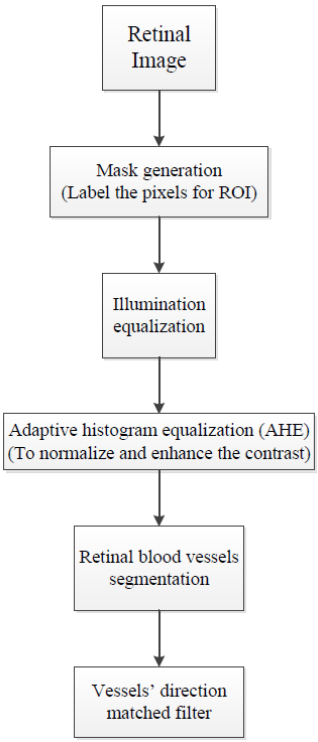

Figure 2.16 Flowchart for algorithm proposed in [16].

A different methodology introduced by Sinha and Babu [45] and Kumar and Sinha [28] is summarized in Figure 2.17. The methodology had two main parts. The first part was OD localization using L1 minimization [45] in which a scale embedded dictionary was created based on manually marked fixed-size sub-images with OD at the center. These sub-images were represented as a column vector to obtain the dictionary elements. Two sets of sparse coefficients, one for the gray intensity image and the other for the red channel image, were obtained. The information from sparse coefficient of each sub-image was converted to a single value, termed confidence measure. Confidence measure calculated the probability of the OD center falling in a given sub-image. The dot products of the confidence values were obtained.

The dot products were rearranged over the 2D image grid to form the probability map representing the possibility of finding the OD. A convolution operation was conducted with Laplacian of Gaussian (LoG) blob detector on the map and the location with the most response was declared as the OD.

The second part of this methodology was OD segmentation [28]. The method considered the difference between the intensity of OD region and the surrounding area. To simplify the process, the search space was minimized by cropping the red channel. The maximum intensity variation points along both horizontal and vertical directions were obtained. The points that did not lie on the OD boundary were considered “false” points and were removed. A Bezier curve was defined by a set of control points to obtain the best closed curve. The curve was then smoothened to obtain the final OD boundary in red color (Figure 2.18). The localization algorithm [45] was evaluated on multiple datasets including DIARETDB0, DIARETDB1, and DRIVE and proved to be successful in 253 out of the total of 259 images from the three datasets (97.68% success rate). The

segmentation algorithm [28] was evaluated on 152 images based on two datasets: DIARETDB1 and MESSIDOR. The average overlapping obtained was 89.5%.

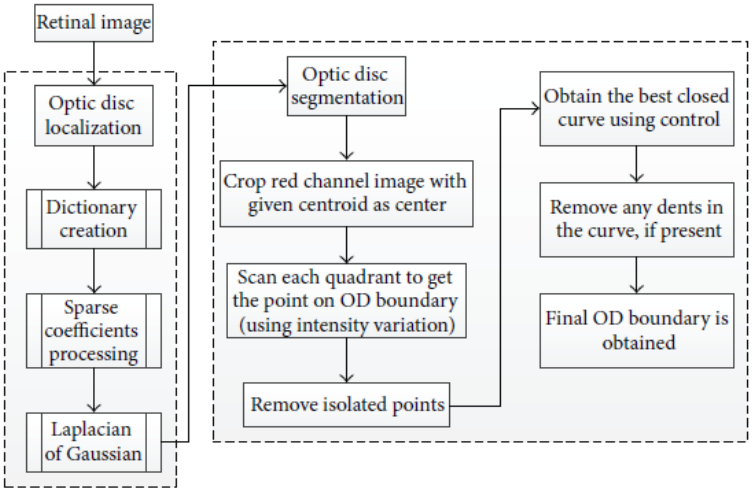

Figure 2.17 Flowchart for algorithms proposed in [28, 40].

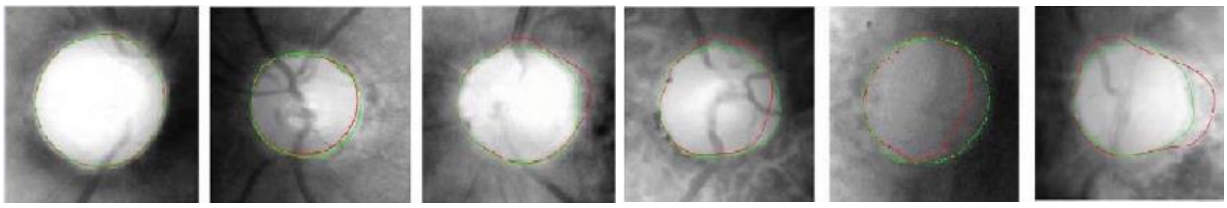

Figure 2.18 Representative results.

2.1.1.2. Optic Cup segmentation approaches

Due to the high density of blood vessels in the optic cup, segmentation of this region is more difficult than optic disc segmentation. Furthermore, the gradual intensity change between the cup and neuroretinal rim causes extra complications for cup segmentation. In addition, glaucoma changes the shape of the optic cup. The OD and OC segmentation techniques, in addition to the techniques used only for OC segmentation, are illustrated in Table 2.3 and the performance results are shown in Table 2.4.

Table 2.3 Categorization optic disc with optic cup segmentation methods.

Authors	Year	Image processing technique	OD/OC	Performance metrics	Dataset	Number of images
Wong et al. [57]	2008	Variational level-set approach	OD/OC	CDR	SERI	104
Wong et al. [58]	2009	Vessel kinking	OD/OC	CDR	SERI	27
Narasimhan and Vijayarekha [59]	2011	K-mean clustering	OD/OC	CDR-ISNT ratio	AEH	36
Ho et al. [60]	2011	Inpainting and active contour mode	OD/OC	CDR-ISNT ratio	CMUH	N/A
Mishra et al. [61]	2011	Active contour method	OD/OC	CDR	ODO, UK	25
Yin et al. [62]	2012	Model-based segmentation	OD/OC	DM, RAD	ORIGA	650
Narasimhan et al. [63]	2012	K-means and openCV code	OD/OC	CDR-ISNT ratio	AEH	50
Cheng et al. [6]	2013	Superpixel classification	OD/OC	CDR	ORIGA + SCES	2326
Annu and Justin [32]	2013	Wavelet energy features	OD/OC	SN – SP – Acc – PPA	N/A	20
Chandrika and Nirmala [64]	2013	K-means clustering and Gabor wavelet transform	OD/OC	CDR	N/A	N/A
Damon et al. [65]	2012	Vessel kinking	OC	Overlap error	SERI	67
Ingle and Mishra [66]	2013	Gradient method	OC	N/A	N/A	N/A

Table 2.4 Performance results for the optic disc and optic cup segmentation.

Authors	Year	Dataset	OD/OC	Sensitivity	Specificity	Overlap error	Success rate (Acc)	AUC	Computation time (s)
Wong et al. [57]	2008	ORIGA	OD/OC			4.81%			N/A
Wong et al. [58]	2009	SERI	OD/OC	0.813	0.455				N/A
Narasimhan and Vijayarekha [59]	2011	AEH	OD/OC				95%		N/A
Yin et al. [62]	2012	ORIGA	OD/OC			9.72%(OD) 32% (OC)			N/A
Narasimhan et al. [63]	2012	AEH	OD/OC	N/A	N/A	N/A	N/A	N/A	N/A
Cheng et al. [6]	2013	ORIGA + SCES	OD/OC			9.5% (OD) 24.1%(OC)		0.800 (ORIGA) 0.822 (SCES)	10.9(OD) 2.6 (OC)
Annu and Justin [32]	2013	N/A	OD/OC	100%	90%		95%		N/A
Chandrika and Nirmala [64]	2013	N/A	OD/OC	N/A	N/A	N/A	N/A	N/A	N/A
Damon et al. [65]	2012	SERI	OC	N/A	N/A	N/A	N/A	N/A	N/A
Ingle and Mishra [66]	2013	N/A	OC	N/A	N/A	N/A	N/A	N/A	N/A

Ingle and Mishra [66] discuss the cup segmentation based on gradient method (Figure 2.19). Gradient is the variation in the intensity or color of an image. The gradient images were obtained from an original image convolved with a filter. Two methods were used to find the gradient: (1) linear gradient, (2) radial gradient. The contrast was improved for all image components (red, blue, and green) by a contrast limited adaptive histogram equalization [67]. The initial threshold was set

for red (R), blue (B), and G (green) components and after much iteration the algorithm identifies the region where R channel pixel value is less than 60 and B and G are greater than 100. Other pixels are neglected giving more details on interested region. The algorithm can be extended to distinguish between the glaucomatous and normal images.

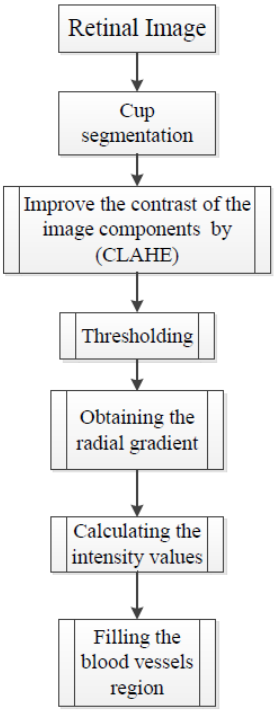

Figure 2.19 Flowchart for algorithm proposed in [66].

Another system for automatic detection of optic cup was proposed by Damon et al. [65] and is based on vessel kinking. To detect the kinks, first the vessels must be detected. The smaller vessels are harder to detect; therefore, a segmentation technique for small vessel detection was introduced by fusing pixel features and a support vector based classification. Patches of interest (POI) were generated within the optic nerve head. Then features for detecting small vessels were generated, where the green channel was chosen for feature generation due to its better visibility for the vessels. A wavelet transform was generated for each POI using Gabor filter to detect the overall

architecture of vessels. A Canny edge detector was applied to detect all possible vessels. Finally, the feature in the vessels segment based approach was fused instead of pixel classification for vessels and non-vessels. Kinking was localized by analyzing the identified vessels segments and locating points of maximum curvature on the vessels (i.e., to fit the segment to a curve). To avoid over or under fitting, a rigorous, nonparametric method was used based on the multiscale shifting window technique. Consequently, the optic cup contour was recognized. The pallor-based cup detection was conducted to detect the cup from the superior to nasal and inferior zones. However, the temporal zone was detected by the kinks. The algorithm was tested on 67 images from the SERI. Figure 2.20 shows the flowchart for the algorithm proposed in [65].

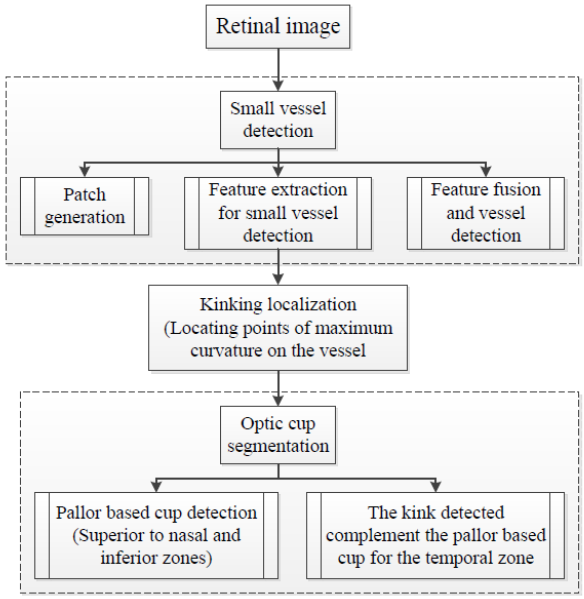

Figure 2.20 Flowchart for the algorithm proposed in [65].

2.1.1.3. Optic disc and optic cup segmentation

To calculate the CDR and ISNT, the optic disc and optic cup should be segmented simultaneously. Elevating the intraocular pressure leads to a posteriorly displacing and thinning of the lamina cribrosa (a sieve-like perforation through which the retinal ganglion cells leave the eye), which

causes deepening of the cup and narrowing of the rim [6, 68]. The neuroretinal rim is an effective factor in glaucoma evaluation according to the ISNT rule, when the optic disc and cup are precisely detected [31, 69].

Wong et al. [58] described a novel technique for detecting blood vessel kinks for optic cup segmentation (Figure 2.21). A preprocessing step was conducted using a level set method to obtain the optic disc and to estimate the initial optic cup boundary. Therefore, a region of interest was extracted and the disc center was identified by thresholding of the red component. Next, variational level set method [70] and direct ellipse fitting approach [71] were applied to obtain and smoothen the optic disc. The initial contour was obtained by extracting the OD region in green channel. The results were then ellipse-fitted in order to provide an approximation of the cup boundary based on pallor. Square pixel size patches were used as guide based on the pallor cup boundary to locate the kinks within the optic disc. Canny edge detection and wavelet transform were applied separately in the green channel to detect the kinks on the intradisc vessel edges. To avoid the effects of protrusion along some of the detected edges, a polynomial application was used to smooth each edge, followed by vectorizing the vessel edges and dividing them into 15 segments. The kinks were identified by calculating the change in the angle between each of the two edges. Finally, the kinks and the additional points with the direct ellipse fitting method were used to determine the OC boundary. The algorithm was evaluated with 27 images from SERI. The CDR calculated by the kink and pallor methods were compared with the ground truth CDR and the average error of each method was calculated. The average errors were 0.139 and 0.093 for pallor method and kink method, respectively.

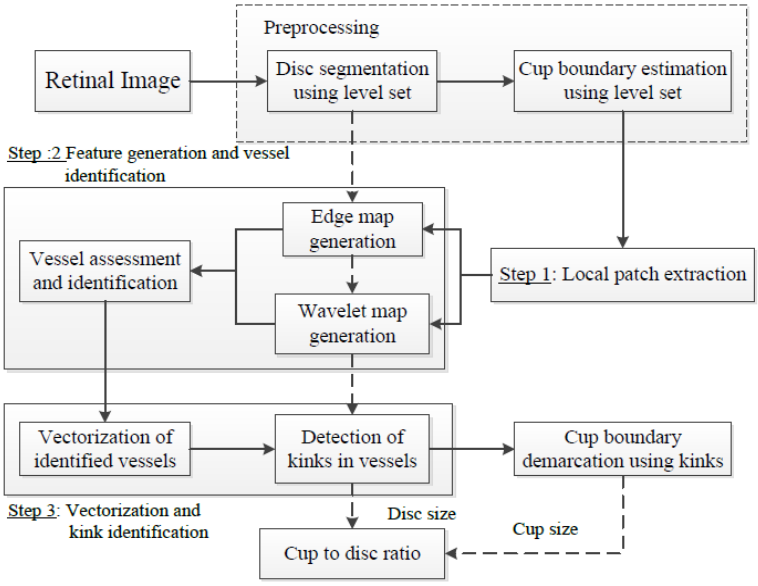

Figure 2.21 Flowchart for algorithm proposed in [58].

Yin et al. [62] introduced a statistical model based method that combines circular Hough transform and a novel optimal channel selection for OD and OC segmentation. The method is summarized in Figure 2.22. The active shape model using 24 landmark points around the OD was used as the first step. A preprocessing was conducted to decrease the effect of blood vessels, and the best image was determined based on the image contrast ratio. Identifying the OD center and approximating the OD size requires a good initialization. Therefore, Canny edge detector and circular Hough transform were applied to obtain the edge map and approximate the OD, respectively. Then the statistical deformable model was initialized to adjust the OD boundary. To update the OD segmentation, the landmark position by minimizing the Mahalanobis distance was conducted, followed by the direct least squared ellipse fitting method to smooth the boundary of the contour (Figure 2.23). On the other hand, the OC boundary was extracted by applying the active shape model in the green channel of the image without blood vessel. The optic cup center is close to the OD center; therefore, the model was initialized by translating the mean cup model

to the OD center (Figure 2.24). The ORIGA dataset consisting of 650 images was used to evaluate the algorithm. The average Dice coefficient for the OD and OC segmentation was 0.92 and 0.81, respectively. The mean absolute CDR error was 0.10.

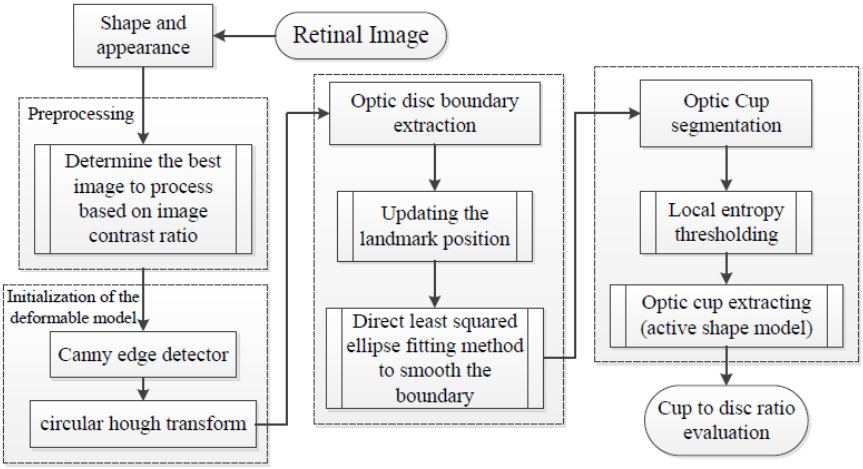

Figure 2.22 Flowchart for algorithm proposed in [62].

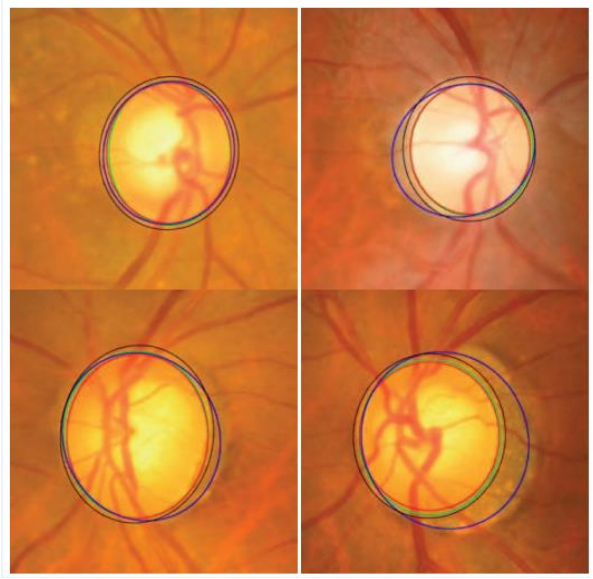

Figure 2.23 OD segmentation using proposed method (red), level set method (blue), and FCM method (black) with ground truth (green).

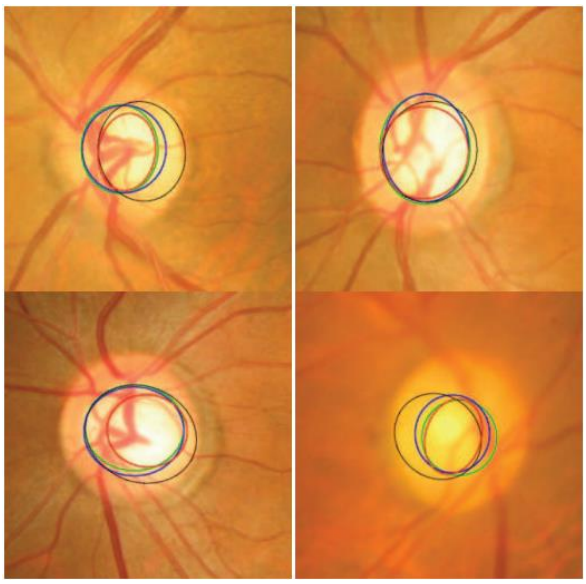

Figure 2.24 Optic cup segmentation using the proposed method (blue), ASM method without vessel removal (red), and level set method (black) with ground truth (green).

Superpixel classification based optic disc and optic cup segmentation for glaucoma screening system was introduced by Cheng et al. [6] and is illustrated in Figure 2.25. Classifying each superpixel as disc or non-disc in the OD segmentation was done based on histograms and center surround statistics. On the other hand, in the OC segmentation the location information was also included. A Simple Linear Iterative Clustering algorithm [72] was used to gather nearby pixels into superpixels. Extracting OD features was achieved by enhancing the contrast using the histogram equalization for the three image components (R, B, and G) and computing the center surround statistics to avoid color similarity in the group of pixels forming the superpixel. A Library for Support Vector Machine (LIBSVM) [73] was used as classifier to extract the OD boundary (Figure 2.26). Detecting the OC boundary was based on the feature extraction where the histogram feature was computed. Red channel histograms were excluded. The center surround statistics was computed similar to the OC feature extraction. Finally, LIBSVM was used as classifier to extract the OC boundary (Figure 2.27). Knowing the OD and OC, the CDR could be computed. The

algorithm was evaluated based on 2326 images from two resources: SiMES and SCEN. Results showed an average overlapping error of 9.5% in optic disc segmentation and 24.1% in optic cup segmentation using only the SiMES dataset.

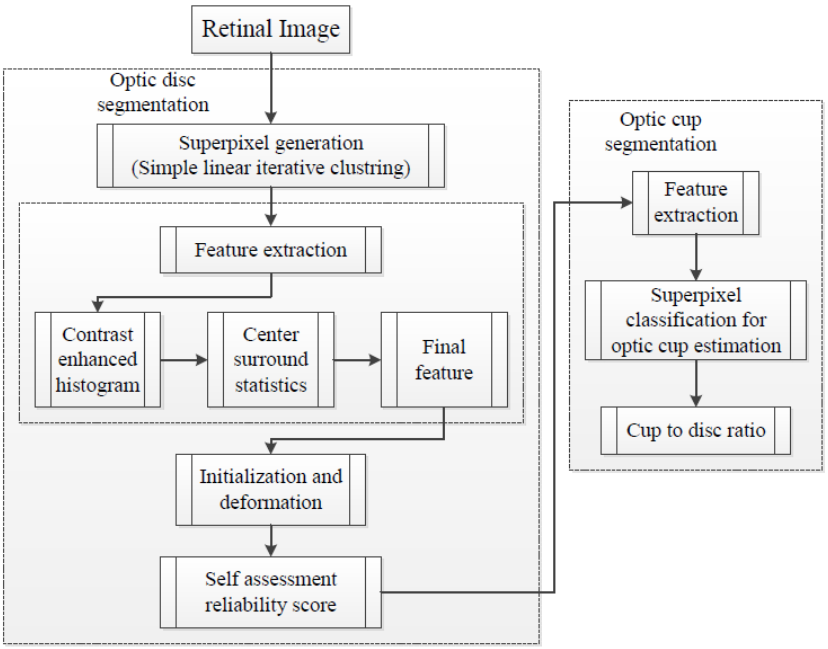

Figure 2.25 Flowchart for algorithm proposed in [6].

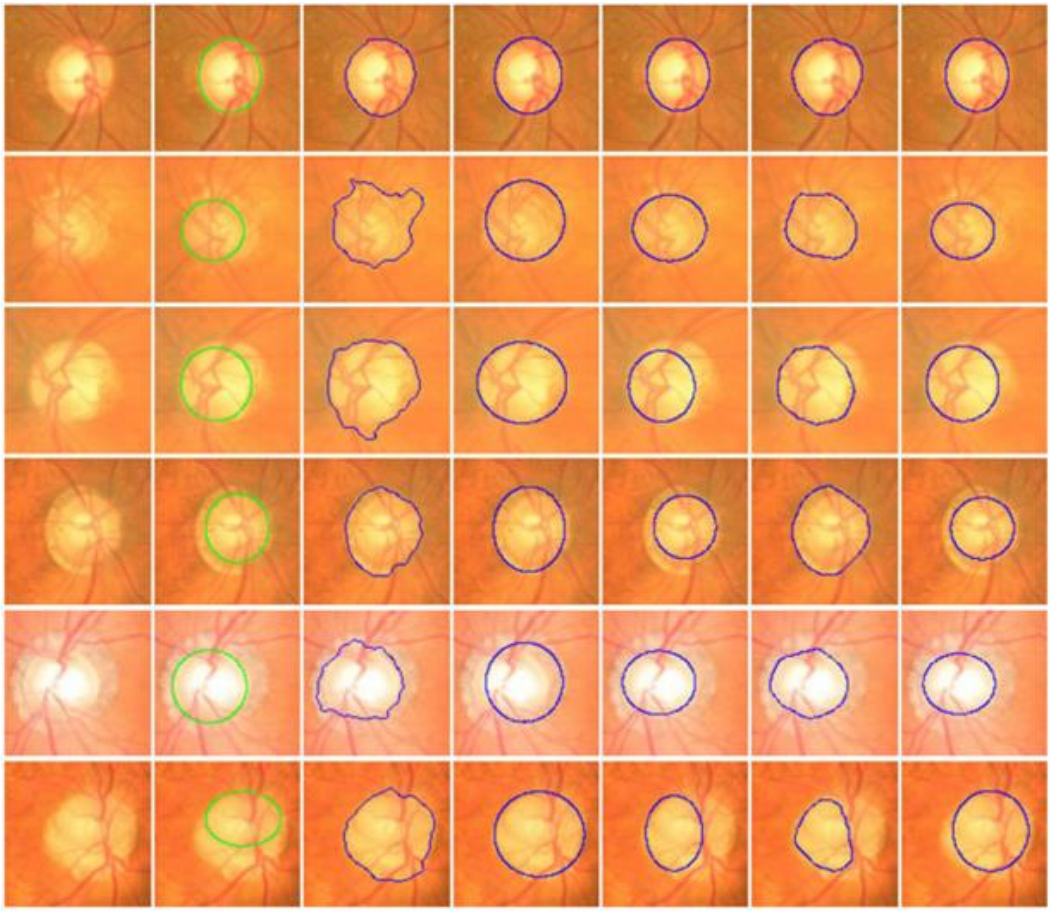

Figure 2.26 Sample results of the optic disc. From left to right columns: (a) the original images, (b) the manual "ground truth," and ((c)–(g)) outlines by the MCV, CHT-ASM, EHT, and MDM.

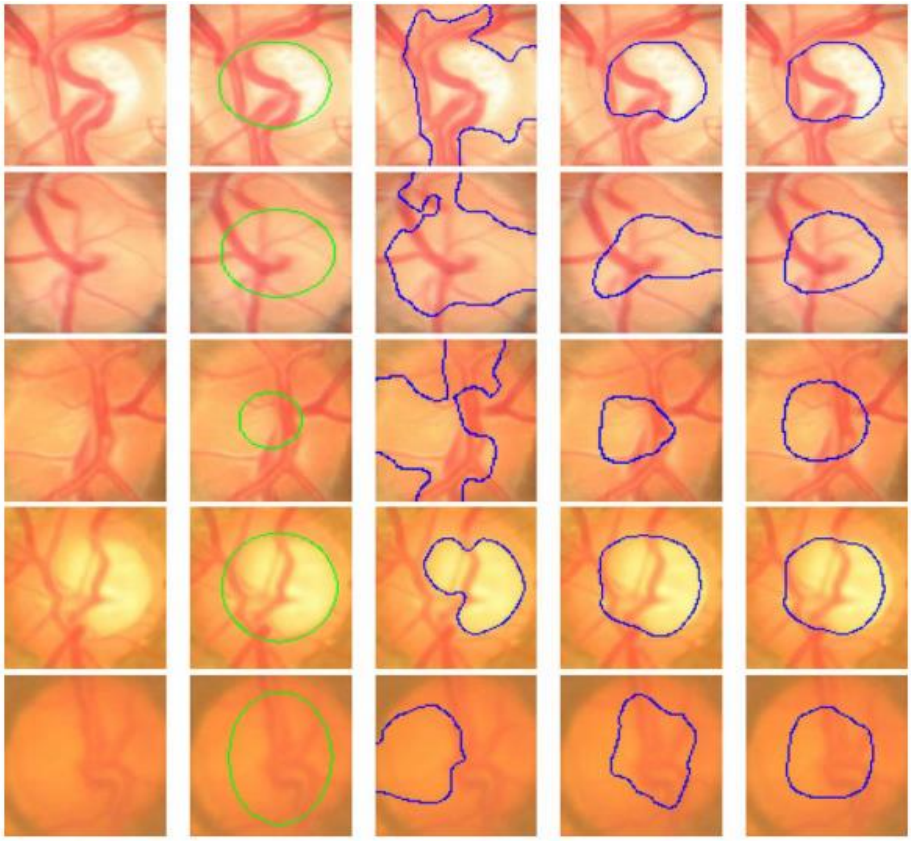

Figure 2.27 Sample results of the optic cup. From left to right columns: (a) the original images, (b) the manual "ground truth," and ((c)–(e)) outlines by the proposed method before ellipse fitting.

Mishra et al. [61] proposed an active contour method to find the CDR in order to determine glaucoma (Figure 2.28). The green channel image was used in the segmentation process similar to the previous algorithms. Illumination was corrected using a mathematical morphology in which the background of the image was estimated by morphological opening process. The blood vessels were removed by applying a morphology based vessel segmentation proposed by Fraz and colleagues [74]. Subsequently, image inpainting was used to replace the blood vessel region with plausible background. Multithresholding and active contour method were used to determine OD and OC boundaries. Thus, the CDR could be calculated. The method was tested on 25 images obtained from an optic disc organization in UK. Preprocessing techniques were required to improve the results.

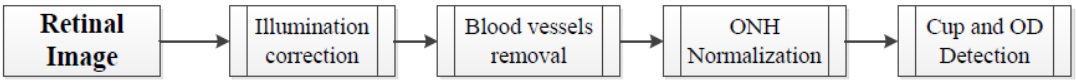

Figure 2.28 Flowchart for algorithm proposed in [61].

Wong et al. [57] proposed an automatic CDR detection algorithm based on a variational level set approach (Figure 2.29). Localizing the OD using intensity information was the first step. Therefore, an image histogram was obtained in which pixels with the highest intensity were selected to be the disc region. Also, the image was divided into 64 regions, and the disc center was the region with the most high intensity pixels. The ROI was identified by a circle with a radius twice as long as the typical normal OD radius. The variational level set algorithm was applied to detect the OD boundary using red channel. Next, ellipse fitting was applied to smooth the boundary. Due to the high density of blood vessels in the OC region, the green channel was selected to be processed. The OC was segmented by applying threshold initialized level set from the segmented disc. The boundary was smoothed by ellipse fitting. The CDR was calculated as the final result. The methodology was evaluated using 104 images from SiMES and the results produced up to 0.2 CDR units from manually graded samples.

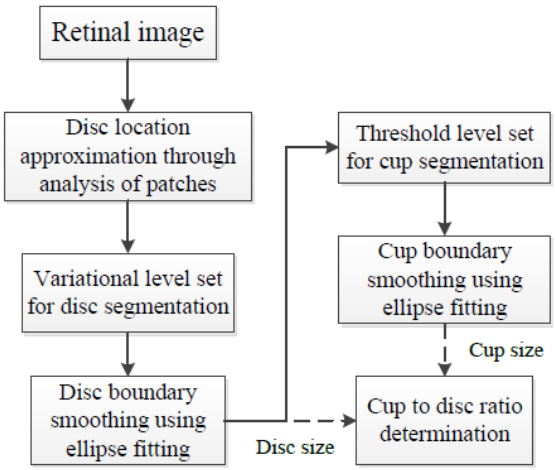

Figure 2.29 Flowchart for algorithm proposed in [57].

To calculate CDR, K-mean pixel clustering technique and Gabor wavelet transform [64] were used to segment the OD and OC separately (Figure 2.30). The K-mean clustering classifies the data into a number of clusters. For each cluster, K centroids were defined and each point in the data was associated to the nearest centroid to create groups. The first step was completed when no point was pending and an early group was created. Then K was recalculated to new centroids as barycenters of the clusters of the previous step. As the result, a new binding had to be made between the same data and the nearest new centroid. A loop was created to track the location of the centroids until centroids did not move any more in order to reduce the objective function (squared error function). The K-mean clustering was conducted on ROI identified by a mask. Finally, OC and OD were segmented using green plane to choose the mean value for background blood vessel. Then the disc and cup were replaced, where the image was mapped in 4 iterations to calculate the mean value of the matrix distance. Morphological feature was performed to smooth the cup and disc boundary. Gabor wavelet transform was also executed to avoid problems due to the presence of blood vessels. Since the vessels have directional pattern, the Gabor wavelet transform was tuned for specific frequencies and orientations to filter out the background noise.

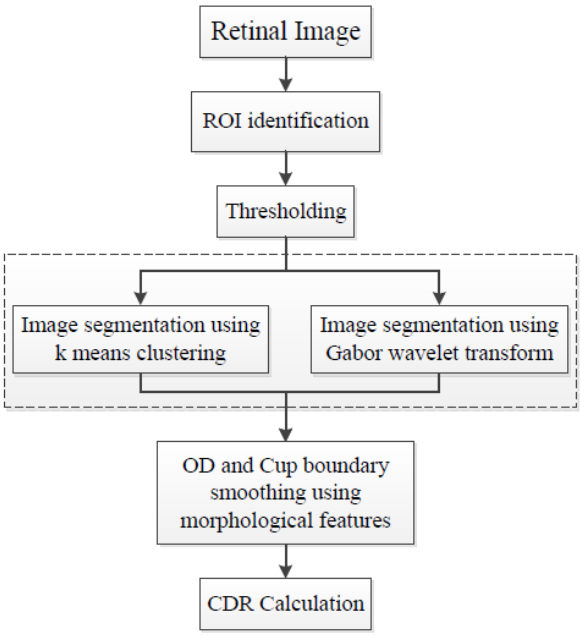

Figure 2.30 Flowchart for algorithm proposed in [64].

Ho et al. [60] developed a novel technique for automatic fundus image analysis for glaucoma screening (Figure 2.31). The technique involved two major steps. Detecting the blood vessels was the initial step and was conducted using two structural characteristics: shape and continuity feature. A Canny edge detector was applied to detect general edges containing the boundaries of blood vessels, where the green channel was used in the analysis. Bayesian rules were used to generate an accurate confidence map by combining the horizontal and vertical confidence maps from the shape and continuity feature. Fast Marching Method was employed to fill the vessels' free spaces and then the peak thresholding from inpainted image histogram was executed for segmentation, where the image was segmented into three regions. Firstly, in order to estimate the disc boundary, the three regions were fitted with two circles and the active contour model was applied to extract the boundaries of the inner cup and surrounding disc. Then the CDR parameter and ISNT rule were calculated. A dynamic histogram equalization technique may be applied to enhance the image

contrast and to avoid wrong identification of the CDR and ISNT due to unclear OC on vessel free images.

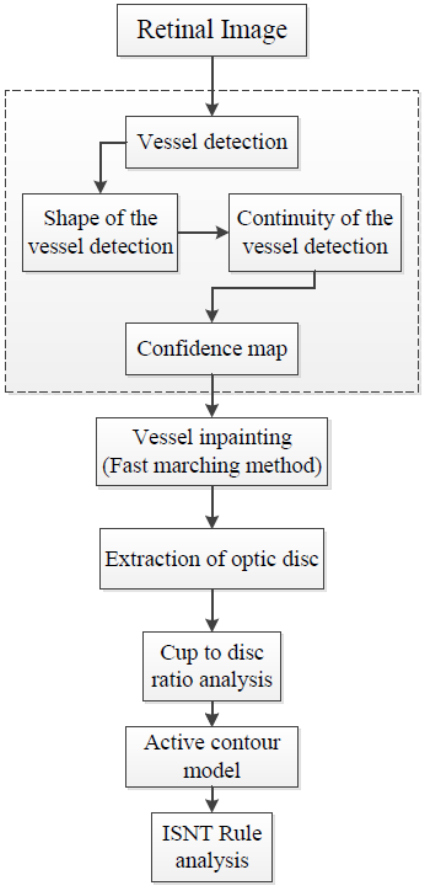

Figure 2.31 Flowchart for algorithm proposed in [60].

Narasimhan and Vijayarekha [59] introduced a new system for glaucoma detection based on K-mean clustering technique to extract OD and OC and also an elliptical fitting technique to calculate the CDR. In addition, a local entropy thresholding approach was applied to detect the blood vessels and compute ISNT. The system consisted of three phases (Figure 2.32). The first phase was ROI extraction considering green plane. The second phase was feature extraction through K-mean clustering [64]. ROI covered the OD, OC, and a small region near the OD in the retinal image; thus, the K value was chosen as 3. The clusters not belonging to OD and OC were removed. As

the result, two clusters from the OD region remained, since the operation was conducted to fill the holes and spaces inside OD and OC clusters.

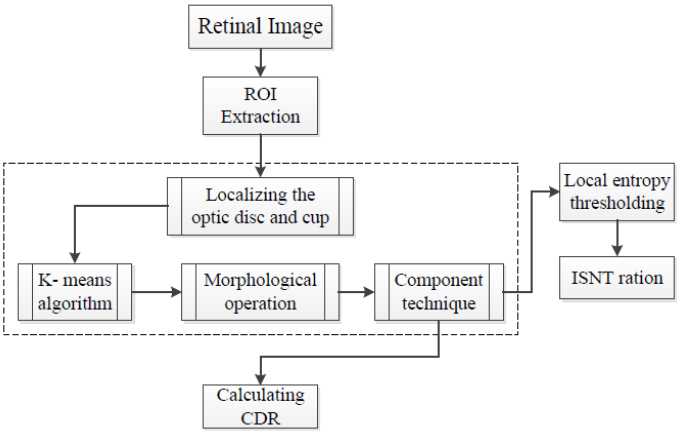

Figure 2.32 Flowchart for algorithm proposed in [59].

Subsequently connected component technique was applied to form rectangles that represented the entire OD and OC. To calculate CDR, elliptical fitting technique was executed on OD and OC and the areas of the ellipse, OC, and OC were computed using a specific formula. The ISNT was computed by measuring the area of the blood vessels in the four quadrants. Therefore, a local entropy thresholding was used to segment the blood vessels and then a mask was applied to measure the four areas. Three classifiers, that is, KNN, BAYES, and SVM, were used to test 15 normal and 21 glaucomatous images. KNN achieved 93.3% and 80.9% success rates; BAYES achieved 86.6% and 95.23% success rates; and SVM achieved 100% 95.23% success rates for normal and abnormal images, respectively.

Annu and Justin [32] proposed another method for automated classification of glaucoma by wavelet energy feature. The technique uses texture features within the image by applying energy distribution over wavelet subbands and efficient glaucoma classification based on Probabilistic Neural Network. Figure 2.33 illustrates a summary of the algorithm. The wavelet features were

gained from the Daubechies (db3), symlets, and biorthogonal wavelet filters. Z-score normalization was applied to the images to equalize the irregular illumination associated with the image. The feature of the retinal image was extracted to simplify the classification process since it provides characteristics of input pixel to the classifier. Therefore, the wavelet transform was applied. Various textures have different energy in the space frequency domain; hence, the energy obtained from the coefficient was used to distinguish between the normal and glaucomatous images. Finally, a Probabilistic Neural Network was used as the classifier to analyze image properties and classify the dataset. This involved two phases: a training phase and a testing phase. In the training phase the known data was given and in the testing phase the unknown data was used. The algorithm was applied on 10 normal and 10 glaucomatous images, and 15 images were used for training. The results showed sensitivity, specificity, positive predictive accuracy, and accuracy of 100%, 90%, 90%, and 95%, respectively.

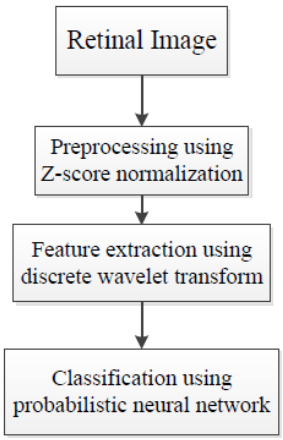

Figure 2.33 Flowchart for algorithm proposed in [32].

The OD and OC segmentation technique proposed by Narasimhan and colleagues [63] implements the open CV library functions based on *K*-mean clustering and elliptic fitting (Figure 2.34) to calculate CDR. The cvMinAreaRect2 was used to draw the ellipse and the blood vessels were

extracted using matched filter in which cv2DRotationMatrix and cvWarpAffine were used to rotate the kernel. Finally local entropy thresholding was applied to compute ISNT ratio. The openCV was mainly used to increase the operation speed. The method was evaluated on 50 images obtained from Aravind Eye Hospital in India.

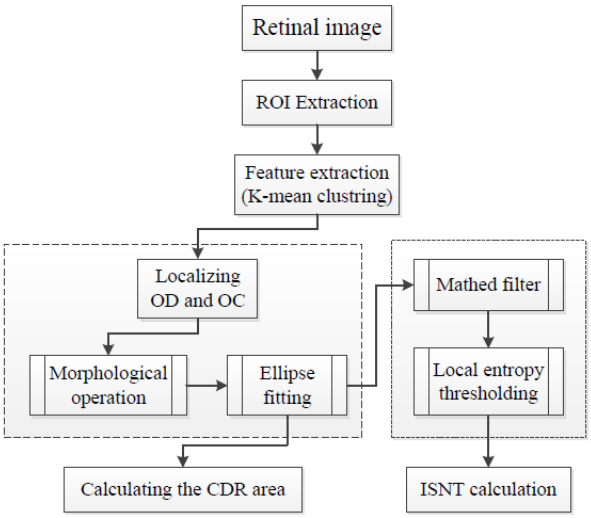

Figure 2.34 Flowchart for algorithm proposed in [63].

2.1.1.4. Discussion

This chapter provided a comprehensive review of the algorithms used for OD and OC detection and segmentation that help with diagnosis of glaucoma by detecting the main structures of the ONH. Many algorithms were limited due to the complexities of ONH structure which is very variable among people and among different pathologies. The variabilities in the ONH structure also cause difficulties in diagnostic observations. Papillary atrophy causes some difficulties for disc segmentation due to its similarity in intensity to disc boundaries. However, there are some algorithms that can segment the disc with PPA perfectly. On the other hand, disc drusen causes greater difficulty for segmentation since the changes that appear on the disc boundaries completely cover the disc, especially in advanced cases. No current segmentation technique considers disc

drusen based on retinal fundus images due to the rarity of the case and its complexity in terms of image processing. Myelinated nerve fibers (MNF) form a white cloud that surrounds the optic disc. In severe cases the ONH is totally covered, making the disc and cup boundaries hard to detect for the professional experts as well as the algorithms. Disc hemorrhage is another case where parts of the optic disc might be covered. Moreover, disc edema is one of the most important cases that make optic disc cup boundaries ambiguous. On the other hand, the ONH, which plays an important role in accurate segmentation of cup boundaries, is partially covered with blood vessels. This is a challenge facing many researchers and there are limited segmentation techniques that address this challenge. The algorithms performed differently depending on the datasets of images. Some approaches used a small dataset, while some used large datasets to train and test the algorithm. Many methods were tested only on normal retinal images, and those that were evaluated on pathological images used different number of glaucomatous images. Also, the severity of the disease was different among the datasets used in different techniques; therefore, the corresponding algorithms cannot be compared with each other. Most OD segmentations were based on the circular Hough transform along with other detection techniques. Aquino et al. [34] obtained excellent results based on a large dataset (MESSIDOR) for both localization and segmentation of OD; however, errors occurred due to ellipse eccentricity that was not suitable for circular approach. Yin et al. [40] introduced edge detection, and a circular Hough transform to estimate the OD center and diameter, and a statistical deformable model to adjust the disc boundary according to the image texture. Utilizing a large dataset, the method showed good results. Cheng et al. [41] also achieved good results by eliminating the peripapillary atrophy based on edge filtering, constraint elliptical Hough transform, and peripapillary atrophy detection. Due to the low contrast of the disc boundary, OD boundary was not detected in some images. Therefore, a preprocessing stage to

select the best image component is necessary to improve the results. Lu [35] gained excellent results based on three datasets: STARE, ARIA, and MESSIDOR. A circular transform was designed to determine the circular shape of OD and also the image variation across the OD boundary with a very short computation time of only 5s. Three sources of error contributed to segmentation failure for a few images; these were as follows: (1) the large color variation across the OC boundary might have caused the PMs to fall on the cup boundary instead of disc boundary, (2) due to ultralow image variation across the OD boundary, much of the OD boundary had no PM detected and therefore the OD boundary remained undetected, and (3) the error introduced by the PMs was created based on symmetry. On the other hand, Cheng et al. [6] obtained perfect results using an OD and OC segmentation algorithm based on superpixel classification utilizing histograms and center surround statistics. However, a preprocessing step was essential to improve the image. Also, to create a robust algorithm multiple kernel learning [75] was required for enhancement and extraction of blood vessels to fine-tune the cup boundary. Sinha and Babu [45] proposed an algorithm to localize the OD based on L1 minimization. The algorithm achieved a high success rate in localizing the OD, and failed in only 6 out of 259 images. The fails were due to the scaling factor which needed to be fixed at the start of a trial for the dataset to down sample the image to suitable size in tune with those in the dictionary. The OD detection was then followed by segmenting technique [28]. This approach sometimes results in false segmentation due to the blood vessels and nerves crossing the OD that appear darker than OD and therefore restrict the search space in the retinal image. In general, in addition to blood vessel extraction, a preprocessing step including image channel selection, illumination normalization, and contrast improvement is necessary for a robust approach in OD and OC segmentation. Retinal pathological images that have captured the effect of the disease on the optic nerve head must be considered in order to

obtain correct computations of the CDR and ISNT for the glaucoma screening. Precise OD and OC localization lead to perfect segmentation. The aforementioned highlights the importance of utilizing an accurate localization technique. Evaluating algorithm based on various datasets will increase the reliability of the outcomes.

2.2. Objectives of this Thesis

Even though there is considerable literature on segmentation of optic disc and optic cup, there is still plenty room for improvement in segmentation techniques. Some of the issues were discussed above. Only few of the existing methodologies, whether for optic disc or optic cup segmentation, can be applied for glaucomatous retinal images. Also, most of the current methods have been tested on a limited number of datasets such as DRIVE and STARE. These datasets do not provide images with many different characteristics. Furthermore, the generally low resolution of the images (ranging from 0.4 to 0.3 megapixels) has made the segmentation process even more challenging [76]. An advanced camera capable of taking high volumes of high resolution retinal images will facilitate glaucoma screening. In order to achieve good outcomes for the images captured by different systems, robust and fast segmentation methods are required. Most of the retinal images used to evaluate segmentation methods have been taken from adults. The retinae of infants, babies, and children have different morphological characteristics than that of adults, and this difference must be considered in segmentation methodologies [76]. The glaucoma screening system complements, but does not replace, the work of eye care specialists in diagnosis; routine examinations have to be conducted in addition to fundus image analysis. However, image processing facilitates diagnosis by calculating the disc and cup structural parameters and showing greater details of ONH, such as the disc and cup areas, the vertical and horizontal cup-to-disc ratios, and cup to disc area ratio, and also checking the ISNT arrangement. This is a shareable

knowledge that could intersect the worlds of eye care specialists and engineers. The main contribution of this thesis is in introducing a novel automatic optic disc and cup image segmentation system for diagnosing glaucoma using a unique image dataset in order to overcome many of the limitations mentioned in the literature review. The segmentation was conducted by computing the ONH structure automatically in four main steps. The newly collected and manually annotated dataset is covered in the next chapter (chapter 3), followed by the two optic disc and cup methodologies algorithms (chapters 4). The results are presented and discussed in Chapter 5. Finally, the conclusion and future work are presented in Chapter 6.

Chapter 3

RIGA dataset

3.1. Introduction

Most of the retinal data are stored locally and are not accessible to researchers. Therefore, an online dataset has been created to share retinal data with interested clinicians and researchers. The clinical reference retinal images were acquired using a fundus camera with or without pupil dilation during routine clinical examinations. The aim is to provide open access to such images for research and educational purposes as well as to benchmark various computer segmentation techniques with reliable outcomes. Currently, a dataset of Retinal Fundus Images for Glaucoma Analysis (RIGA) has been created that contains 750 retinal images obtained from three different sources. The images were manually annotated by 6 ophthalmologists, making the dataset unique in that each image was analyzed by multiple professionals instead of just one person, in order to decide whether the image is eligible for training and testing of any developed system. A wide collection of signs, critical for diagnosis of glaucoma, were annotated. Six geometrical parameters were calculated for every member of the dataset. The dataset will be updated continuously with more manually annotated images.

This research received all necessary approval and clearance from the Office of Research Ethics of the University of Waterloo. There is no disclosure of any personal information such as names, addresses, race, etc. and the methodology conforms to ethics standards set by the University.

3.2. Images resources

The dataset described here consists of 750 fundus images (pairs of images from right and left eye) collected from three different resources (Table 3.1). Four hundred and sixty images were collected from MESSIDOR dataset, and 195 images from Bin Rushed Ophthalmic center in Riyadh, Saudi Arabia (71 images from females, and 124 images from males; participants were between 21 to 77 years old). The Saudi Arabian images were obtained in 2014 using a Canon CR2 non-mydriatic digital retinal camera. The dataset contains both normal and glaucomatous fundus images. The images are 2376X1584p. An additional 95 images were obtained from Magrabi Eye center in Riyadh, Saudi Arabia (48 images from females and 47 images from males; participants were between 9 to 83 years old). The images were obtained between 2012 and 2014 using a TOPCON TRC 50DX mydriatic retinal camera. The images are 2743X1936p. The images were chosen randomly with regard to glaucomatous and normal images.

Table 3.1 Details of the RIGA dataset**.**

	Images numbers	**Images sizes**	**Capture data**
MESSIDOR images	460 images	2240X1488p 1440X960p	2004
Bin Rushed images	195 images	2376X1584p	2014
Magrabi	95 images	2743X1936p	2012-2014
Total	750 images		

3.3. Optic disc and optic cup manual annotations

Six glaucoma specialists from different eye centers in Saudi Arabia annotated the optic disc and cup boundaries manually using high resolution tablets (Microsoft surface Pro 3). Each tablet's screen size was 12 inches with a resolution of 2160x1440. Every ophthalmologist manually annotated each of the 750 images; therefore, in total 4500 annotated images were obtained. The images were annotated using the terms shown in Table 3.2.

The major problems in annotating the disc and cup were hazy and unfocused images, tilted discs and myopic discs. Other factors that might have led to inaccurate annotation were examiner's fatigue and tiredness (annotating at the end of the day), and also the busy and unfocused examiners who tried to do the annotation quickly and during their busy clinic hours.

Table 3.2 Notations used for the images.

Annotation Term	**Details**
Image Quality Cup	Clear/ Non clear
Glaucoma suspicious	Normal/ suspicious/ highly suspicious
Disc Size	Large Disc / Middle Disc / Small Disc
Vertical cup to disc ratio	automatically calculated
Horizontal cup to disc ratio	automatically calculated
Cup to disc area ratio	automatically calculated
ISNT rule	Follow ISNT rule / Not follow ISNT rule
Notch	Yes / No
Disc Hemorrhage	Presented / not presented
Alpha PPA	Presented / not presented
Beta PPA	Presented / not presented

3.4. Manual annotation segmentation and calculating the geometrical parameters

The manual annotation was found by subtracting the original image (without annotation) from the annotated image. The difference was manual annotations, i.e., two closed areas which were nearly circular (Figure 3.1).

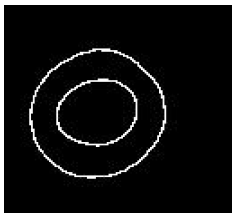

Figure 3.1 The manual annotation image segmentation.

The pixels of two circles were detected by dividing the image vertically into two pieces and then detecting the white spot. After segmenting the manual annotations, for every single image annotated by all six ophthalmologists, six geometrical parameters were calculated, namely, disc area and centroid, cup area and centroid, and horizontal and vertical cup to disc ratio (Figure 3.2).

For the horizontal and vertical cup to disc ratio calculations, the technique was to find the maximum and minimum pixels for both optic disc and cup, then the cup to disc area ratio was calculated. This information will be used in analyzing the variations between the 6 experts and will also be a reference to train and test the automatic disc and cup segmentation techniques.

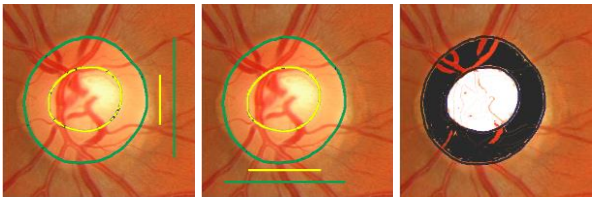

(a) (b) (c)

Figure 3.2 The geometrical parameters for the optic disc and cup. a) Vertical cup to disc ratio; b) Horizontal cup to disc ratio; c) disc area and centroid and cup area and centroid.

Six opinions were applied on every single image of RIGA dataset. Figure 3.3 shows an example of how the optic disc and optic cup were annotated by the experts and the results are compared in Figure 3.4. Clearly the disc areas were between the tight range of 36000 and 37000 pixels. While the cup areas were between 15000 and 18000 pixels, indicating more variation due to blood vessels in the nasal side. This caused a greater variation in the horizontal cup to disc ratio; the horizontal cup to disc ratio ranged between 0.63 and 0.73, a variation of 0.1. The vertical cup to disc ratios however, were between 0.64 and 0.67; a variation of 0.03.

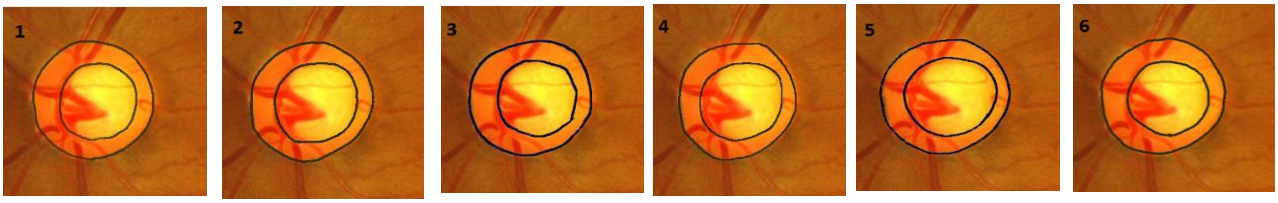

Figure 3.3 Example for a clear cup and disc annotated by 6 Ophthalmologists.

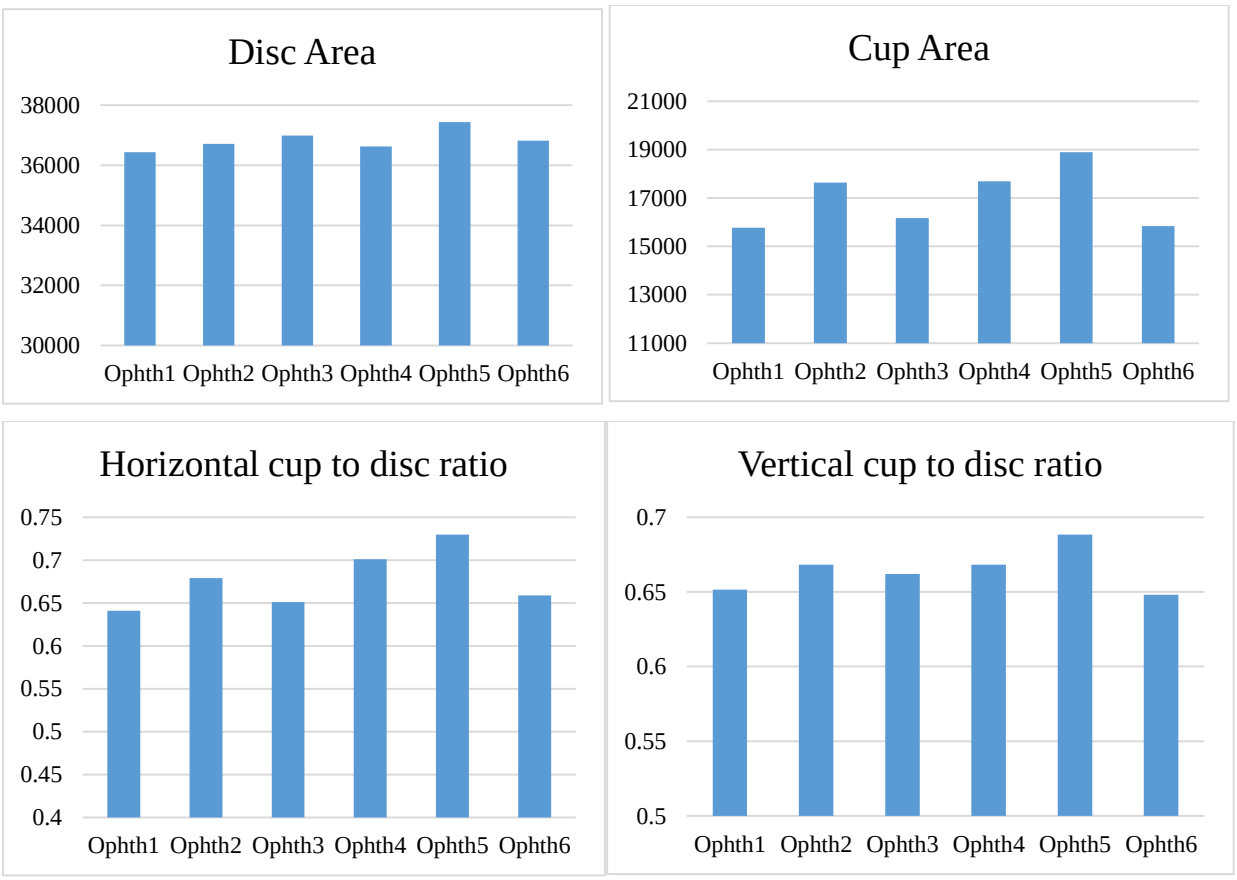

Figure 3.4 Results of the geometrical parameters for the 6 ophthalmologists for figure 3.3. The X axis represents the number of 6 ophthalmologists and the Y axis represents the number of pixels for the top graphs and represents ratio for the bottom graphs.

Figure 3.5 shows an example of a hazy image in which the cup boundary was annotated by six ophthalmologists. The differences between the annotations can be easily seen. The variation in the vertical cup to disc ratio was between 0.5 and 0.63, and in the horizontal cup to disc ratio was between 0.5 and 0.6 (Figure 3.6). The annotations done by the 6 ophthalmologists are clearly different from each other.

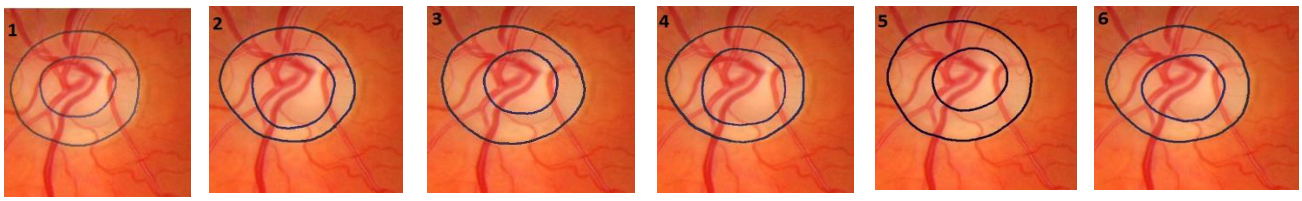

Figure 3.5 Example for an unclear cup annotated by 6 Ophthalmologists.

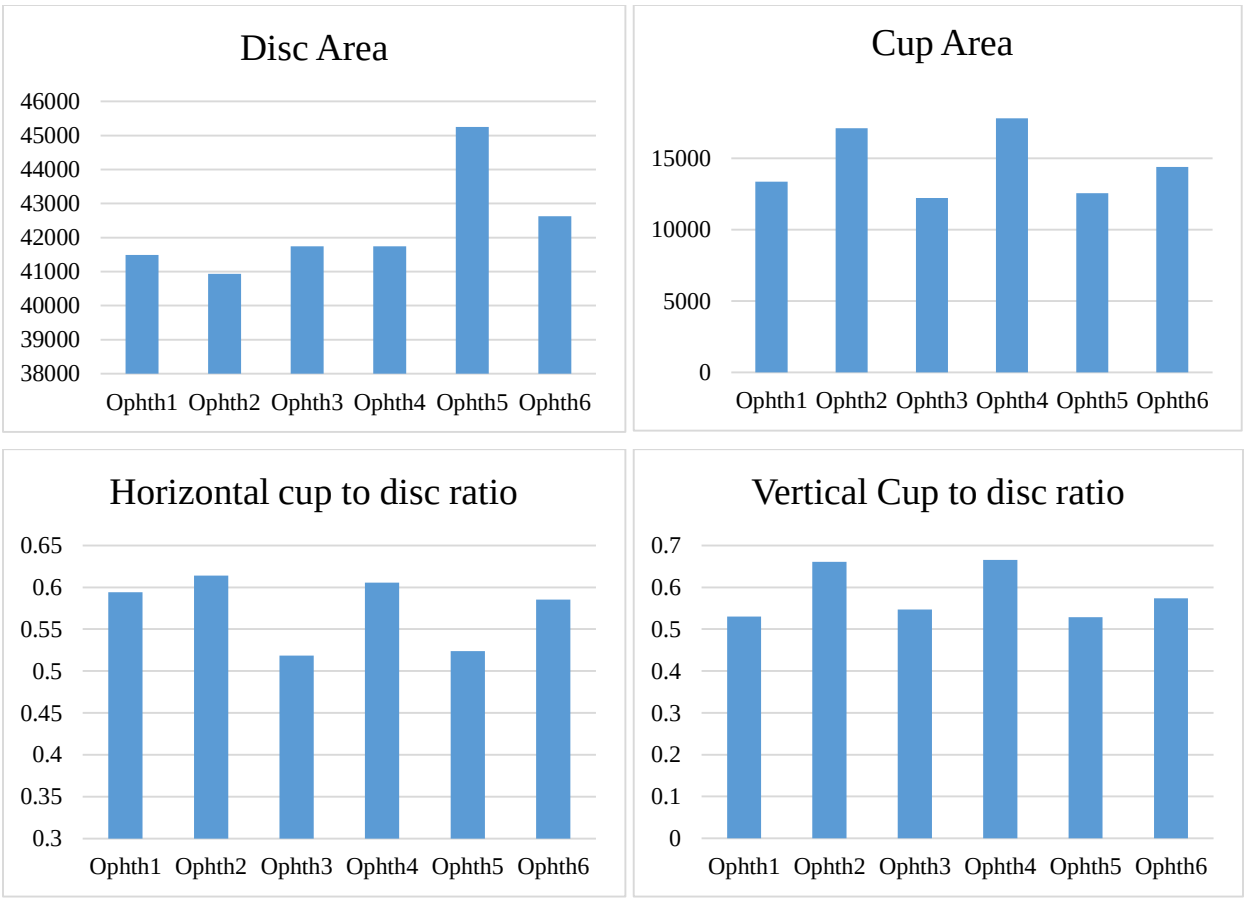

Figure 3.6 Results of the geometrical parameters for the 6 ophthalmologists for figure 3.5. The X axis represents the number of 6 ophthalmologists and the Y axis represents the number of pixels for the top graphs and represents ratio for the bottom graphs.

As can be seen in Figure 3.6, the annotations of ophthalmologists number 1 and 6 have some similarity, those by ophthalmologists number 2 and 4 are also similar, so are the ones annotated by ophthalmologists number 3 and 5. As a result, there are three groups which will be taken into account for any automatic optic disc and cup segmentation technique evaluation. If human beings

cannot make a definite decision about a given image due to the difficulty of finding the cup, software won't be able to do so either.

3.5. Variation between the 6 ophthalmologists in the manual annotations

To compare the annotations of the 6 ophthalmologists, the disc and cup area and centroid were considered as well as the vertical and horizontal cup to disc ratio. MESSIDOR dataset, Bin Rushed dataset and Magrabi dataset were analyzed separately and together. The comparisons were organized as (1) optic disc area and centroid, (2) optic cup area and centroid, (3) horizontal cup to disc ratio (HCDR), and finally (4) vertical cup to disc area (VCDR).

3.5.1. Optic disc area and centroid

The OD areas were measured in pixels in order to compare the areas annotated by the six ophthalmologists. The X and Y coordinates of the disc centroid were also recorded. For every image, the standard deviations (SD) of the measurements recorded by the six ophthalmologists were calculated (in pixels). Then the mean of the SDs of all the images within each dataset was calculated and this value was considered as the standard measure (Table 3.3). As shown in the table, each dataset has a different SD and this is due to the fact that the image sizes varied among the three datasets. Voting procedures were used in order to determine whether there is any bad annotation among the six ophthalmologists for every image based on the statistical conditions (Figure 3.7). If an image has an SD which is greater than the mean SD, this means that an ophthalmologist has created an outlier by annotating either a very small or a very large area as the OD area. The outliers should be removed in order to keep the SD close to the mean SD. Some of the manual annotations have exceeded the mean SD by up to 150 pixels. These annotations have not been removed from the data since they do not influence the area size.

Table 3.3 The mean SD for the disc area for the three datasets.

Image Resources	MESSIDOR Images	Bin Rushed Images	Magrabi Images
SD in Pixel	1500	1650	6400

Table 3.4 shows the SD in pixel for X and Y coordinates. Again, a voting procedure was used here and any manual annotation that exceeded this standard was considered an outlier. The manual annotation exceeding the SD by only 1 or 1.5 pixels have been kept in the data.

Table 3.4 The mean SD for the disc centroid for the three datasets.

Image Resources	MESSIDOR Images	Bin Rushed Images	Magrabi Images
SD in Pixel	3	3	4

After calculating the SD for area and centroid individually for all three datasets and extracting the outliers from both datasets (Figure 3.7), the number of images agreed between the six ophthalmologists was then taken into account.

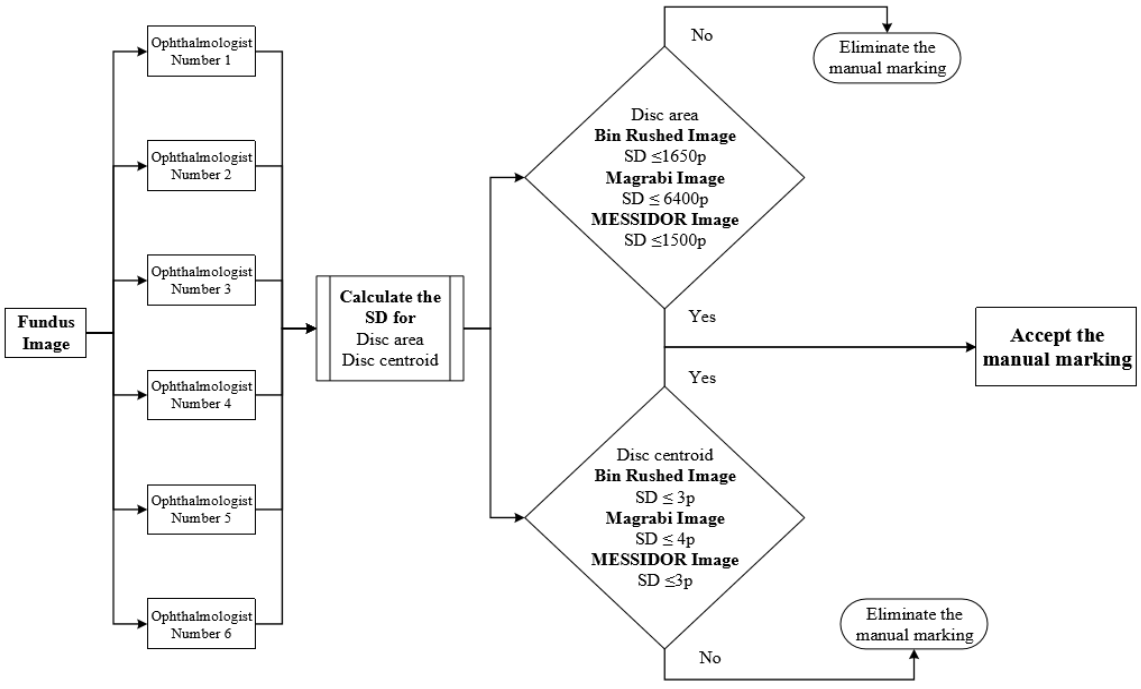

Figure 3.7 Flowchart for the disc annotations analysis.

Figure 3.8 shows two original images (the far left one in each row) and the six disc manual annotations for each image done by the six ophthalmologists. For the image in the top row, the annotations of OD area by ophthalmologists number one and six were considered as outliers (based on the analysis shown in Figure 3.7) and were eliminated from the dataset. For the image in the bottom row, the annotations of OD area by ophthalmologists number two, three and four were outliers, and the centroids annotated by ophthalmologists number five and six were outliers. Therefore, this image will not be considered for calculating the accuracy.

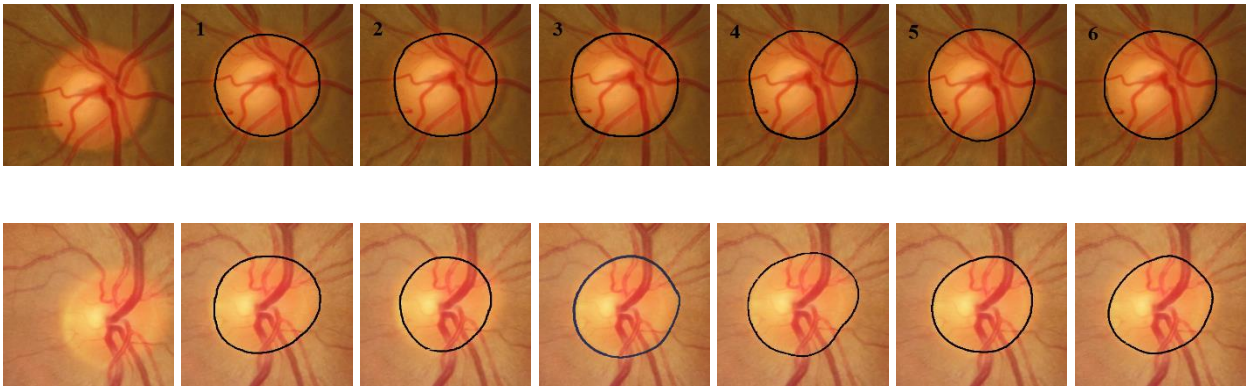

Figure 3.8 Example of the six disc annotations.

Table 3.5 shows the similarity or agreement among the six ophthalmologists' annotations. It can be seen in Table 3.5 and Figure 3.9 that ophthalmologist number one clearly had the best agreement with ophthalmologist number four in 563 images (75%) and the least agreement with ophthalmologist number two in 479 images (63.8%). Ophthalmologist number two had the best agreement with ophthalmologist number four in 523 images (69.7%), and the least agreement with ophthalmologists number three and six in 469 images (62.5%). Ophthalmologist number three also had the best agreement with ophthalmologist number four in 557 images (74.2%). Ophthalmologist number four had the best agreement with ophthalmologist number six in 594 images (79.2%). Ophthalmologist number five had the best agreement with ophthalmologist

number four in 553 images (73.7%). Finally, ophthalmologist number six was in best agreement with ophthalmologist number four.

In conclusion, ophthalmologist number four had the best agreement with all other ophthalmologists in terms of disc area and centroid annotations (agreement in 523 to 594 images out of 750 images). This means ophthalmologist number four had provided good disc boundary annotations as shown by the total number of images annotated by this ophthalmologist which were in agreement with the annotations by other ophthalmologists (Table 3.5). Ophthalmologists number six and one were in the 2nd and 3rd place. However, ophthalmologist number two provided the worst performance in terms of agreement with other ophthalmologists in annotation of the disc area and centroid.

Table 3.5 The number of images agreed between the six ophthalmologists for the disc area and centroid.

	Ophth1	Ophth2	Ophth3	Ophth4	Ophth5	Ophth6
Ophth1	750	479	513	563	512	543
Ophth2	479	750	469	523	479	469
Ophth3	513	469	750	557	510	542
Ophth4	563	523	557	750	553	594
Ophth5	512	479	510	553	750	533
Ophth6	543	469	542	594	533	750
Total	2610	2419	2591	2790	2587	2681

Figure 3.9 shows the agreement among the six ophthalmologists in the annotations of the disc area and centroid. From the figure it can be seen that ophthalmologist number 4 had the closest match with most others over the 750 images that were considered.

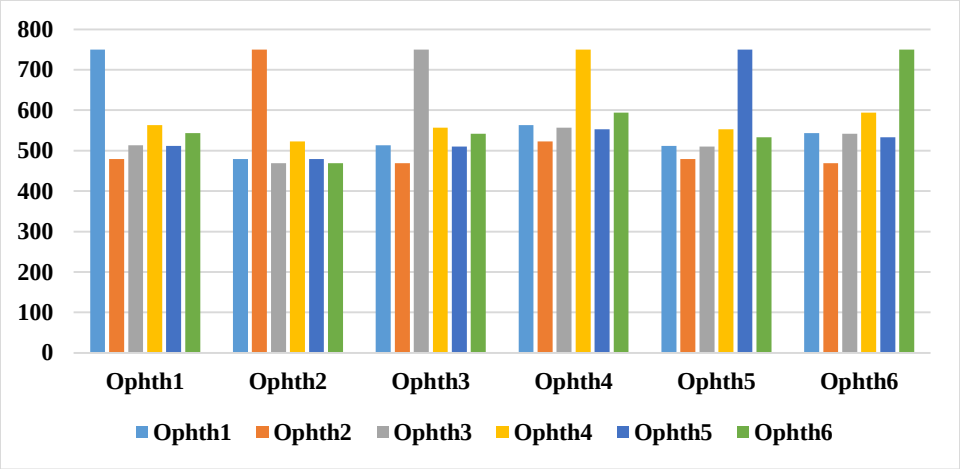

Figure 3.9 Compering the agreement between the six ophthalmologists in the disc area and centroid annotations in terms of the number of images. X axis represents the number of 6 ophthalmologists. Y axis represents the number of agreed images.

3.5.2. Optic cup area and centroid

The cup area and centroid were analyzed using the voting procedure (Figure 3.10). As can be seen in Table 3.6, the SDs for the three datasets were larger than disc SDs reported in Table 3.3.

The variation among the six ophthalmologists in the cup annotation was greater than the variation in the disc annotation. As shown in tables 3.6 and 3.3, for MESSIDOR dataset the mean SDs were 1500 and 2150 pixels for disc and cup, respectively, an increase of about 30%. For Bin Rushed dataset, the mean SDs were 1650 and 3000 pixels for disc and cup, respectively, an increase of about 45%. Finally, for Magrabi dataset the mean SDs were 6400 and 8800 pixels for disc and cup, respectively, an increase of about 30%. In conclusion, it seems that the annotation of the cup was more difficult than the annotation of the disc, particularly with Bin Rushed dataset. This is most probably due to the complexity of the optic cup structure with the blood vessel confounds.

Table 3.6 The mean SD for the cup area for the three datasets.

Image Resources	MESSIDOR Images	Bin Rushed Images	Magrabi Images
SD in Pixel	2150	3000	8800

Table 3.7 shows the mean SD for the X and Y coordinates of the cup boundaries obtained by manual annotation. These values were clearly greater than the coordinates of disc boundaries. The difference between the disc and cup for both MESSIDOR and Bin Rushed datasets were two pixels. The difference between disc and cup for Magrabi dataset however, was six pixels, indicating that the annotations of the cup of the images in Magrabi dataset has been challenging for the ophthalmologists.

Table 3.7 The mean SD for the cup centroid for the three datasets.

Image Resources	MESSIDOR Images	Bin Rushed Images	Magrabi Images
SD in Pixel	5	5	10

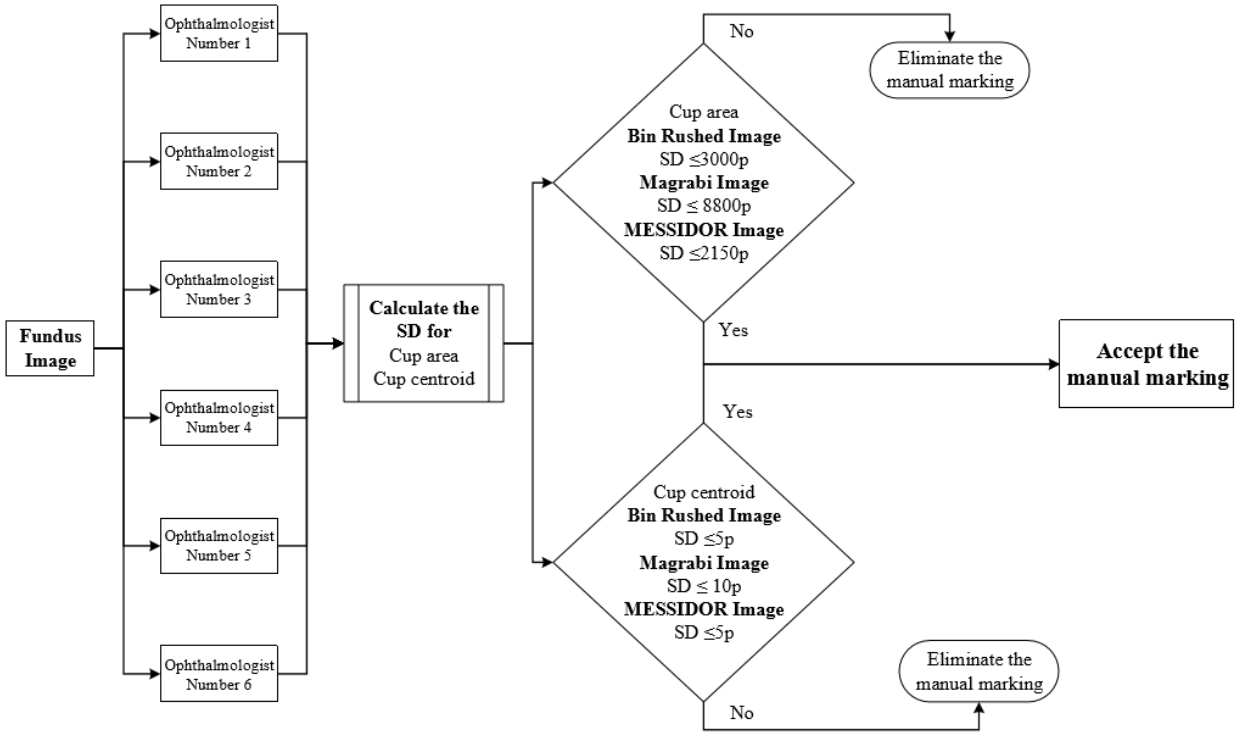

Figure 3.10 Flowchart for the cup annotations analysis.

Figure 3.11 shows two original images (the far left one in each row) and the six cup annotations for each image done by the six ophthalmologists. For the image in the top row, all six annotations

gave SDs close to the mean SD for both area and centroid (tables 3.6 and 3.7). For the image in the bottom row, the centroids annotated by ophthalmologists two and six were outliers, and therefore were eliminated from analysis. In the same image, the areas annotated by ophthalmologists three and five were outliers, thus they were eliminated. This means in total for the image in the bottom row, four annotated images had to be removed. Therefore, since the annotations of this image showed poor agreement among the ophthalmologists, the image will not be considered in the evaluation of accuracy.

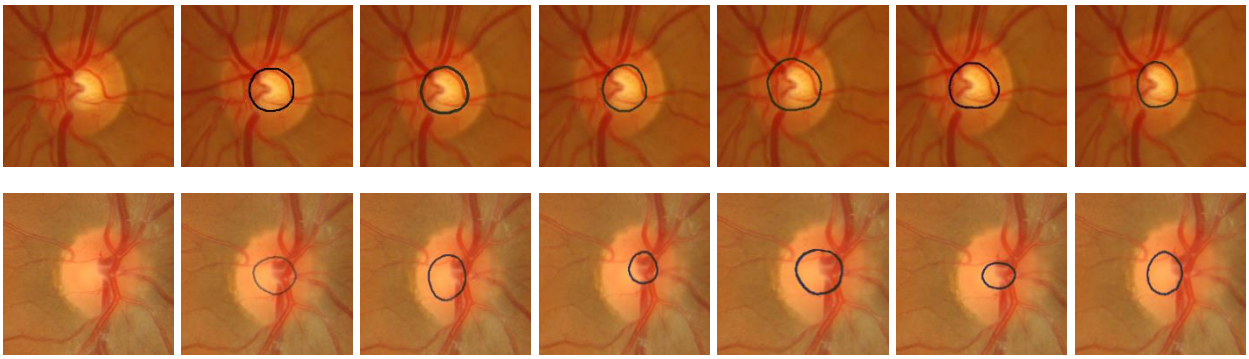

Figure 3.11 Example of the six cup annotations.

Table 3.8 and Figure 3.12 show the similarity or agreement among the six ophthalmologists in annotating the cup area and centroid. Ophthalmologist number one agreed with ophthalmologist number two and five in 565 images (75.3% of the total images). On the other hand, ophthalmologist number one had the lowest agreement with ophthalmologist number four in 439 images (58.5% of the total images). Ophthalmologist number two had the best agreement with ophthalmologist number one too, while the lowest agreement was with ophthalmologist number four in only 435 images (58%). Ophthalmologist number three agreed with ophthalmologist number five in 538 images (71.7%). Ophthalmologist number four had low agreement with all other five ophthalmologists, with the best agreement with ophthalmologist number one in 439

images (58.5%) and the lowest agreement with ophthalmologist number three in 413 images (55%). Ophthalmologist number five agreed with ophthalmologist number one with the same number of images and his lowest agreement was with ophthalmologist number four in 432 images (57.6%). Finally, ophthalmologist number six agreed with ophthalmologist number one in 543 (72.4%) and his lowest agreement was with ophthalmologist number four in 420 images (56%).

In conclusion, ophthalmologist number one had the best agreement with all other five ophthalmologists (agreement in 439 to 565 images of 750 images), which was obviously less than the disc best agreement (agreement in 523 to 594 images). The difference was only 71 images for the disc annotations, and 126 images for the cup annotations. This means the annotations of the cup was less consistent, further confirming the bigger difference in the mean SDs of the cup in comparison with the disc.

Table 3.8 The number of images agreed between the six ophthalmologists for the cup area and centroid.

	Ophth1	Ophth2	Ophth3	Ophth4	Ophth5	Ophth6
Ophth1	750	565	531	439	565	543
Ophth2	565	750	521	435	555	544
Ophth3	531	521	750	413	538	511
Ophth4	439	435	413	750	432	420
Ophth5	565	555	538	432	750	545
Ophth6	543	544	511	420	545	750
Total	2643	2620	2514	2139	2635	2563

Figure 3.12 shows the similarity or agreement among the six ophthalmologists. It is clear that ophthalmologists number one, five and two had the closest match compared with the others. On the other hand, ophthalmologist number four had the least agreement with others in annotating the cup area and centroid even though he had the highest agreement with others in annotating the disc boundaries.

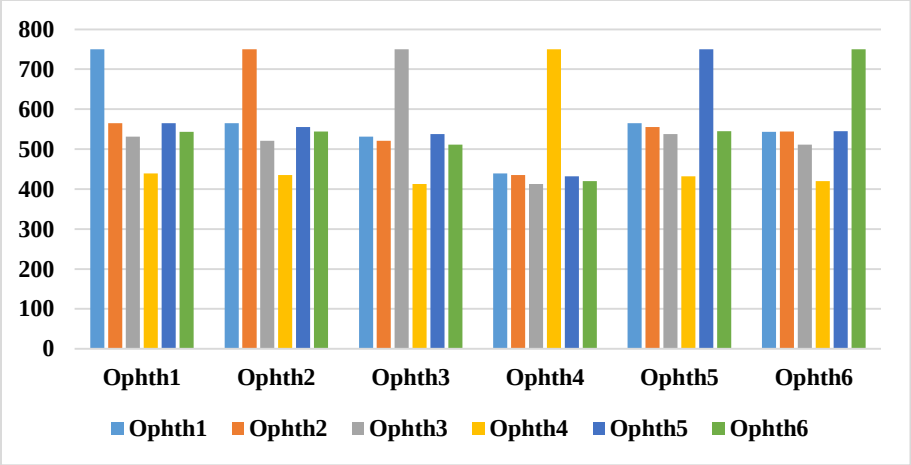

Figure 3.12 Compering the agreement in the cup area and centroid among the six ophthalmologists in term of number of images. The X axis represents the number of 6 ophthalmologists. The Y axis represents the number of agreed images.

Figure 3.13 provides an overview of the total number of image agreements among the six ophthalmologists in the annotations of cup and disc area. The figure shows that ophthalmologists number 3, 4, and 6, were better in disc annotation. On the other hand, ophthalmologists number one, two and five were better in annotating the cup. Ophthalmologist number four has lost more than 700 images in cup annotations due to lack of agreement with other five ophthalmologists. Ophthalmologist number one, three and five have very similar number of images for both disc and cup. For ophthalmologists number two and six the difference in the number of images in agreement with the other five ophthalmologists for disc and cup is noticeable and around 200 images.

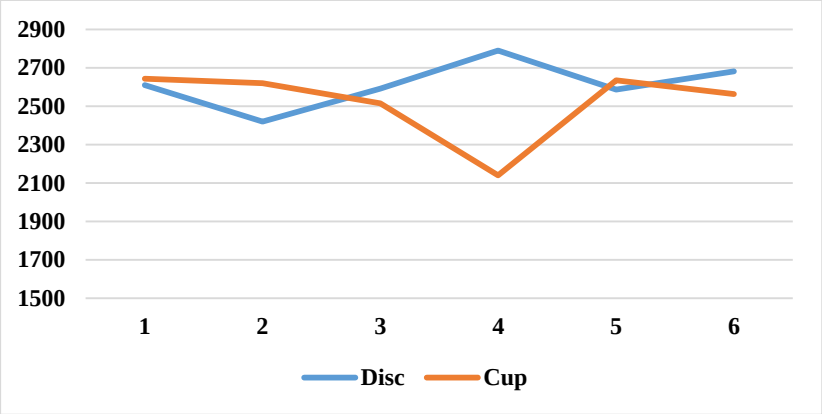

Figure 3.13 Comparison between the disc and cup for the agreement in number of the images for every ophthalmologist. The X axis represents the number of 6 ophthalmologists. The Y axis represents the number of total agreed images.

3.5.3. Horizontal cup to disc ratio (HCDR)

The horizontal cup to disc ratio (HCDR) for the ophthalmologists annotations were calculated for all the images and for all the six ophthalmologists based on the furthest pixel horizontally on the two sides of the disc and cup. The SD for HCDR was calculated for all the images, then the mean SD was calculated, which was 0.075. The outliers, those with SD among the six ophthalmologists greater than the mean SD, were eliminated (Figure 3.14). The disc and cup area and centroid outliers reduced the number of images agreed upon for HCDR. Therefore, the number of images in agreement for HCDR were less than the number of images agreed upon for the disc and cup (Table 3.9) because for HCDR three parameters were considered for agreement: disc (area and centroid), cup (area and centroid) and horizontal cup to disc ratio (unlike disc and cup for which only two parameters, i.e., the area and centroid, were considered).

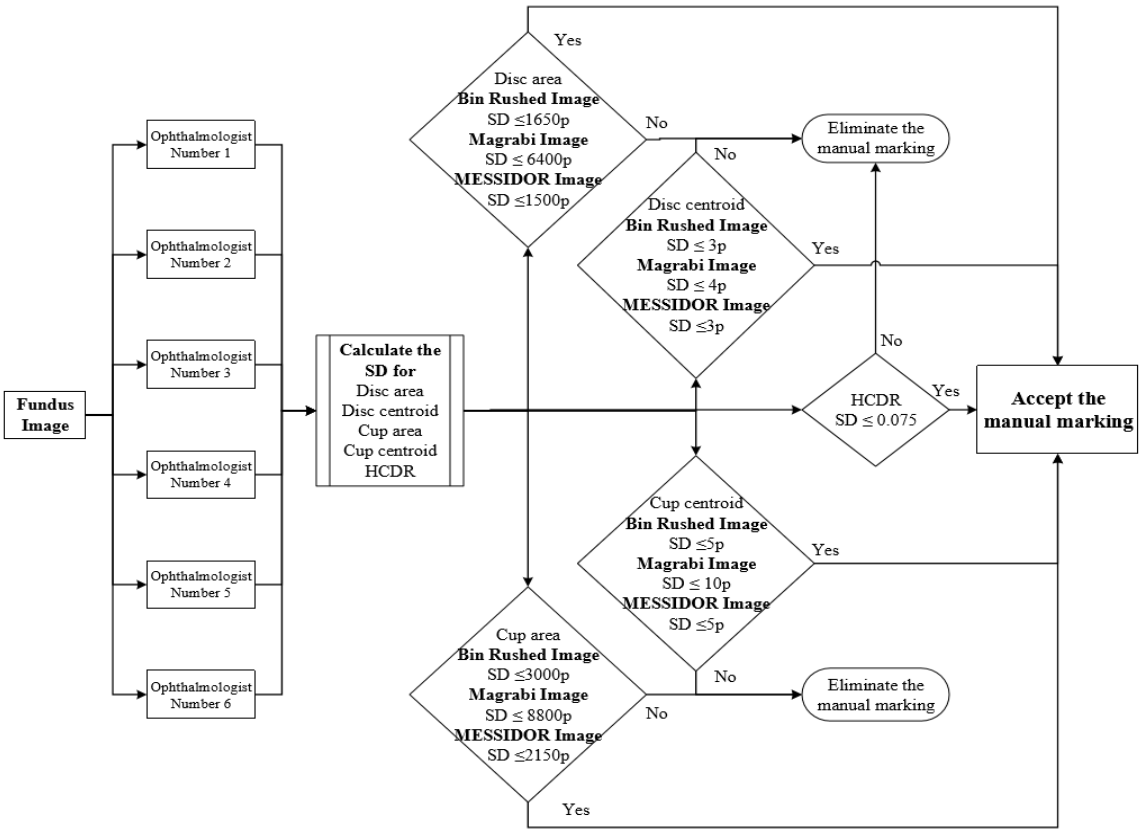

Figure 3.14 Flowchart for the HCDR annotations analysis.

Figure 3.15 shows two original images (the far left one in each row) and the six annotations for each image done by the six ophthalmologists. For the image in the top row, the images annotated by three ophthalmologists were eliminated due to different reasons (disc area, cup area, and centroid) which clearly affect the HCDRs. Therefore, this image was considered an unclear image and was not included in further analysis. For the image in the bottom row, the HCDRs were 0.69, 0.66, 0.70, 0.73, 0.68, and 0.66 for the six ophthalmologists, respectively, and the SD was less than 0.075.

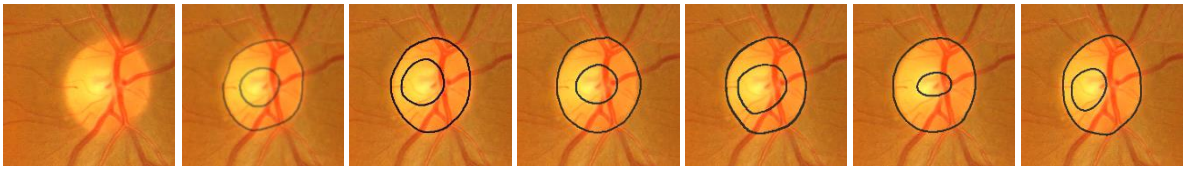

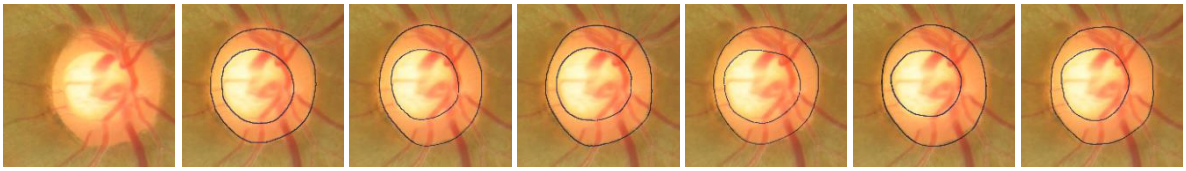

Original image Ophtha1 Ophtha2 Ophtha3 Ophtha4 Ophtha5 Ophtha6

Figure 3.15 Example of the six HCDR annotations.

As shown in Table 3.9 and Figure 3.16, the disc and cup areas and centroids influenced the agreement between the six ophthalmologists. Ophthalmologist number one had best agreement with the other five ophthalmologists in 364 images (48.5%) and the lowest agreement was with ophthalmologist number four in 295 images (39.3%). Ophthalmologist number two had the best agreement with ophthalmologist number one in 349 images (46.5%). Ophthalmologist number three agreed with ophthalmologist number one in 360 images (48%) and the lowest agreement was with ophthalmologist number four in 277 images (36.9%). Ophthalmologist number four had the best agreement with ophthalmologist number one in 295 images (39.3%), and had almost low agreement with all other four ophthalmologists (in 264 to 295 images or 35.2% to 39.3%). However, it should be noted that the reason for agreement in a small number of images is that many outliers were eliminated from the cup calculations for ophthalmologist number four. Ophthalmologist number five had the best agreement with ophthalmologist number one, while the lowest agreement was with ophthalmologist number four in 274 images (36.5%). Finally, ophthalmologist number six agreed with ophthalmologist number five in 349 images (46.5%) and the lowest agreement was with ophthalmologist number four in 267 images (35.6%). Obviously, here the number of images in agreement was less than what we observed for the disc and cup. In case of HCDR, only the revised dataset was considered. Therefore, too many images had already been removed from the dataset before arriving to the HCDR analysis.

Table 3.9 The number of images agreed between the six ophthalmologists for the HCDR.

	Ophth1	Ophth2	Ophth3	Ophth4	Ophth5	Ophth6
Ophth1	750	349	360	295	364	345
Ophth2	349	750	328	264	334	317
Ophth3	360	328	750	277	351	337
Ophth4	295	264	277	750	274	267
Ophth5	364	334	351	274	750	349
Ophth6	345	317	337	267	349	750
Total	1713	1592	1653	1377	1672	1615

In conclusion, as can be seen in Table 3.9 as well as the aforementioned comparisons, ophthalmologist number one had the best agreement with the others, followed by ophthalmologist number five, and then ophthalmologist number three in HCDR including the disc and cup parameters. Figure 3.16 provides a clear comparison among all six ophthalmologists.

HCDR calculations were more challenging due to the density of the blood vessels which made the ophthalmologists uncertain when annotating the optic cup boundary underneath the blood vessels, and also due to the peripapillary atrophy which occurs mostly on the two sides of the disc.

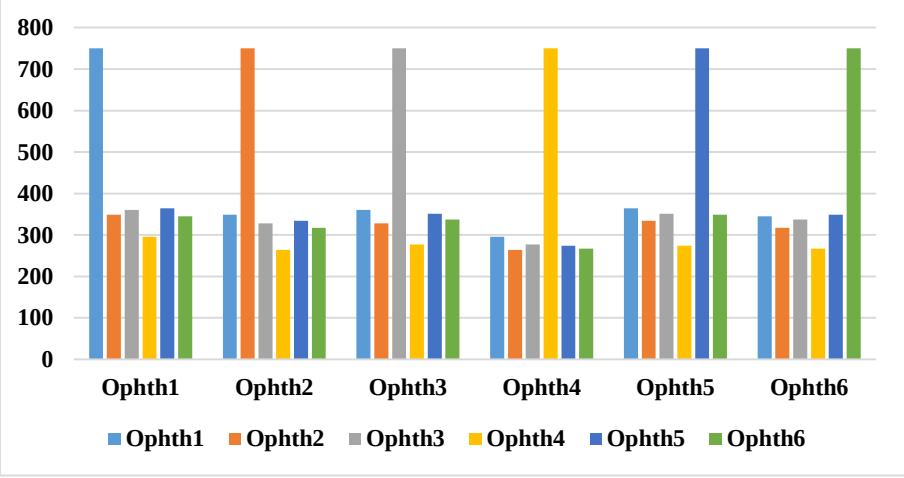

Figure 3.16 Compering the agreement in the HCDR between the six ophthalmologists in term of number of images. The X axis represents the number of 6 ophthalmologists. The Y axis represents the number of agreed images.

3.5.4. Vertical cup to disc ratio (VCDR)

The vertical cup to disc ratio (VCDR) was calculated following the same steps used in calculation of the horizontal cup to disc ratio, except that in this case the furthest top pixel and furthest bottom pixel for the disc and cup were considered to compute the ratio. The SD of VCDR was calculated for all images annotated by the six ophthalmologists in order to find the outliers and eliminate them (Figure 3.17).

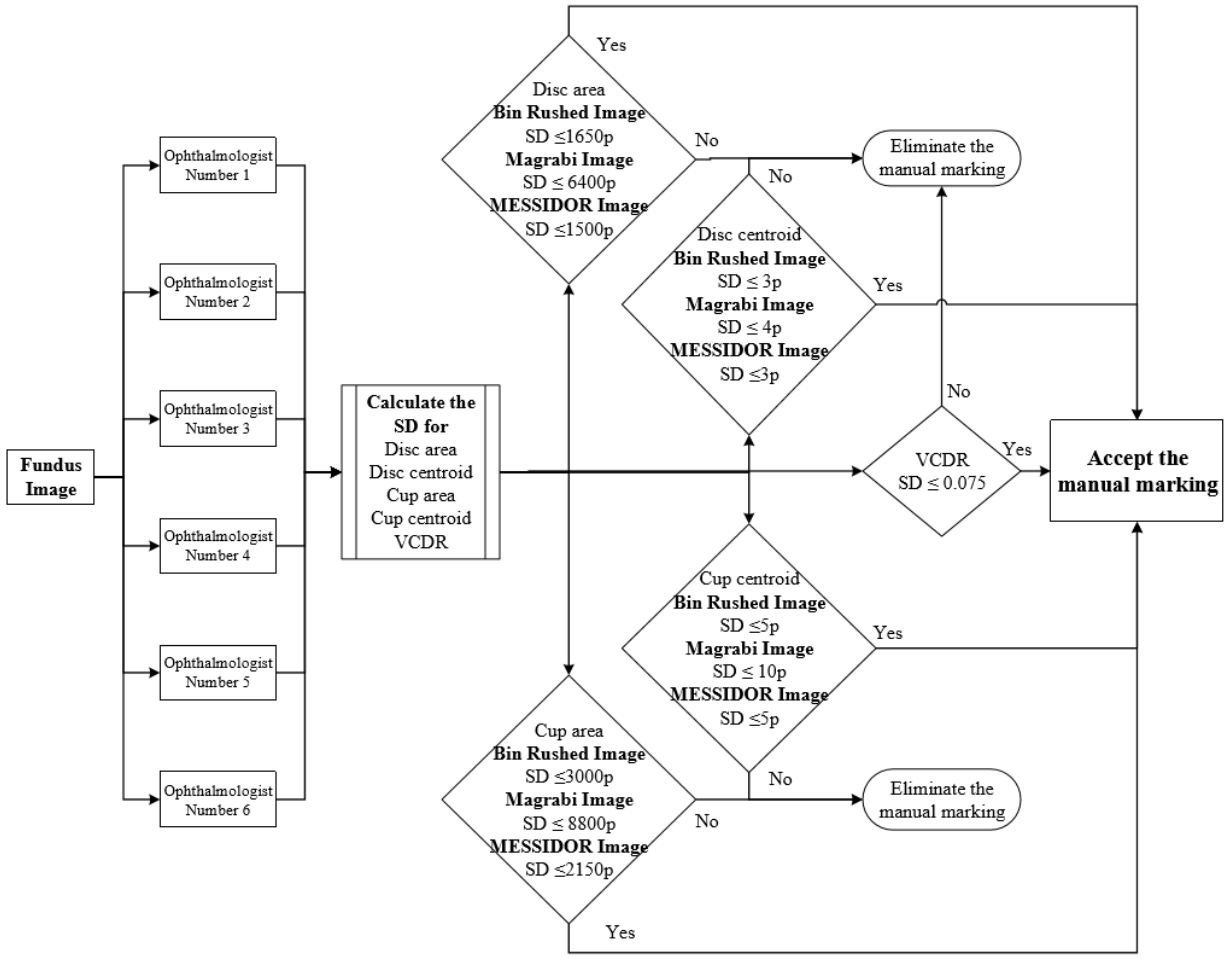

Figure 3.17 Flowchart for the VCDR annotations analysis.

Figure 3.18 shows two original images (the far left one in each row) and the six disc annotations for each image done by the six ophthalmologists. For the image in the top row, the SD was 0.03

where the VCDR was 0.63, 0.63, 0.67, 0.70, 0.64, and 0.62 for the ophthalmologists, which indicated good results for disc and cup too. For the image in the bottom row, there is clearly a large variation in the annotations. Therefore, this image was not considered a good image for evaluation of accuracy.

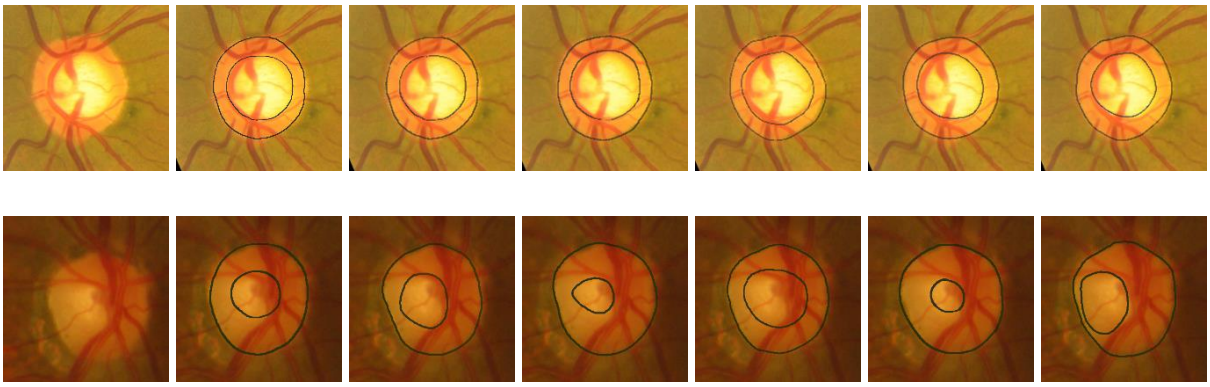

Figure 3.18 Example of the six VCDR annotations.

The mean SD for the VCDR was 0.075; the same as the mean SD for the HCDR. The optic disc and cup parameters were brought again here without considering the HCDR. Therefore, three parameters were included in order to compute the VCDR, which were disc (area and centroid), cup (area and centroid), and the VCDR. As can be seen in Table 3.10, here the number of images agreed between the six ophthalmologists was less than the number of images agreed upon in the disc and cup calculations. This was due to the many outliers for all the three parameters which were deleted. In contrast the VCDR was close to the HCDR.

As can be seen in Table 3.10, ophthalmologist number one had the best agreement with ophthalmologist number six in 382 images (50.9%) while the lowest agreement was with ophthalmologist number four in 294 images (39.2%). Ophthalmologist number two had the best agreement with ophthalmologist number four in 367 images (48.9%) and the lowest agreement

with ophthalmologist number five in 306 images (40.8%). Ophthalmologist number three had the best agreement with ophthalmologist number one in 370 images (49.3%) and the lowest agreement with ophthalmologist number four in 280 images (37.3%). Ophthalmologist number four had the best agreement with ophthalmologist number two and low agreement (between 255 to 294 images) with all other four ophthalmologists (34% to 39.2%). Ophthalmologist number five had best agreement with ophthalmologist number six in 352 images (46.9%) while the lowest agreement was with ophthalmologist number four in 255 images. Finally, ophthalmologist number six best agreed with ophthalmologist number one, and the lowest agreement was with ophthalmologist number four in 279 images (37.2%).

In conclusion, ophthalmologists number one and six had the highest agreement with the others. The best agreement for VCDR was between the images annotated by ophthalmologists one and three (49.3%), while the best agreement for HCDR was between ophthalmologists one and five (in 364 images equivalent to 48.5%). On the other hand, the lowest agreement was between the images annotated by ophthalmologists five and four, and was 34% for VCDR and 35.2% for HCDR.

Table 3.10 The number of images agreed between the six ophthalmologists for VCDR.

	Ophth1	Ophth2	Ophth3	Ophth4	Ophth5	Ophth6
Ophth1	750	340	370	294	351	382
Ophth2	340	750	324	367	306	335
Ophth3	370	324	750	280	337	362
Ophth4	294	367	280	750	255	279
Ophth5	351	306	337	255	750	352
Ophth6	382	335	362	279	352	750
Total	1737	1672	1673	1475	1601	1710

Figure 3.19 shows the VCDRs annotated by all six ophthalmologists. The range of the number of images is close to HCDR. Clearly, ophthalmologist number one had the maximum agreement with the others (Figure 3.19).

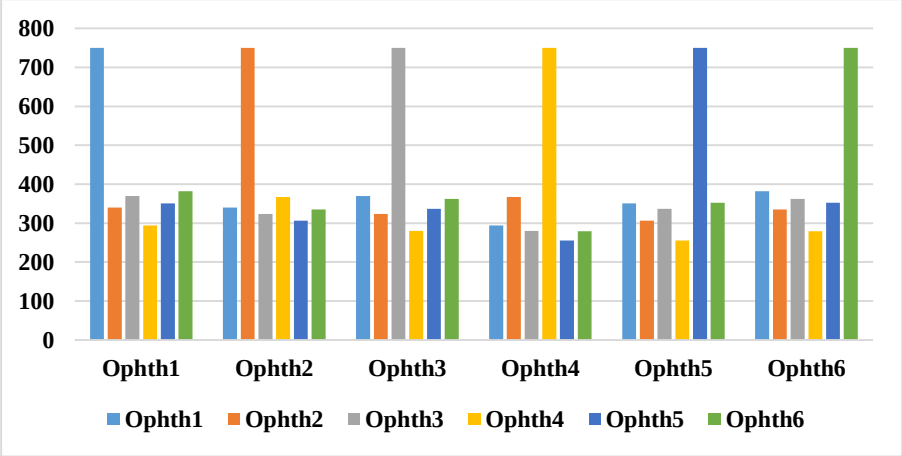

Figure 3.19 Compering the agreement in the VCDR between the six ophthalmologists in term of number of images. The X axis represents the number of 6 ophthalmologists. The Y axis represents the number of agreed images.

Figure 3.20 shows that there was a greater agreement in terms of total images in VCDR than in HCDR (the difference of approximately 100 images) for the images annotated by ophthalmologists number two, four and six. This difference was small for the images annotated by ophthalmologists number one and three. For ophthalmologist number five, there was a greater agreement in HCDR than in VCDR (the difference of approximately 75 images). Overall, there was a greater agreement in VCDR than in HCDR for images annotated by five ophthalmologists indicating that for these ophthalmologists the VCDR was easier to annotate than HCDR.

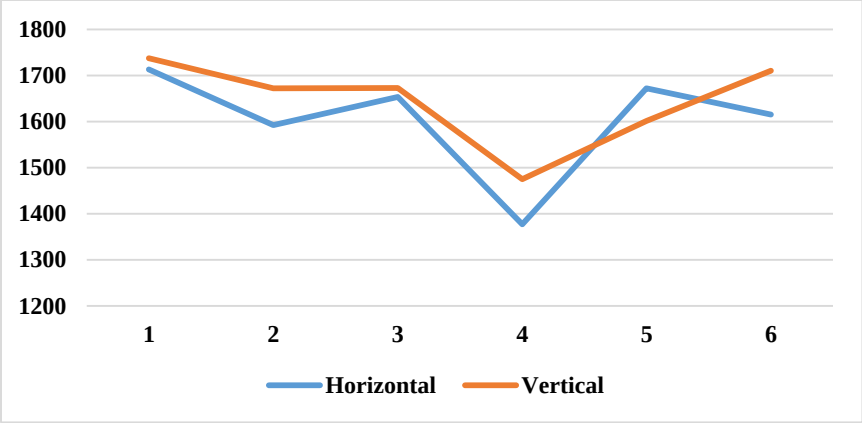

Figure 3.20 Comparison between the HCDR and VCDR for the agreement in number of the images for every ophthalmologist. The X axis represents the number of 6 ophthalmologists. The Y axis represents the number of total agreed images.

3.5.5. Consolidated results

In order to comprehensively evaluate the agreement among the six ophthalmologists, all the four parameters discussed so far, i.e., disc, cup, HCDR and CVDR, were brought together to find the agreement on all these parameters for every single image. The images were revised based on the flowchart shown in Figure 3.21.

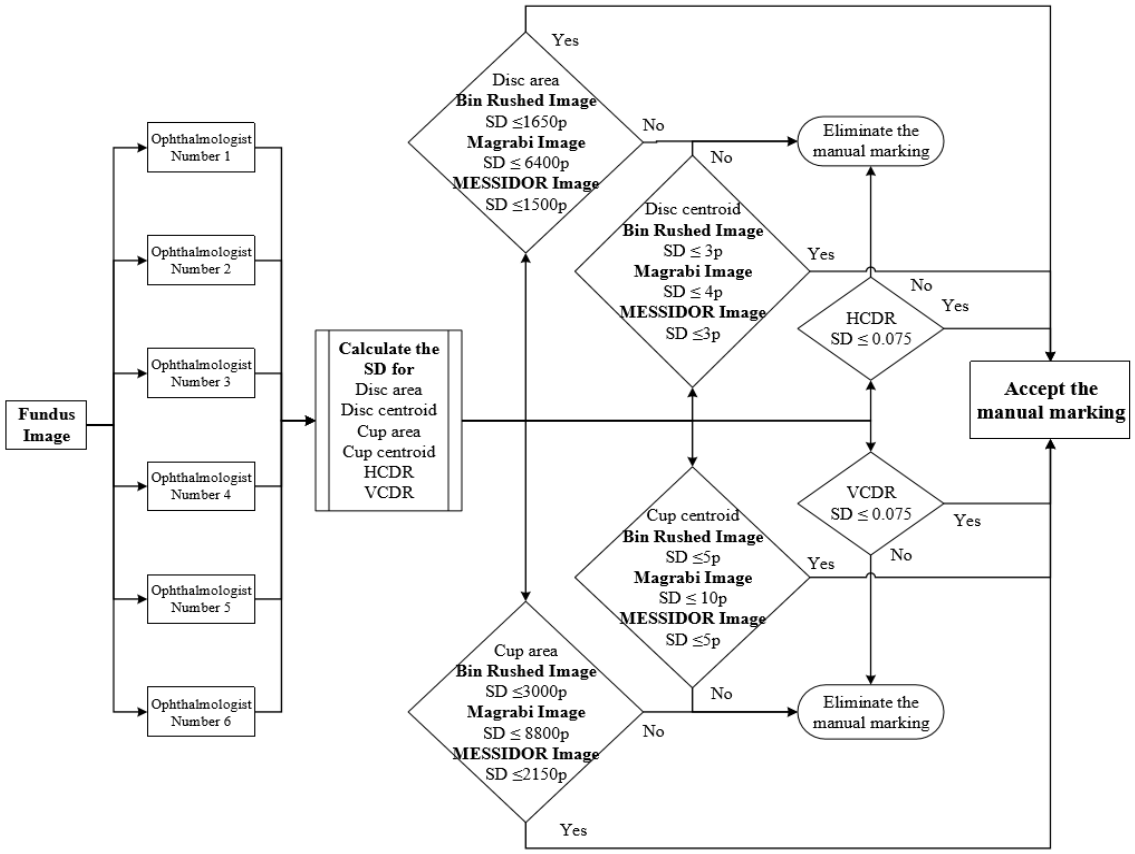

Figure 3.21 Flowchart for the annotations analysis with all the parameters.

In the image shown in Figure 3.22, the HCDRs annotations of the six ophthalmologists were 0.58, 0.54, 0.50, 0.54, 0.47, and 0.52, with SD of 0.03. The VCDRs annotations of the six ophthalmologists were 0.47, 0.45, 0.44, 0.45, 0.39, and 0.45, with SD of 0.03. In both cases the SD was less than the mean SD, i.e., 0.075.

Original image | Ophtha1 | Ophtha2 | Ophtha3 | Ophtha4 | Ophtha5 | Ophtha6

Figure 3.22 Example of the six ophthalmologists' final annotations (Disc, Cup, HCDR and VCDR).

As can be seen in the Table 3.11, the number of images agreed upon all four parameters was less than the number of images agreed upon HCDR and VCDR separately. Ophthalmologist number one had the best agreement with ophthalmologist number three in 350 images (46.6%). Ophthalmologist number two had the best agreement with ophthalmologist number one in 321 images (42.8%). Ophthalmologist number three had the best agreement with ophthalmologist number one in 350 images. Ophthalmologist number four had the best agreement with ophthalmologist number one in 260 images (34.6%). Ophthalmologist number five had the best agreement with ophthalmologist number one in 332 images (44.2%). Finally, ophthalmologist number six had the best agreement with ophthalmologist number one in 333 images (44.4%).

In conclusion, ophthalmologist number one had shown the best performance as indicated by the greatest agreement in the images annotated by him/her, considering all the eliminated outliers. Ophthalmologist number six was in the second place (with 80 images less), and on the third place was ophthalmologist number five with 15 images less than ophthalmologist number six. Ophthalmologist number four showed the poorest performance as indicated by the many outliers occurred in the cup calculation.

Table 3.11 The number of images agreed among the six ophthalmologists for the consolidated results.

	Ophth1	Ophth2	Ophth3	Ophth4	Ophth5	Ophth6
Ophth1	750	321	350	260	332	333
Ophth2	321	750	310	234	294	298
Ophth3	350	310	750	248	322	327
Ophth4	260	234	248	750	235	240
Ophth5	332	294	322	235	750	318
Ophth6	333	298	237	240	318	750
Total	1596	1457	1467	1217	1501	1516

Figure 3.23 shows the agreement in the annotations of the six ophthalmologists. Clearly ophthalmologist number four had the least agreement with the others. On the other side, ophthalmologist number one had the highest agreement. Ophthalmologists number five, six and three had almost the same level of agreement with the others.

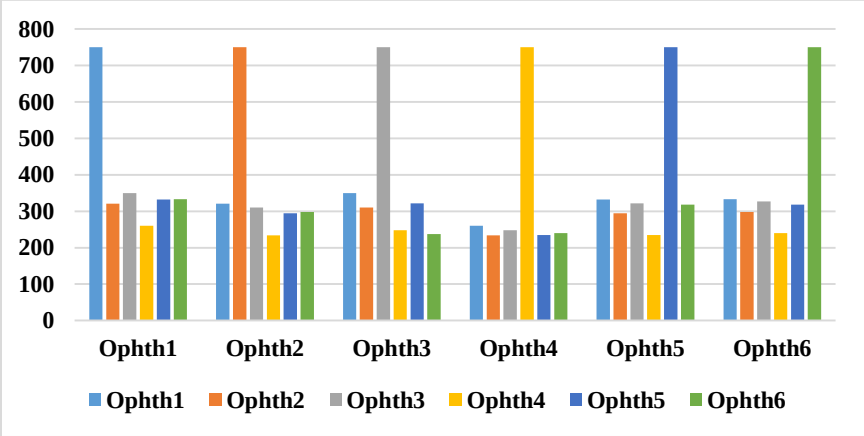

Figure 3.23 Compering the agreement in the total six parameters between the six ophthalmologists. The X axis represents the number of 6 ophthalmologists. The Y axis represents the number of agreed images.

Figure 3.24 provides a general overview of the level of agreement among the six ophthalmologists on annotating each of the four parameters, where the disc and cup include the area and centroid. For disc, ophthalmologist number four showed the greatest agreement. For cup, ophthalmologist number one showed the greatest agreement, while number four showed the lowest agreement with others. Three ophthalmologists had more images agreed for the cup than for the disc, and three ophthalmologists had more images agreed for the disc than the cup. As can be seen in the figure, there was a clear gap between the disc and cup on one side and HCDR, VCDR and the total on the other side in terms of the number of images agreed. For HCDR, ophthalmologist number one showed the highest agreement, then ophthalmologists number three and five, and then ophthalmologist number six. The level of agreement was generally better for VCDR than HCDR, except for ophthalmologist number five. For VCDR ophthalmologist number one had the best

agreement, then ophthalmologist number six, then ophthalmologist number two and three. Finally, for the total the pattern of agreement among the annotations of the six ophthalmologists was almost similar to that for HCDR.

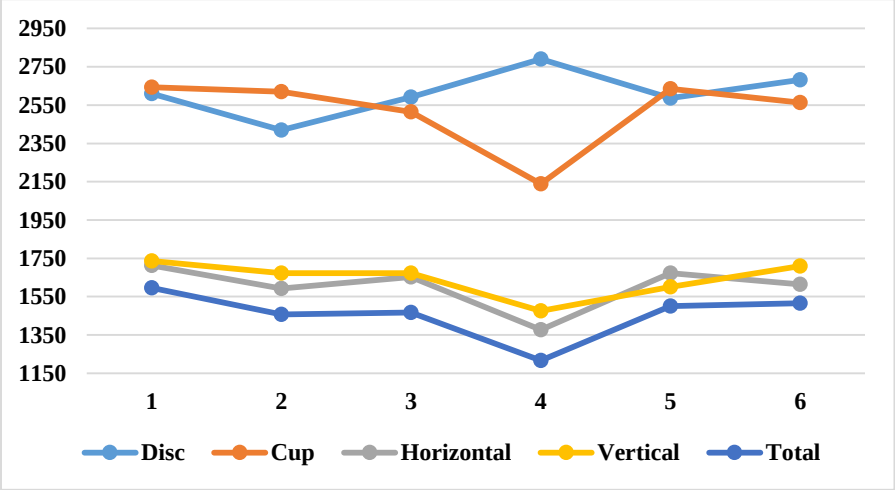

Fig 3.24 comparison between all the parameters as well as the total for the agreement in number of the images for every ophthalmologist. The X axis represents the number of 6 ophthalmologists. The Y axis represents the number of total agreed images.

3.6. Potential use of RIGA Dataset

All these parameters were calculated for all the images in RIGA dataset in order to recognize the similarity between the annotations of the 6 experts as well as to create a reference for every parameter. Such reference would be useful to researchers developing algorithms to detect the optic disc and cup boundaries. In cases where the images are used to train a neural net, the RIGA dataset can be divided into two sets: a training set and a test set. The database will be available in the public domain for use by researchers.

Chapter 4

Optic disc and cup segmentation methodologies

4.1. Introduction

In this chapter, the automatic image segmentation of the optic disc and cup system is introduced. First, the optic disc segmentation algorithm and its results are discussed in details. Second, the optic cup segmentation algorithm and its results are discussed in order to be able to analyze the HCDR and VCDR in chapter 5.

Basically, the system will facilitate diagnosis of glaucoma by computing the ONH structure in the four main steps shown in Figure 4.1.

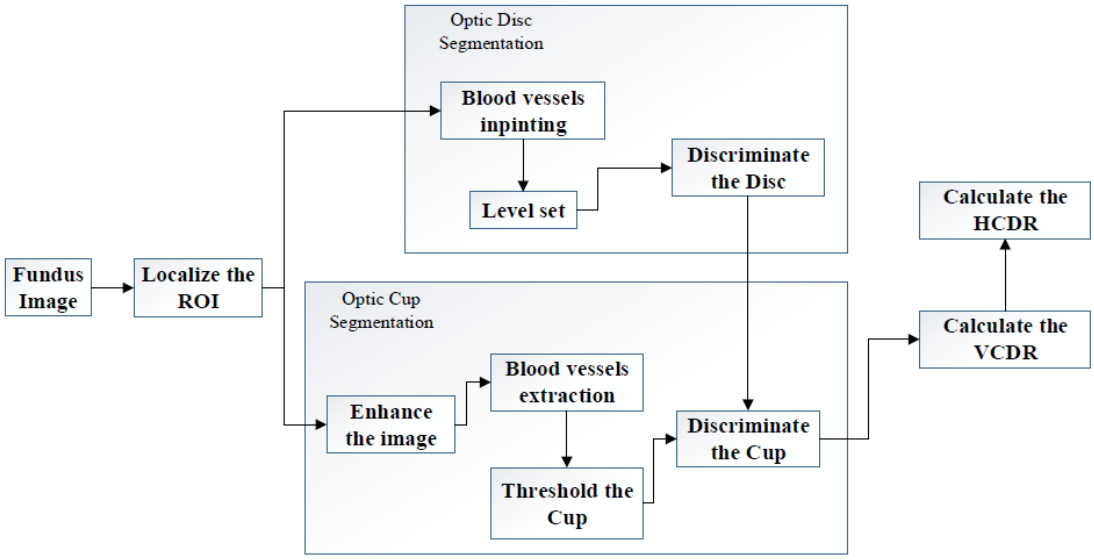

Figure 4.1 General flowchart for the new system.

A preprocessing step represented by finding the region of interest (ROI) was necessary to reduce the deteriorations that might occur during the main processing step and to decrease the computing

time by dealing with a small part of an image instead of the whole image. Two algorithms were applied in the processing step (Figure 4.1): one for optic disc segmentation based on active contour model implemented by level set approach, and the other for optic cup segmentation concerning images thresholding. Finally, the fourth step was a post processing step and was concerned with the optic nerve head parameters. In this step the horizontal and vertical cup to disc ratios were computed. The first three steps of the new system will be discussed in more details in this chapter. The post processing step will be discussed in the next chapter.

4.2. Image Segmentation and Thresholding

Determining the features or objects within an image is a necessary prerequisite for most image measurements or analyses. These features are used to define a range of brightness values by scanning the image pixel by pixel, where the pixels within this range belong to the foreground and others belong to the background. Thus, the image is displayed as a two level image, white and black, in order to distinguish the regions and this determination process is called thresholding [77]. Because of its simplicity of implementation and intuitive properties, image thresholding has enormous applications in image segmentation [51].

Image histograms play an important role in image thresholding. The histogram of a gray image (Figure 4.2) shows the number of pixels in the image having each of the 256 possible values of brightness. Peaks in the histogram indicate the brightness pixel values and represent specific structures in the image, while the valleys correspond to less common structures in the image [77]. Moreover, histograms are the basis for numerous spatial domain processing approaches in which they are manipulated effectively in order to enhance the images and to provide useful image statistics. In addition, histograms are useful for other image processing applications such as image compressions [51].

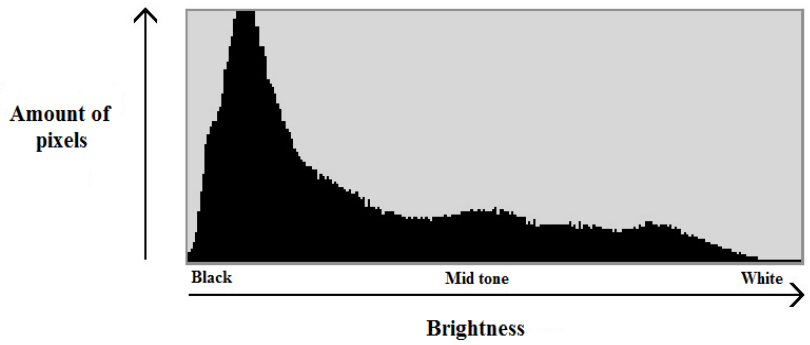

Figure 4.2 Image histogram.

Basically, the threshold value is chosen (automatically or manually) in order to distinguish the foreground from the background. The pixels with values greater than the threshold are assigned to one region, and those with values less than the threshold are assigned to another region. Clearly, the success of the process depends on how well the histogram can be divided. Multiple thresholds are introduced in order to detect many objects in the image. Recently, several thresholding techniques have been developed in order to remove the grayness ambiguity/vagueness during the task of threshold selection. An Interval Type-II fuzzy entropy based thresholding is one of these techniques and will be discussed in this chapter.

4.2.1. Fuzzy set

Fuzzy sets basically are sets with elements that have degrees of membership, and were first introduced by Lotfi Zadeh and Dieter Klaua in 1965 [78]. The membership of elements in a set is evaluated based on a bivalent condition, i.e., whether the element belongs to the set or not. An Interval Type-II fuzzy entropy based thresholding

The Interval Type-II fuzzy entropy based thresholding is also called ultrafuzzy sets and aims to capture/eliminate the uncertainties within fuzzy systems using type I fuzzy sets. The theoretical

approach is based on minimizing or maximizing measures of fuzziness and image information such as index of fuzziness or crispness, fuzzy entropy, and fuzzy divergence. This approach is the most used fuzzy technique due to its simplicity and high speed [79-80]. If the image is a fuzzy set, we need to determine how fuzzy it is. If the membership function is flat, then the image is very fuzzy; however, if the function is steep it means the image is crisp. Therefore, high fuzziness is represented by a flat membership function, which means the image data is very vague and thus thresholding would be difficult. Measures of fuzziness provide a quantitative answer to this issue [80]. The most common measure of fuzziness is the linear index of fuzziness [80]. The general algorithm using measures of fuzziness for image thresholding can be simplified as follows (Figure 4.3) [79].

1- Select the membership function.

2- Select a measure of fuzziness (e.g. linear index of fuzziness).

3- Calculate the image histogram.

4- Initialize the membership function position.

5- Move the membership function along the gray level range in order to calculate the amount of fuzziness in each position.

6- Localize the minimum / maximum fuzziness positions.

7- Threshold the image with T.

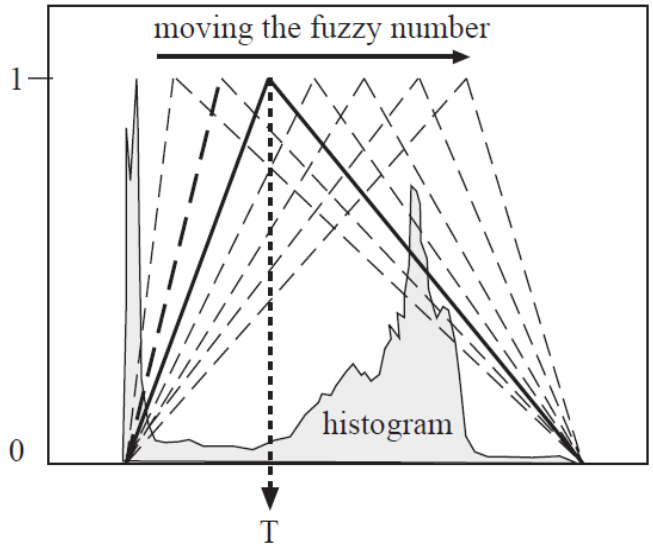

Figure 4.3 "The membership function is shifted over the gray-level range to calculate the amount of fuzziness in each position. The maximum fuzziness indicates the optimal threshold" [79].

The major goal for using type II fuzzy sets is to eliminate the uncertainty of the membership values. Unfortunately, type II fuzzy set is more complicated than type I. Since type I fuzzy set has the major problem of uncertainty in assigning a membership degree to pixel, type II fuzzy sets are introduced [80]. The different sources of uncertainties in type I fuzzy sets are [80]: (1) different interpretation of the same thing by different people; (2) measurements that activate type I fuzzy sets may be noisy; (3) the data used to adjust the parameters may also be noisy. According to Mendel and Bob John [80] "Type I fuzzy sets are not able to directly model such uncertainties because their membership functions are totally crisp. On the other hand, type-II fuzzy sets are able to model such uncertainties because their membership functions are themselves fuzzy". The footprint of uncertainty concept (FOU) is used to indicate a graph of type II fuzzy set more easily (the shaded area in Figure 4.4). The shadow for FOU represents the entire interval type II fuzzy set, which is described by upper and lower membership functions [79]. If the image is interpreted as type II fuzzy sets, then the question is how ultrafuzzy the fuzzy sets are? The ultrafuzziness

associated with fuzzy sets gives a zero value when the membership values can be defined without any uncertainty, and increases to one when membership values can be indicated within an interval.

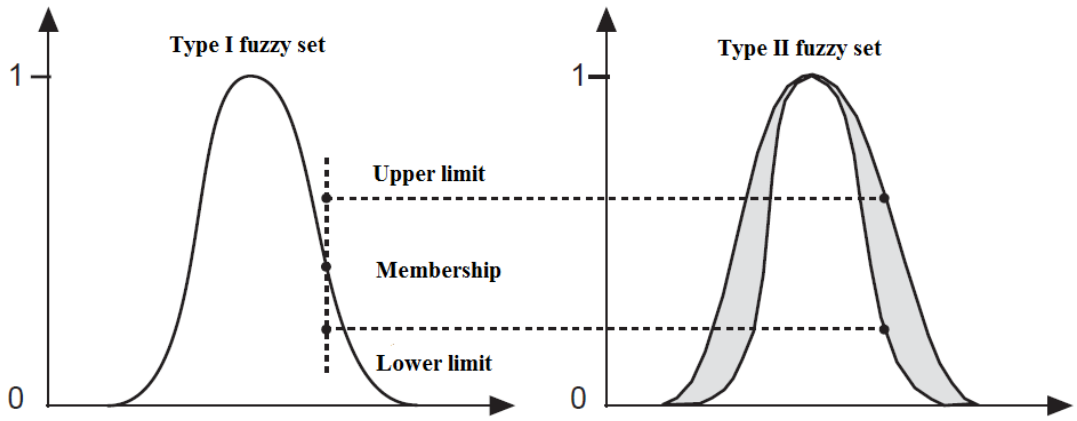

Figure 4.4 "A possible way to construct type II fuzzy sets. The interval between lower and upper membership values (shaded area) should capture the footprint of uncertainty (FOU)" [79].

4.3. Active contours and level set approach

This approach is based on using deformable contours that move under the influence of forces and are used to track boundaries and motions. The idea is to use a deformable pattern for selecting particular features of an image. The goal is to find the equation that will drive the contour to the object boundaries [81]

There are two deformable models: parametric models (snakes) and geometric models (level sets). Snakes explicitly move predefined snake points based on an energy minimization scheme, while level sets move contours implicitly as a particular level of a function. Level set theory provides a formulation to implement active contours. The use of level set theory has provided more flexibility and greater convenience for implementation of active contours.

The level set method was initially proposed in 1988 by Osher and Sethian [82] to track moving interfaces and was extended to various imaging application in late 90s [83].

The basic idea is to start with initial boundary shapes represented in form of closed curves, i.e., contours, and iteratively modify them by applying shrink or expansion operations according to the constraints of the image. The shrink or expansion operations, called contour evolution, are performed by minimization of an energy function like traditional region-based segmentation methods, or by simulation of a geometric partial differential equation (PDE), i.e., a progressive evaluation of the differences among neighboring pixels to find object boundaries. The level set function is then evolved under the control of a differential equation. The main idea of Osher and Sethian [82] is to represent the evolving contour using a signed function where its zero corresponds to the actual contour. Then, according to the motion equation of the contour, a similar flow can be easily derived for the implicit surface that when applied to the zero level will reflect the propagation of the contour. Ideally, the function will be accomplished at the boundary of the object where the differences are the highest.

Geometric active contours, i.e., active contours implemented via level set methods, have been proposed to solve a wide range of image segmentation problems. The active contour models were first introduced by Kass, Witkins, and Terzopoulos [81], and related to the most popular level set methods in image processing [82]. Geometric active contours were independently introduced by Caselles et al. and Malladi et al. [84]. The basic idea is to represent contours as the zero level set of an implicit function defined in a higher dimension, usually referred as the level set function, and to evolve the level set function according to a partial differential equation (PDE). In the traditional level set formulation, the level set function can develop very sharp during the evolution causes more computation highly inaccurate. Therefore, a numerical scheme initializes the level set function as a signed distance function before the evolution and then re-initializes the level set function to be a signed distance function periodically during the evolution in order to avoid the

aforementioned problems. However, another problem that might occur if the re-initialized function is not smooth is that the zero level set of the resulting function can be moved incorrectly from the original function. Moreover, in practice the evolving level set function can deviate greatly from its value as signed distance in a few iterations, especially when the time step is not small enough. Therefore, a new variation formulation for geometric active contours was introduced by Li et al. [85]. This variational formulation forces the level set function to be close to a signed distance function, and therefore completely eliminates the need of the costly re-initialization procedure. The proposed method can be implemented by using simple finite difference scheme and is computationally more efficient. A region-based initialization of level set function is proposed, which is not only computationally more efficient than computing signed distance function, but also allows for more flexible applications. The evolution PDE of the level set function can be directly derived from the problem of minimizing a certain energy functional defined on the level set function. Figure 4.5 illustrates the new level set method applied for an ultrasound image of carotid artery where the initial level set functions are computed from an arbitrary region in the image domain. The arbitrary region can be identified by simple morphological operations, then the initial level set function will be easily defined. Then it will evolve stably according to the evolution equation, with its zero level curve converged to the exact boundary of the region of interest.

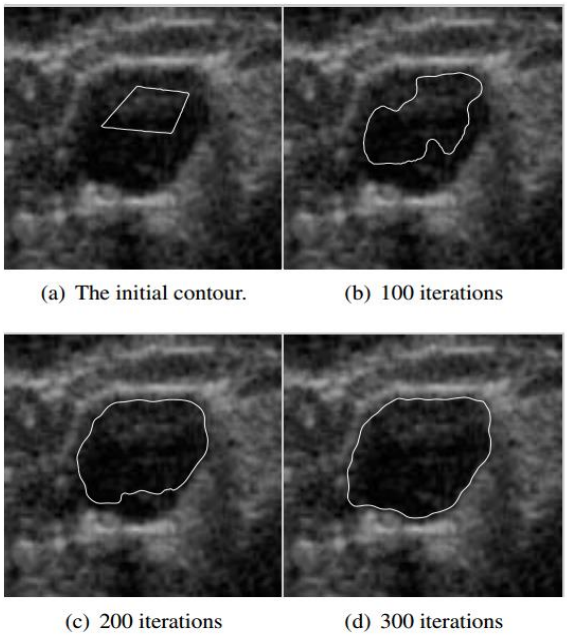

Figure 4.5 Result for an ultrasound image of carotid artery [85].

4.4. Preprocessing

4.4.1. Localizing the region of interest

In order to separate the region of interest (ROI) from the entire image, a localizing technique was applied. The technique was introduced by Burman et al. [86] and used an Interval Type-II fuzzy entropy based thresholding scheme along with Differential Evolution, which was a powerful meta-heuristic technique for faster convergence and less computational time complexity in order to determine the location of the optic disc. The multi-level image segmentation was a method used to segment an image into various objects in order to find the brightest object on the image, which was located in the OC, and hence a part of the OD. A range of membership values were introduced, instead of a single membership value as in Type-I Fuzzy Technique. A measurement called ultrafuzziness had been used to obtain the image thresholds [86]. Two thresholds were applied after transferring the image to gray scale in order to divide the image into three objects or

backgrounds as shown in the second column of Figure 4.6. The brightest region of the image was given by the upper threshold value in the multi-level segmented image. Some bright spots might be present due to pathology as in the second column of Figure 4.6 (B). Therefore, we had improved localization accuracy by choosing the biggest white spot as the cup location. Also the fundus image borders were eliminated in order to avoid large white spots that might appear due to bad image acquisition as in the second column of Figure 4.6 (C). Images of some pathological cases might have white spots bigger than the optic cup which results in bad localization as in Figure 4.6 (D). The localized image size for MESSIDOR and Bin Rushed images is 351X351 pixels. However, the localized image size for Magrabi images is 701X701 pixels due to the large images in that image set. The algorithm had been tested using RIGA dataset for all 750 fundus images and the localization accuracy and time consumed are shown in Table 4.1. This was done utilizing Matlab 2014b environment in a workstation with Intel Core i-7 2.50 GHz processor. Out of 750 images, 723 (96.4%) were successfully localized. Magrabi images were the worst with unsuccessful localization of 6 images and the percentage accuracy of 93.6%.

Table 4.1 The localization algorithm results.

	MESSIDOR Images	**Magrabi Images**	**Bin Rushed Images**	**Overall**
Number of Images	460	95	195	750
Success	449	89	185	724
Accuracy (Percentage)	97.6	93.6	94.8	96.5
Average time (sec)	4.437	4.881	4.742	4.686

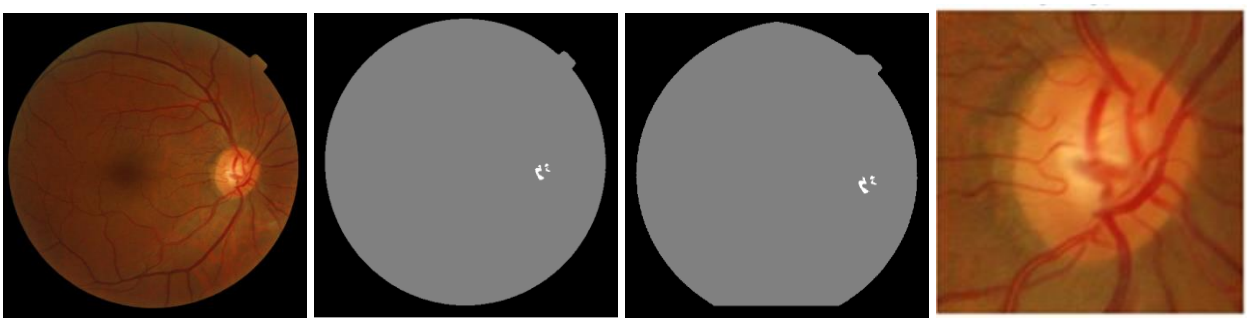

(A)

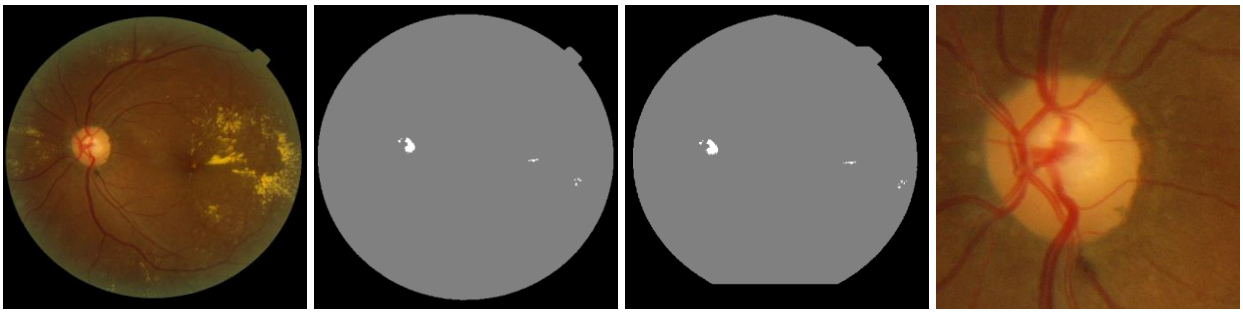

(B)

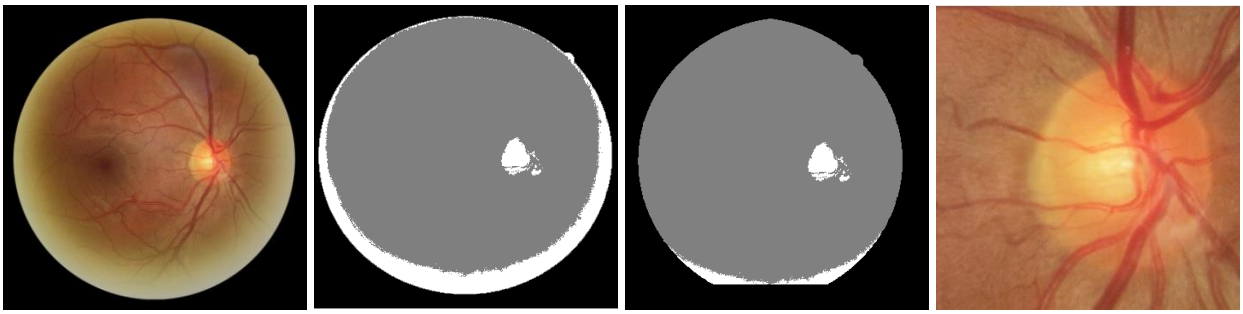

(C)

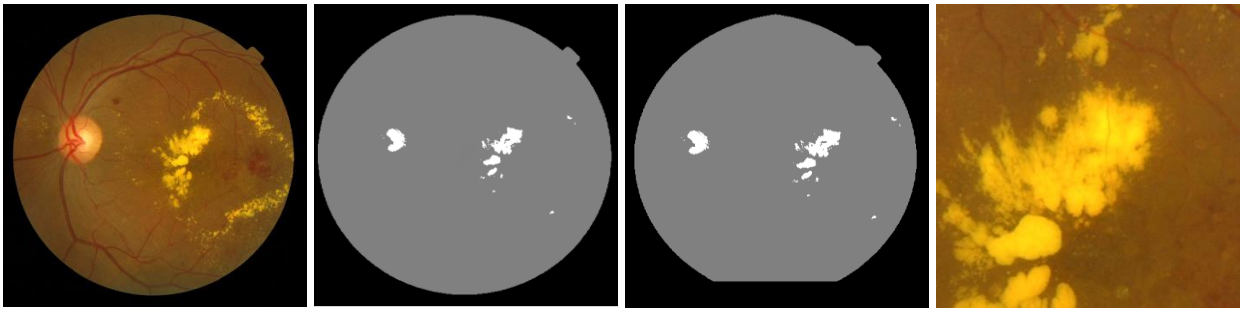

(D)

Figure 4.6 The results of the localizing algorithm.

4.5. Processing

4.5.1. Optic disc boundary segmentation

4.5.1.1. Algorithm

Optic disc (optic nerve head) is the round area containing the cup where the ganglion cell axons leave the eye. The area between the cup boundaries and disc boundaries is called neuroretinal rim area. Disc boundaries segmentation was concentrated on the borders between the disc and retina. The internal part in the disc represented by the cup boundaries will be discussed later in this chapter.

The gradual change in intensity between the disc and retina is obvious except in some pathological cases such as optic disc drusen, optic disc edema, peripapillary atrophy, optic pits, etc. which negatively affect the disc boundaries segmentation and reduce its accuracy.

In this thesis, the optic disc segmentation using an active counter model implemented via level set function has been utilized to detect the disc boundaries. In particular, a new variation formulation introduced by Li et al. [85], which was discussed in section 4.3, has been used.

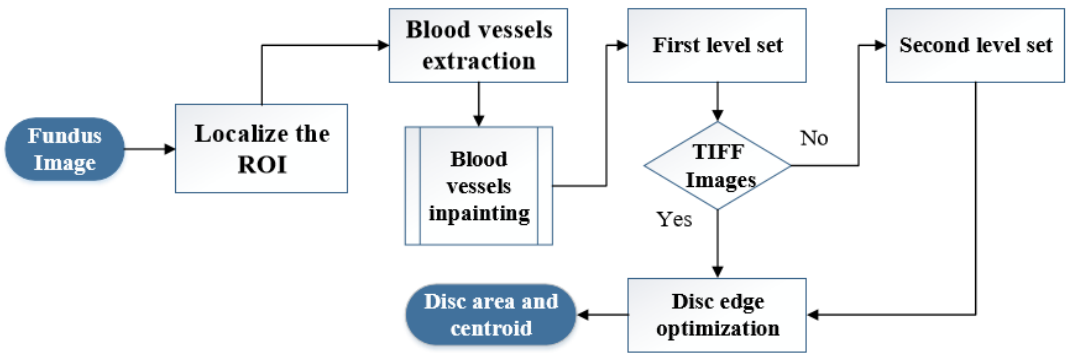

Figure 4.7 The flowchart for the disc segmentation algorithm.

As can be seen in Figurer 4.7, there was no more complication in the algorithm. Two hundred images from RIGA dataset have been used to train the algorithm. After localizing the ROI, the blood vessels were extracted via a top-hat transform on the G-channel of the fundus image. Then a fast digital image inpainting technique introduced by [87] was applied where the extracted blood vessels were the mask identifying the area to be inpainted. As the diffusion process is iterated, the inpainting progresses from the area boundary into the area itself. Basically, the user can specify the number of iterations; therefore, the algorithm works perfectly to inpaint a small area of the image. Since the area is small, the inpainting procedure can be approximated by an isotropic diffusion process which spreads the information from the area boundaries into the area itself in the gray scale image by repeatedly convolving the region to be inpainted with a diffusion kernel. Convolving an image with a Gaussian kernel (i.e., computing weighted averages of pixels' neighborhood) is equivalent to isotropic diffusion. The algorithm uses a weighted average kernel that only considers contributions from the neighboring pixels. Increasing the inpainted area reduces the quality as well as the number of iterations, making the process slower as shown later in the Results section (4.5.1.2.2). The algorithm worked well with good quality fundus images; however, it did not work properly with low quality fundus images because the blood vessels occupying big areas of the image made the process lengthy due to the greater number of iterations that needed to be applied to achieve good inpainting.

The disc segmentation algorithm used for RIGA dataset had two paths, one for TIFF images and another for JPG images. As illustrated in Figure 4.8, the algorithm was applied to TIFF images which have better contrast. The image in the second column shows the inpainted image in red channel where the contrast was clearly distinguishable between the disc and retina and the curve evolution had been set for 500 iterations. Therefore, the segmentation process represented by the

active contour model implemented by the level set [85] will be easy and more accurate, as shown in the third panel from the left. With trial and error, the level set was set to 70 iterations to allow best disc boundary detection. However, the disc edge had been influenced by the blood vessels as shown in the third panel of the same image. Therefore, a disc edge optimization algorithm was developed to optimize the disc edges and improve the accuracy (as shown in the last image) by converting the segmented disc to binary image and calculating the central point of circle disc edge and making it the origin of the coordinate system. From the central point, the angles and corresponding radius of each disc edge point to origin were calculated in order to compute the differences among radiuses to the angles. With the prior knowledge that every part of disc edge should be a smooth curve, the big difference between the radius of neighboring edge points was computed in order to detect where the disc edge was influenced by the blood vessels and then the edge was optimized by correcting the radius.

Figure 4.8 The disc segmentation procedures for TIFF images.

JPG images had gone through more processing due to their low contrast quality. In Figure 4.9, the second column of the first row represents the inpainted image in red channel. There were still some blood vessels after inpainting; however, they didn't affect the segmentation process. The third column represents the first level set applied on the inpainted image and it is clear that the first level set went outside the actual boundary. Therefore, the first level set was considered as more localized

optic disc in order to eliminate the big contrast variation that reduces the accuracy. After localizing the optic disc again and obtaining the rough disc boundaries, the newly localized image was split into left and right disc by a central point as shown in the fourth column. Finally, the second level set was applied on each of the two parts. The final results are shown in the fifth column. An edge optimization algorithm was needed to improve the contour in this image. In the second row, the first level set shows the worst case due to the large variation in the retina, specifically in the top right area of the image.

Sometimes there were blank areas in the concatenated disc edge from double level set, which can deteriorate the result. Therefore, blank elimination was developed to restore the edge by automatically detecting blank areas through analysis of the radius to angle and inpainting the edge binary image by adding some edge points to the blank according to the radius and angles of the two breakpoints in the blank.

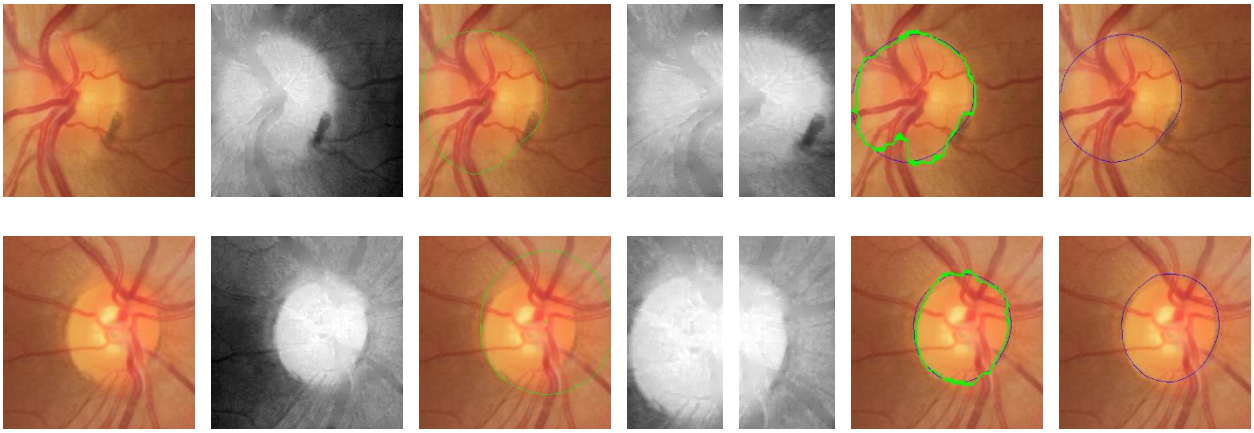

Figure 4.9 The disc segmentation procedures for JPG images.

4.5.1.2. Results

As seen in Figure 4.10, the disc segmentation algorithm went through the same steps that were used by the 6 ophthalmologists to evaluate the agreement on the images (presented in chapter 3).

The images with optic disc area and centroid agreed upon by at least four ophthalmologists were selected and used to evaluate the new algorithm. For every segmented image, the area and centroid were calculated in order to test their accuracy by comparing the newly computed SDs with those computed by the ophthalmologists as well as the algorithm, and then it was decided whether the segmentation was acceptable or not.

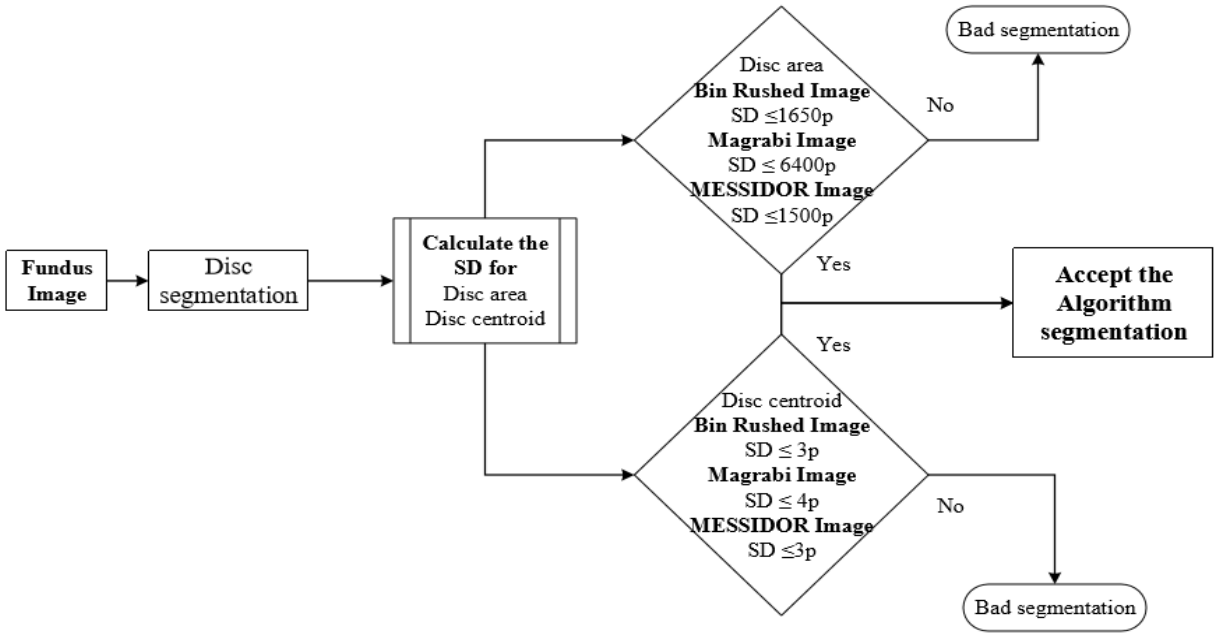

Figure 4.10 Flowchart for the analysis of the disc segmentation.

Figure 4.11 shows the comparison between the automatic segmentation and the one performed by the six ophthalmologists. The first column represents the annotation by the first ophthalmologist, the second column represents the annotation by the second ophthalmologist, and so on. The seventh column represents the result of the automatic segmentation by the algorithm. The first image is represented on the first row, the second image is represented on the second row, and so on. As mentioned in chapter 3, the mean SD was 1500 pixels for the disc area and 3 pixels for centroid. The annotations by ophthalmologists number one and six have been eliminated (since

they were outliers in terms of area) from the first image. Using the remaining images (the annotations by the other four ophthalmologists) for analysis of the area, the algorithm gave 1550 pixels as mean SD for disc area and 3 pixels as mean SD of the centroid. For the second image, the annotations by the first ophthalmologist were eliminated since they were outliers in terms of centroid. The algorithm's mean SD was 1600 pixels for area and 2.5 pixels for centroid. In the third image, the annotations by the first ophthalmologist were removed since the measurements of the centroid by this ophthalmologist increased the mean SD for all annotations to more than 3 pixels. The mean SD calculated by the algorithm was 1100 pixels for area and 2.5 pixels for centroid. In the last image, the annotations by ophthalmologists number one and three were considered as outliers in terms of area. The algorithm's mean SD was 1800 pixels for area and 4 pixels for centroid, which can be acceptable.

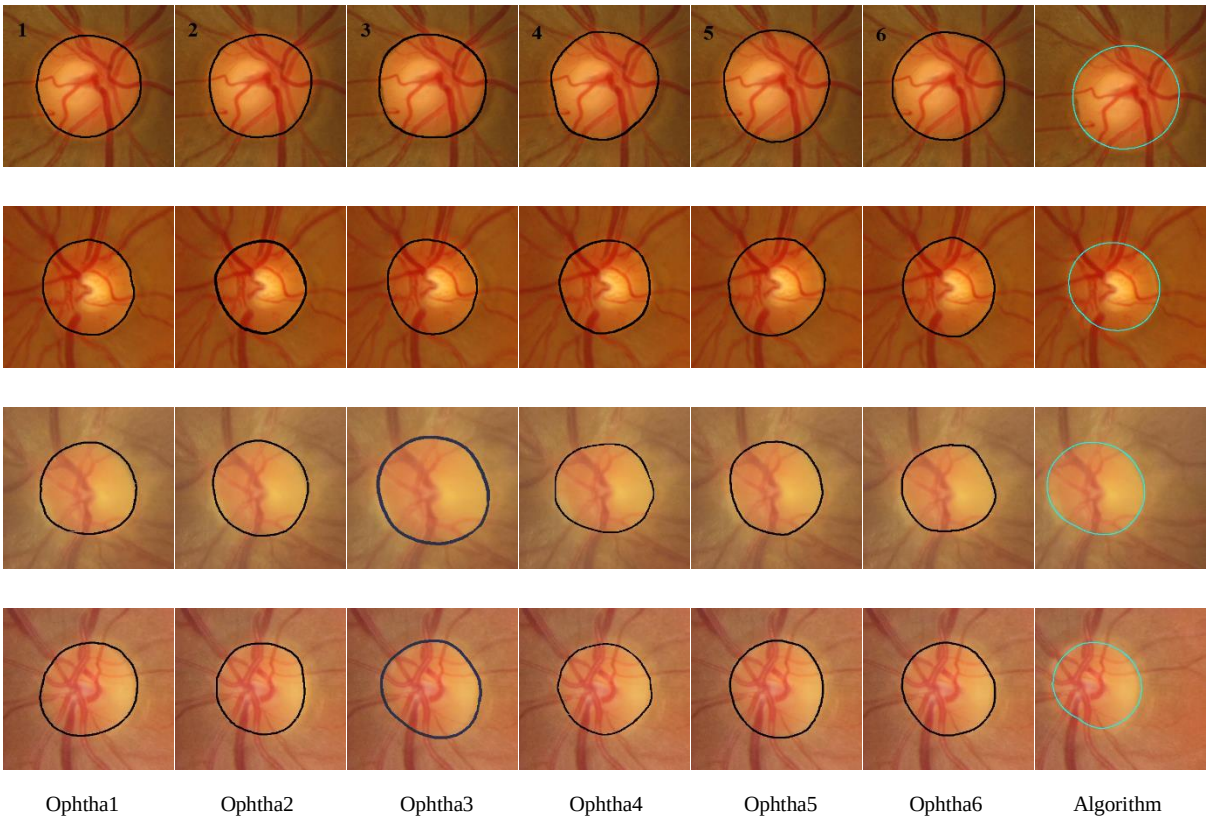

Figure 4.11 Examples for the good disc segmentation results for both TIFF and JPG images.

In Figure 4.12, the first image shows a huge variation in the annotations by the six ophthalmologists. The annotations by ophthalmologists number one and two were considered as outliers in terms of centroid. The annotations by ophthalmologist number three were considered as outliers in both area and centroid. The annotations by ophthalmologist number six were outliers in terms of area. The algorithm produced very poor results for both area and centroid. The right side of the disc boundaries was not clear due to some abnormalities. We conclude that this image should not be considered for evaluating the algorithm since the annotations by at least three ophthalmologists were eliminated due to outliers. In the second image, the Y axis of the centroid as annotated by ophthalmologist number six was an outlier. The algorithm gave poor results for both area and centroid due to the fact that the right and lower sides of the disc boundaries had almost the same intensity. In the third image, there were no outliers in the annotations by the six ophthalmologists. The algorithm gave good results in terms of area and centroid. In the last image, the annotations by ophthalmologists number two, three and four were outliers in terms of area, while the annotations by ophthalmologists number five and six were outliers in terms of centroid. Therefore, this image was not considered for evaluating the algorithm. This indicates that in this procedure the best agreed upon image was precisely selected for evaluating the algorithm.

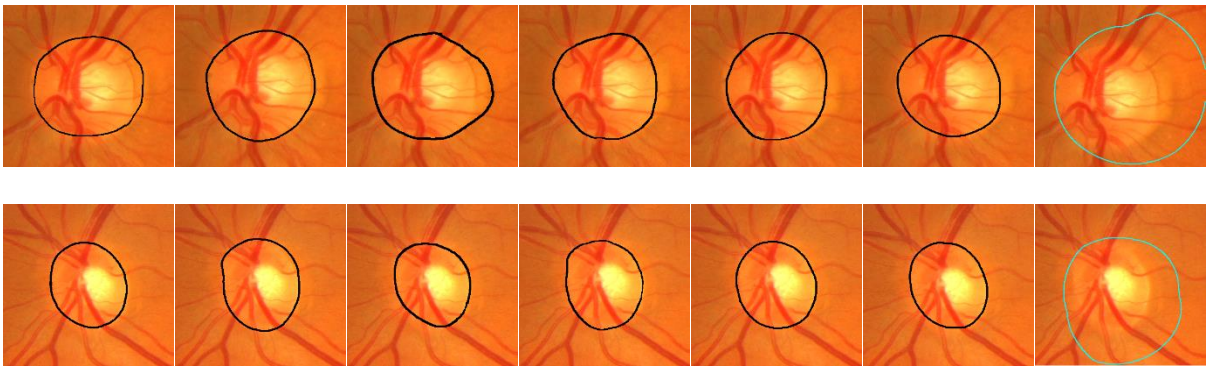

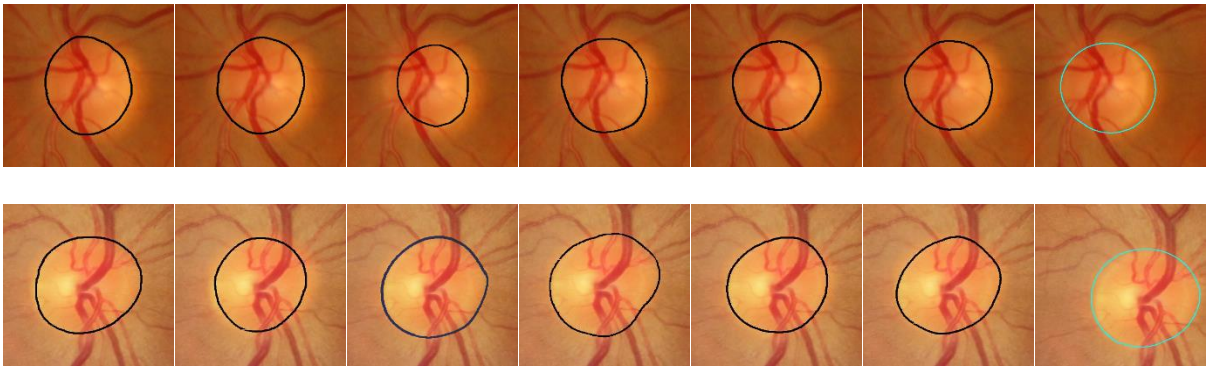

Figure 4.12 Examples for the bad disc segmentation results for both TIFF and JPG images.

4.5.1.2.1. Results of Bin Rushed dataset

Table 4.2 shows the results for Bin Rushed image set. The algorithm was tested using 195 images from which 10 images could not be localized. For area, an additional 7 images were eliminated since their area annotations by three ophthalmologists were outliers. Therefore, in total 178 images were tested for area and the accuracy was 155 images or 88.2%. On the other hand, 15 images were eliminated from the analysis of centroid. Therefore, in total 170 images were tested for centroid and the accuracy was 149 images or 87.6%. Thirty four images were removed from the analysis of both area and centroid. Many images were good in area but had problems in centroid and vice versa. In total, 151 images were tested and the accuracy was 130 images or 86%.

Table 4.2 The disc segmentation results for Bin Rushed images set.

	Disc Area	Disc Centroid	Both
Total number of images	195	195	195
# of images removed due to the lack agreement between the ophthalmologists	7	15	34
Images not localized	10	10	10
Total number of images tested	178	170	151
Accuracy (number of images)	155	149	130
Accuracy (percentage)	88.2	87.6	86
Average Time (s)	20-30s		

As can be seen in table 4.3, the accuracy of the annotations by each ophthalmologist was computed based on the other five ophthalmologists best images, i.e., if for an image there were at least three outliers in terms of disc area or centroid among the annotations by five ophthalmologists, then the image was eliminated from measuring the accuracy of the annotations by the sixth ophthalmologist. While the algorithm accuracy was evaluated based on the annotations by each of the six ophthalmologists. Based on the 156 images tested, the annotations by ophthalmologist number four with 92.9% accuracy were the most accurate. The algorithm results were the second best. The algorithm was tested using 151 images (5 fewer images) and the accuracy was 86%. Then, the annotations by ophthalmologist number six followed by those by ophthalmologist number five which were tested using 163 and 162 images and their accuracies were 85.2% and 84.5%, respectively. Figure 4.13 shows these results. The average computation time was between 20 to 30 seconds for this image set due to the number of iterations set for the level set as well as the inpainting. 19 to 34 images, representing 9 to 17 percent of the total number of images in the set, were eliminated due to lack of agreement.

Table 4.3 The disc accuracy results for the six ophthalmologists and the segmentation algorithm for Bin Rushed images set.

	Ophth1	Ophth2	Ophth3	Ophth4	Ophth5	Ophth6	Auto
Total number of images	195	195	195	195	195	195	195
# of images removed due to the lack agreement between the ophthalmologists	19	22	21	29	23	22	34
Images not localized	10	10	10	10	10	10	10
Total number of images tested	166	163	164	156	162	163	151
Accuracy (number of images)	134	124	115	145	137	139	130
Accuracy (percentage)	80.7	76	70.1	92.9	84.5	85.2	86

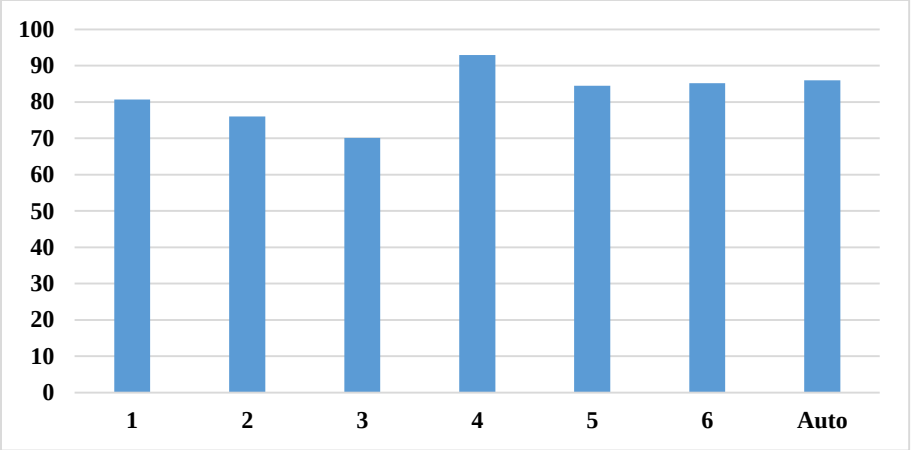

Figure 4.13 The disc accuracy results for all the six ophthalmologists as well as the algorithm for Bin Rushed images set. The X axis represents the number of 6 ophthalmologists and the algorithm. The Y axis represents the accuracy (percentage).

4.5.1.2.2. Results of Magrabi dataset

Table 4.4 shows the results of the second image resources for RIGA dataset (Magrabi dataset). Ninety five images were tested from which 6 images were not localized. In terms of area, 8 images were eliminated because of huge variation among the annotations by the six ophthalmologists. Therefore, the total images tested were 81 images. Seventy three images (90.1%) were segmented successfully. On the other hand, 10 images were eliminated in terms of centroid, therefore, the total images tested were 79 images, and the accuracy was 89.8%. For testing both the area and centroid, 21 images were eliminated. Therefore, in total 68 images were tested from which 61 images were correctly segmented (89.7% accuracy). Magrabi dataset seems to be better than Bin Rushed dataset in terms of accuracy. However, it took longer to run Magrabi dataset (between 70 and 120 seconds) due to the size of the images; the images in Magrabi dataset are larger than the images in the other two datasets.

Table 4.4 The disc segmentation results for Magrabi images set.

	Disc Area	Disc Centroid	Both
Total number of images	95	95	95
# of images removed due to the lack agreement between the ophthalmologists	8	10	21
Images not localized	6	6	6
Total number of images tested	81	79	68
Accuracy (number of images)	73	71	61
Accuracy (percentage)	90.1	89.8	89.7
Average Time (s)	70-120s due to the big size of the images		

The annotations by ophthalmologist number four for this image set showed a high accuracy (Table 4.5). Sixteen images were removed due to the variations among the annotations by the ophthalmologists. The total tested images were 73 images and the accuracy was 94.5%. Ophthalmologist number two had the second best annotations. Here 18 images were eliminated, hence the total tested images were 71 and the accuracy was 91.5%. The algorithm was the third best where the total tested images were 68, which was less than the previous two, and the accuracy was 89.7% (Figure 4.14). Between 14 and 21 images, i.e., 14% and 22% of the total number of images in the dataset, were eliminated from the test.

Table 4.5 The disc accuracy results for the six ophthalmologists and the segmentation algorithm for Magrabi images set.

	Ophth1	Ophth2	Ophth3	Ophth4	Ophth5	Ophth6	Auto
Total number of images	95	95	95	95	95	95	95
# of images removed due to the lack agreement between the ophthalmologists	14	15	15	18	15	16	21
Images not localized	6	6	6	6	6	6	6
Total number of images tested	75	74	74	71	74	73	68
Accuracy (number of images)	58	56	58	65	60	69	61
Accuracy (percentage)	77.3	75.6	78.36	91.5	81	94.5	89.7

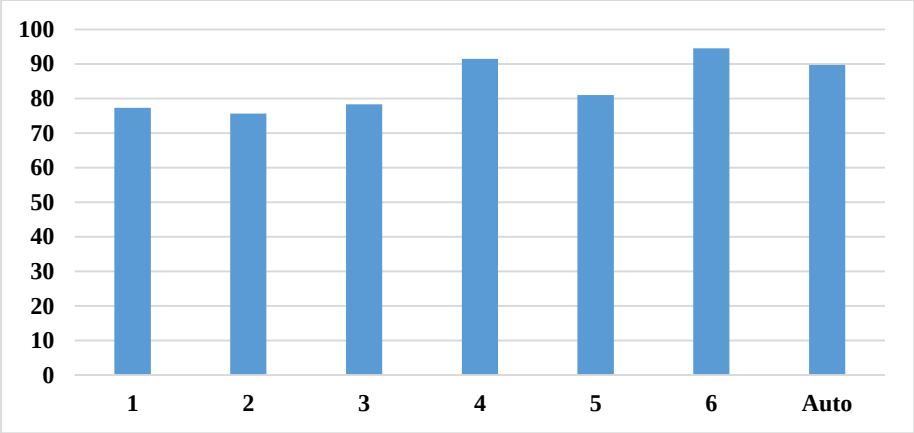

Figure 4.14 The disc accuracy results for all the six ophthalmologists as well as the algorithm for Magrabi images set. The X axis represents the number of 6 ophthalmologists and the algorithm. The Y axis represents the accuracy (percentage).

4.5.1.2.3. Results of MESSIDOR dataset

Finally, the last image set used to evaluate the algorithm was MESSIDOR dataset with 260 images (Table 4.6). Ten images were not localized. Only two images were removed in terms of area, hence 248 images were tested for area. Forty images were unsuccessfully segmented; therefore, the accuracy was 86.6%. Five images were eliminated from centroid evaluation. Therefore, in total 245 images were tested for centroid. Forty two images failed in this test, i.e., the accuracy was 82%. For both area and centroid, 28 images were removed from the test; therefore, 222 images were tested and the accuracy was 80%. It took 20 to 30 seconds to run MESSIDOR dataset, which is the same as the time required to run Bin Rushed dataset. This is due to the fact that the images in the two datasets are similar in size.

In terms of accuracy, the algorithm performed best with Magrabi, then Bin Rushed, and finally MESSIDOR dataset.

Table 4.6 The disc segmentation results for MESSIDOR images set.

	Disc Area	Disc Centroid	Both
Total number of images	260	260	260
# of images removed due to the lack agreement between the ophthalmologists	2	5	28
Images not localized	10	10	10
Total number of images tested	248	245	222
Accuracy (number of images)	208	203	179
Accuracy (percentage)	86.6	82	80
Average Time (s)	20-30s		

Based on the data presented in Table 4.7, ophthalmologists number three and four showed the best performance in the annotation using 227 and 229 images with 91.6% and 91.2% accuracy, respectively. The algorithm accuracy in this dataset was the second last and was close to that of ophthalmologists number five and one (Figure 4.15). Between 14 and 28 images (5% to 10.7% of images) were eliminated among all the 6 ophthalmologists and the algorithm. Magrabi dataset had the greatest percentage of eliminated images, followed by Bin Rushed dataset, and finally MESSIDOER dataset. The variations in the annotation of the three image sets obviously influenced the agreement and this is represented in the variation of the mean SD.

Table 4.7 The disc accuracy results for the six ophthalmologists and the segmentation algorithm for MESSIDOR images set.

	Ophth1	Ophth2	Ophth3	Ophth4	Ophth5	Ophth6	Auto
Total number of images	260	260	260	260	260	260	260
# of images removed due to the lack agreement between the ophthalmologists	14	16	23	21	21	20	28
Images not localized	10	10	10	10	10	10	10
Total number of images tested	236	234	227	229	229	230	222
Accuracy (number of images)	195	177	208	209	187	199	179
Accuracy (percentage)	82.6	75.6	91.6	91.2	81.6	86.5	80

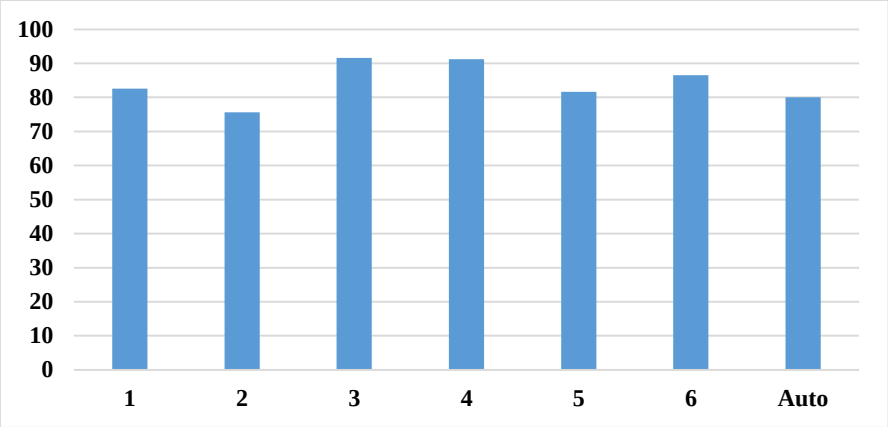

Figure 4.15 The disc accuracy results for all the six ophthalmologists as well as the algorithm for MESSIDOR images set. The X axis represents the number of 6 ophthalmologists and the algorithm. The Y axis represents the accuracy (percentage).

4.5.1.2.4. Consolidated results for the disc

This section presents a comprehensive evaluation of the annotations done either automatically by the algorithm or manually by the six ophthalmologists. In total, 550 images were used from the three image sources of RIGA dataset (Table 4.8) from which 26 images were not localized. Seventeen images were eliminated from area evaluation. The total number of images tested was 507, and the number of successfully segmented images was 436 (85.9%). Thirty images were eliminated from evaluation of centroid accuracy. Therefore, a total of 494 images were tested and 423 images (85.6%) were successfully segmented. For both area and centroid 83 images were eliminated. In total 441 images were tested from which 71 images failed in segmentation, giving the final accuracy of 83.9% for the disc algorithm segmentation for RIGA dataset.

Table 4.8 The disc segmentation results for all the three images sets together.

	Disc Area	Disc Centroid	Both
Total number of images	550	550	550
# of images removed due to the lack agreement between the ophthalmologists	17	30	83
Images not localized	26	26	26
Total number of images tested	507	494	441
Accuracy (number of images)	436	423	370
Accuracy (percentage)	85.9	85.6	83.9

Table 4.9 compares the accuracy of disc segmentation in terms of disc area and centroid. Ophthalmologist number four tested 472 images for disc annotation and obtained the best disc annotation (88.7% accuracy). Ophthalmologist number six was the second best in disc annotation, testing 466 images with 87.3% accuracy. The algorithm was the third best in disc boundaries annotation. The algorithm tested 441 images with 83.9% accuracy. The lowest accuracy was 75.7% based on testing 471 images. In conclusion, the accuracy of annotating the disc boundaries was high for both manual annotation and automatic segmentation due to the clarity of the disc intensity. The abnormalities occurring on the two sides of the disc boundaries caused most of the challenges. Figure 4.16 provides an easy comparison of the performance of the six ophthalmologists and the algorithm in detecting disc boundaries.

Table 4.9 The disc accuracy results for the six ophthalmologists and the segmentation algorithm for all the three images sets together.

	Ophth1	Ophth2	Ophth3	Ophth4	Ophth5	Ophth6	Auto
Total number of images	550	550	550	550	550	550	550
# of images removed due to the lack agreement between the ophthalmologists	47	53	59	68	59	58	83
Images not localized	26	26	26	10	26	26	26
Total number of images tested	477	471	465	472	465	466	441
Accuracy (number of images)	387	357	381	419	384	407	370
Accuracy (percentage)	81.1	75.7	81.9	88.7	82.5	87.3	83.9

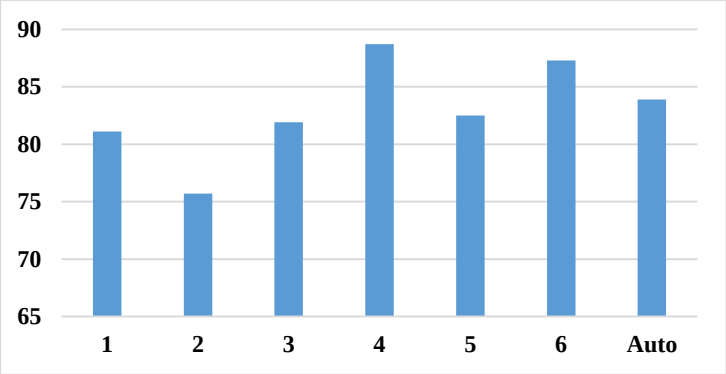

Figure 4.16 The disc accuracy results for all the six ophthalmologists as well as the algorithm for the three images sets. The X axis represents the number of 6 ophthalmologists and the algorithm. The Y axis represents the accuracy (percentage).

Figure 4.17 shows the variation in the performance on the three image sets. Ophthalmologists number one, two, four and five showed similar performance regardless of the image set used. Ophthalmologist number three showed different performance; he/she performed best for MESSIDOER image set and worst for Bin Rushed image set. Ophthalmologist number six showed a performance similar to that of the algorithm in terms of stability. Still the lowest accuracy was around 70% which was assumed to be high. Ophthalmologist number four showed a precise, stable and high performance for detecting the disc boundaries regardless of the dataset.

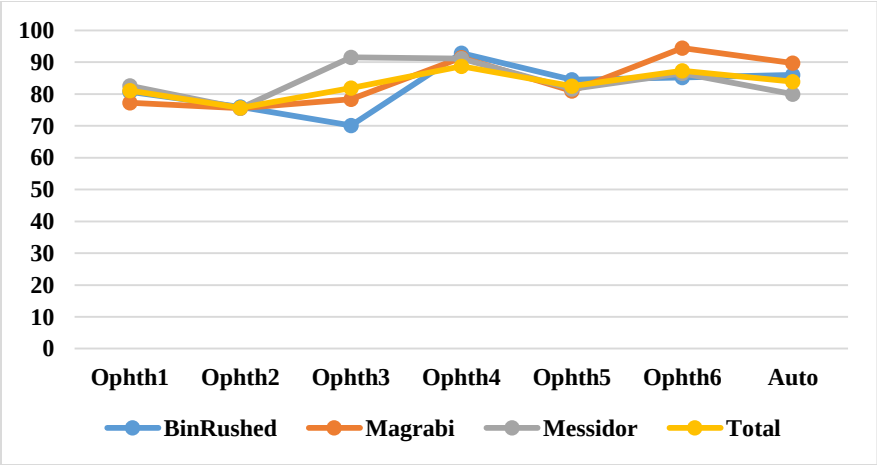

Figure 4.17 The disc accuracy results for all the six ophthalmologists as well as the algorithm for the three images sets individually. The X axis represents the number of 6 ophthalmologists and the algorithm. The Y axis represents the accuracy (percentage).

4.5.1.2.5. Agreement for the disc

Table 4.10 shows the number of images agreed in the disc area and centroid among the six ophthalmologists as well as the disc algorithm segmentation. The accuracy calculations reflected how every ophthalmologist agreed with the others and who had the best performance. All ophthalmologists had the best agreement with ophthalmologist number four, then ophthalmologist number six. The least agreement was seen for the work of ophthalmologist number two. Ophthalmologist number three was the second last. The best agreement for the algorithm was with the annotations by ophthalmologist number four in 349 images (63.4%) while the lowest agreement was with the annotations by ophthalmologist number two in 316 images (57.4%). On the other hand, the best overall agreement was between the annotations by ophthalmologists number four and six in 410 images (74.5%) and the lowest agreement was between the annotations by ophthalmologists number two and three in 312 images (56.7%).

As the 'Total' values in Table 4.10 indicate, the annotations by ophthalmologist number four were the best, followed by the annotations by ophthalmologist number six, then the annotations by ophthalmologist number five, then those by the algorithm and ophthalmologist number one, then the annotations by ophthalmologist number three and finally the annotations by ophthalmologist number two. The accuracy of performance was the same for ophthalmologists number four, six and two, followed by the algorithm, and then ophthalmologist number five, and then three, and finally ophthalmologist number one. As the result, having annotations in a high number of images in agreement with the others does not mean good accuracy in disc detection. Figure 4.18 shows how the agreements are in groups.

Table 4.10 The disc number of images agreement between the ophthalmologists as well as the algorithm.

	Ophth1	Ophth2	Ophth3	Ophth4	Ophth5	Ophth6	Auto
Ophth1	550	318	336	378	345	364	344
Ophth2	318	550	312	356	324	336	316
Ophth3	336	312	550	375	344	362	335
Ophth4	378	356	375	550	383	410	379
Ophth5	345	324	344	383	550	364	349
Ophth6	364	336	362	410	364	550	361
Auto	344	316	335	379	349	361	550
Total	2085	2046	2064	2281	2109	2197	2084

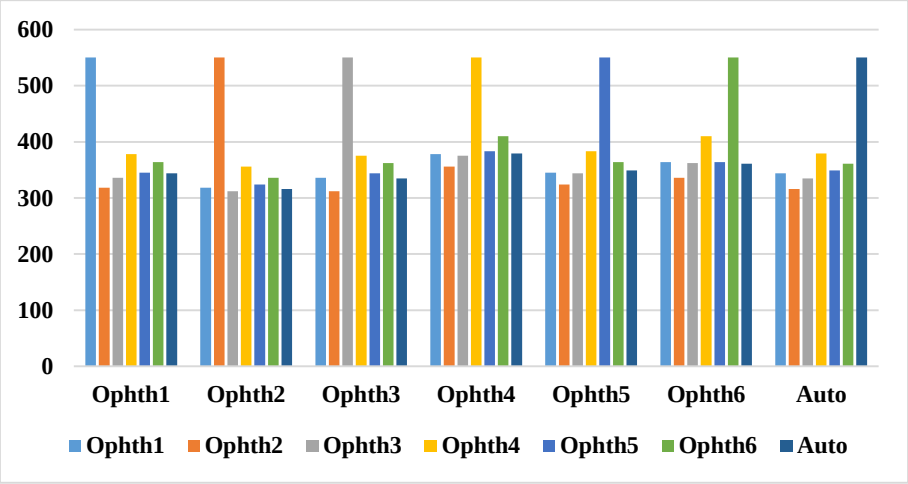

Figure 4.18 The disc agreement results for all the six ophthalmologists as well as the algorithm for all images sets. The X axis represents the number of 6 ophthalmologists and algorithm. The Y axis represents the number of agreed images.

Figure 4.19 demonstrates how the ophthalmologists' performance was regarding the agreement in the number of images. Clearly ophthalmologist number four had the best agreement with the others due to his high accuracy in detecting the disc boundaries where he had 2281 images agreed with the other five ophthalmologists in addition to the algorithm. On the other hand, ophthalmologist number two had the lowest agreement; only in 2046 images. However, the difference between the

highest and lowest agreement was only in 235 images, proving that all six ophthalmologists as well as the algorithm detected the disc boundaries properly.

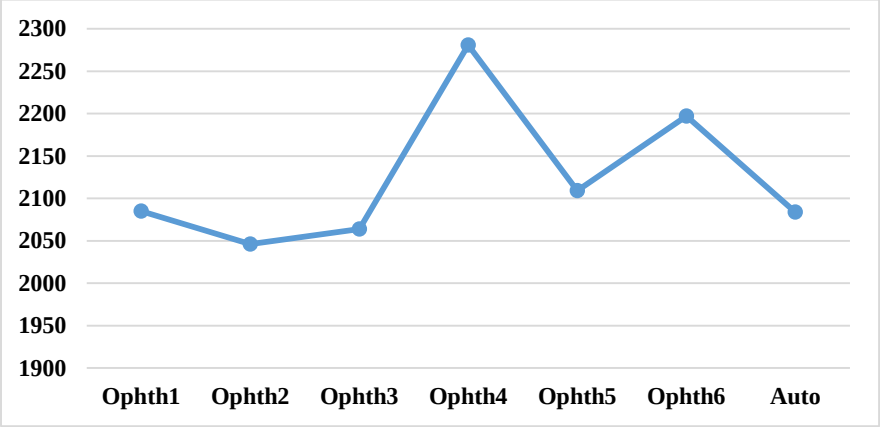

Figure 4.19 The disc agreement results for all the six ophthalmologists as well as the algorithm for all images sets. The X axis represents the number of 6 ophthalmologists and algorithm. The Y axis represents the number of total agreed images.

4.5.2. Optic cup boundary segmentation

4.5.2.1. Algorithm

Cup segmentation was the most challenging part of image processing of the optic nerve head (ONH) due to the complexity of its structure. In some cases, blood vessels densely cover the cup boundary, while in other cases they form the boundaries.

The gradual intensity change between the cup and neuroretinal rim (the area surrounding the cup) ending with the disc boundary caused additional complications for cup segmentation using image processing methods. The cup segmentation based on intensity gradient and blood vessel kinks extraction, and the different algorithms that had been developed were introduced in the Literature Review chapter.

In this thesis we considered the image intensity and vessel kinking in development of a new algorithm for automatic image segmentation of optic cup, which leads to a comprehensive system for diagnosis of glaucoma with the optic disc image segmentation.

Figure 4.21 shows the flowchart of the optic cup segmentation algorithm. The obtained outcomes were cup area and centroid. To evaluate the accuracy of the algorithm, the results were compared with the results reported by the six ophthalmologists using RIGA dataset.

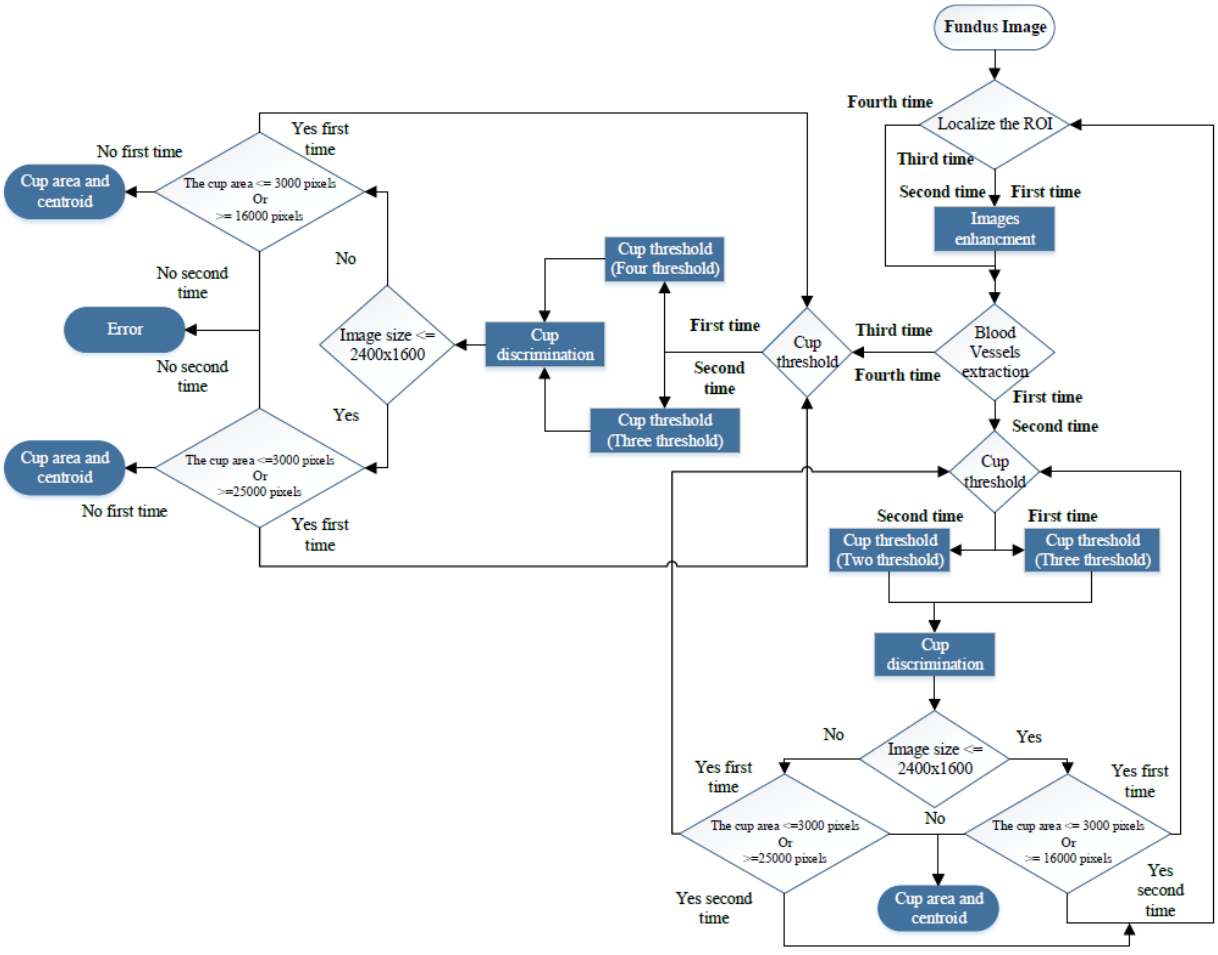

Figure 4.20 Flowchart for the cup segmentation algorithm.

As the flowchart in Figure 4.20 shows, the localized image was the starting point. Basically, four loops were used to achieve the goal of this algorithm for segmenting the cup boundaries. This algorithm was built based on 200 training images from RIGA dataset. Trial and error technique was used to reach the best results. Therefore, the four loops are now automatically leading to the best cup segmentation. After localizing the ONH, the image was enhanced by stretching the image contrast and equalizing the histogram to increase the variation between the image parts including retina, rim, blood vessels and cup as can be seen in the first column for the original image in Figure 4.21. The blood vessels were extracted using a top-hat transform on the G-channel of the fundus image. As mentioned in section 5.4.1.1., the blood vessels have more contrast in the G-channel, making the top-hat transform suitable for extraction of small vessels. That led to detecting small vessel kinks, which helped with detecting the cup boundaries as can be seen in the second column of Figure 4.21. Then the blood vessels were thresholded using *Otsu's* algorithm [49]. Top-hat transform is basically the difference between the original image and its opening operation. On the other hand *Otsu's* algorithm is clustering based image thresholding, which assumes the image has two classes of pixels (foreground pixels and background pixels), then computes the best threshold value. The blood vessels extracting operation was used to detect the curvature of the blood vessels (kinks), which indicated the cup boundary. The blood vessels were removed since they restricted the cup threshold intensity as can be seen in the third column of Figure 4.21. Based on the flowchart, image thresholding was applied using an Interval Type-II fuzzy entropy based thresholding scheme with Differential Evolution on the localized image to detect the intensity of the optic cup borders. In the localized image, the thresholds were more accurate than the entire image which was applied to find the optic disc in the preprocessing. Here the variation in the contrast was more limited since it was applied on a small portion of the image. There were clear

variations among the retina, blood vessels, rim area and cup as can be seen in the original images shown in the first column of Figure 4.21. The four loops were considered for four different threshold values based on some conditions. Three thresholds were applied as the first loop in the cup detection case to have four parts or backgrounds. Increasing the threshold values worked very well with good quality images; however, it did not give better thresholding for images with poor quality. In some cases the analysis took too much time and still gave worse thresholding. Therefore, after trying different threshold values of up to 30, we decided to start apply only three thresholds due to their effectiveness in terms of area and centroid. After applying the threshold, the cup was estimated as the brightest spot in the localized images. However, some small bright spots might appear; therefore, the white spots of less than 50 pixels were eliminated to reduce the error that might occur when approximating the cup. The blood vessels were brought back in order to fill out the gaps in the white spots as shown in the fourth column of Figure 4.21. Then a morphological closing operation was applied to close the small gaps that remained in the white spots even after adding the blood vessels to prevent errors that might occur when applying Hough transform [88] to distinguish the cup. Two threshold was applied as the second loop as shown in the flowchart in Figure 4.20. Two conditions were considered in order to go to the second loop (Figure 4.20). These were (1) if the cup size is less than 3000 pixels, (2) if the cup size is greater than 16000 pixels. Where 16000 pixels we estimated for the disc area size and that was for images size less or equal to 2400x1600p. While for images equal or greater than 2400x1600p the two conditions were (1) if the cup size is less than 3000 pixels, (2) if the cup size is greater than 25000 pixels. Same conditions were considered for the third loop, while in this case four thresholds were applied, however without image enhancement which was used for the first two loops. If the segmentation for the third loop matched the two aforementioned conditions, then the fourth loop

was applied for three thresholds without image enhancement similar to what was done for the third loop. For any loop, the cup area and centroid were calculated when the process did not pass the two conditions.

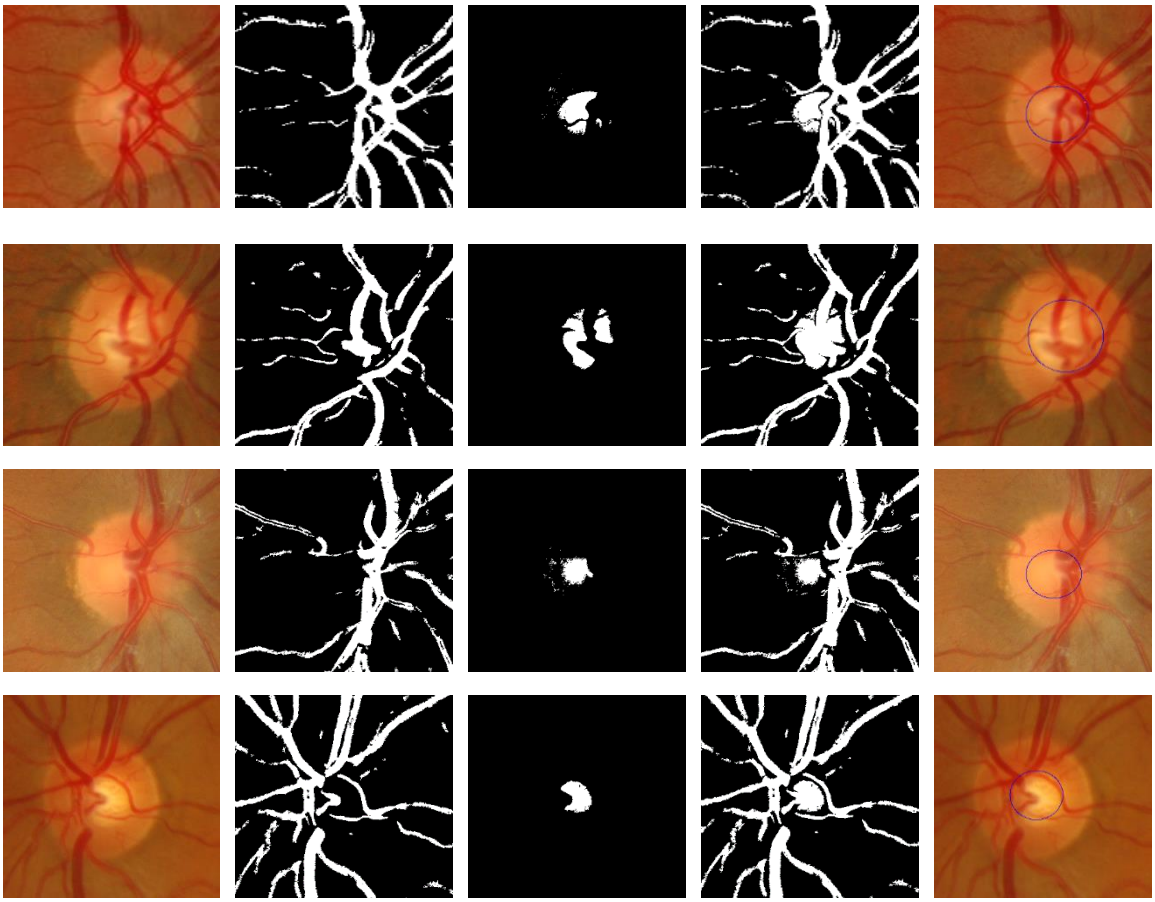

Figure 4.21 The cup segmentation procedures.

Figure 4.21 shows different images with different cup situations. The image on the first row represents unclear cup intensity with clear blood vessel kinks; the image on the second row represents clear cup intensity with some blood vessel kinks; the image on the third row represents unclear cup intensity without any blood vessel kinks; and finally the image on the last row represents clear cup intensity with clear blood vessel kinks. The area calculations showed good results when compared with manual annotations. The calculations of centroids did not give good

results practically on the X axis due to the blood vessels specifically in the nasal side. The algorithm up to this point has been tested on 100 images from MESSIDOR dataset and the results are shown in Table 4.11 [88]. Therefore, a function was developed as well as the disc segmentation centroid was involved to improve the cup centroid. The main goal of the function was to include the blood vessels in the nasal side of the cup.

Table 4.11 The cup segmentation results for the 100 images from MESSIDOR images set.

	Area		Centroid		Both	
Success	81	89 %	72	79.1%	66	72.5%
Fail	10	11%	19	20.8%	25	27.4%
Total	92	100%	92	100%	92	100%
Computational time in sec			9.13s			

The area inside the disc was considered as a more localized image for solving the centroid problem only on X axis. Three small squares of 25x25 pixels were created on the same centroid X axis of the segmented cup in order to measure the highest intensity of blood vessels among the three squares (Figure 4.22), then the cup segmented border was dragged inside the chosen square. If the segmented image was on the right side, then the three squares would be on the right half of the segmented disc and vice versa. Three options were considered inside that square: (1) near edge to the cup segmented centroid, (2) middle of the square, and (3) far away edge which was always close to the disc boundaries as shown in the second row of Figure 4.22 (A-B-C-D). The decision for the three options was based on the disc centroid, i.e., the cup was going through all three options and the one with the cup centroid as close as possible to the disc centroid was chosen as the best X segmented cup centroid. That made the blood vessels on the nasal side 100% inside the cup boundary segmentation, which always cover the cup boundaries in this area. On the other hand, after choosing the best X axis, the Y axis was fixed so that the length of the maximum distance between the disc and cup Y axes was equal or less than 10 pixels. For example, if the difference

between the disc and cup in Y axis was 12 pixels, the cup was automatically moved down two pixels (Figure 4.22(A)). In the first row of Figure 4.22(A), the first panel represents the localized image, the second panel represents the thresholded cup with the extracted blood vessels, while the third panel is the segmented cup, which was the final step for the 100 images tested previously. In this image, the centroid made the segmentation results bad in comparison with the results of the annotations by the six ophthalmologists. The last panel in this row is the new function, where the middle square had the most blood vessels pixels intensity, therefore, the nasal cup boundaries must be dragged inside it. As long as the boundaries were already inside the square (as shown in the first image in the second row), the difference between the disc centroid and cup centroid in the Y axis was more than 10 pixels. Therefore, the cup was moved down until the difference between the two centroids was exactly 10 pixels. The second image shows the near edge adjustment with the new Y axis. The third image shows the middle edge adjustment which was the same as the original, while the last image is the far away adjustment. Based on the aforementioned criteria, the best decision matching the annotations of centroid by the six ophthalmologists was the middle edge adjustment, which was the same as the original and that was the shortest distance between the disc centroid and cup centroid. The same procedures were applied to the second image in figure 4.22 (B). The middle square had the most blood vessels pixels intensity as shown in the last panel of the first row. For Y axis, the distance between the disc centroid and cup centroid was less than 10 pixels; therefore, there was no need to move down the cup Y centroid any more. While for X axis, the segmentation was tested for all the three adjustments in addition to the original position as shown in the second row. The best decision made based on the shortest distance between the two centroids was far away adjustment as can be seen in the first image in the second row, and gave good results in comparison with the six manual annotations. The same was true for case (C)

in which the best decision was the edge middle adjustment, and there was no need to change the Y axis. In the last case, i.e., case (D), there was no need for any change because the Y axis gave good results and in the X axis the original segmentation gave the shortest distance between the two centroids. Finally, the segmented disc boundaries were considered now for the loops conditions rather than the number of pixels, which were 16000 pixels for images less or equal to 2400X1600p and 25000 pixels for larger images.

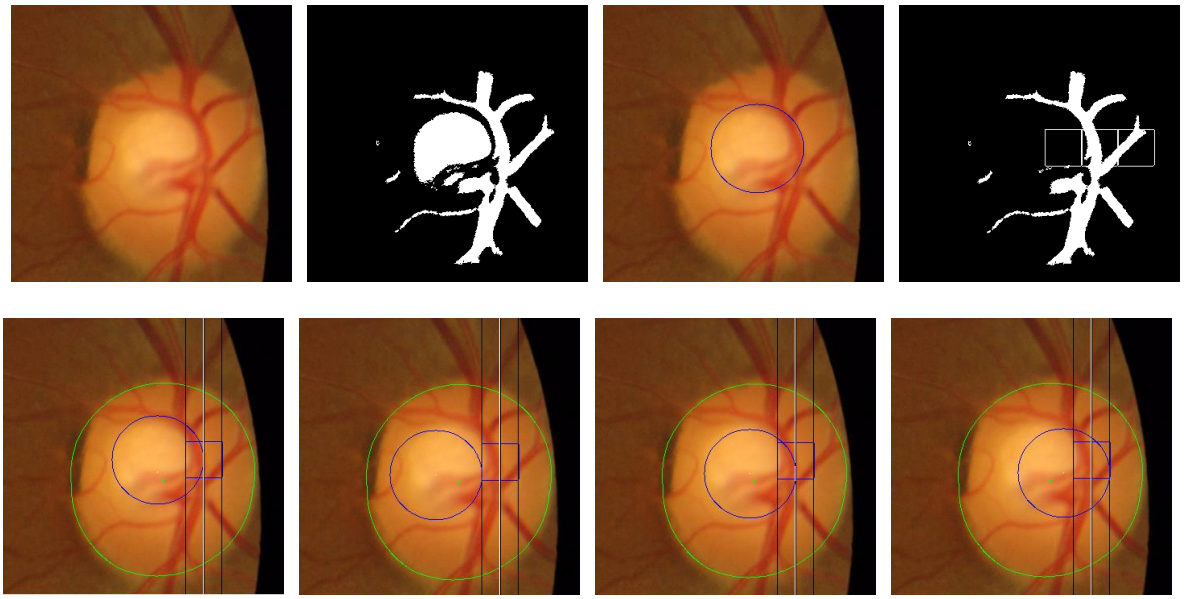

(A)

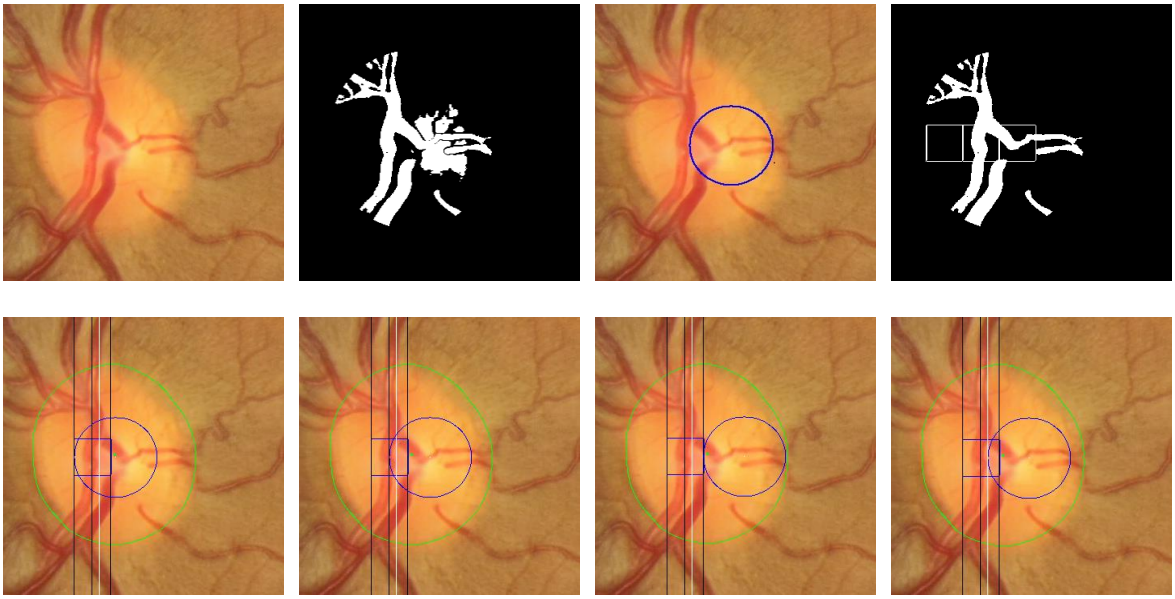

(B)

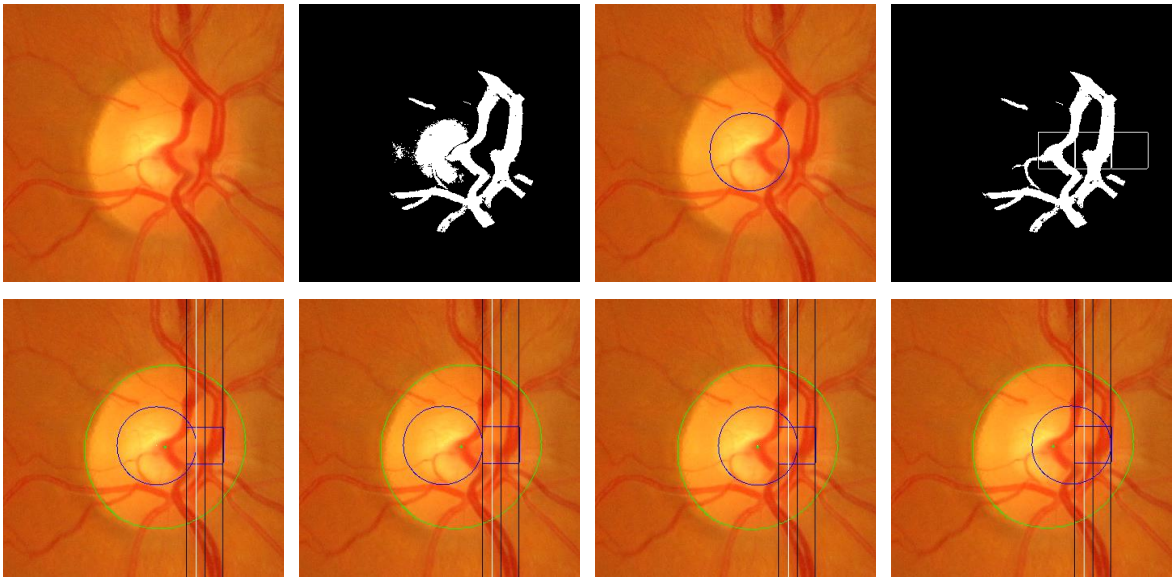

(C)

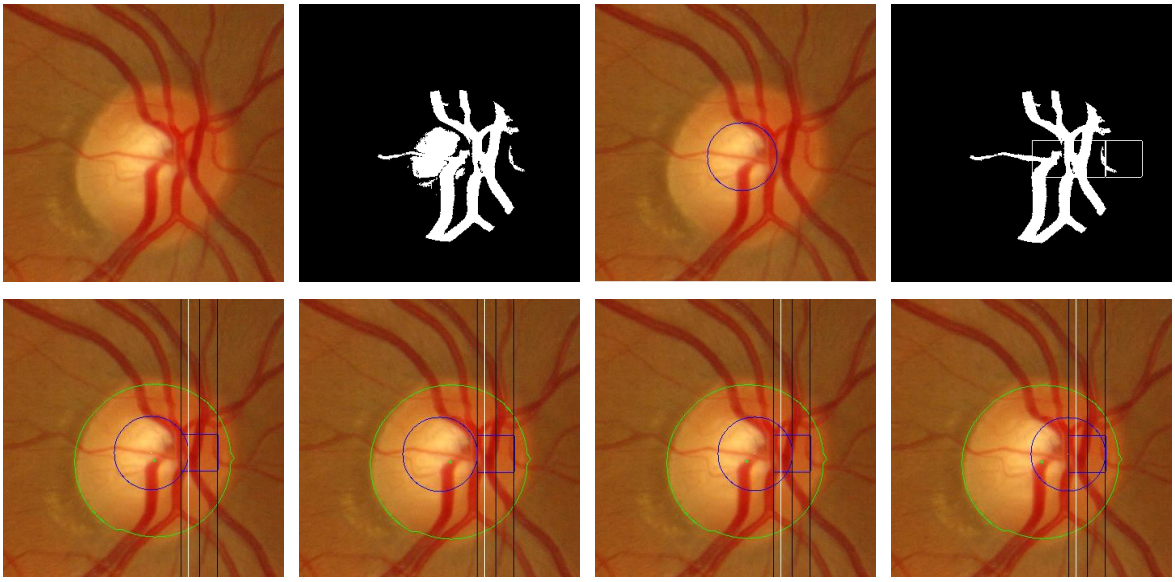

(D)

Figure 4.22 The function of the cup centroid for X and Y.

4.5.2.2. Results

The analyses conducted for calculations of OD were repeated for calculations of OC (Figure 4.23).

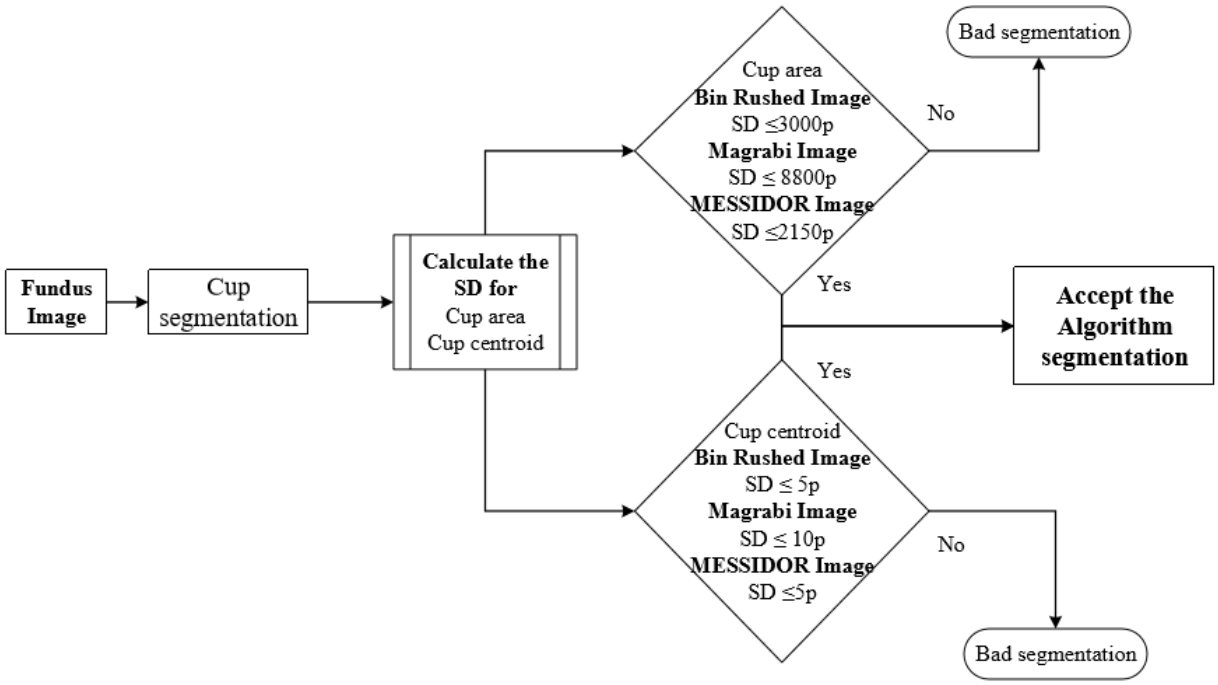

Figure 4.23 Flowchart for the analysis of the cup segmentation.

Figure 4.24 compares the results of automatic segmentation and the annotations by the six ophthalmologists. The first column shows the annotations by the first ophthalmologist, the second column shows the annotations by the second ophthalmologist and so on. The seventh column represents the result of automatic segmentation. The four rows represent four different images with different situations. In the first row, the annotations by all six ophthalmologists were close to each other in terms of area and centroid and the algorithm gave the same results. In the second row, the annotation by ophthalmologist number five was an outlier in the area size and was eliminated from the analysis. In this row, the results of the algorithm were in good agreement with the annotations

by the other five ophthalmologists. For the first three images, the algorithm gave perfect results in terms of area and centroid. In the last image, the annotations by ophthalmologists number two and six were outliers in their centroid, therefore they were eliminated. In the same image the annotations by ophthalmologists three and five were outliers in their area, thus they were eliminated too. As a result, four images were removed. Here, there was no agreement among the ophthalmologists' annotations, and therefore, the image was not considered in the evaluation of the algorithm. The automatic algorithm produced results similar to the annotations by two ophthalmologists.

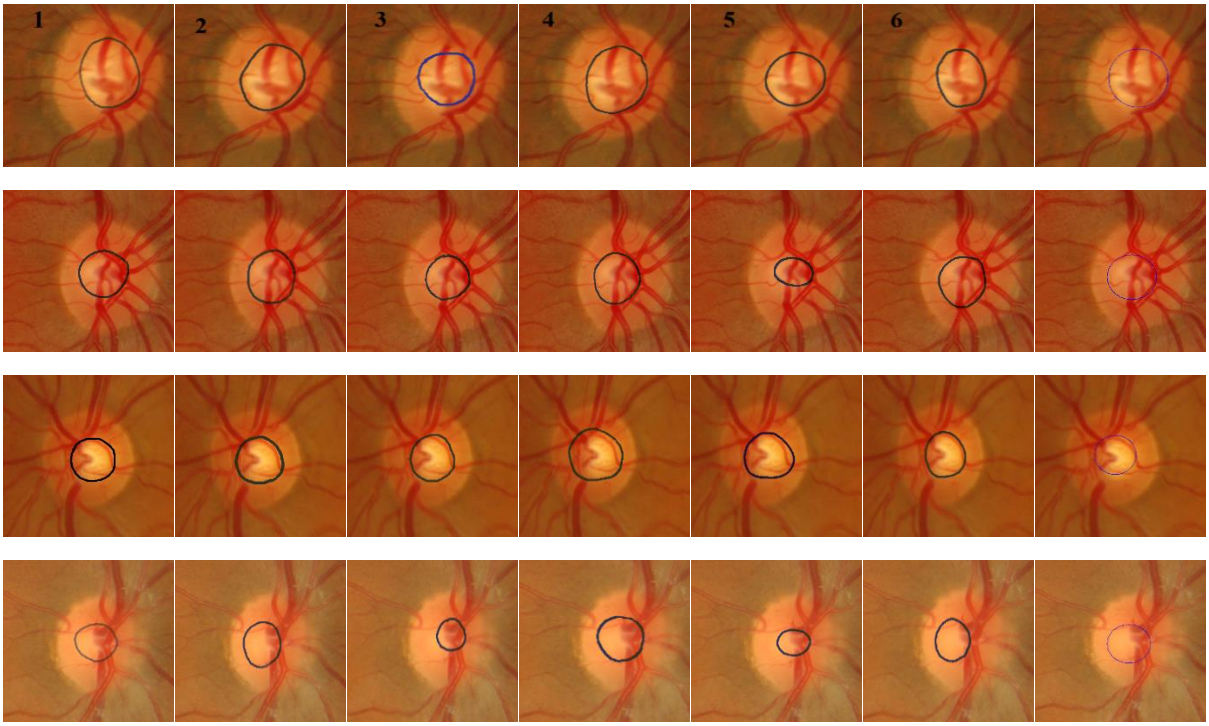

Figure 4.24 Examples for the good cup segmentation results.

On the other hand, in figure 4.25 the cup segmentations show bad results. The six ophthalmologists' annotations of cup are arranged in the six columns from left to right starting from one to six, and the last column shows the automatic cup segmentation. In terms of area and

centroid, there was agreement in the annotation of the first image among all six ophthalmologists, while the segmentation algorithm gave bigger cup area and therefore it was considered an outlier. For the second image, the annotations by ophthalmologists number two and four were eliminated because they were outliers in cup area. The algorithm also annotated a small area as cup area which was considered an outlier. As can be seen in the localized image, the right half of retina had different intensity and that affected the cup thresholding. For the last case, only the annotation by the fourth ophthalmologist was eliminated. The automatic segmentation marked a small area and far away centroid. Also in this case, the intensity of the retinal part was variable as well as the rim area particularly the right side, which negatively affected the cup thresholding.

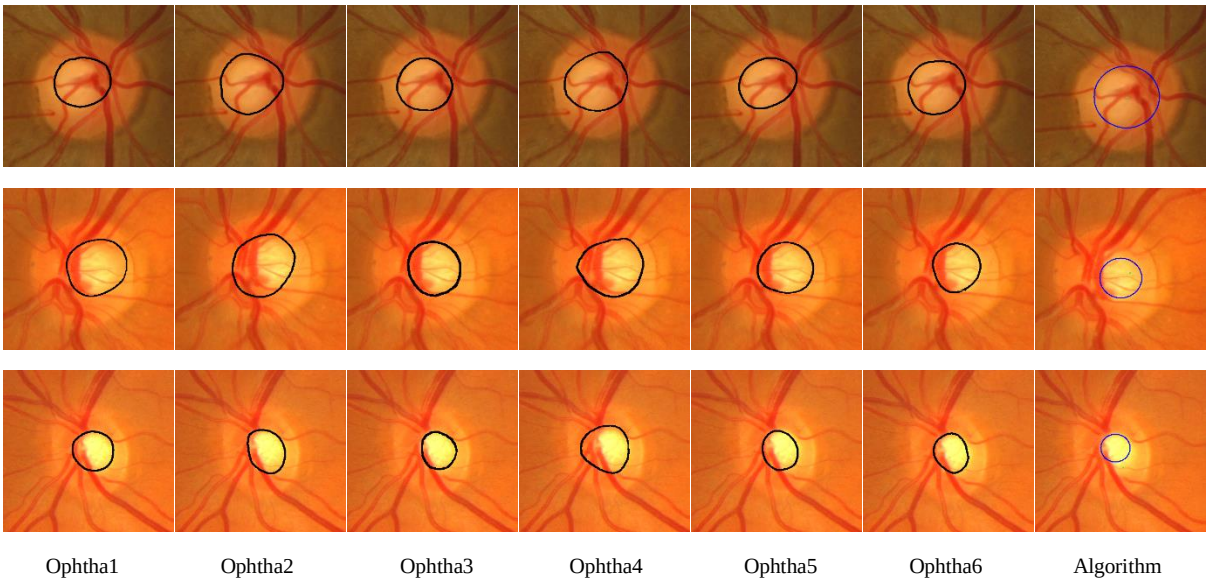

Figure 4.25 Examples for the bad cup segmentation results.

4.5.2.2.1. Results of Bin Rushed dataset

Table 4.12 shows the cup segmentation with details for Bin Rushed dataset, the first image resource of RIGA dataset, which includes 195 images. Ten images were not localized, therefore, they were eliminated. For the cup area, only one image that made the mean SD among the six

ophthalmologists more than 2150 pixels was eliminated (Figure 3.10). In total 184 images were tested. The cup area was successfully segmented in 152 images (82.6%).

For the cup centroid, there were 10 images for which the annotations by more than three ophthalmologists were considered as outliers, and therefore were eliminated. In total 175 images were tested for cup centroid, and the cup was successfully segmented in 151 images (86.2%). For both area and centroid, 30 images were eliminated. These were images with either poor area annotation or poor centroid annotation. Therefore, in total 155 images were tested and 118 images were successfully segmented in terms of area and centroid (76.1%). The average time to run the algorithm was between 20 to 30 seconds.

Table 4.12 The cup segmentation results for Bin Rushed images set.

	Cup Area	Cup Centroid	Both
Total number of images	195	195	195
# of images removed due to the lack agreement between the ophthalmologists	1	10	30
Images not localized	10	10	10
Total number of images tested	184	175	155
Accuracy (number of images)	152	151	118
Accuracy (percentage)	82.6	86.2	76.1
Average Time (s)	20-30s		

To further evaluate the result of automatic segmentation, its accuracy was compared with the accuracy of the annotations by the six ophthalmologists (Table 4.13). Similar to the analysis of the optic disc, the performance of each ophthalmologist was evaluated based on its agreement with the performance of the other five ophthalmologists. An image was eliminated if there was no agreement between at least three ophthalmologists in area or centroid. If the annotations by two ophthalmologists were outliers for area, and the annotation by a third ophthalmologist for the same image was an outlier for centroid, then the image was removed based on the analysis shown in

Figure 3.10. Twenty four images annotated by the first ophthalmologist were removed from the evaluation due to the lack of agreement with annotations by other ophthalmologists. In total 161 images were tested and the accuracy was 143 images (88.8%). For the second ophthalmologist, the annotations of 16 images did not agree with the annotations by the others, therefore, these images were removed from further analysis. In total 169 images were tested and the accuracy was 139 images (82.2%). For the third ophthalmologist, 21 images were removed, therefore, in total 164 images were tested and the accuracy was 134 images (81.7%). In total 173 images were tested for the fourth ophthalmologist and the accuracy was only 85 images (49.1%). The total number of images tested for the fifth ophthalmologist was 165 images, and the accuracy was 136 images (82.4%). Finally, the total number of tested images for the sixth ophthalmologist was 165 images and the accuracy was 133 images (80.6%). 12 to 24 images were eliminated from each analysis.

Table 4.13 The cup accuracy results for the six ophthalmologists and the segmentation algorithm for Bin Rushed images set.

	Ophth1	Ophth2	Ophth3	Ophth4	Ophth5	Ophth6	Auto
Total number of images	195	195	195	195	195	195	195
# of images removed due to the lack agreement between the ophthalmologists	24	16	21	12	20	20	30
Images not localized	10	10	10	10	10	10	10
Total number of images tested	161	169	164	173	165	165	155
Accuracy (number of images)	143	139	134	85	136	133	118
Accuracy (percentage)	88.8	82.2	81.7	49.1	82.4	80.6	76.1

Also, the annotations by the ophthalmologists were evaluated based on only five opinions while the automatic cup segmentation was evaluated based on six opinions (ophthalmologists' annotations), which supposed to give more outliers and therefore negatively affect the accuracy. However, the cup segmentation accuracy was still within the range when compared with the

annotations by the six ophthalmologists (Figure 4.26), and was close to the accuracy of annotations by ophthalmologists number two, three, five and six.

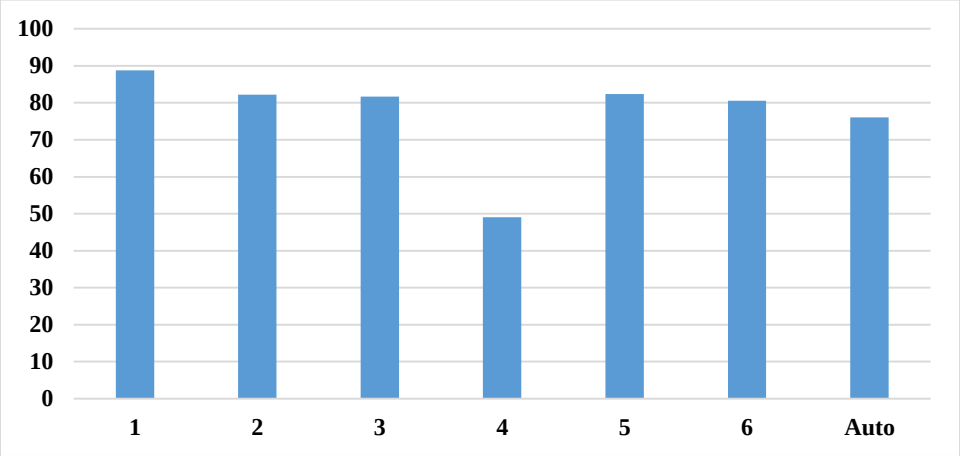

Figure 4.26 The cup accuracy results for all the six ophthalmologists as well as the algorithm for Bin Rushed images set. The X axis represents the number of 6 ophthalmologists and the algorithm. The Y axis represents the accuracy (percentage).

4.5.2.2.2. Results of Magrabi dataset

Table 4.14 shows the results for the second image resources, i.e., Magrabi dataset. As mentioned in chapter 3, Magrabi dataset includes large images. The mean SD for the cup area as annotated by the ophthalmologists was 8800 pixels, while the mean SD for the cup centroid was 11 pixels. The mean SD for area and centroid among the six ophthalmologists was more accurate in this image set than the two other image sets due to image sizes as well as the fact that the images had been captured by mydriatic fundus camera and therefore were clearer and easier to annotate. Ten images were excluded; four due to lack of agreement among the ophthalmologists and six images because they could not be localized. Therefore, in total 85 images were tested. The algorithm segmentation accuracy was 70 images or 82.3%. Eleven images were eliminated due to disagreement among the ophthalmologists for the cup centroid. Therefore in total 78 images were tested and the algorithm segmentation accuracy was 63 images or 80.7%. Twenty images were

removed when testing for both area and centroid, therefore, in total 50 images (72.4%) were tested which was less than the percentage of images that were tested from Bin Rushed dataset. The average time to run the algorithm was between 70 to 120 seconds due to the size of the images which increased the time required to achieve the level set approach used lately in order to improve the cup centroid.

Table 4.14 The cup segmentation results for Magrabi images set.

	Cup Area	Cup Centroid	Both
Total number of images	95	95	95
# of images removed due to the lack agreement between the ophthalmologists	4	11	20
Images not localized	6	6	6
Total number of images tested	85	78	69
Accuracy (number of images)	70	63	50
Accuracy (percentage)	82.3	80.7	72.4
Average Time (s)	70-120s due to the big size of the images		

The cup segmentation accuracy (Table 4.15) was close to the accuracy of the annotations by ophthalmologists number three and four. Twenty images were removed due to disagreement among the six ophthalmologists. Therefore, the accuracy of the annotation by the algorithm might have suffered due to the fact that fewer images were used to test the algorithm.

Table 4.15 The cup accuracy results for the six ophthalmologists and the segmentation algorithm for Magrabi images set.

	Ophth1	Ophth2	Ophth3	Ophth4	Ophth5	Ophth6	Auto
Total number of images	95	95	95	95	95	95	95
# of images removed due to the lack agreement between the ophthalmologists	15	14	14	16	12	11	20
Images not localized	6	6	6	6	6	6	6
Total number of images tested	74	75	75	73	77	78	69
Accuracy (number of images)	67	69	55	52	66	63	50
Accuracy (percentage)	90.5	92	73.3	71.2	85.7	80.7	72.4

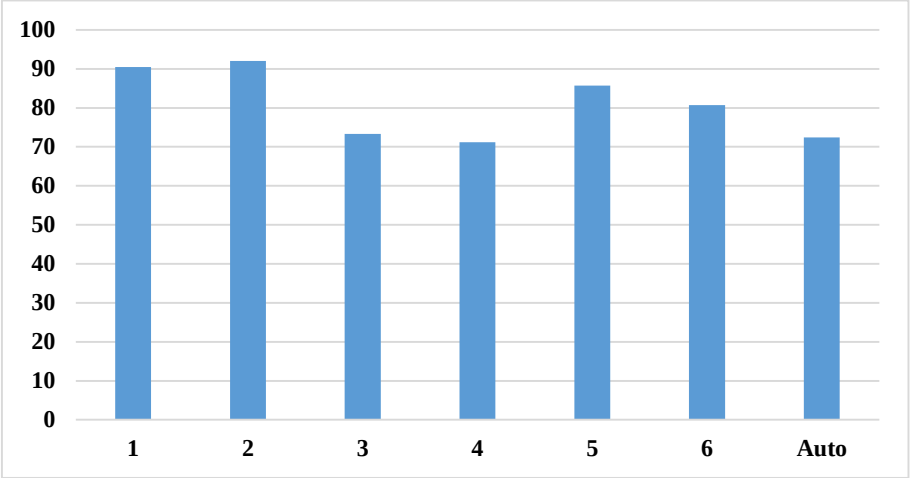

Figure 4.27 The cup accuracy results for all the six ophthalmologists as well as the algorithm for Magrabi images set. The X axis represents the number of 6 ophthalmologists and the algorithm. The Y axis represents the accuracy (percentage).

4.5.2.2.3. Results of MESSIDOR dataset

The results of the MESSIDOR dataset are shown in Table 4.16. The high number of images in this dataset and their good quality contributed to more accurate results; indeed the accuracy of the annotations using this dataset was higher than the accuracy of the annotations using the other two datasets. Similar to Bin Rushed dataset, ten images from MESSIDOR dataset were not localized. Five images were eliminated from calculation of the area. In total 245 images were tested and the accuracy was 206 images (84%). A higher percentage of accuracy was obtained for calculation of centroid. Twelve images were eliminated from calculation of centroid. Therefore, in total 238 images were tested for centroid and the accuracy was 216 images (90.7%). Thirty three images were removed from evaluation of both area and centroid. In total 217 images were tested for both area and centroid, and the accuracy was 177 images (81.5%). The average time for running the algorithm was 20 to 30 seconds which was similar to the time required for running the algorithm for Bin Rushed dataset, and this was due to their similarity in size.

Table 4.16 The cup segmentation results for MESSIDOR images set.

	Disc Area	Disc Centroid	Both
Total number of images	260	260	260
# of images removed due to the lack agreement between the ophthalmologists	5	12	33
Images not localized	10	10	10
Total number of images tested	245	238	217
Accuracy (number of images)	206	216	177
Accuracy (percentage)	84	90.7	81.5
Average Time S	20-30s		

The average accuracy of the annotations by the six ophthalmologists was 86% to 89%, while the algorithm's accuracy was 81.5%. The algorithm was tested on a total of 177 images, while 195 to 203 images were used to test the accuracy of the annotations by the ophthalmologists, except for ophthalmologist number four (Table 4.17). As mentioned previously, increasing the number of test images boosts the accuracy. In Figure 4.28, the algorithm shows good accuracy, especially when compared with the accuracy of the annotations by ophthalmologists number one, two and six.

Table 4.17 The cup accuracy results for the six ophthalmologists and the segmentation algorithm for MESSIDOR images set.

	Ophth1	Ophth2	Ophth3	Ophth4	Ophth5	Ophth6	Auto
Total number of images	260	260	260	260	260	260	260
# of images removed due to the lack agreement between the ophthalmologists	23	26	25	20	23	23	33
Images not localized	10	10	10	10	10	10	10
Total number of images tested	227	224	225	230	227	227	217
Accuracy (number of images)	203	195	201	162	203	198	177
Accuracy (percentage)	86.4	87	89.3	70.4	89.4	87.2	81.5

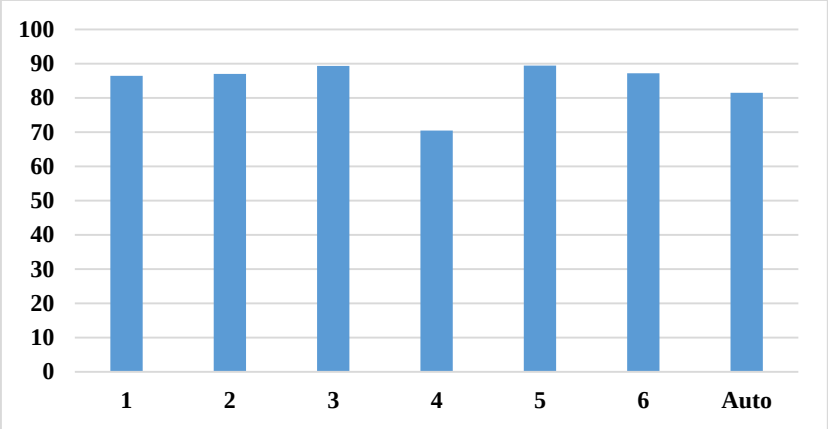

Figure 4.28 The cup accuracy results for all the six ophthalmologists as well as the algorithm for MESSIDO images set. The X axis represents the number of 6 ophthalmologists and the algorithm. The Y axis represents the accuracy (percentage).

4.5.2.2.4. Consolidated results for the cup

In this section, all images are gathered in order to allow a comprehensive analysis of annotations by the ophthalmologists and algorithm. 550 images from all three datasets were tested to evaluate the algorithm and the annotations by the six ophthalmologists. When an image had three outliers or more in the area or centroid or both, it was considered as a bad image and was removed from the corresponding analysis. From the three datasets, 10 images were eliminated from cup area analysis due to disagreement among the ophthalmologists. Also 26 images were eliminated due to bad localization. Therefore, in total 514 images were tested and the accuracy was 428 images or 83.2% (Table 4.18). On the other hand, 33 images were removed from analysis of cup centroid due to the disagreement and 26 images were eliminated due to bad localization. Therefore, in total 491 images were tested and the accuracy was 430 images or 87.5%. This result was better than the result of area analysis; however, the number of the images accurately annotated is very similar for the cup area and centroid, i.e., 428 vs. 430 images for area and centroid, respectively. Therefore, the number of images had been eliminated for the centroid due to the lack of agreement had given an advantage to increase the accuracy for the disc centroid over the disc area. 83 images had been

eliminated from analysis of both area and centroid in addition to 26 images that were not localized. Therefore, in total 441 images were tested, and the accuracy was 345 images or 78.2%. This was obviously due to the fact that there were many images with good accuracy in terms of area that were outliers in terms of centroid and vice versa.

Table 4.18 The cup segmentation results for all the three images sets together.

	Disc Area	Disc Centroid	Both
Total number of images	550	550	550
# of images removed due to the lack agreement between the ophthalmologists	10	33	83
Images not localized	26	26	26
Total number of images tested	514	491	441
Accuracy (number of images)	428	430	345
Accuracy (percentage)	83.2	87.5	78.2

As can be seen in Table 4.19, ophthalmologist number one had the best accuracy among the six ophthalmologists even though his annotations were tested using only 462 images, the lowest number of images among all ophthalmologists. The algorithm was tested using 441 images and its accuracy was 345 images (78.2%). The performance of the algorithm in terms of percentage accuracy in cup segmentation was close to that of ophthalmologist number six, then ophthalmologist three, then ophthalmologist two, and finally ophthalmologist five. This is clearly shown in Figure 4.29.

Table 4.19 The cup accuracy results for the six ophthalmologists and the segmentation algorithm for all the three images sets together.

	Ophth1	Ophth2	Ophth3	Ophth4	Ophth5	Ophth6	Auto
Total number of images	550	550	550	550	550	550	550
# of images removed due to the lack agreement between the ophthalmologists	62	56	60	48	55	54	83
Images not localized	26	26	26	10	26	26	26
Total number of images tested	462	468	464	492	469	470	441
Accuracy (number of images)	413	403	390	229	405	394	345
Accuracy (percentage)	89.3	86.1	84	46.5	86.3	83.8	78.2

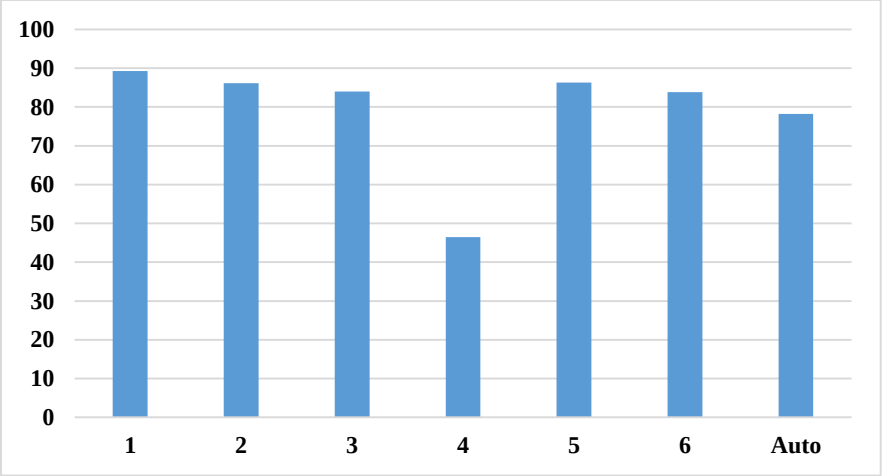

Figure 4.29 The cup accuracy results for all the six ophthalmologists as well as the algorithm for the three images sets. The X axis represents the number of 6 ophthalmologists and the algorithm. The Y axis represents the accuracy (percentage).

Figure 4.30 shows the results of the annotations by all six ophthalmologists as well as the automatic algorithm for all three datasets. The blue line represents Bin Rushed dataset, the dark orange line represents Magrabi, and the gray line represents MESSIDOR images, while the bright orange line represents all images together. As can be seen in the figure, ophthalmologists number one, five and six and the algorithm showed similar performances in terms of accuracy of cup segmentation for all the three datasets. Magrabi images were most accurately annotated by ophthalmologists number one, two, and four. While MESSIDOR images were most accurately annotated by

ophthalmologists number three, five and six. Annotations of Magrabi images by ophthalmologists number three and four as well as the algorithm had low accuracy. Overall, annotations by ophthalmologist number six were closest to the markings by the algorithm.

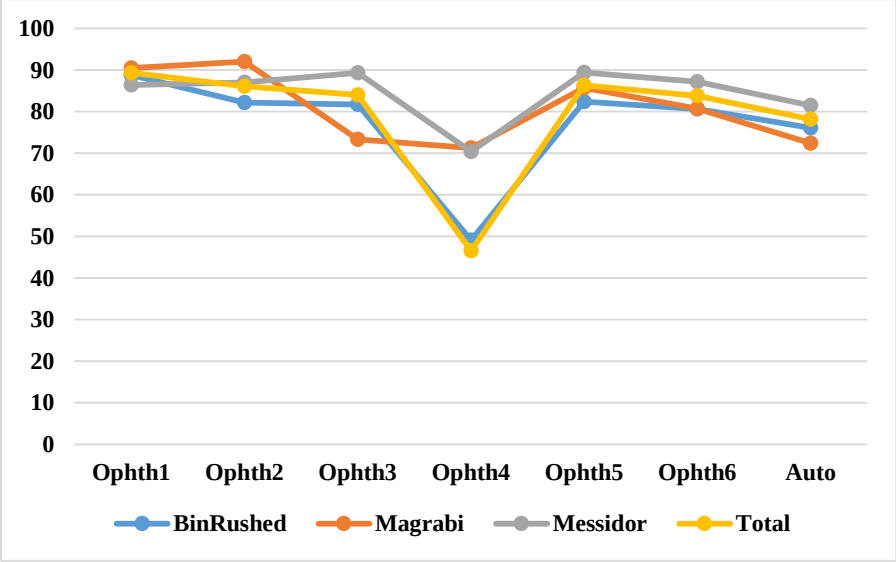

Figure 4.30 The cup accuracy results for all the six ophthalmologists as well as the algorithm for the three images sets individually. The X axis represents the number of 6 ophthalmologists and the algorithm. The Y axis represents the accuracy (percentage).

4.5.2.2.5. Agreement for the cup

In terms of cup area and centroid agreement and similarity, the annotations by all ophthalmologists had the best agreement with the annotations by ophthalmologist number one (Table 4.20). The best agreement for the algorithm was with ophthalmologist number one in 359 images (65.2%), while the lowest agreement was with ophthalmologist number six in 329 images (59.8%). On the other hand, the best overall agreement was between ophthalmologist number one and ophthalmologists two and five in 398 images (72.3%), and the lowest agreement was between ophthalmologist number four and the algorithm. Agreement between the algorithm and manual annotations in disc segmentation varied between 57.4% and 63.4%, which is slightly better than

the comparable values for cup segmentation. Variations of the overall agreement in manual annotations of the disc were between 56.7% and 74.5%, which is also slightly better than the cup.

Table 4.20 The cup number of images agreement between the ophthalmologists as well as the algorithm

	Ophth1	Ophth2	Ophth3	Ophth4	Ophth5	Ophth6	Auto
Ophth1	550	398	385	296	398	378	356
Ophth2	398	550	368	290	384	375	345
Ophth3	385	368	550	278	378	357	336
Ophth4	296	290	278	550	286	277	248
Ophth5	398	384	378	286	550	370	345
Ophth6	378	375	357	277	370	550	329
Auto	356	336	336	248	345	329	550
Total	2211	2151	2102	1675	2161	2086	1959

Figure 4.31 shows the agreement for every ophthalmologist in addition to the algorithm. The algorithm clearly had the best agreement with ophthalmologist number one, then ophthalmologist number five, then ophthalmologist number two and three, then ophthalmologist number six and finally with ophthalmologist number four.

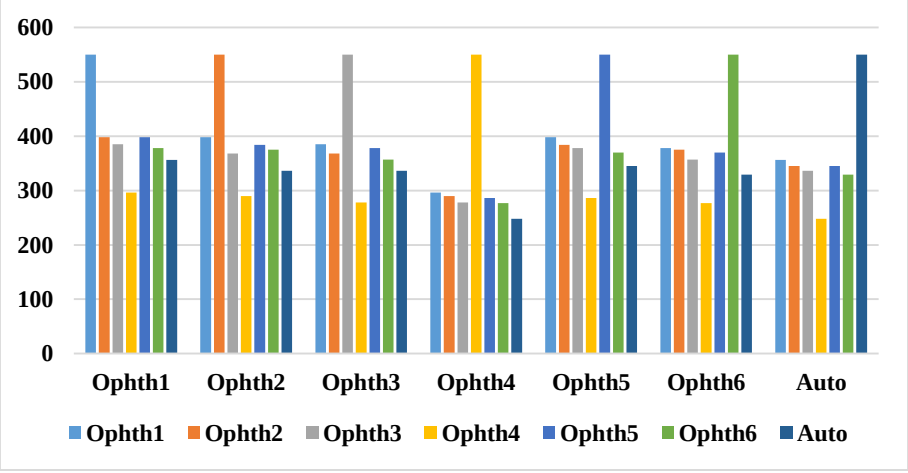

Figure 4.31 The cup agreement results for all the six ophthalmologists as well as the algorithm for all images sets. The X axis represents the number of 6 ophthalmologists. The Y axis represents the number of agreed images.

Figure 4.32 shows the total number of agreements for all ophthalmologists as well as the algorithm. Ophthalmologist number one is the best, followed by ophthalmologists number five, two, three, and six, then the algorithm, and finally ophthalmologist number four. Except for ophthalmologist number four and the algorithm which had close to 2000 images, all other ophthalmologists had more than 2000 images in total.

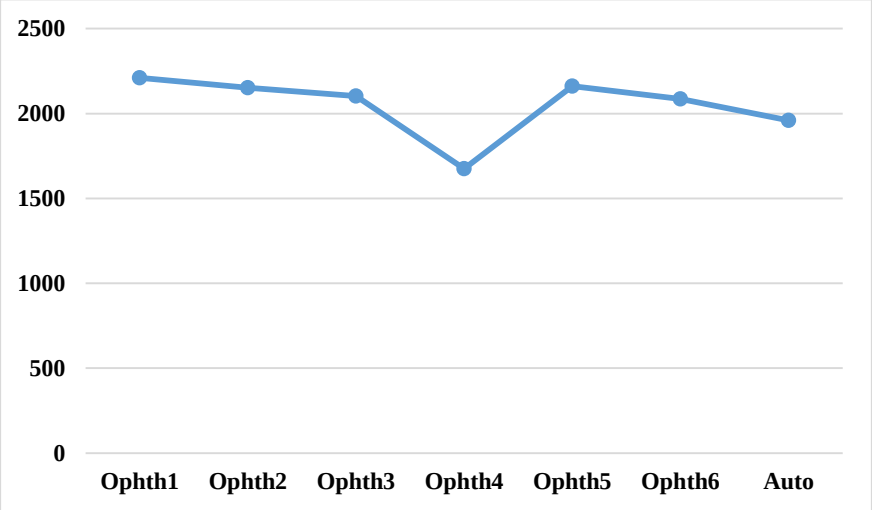

Figure 4.32 The cup agreement results for all the six ophthalmologists as well as the algorithm for all images sets. The X axis represents the number of 6 ophthalmologists and the algorithm. The Y axis represents the total agreed images.

4.5.3. Comparison between the disc and cup

As illustrated in Figure 4.33 (A), the cup accuracy was clearly better for ophthalmologist number one and two (by 10%), while it was slightly better for ophthalmologists number three and five. The disc accuracy for ophthalmologist number four was around 90% while the cup accuracy was around 45%. In comparison with others, this ophthalmologist annotated larger areas as the cup, causing too many outliers in his annotations. Ophthalmologist number six and the algorithm had better accuracy in the disc boundary detection (by almost 5%). On the other hand, the total number of images agreed upon by the ophthalmologists as well as the algorithm precisely follows the

accuracy results as shown in Figure 4.34 (B). The preference of the cup over the disc belonged to ophthalmologists number one, two, three and five while the preference of the disc over the cup belonged to ophthalmologists number four, six and the algorithm. In conclusion, the total number of agreement for every ophthalmologist was an indication for the accuracy in between the ophthalmologists.

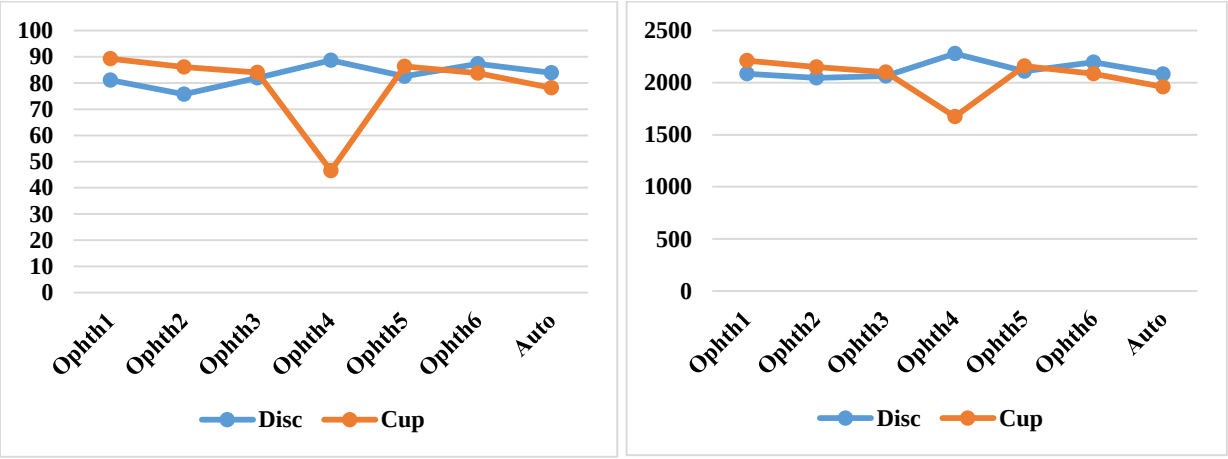

(A) **(B)**

Figure 4.33 The total accuracy percentage for the disc and cup versus the total images agreement between the six ophthalmologists as well as the algorithm. The X axis represents the number of 6 ophthalmologists and the algorithm. The Y axis represents the accuracy (percentage) in (A) and total agreed images in (B).

Chapter 5

The Cup to Disc Ratios

5.1. Introduction

In this chapter, the clinical parameters for the optic nerve head represented by the cup to disc ratios are considered. Here the horizontal and vertical cup to disc ratio (HCDR and VCDR) for the two segmentation algorithms are calculated and evaluated based on the RIGA dataset.

Figure 5.1 illustrates the final algorithm steps, i.e., after including the optic disc segmentation into the cup segmentation process in order to improve the cup segmentation centroid. Therefore, the segmented disc with the final contour based on either the TIFF or JPG images on the localized image was the starting point for the cup segmentation process because the disc counter and centroid served the cup segmentation by pulling the cup into the best position according to the chosen square with the most intensity. The disc contour also served the cup, instead of estimating the disc size. As shown in the previous chapter, once the cup contour touches the disc contour, it gives an error and then goes to the next loop for the threshold number purpose. The post process in the total algorithm procedures was calculating the horizontal cup to disc ratio (HCDR) and the vertical cup to disc ratio (VCDR) (see the appendix for the matlab codes).

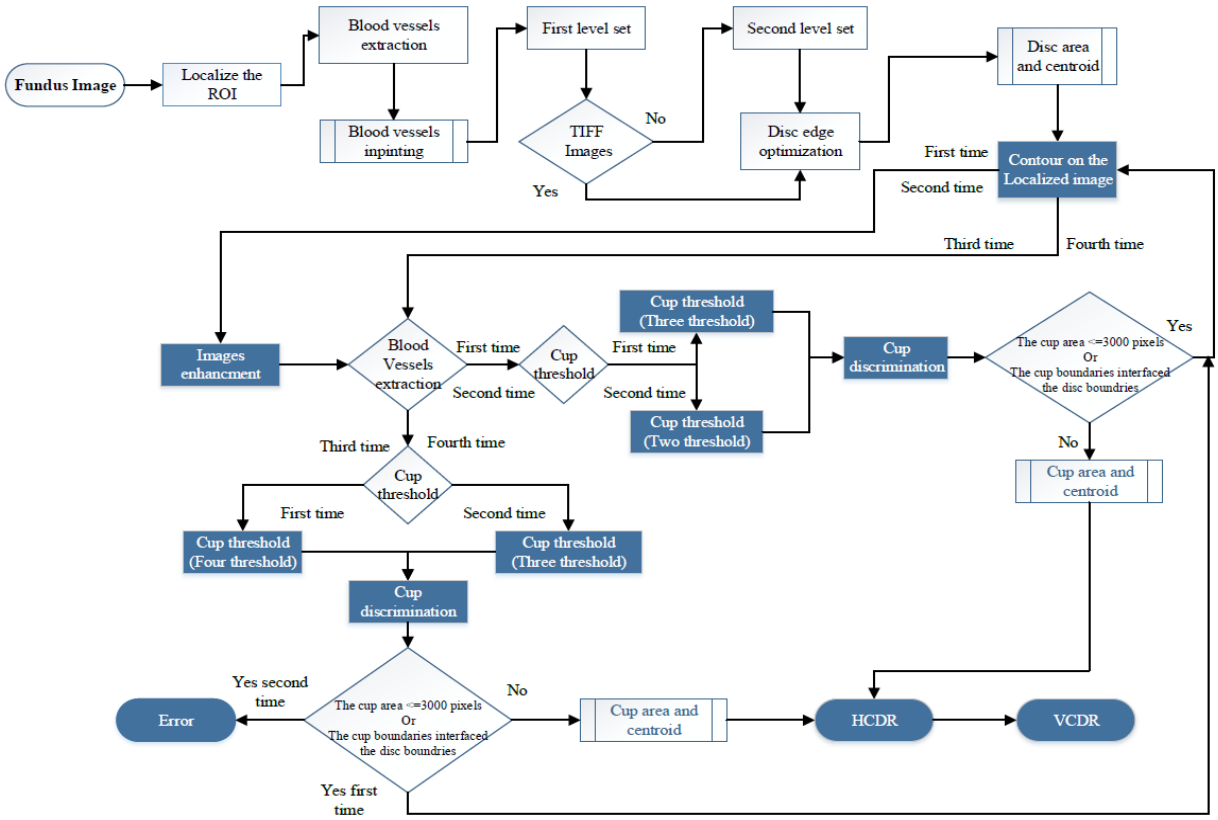

Figure 5.1 The final algorithm flowchart.

5.2. Horizontal Cup to Disc Ratio (HCDR)

To calculate the HCDR for the annotations of the disc and cup, the furthest two pixels horizontally were considered for the disc and cup separately (Figure 3.2 (b)), and then their ratio was calculated. The same procedure was followed for calculating HCDR for the automated system after segmenting the disc and cup. To eliminate the annotations for the HCDR represented by outliers, three parameters were considered: 1) the disc outliers (area and centroid), 2) the cup outliers (area and centroid), and 3) the HCDR individually based on the analysis in Figure 3.14.

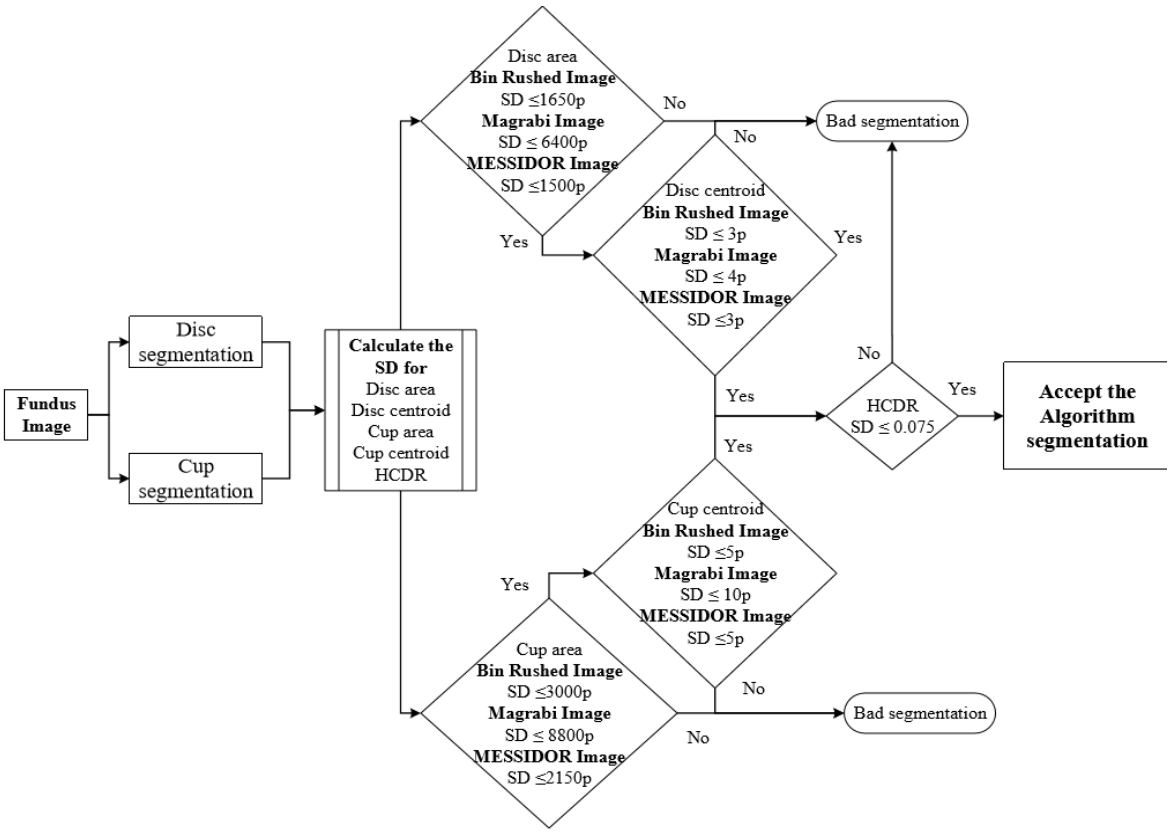

Figure 5.2 Flowchart for the analysis of the HCDR calculation.

The mean SD for the HCDR was 0.075 in terms of ratio since the measurement here was the ratio instead of number of pixels which was used with the disc and cup. Therefore, any annotation with the HCDR mean SD more than 0.075 was considered as an outlier. The same was true for the automated system (Figure 5.2). Thus, many images were eliminated. For example, there were at least three annotations with mean SD for either disc, cup or HCDR exceeding the threshold. The aforementioned obviously affects the number of agreement in the annotations by the ophthalmologists as well as the algorithm. As the result, three parameters were considered in this part in order to decide whether an image is eligible to evaluate the algorithm or not. If there were at least three outliers for a certain parameter, e.g. disc area, for an image, then the image was eliminated from evaluating the algorithm. While based on Figure 3.14 if there were three outliers

from different parameters, e.g. one for disc centroid, one for cup area and one for HCDR, then the image was not eliminated. However, if there were four outliers with two of them on the same parameter, e.g. two outliers for the disc area, one for the cup area and one for the HCDR, the image was eliminated.

Figure 5.3 shows the bad segmentation results for the HCDR with different cases. For the first image, represented in the first row, the annotation by ophthalmologist number six was eliminated due to the disc area which affected the HCDR, while the algorithm gave bad results due to the cup size. In the second image, represented in the second row, the annotations by ophthalmologists number four and six were eliminated because of the cup area and centroid, respectively. The algorithm gave bad results due to bad disc segmentation. In the third image, the annotations by three ophthalmologists were eliminated for different reasons, therefore this image was not eligible to evaluate the algorithm. In the fourth image, the annotations by ophthalmologists number four and six were eliminated due to the cup area and disc centroid, respectively. While the algorithm gave bad result due to the bad cup area segmentation.

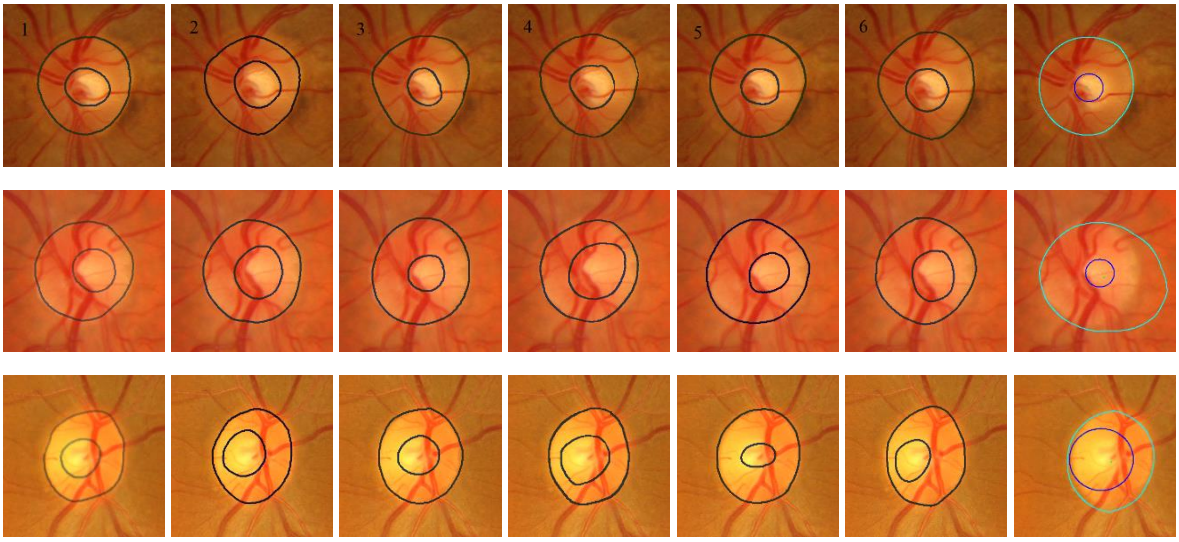

Ophtha1 Ophtha2 Ophtha3 Ophtha4 Ophtha5 Ophtha6 Algorithm

Figure 5.3 The algorithm bad HCDR results.

On the other hand, in the first image in Figure 5.4, represented in the first row, the algorithm gave good results for the disc, cup and HCDR for MESSIDOR dataset where the SD was 0.04 among the six ophthalmologists and became 0.55 with the algorithm results which was still less than the mean SD (0.075). Furthermore, the HCDR given by the algorithm was 0.58, while it was reported to be 0.54, 0.55, 0.51, 0.56, 0.55, and 0.45 by ophthalmologists number one to six, respectively. In the second image, shown in the second row, the algorithm gave good result for Bin Rushed dataset where the SD was 0.06 among the six ophthalmologists and it became 0.065 with the algorithm results. Furthermore, the HCDR given by the algorithm was 0.58, while it was reported to be 0.54, 0.51, 0.49, 0.54, 0.43, and 0.40 by ophthalmologists number one to six, respectively. Finally, in the last image, the algorithm gave good results for Magrabi dataset where the mean SD was 0.03 and it became 0.025. Furthermore, for this dataset the HCDR given by the algorithm was 0.68, while it was reported to be 0.69, 0.66, 0.70, 0.73, 0.68, and 0.66 by ophthalmologists number one to six, respectively.

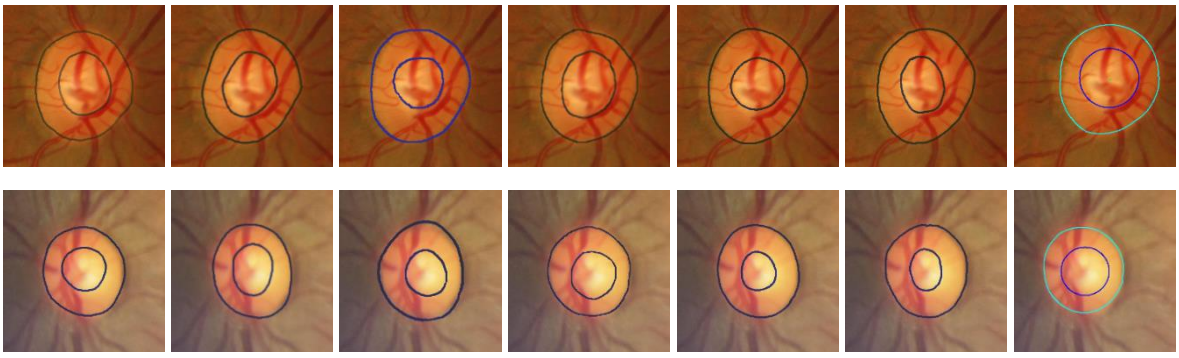

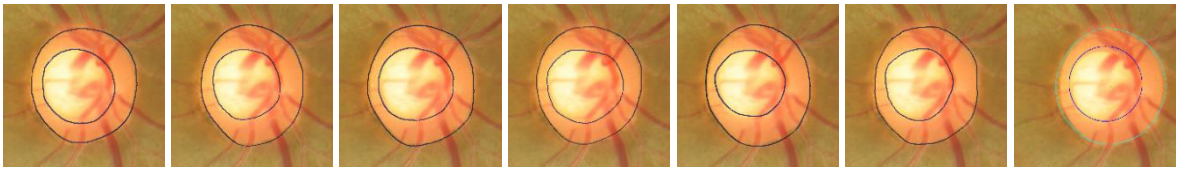

Ophtha1 Ophtha2 Ophtha3 Ophtha4 Ophtha5 Ophtha6 Algorithm

Figure 5.4 The algorithm good HCDR results.

5.2.1. Results of Bin Rushed dataset

As can be seen in Table 5.1, the algorithm achieved 73.8% accuracy, the second best accuracy, when testing a total of 111 images. 84 images were eliminated; 74 of them had at least three outliers in disc, cup or HCDR calculations and 10 images had not been localized. Ophthalmologist number one had the best performance in calculating HCDR; he annotated the HCDR accurately in 79.6% of the 108 total tested images. As can be seen, most outliers that had to be removed from the analysis were annotated by ophthalmologists number three and four. The accuracies of performances of the six ophthalmologists as well as the algorithm were in the close range of 74 to 86 images. However, the total number of tested images had obviously affected the accuracy.

Table 5.1 The HCDR results for Bin Rushed images set.

	Ophth1	Ophth2	Ophth3	Ophth4	Ophth5	Ophth6	Auto
Total number of images	195	195	195	195	195	195	195
# of images removed due to the lack agreement between the ophthalmologists	77	67	58	58	76	76	74
Images not localized	10	10	10	10	10	10	10
Total number of images tested	108	118	127	127	109	109	111
Accuracy (number of images)	86	85	82	77	79	74	82
Accuracy (percentage)	79.6	72	64.5	60.6	72.4	67.8	73.8

Figure 5.5 shows that the poorest accuracy of around 60% was observed for the annotations by ophthalmologist number four (mainly due to poor cup annotations). The annotations by ophthalmologist number one were most accurate (80% accuracy) mainly due to good disc annotation and best cup annotation.

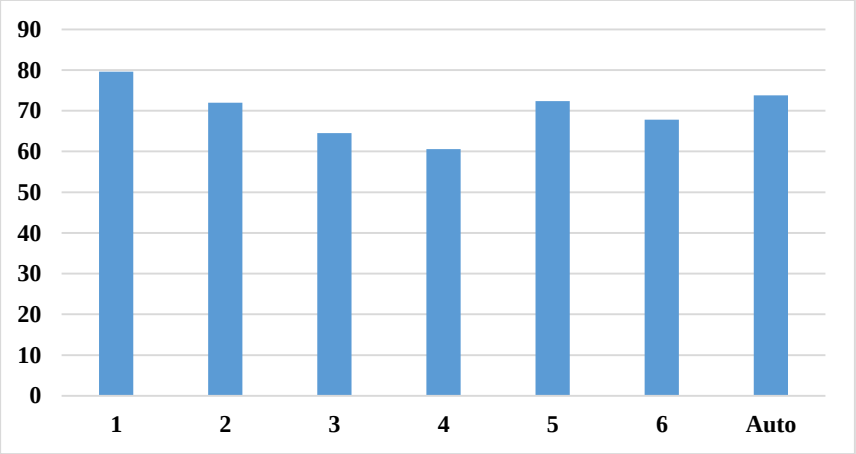

Figure 5.5 The percentage accuracy of the HCDR results for Bin Rushed images set. The percentage accuracy of the HCDR results for Bin Rushed images set. The X axis represents the number of 6 ophthalmologists and the algorithm. The Y axis represents the accuracy (percentage).

5.2.2. Results of Magrabi dataset

Fewer images from Magrabi dataset were used for evaluating the algorithm. As shown in Table 5.2, in total 95 images were used from which 6 images were not localized and 31 to 43 images were eliminated due to the outliers in the annotations of disc, cup or HCDR. In this image set, the performance of the algorithm was the second best after that of ophthalmologist number two who tested 51 images in total and his accuracy was 39 images. The total number of images tested by the algorithm was 46 images. Most of the outliers that resulted in eliminating the images were due to errors in the annotations by ophthalmologists number six, three and five.

Table 5.2 The HCDR results for Magrabi images set.

	Ophth1	Ophth2	Ophth3	Ophth4	Ophth5	Ophth6	Auto
Total number of images	95	95	95	95	95	95	95
# of images removed due to the lack agreement between the ophthalmologists	40	38	35	40	35	31	43
Images not localized	6	6	6	6	6	6	6
Total number of images tested	49	51	54	49	54	58	46
Accuracy (number of images)	35	39	28	32	35	39	35
Accuracy (percentage)	71.4	76.4	51.8	65.3	64.8	67.2	76

Figure 5.6 shows the accuracies of annotations by the six ophthalmologists as well as the algorithm which were between approximately 50% for ophthalmologist number three and 75% for ophthalmologist number two. These accuracies were lower than the accuracies of Bin Rushed dataset analysis. The accuracy of the annotations by ophthalmologist number two was almost the same as the accuracy of the annotations by the algorithm.

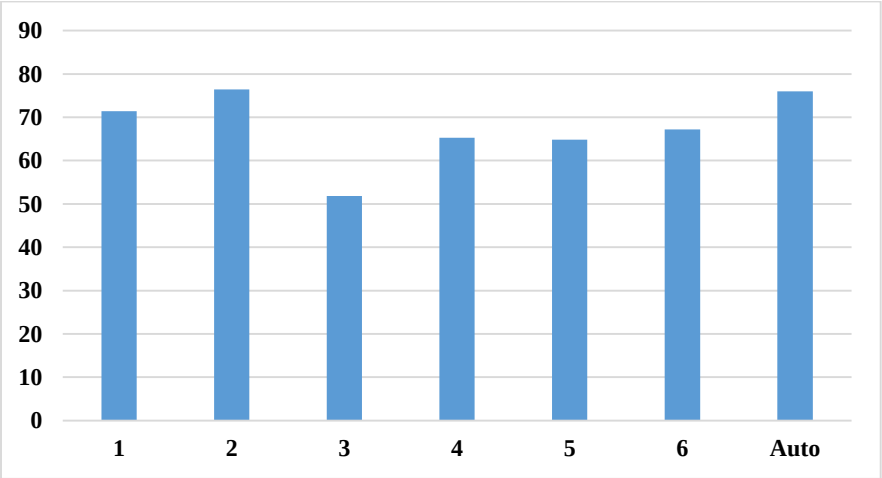

Figure 5.6 The percentage accuracy of the HCDR results for Magrabi images set. The percentage accuracy of the HCDR results for Bin Rushed images set. The X axis represents the number of 6 ophthalmologists and the algorithm. The Y axis represents the accuracy (percentage).

5.2.3. Results of MESSIDOR dataset

Finally, the algorithm was tested on MESSIDOR dataset containing 260 images (Table 5.3). Here 10 images were not localized. Furthermore, 63 to 73 images were eliminated from further analysis since their annotations were outliers. Ophthalmologist number one had fewer outliers, i.e., only in 56 images. The best accuracy result was obtained by ophthalmologist number three based on testing 177 images; the accuracy was 143 images. The accuracy of annotations by ophthalmologist number one was 76.2%, i.e., 148 images were accurately annotated. The algorithm was the third best in terms of accuracy; from 186 images tested, 139 were accurately annotated.

Table 5.3 The HCDR results for MESSIDOR images set.

	Ophth1	Ophth2	Ophth3	Ophth4	Ophth5	Ophth6	Auto
Total number of images	260	260	260	260	260	260	260
# of images removed due to the lack agreement between the ophthalmologists	56	65	73	63	67	63	64
Images not localized	10	10	10	10	10	10	10
Total number of images tested	194	185	177	187	183	187	186
Accuracy (number of images)	148	127	143	111	136	130	139
Accuracy (percentage)	76.2	68.6	80.7	59.3	74.3	69.5	74.7

The percentages of accuracy are shown in Figure 5.7. The percentages of accuracy were between almost 60% and slightly over 80%, which was better than the accuracies of analysis of images in Magrabi dataset and close to the accuracies of analysis of Bin Rushed dataset. However, the mean SD for the disc area and centroid were less for images in MESSIDOR dataset, giving it an advantage over Bin Rushed dataset.

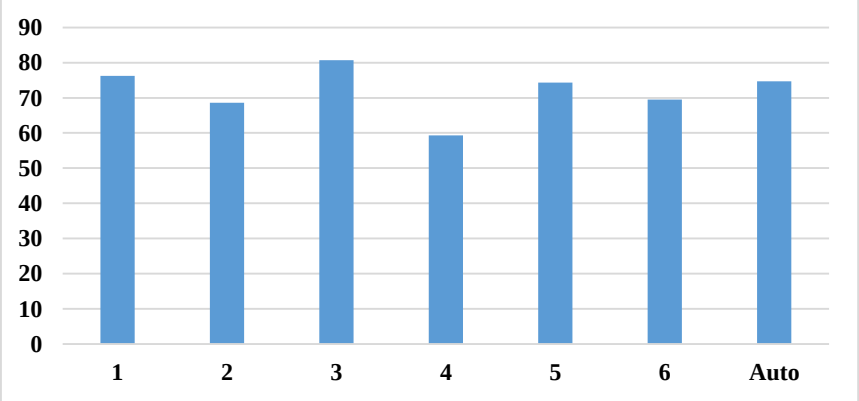

Figure 5.7 The percentage accuracy of the HCDR results for MESSIDOR images set. The X axis represents the number of 6 ophthalmologists and the algorithm. The Y axis represents the accuracy (percentage).

5.2.4. Consolidated results for HCDR

As a conclusion, the final results for all three datasets are illustrated in Table 5.4. With 269 images accurately annotated, the annotations by ophthalmologist number one had the highest percentage of accuracy (76.6%). The algorithm was the second best with 74.6% accuracy and 256 images

accurately segmented. The annotations by ophthalmologist number 4 had the most outliers. The number of eliminated images was between 161 images for ophthalmologist number four and 181 images for the algorithm.

Table 5.4 The consolidated results for the HCDR.

	Ophth1	Ophth2	Ophth3	Ophth4	Ophth5	Ophth6	Auto
Total number of images	550	550	550	550	550	550	550
# of images removed due to the lack agreement between the ophthalmologists	173	170	166	161	178	170	181
Images not localized	26	26	26	10	26	26	26
Total number of images tested	351	354	358	379	346	354	343
Accuracy (number of images)	269	251	253	220	250	243	256
Accuracy (percentage)	76.6	70.9	70.6	58	72.2	68.6	74.6

Figure 5.8 shows the percentages of accuracy which ranged from around 60% to 75%. The percentages of accuracy of the annotations by five ophthalmologists as well as the algorithm were very close (between 70 to 75%).

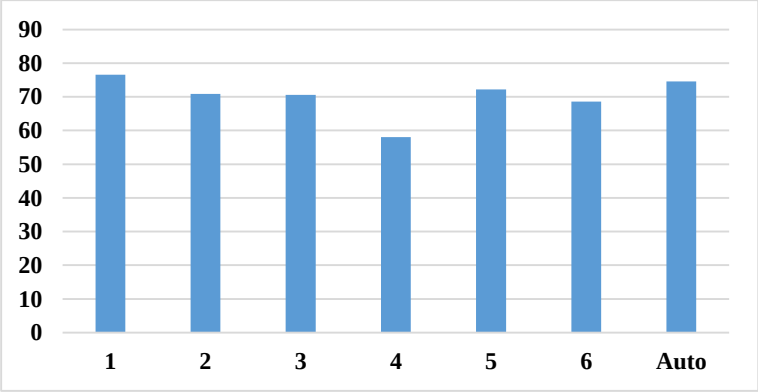

Figure 5.8 The percentage accuracy of the HCDR results for the total of the three images sets. The X axis represents the number of 6 ophthalmologists and the algorithm. The Y axis represents the accuracy (percentage).

Figure 5.9 illustrates the variation in accuracy percentage among the three datasets. Ophthalmologist number six and the algorithm showed the same results for all images despite their differences in quality and size. However, the performance of ophthalmologist number three varied

significantly; he/she showed greatest accuracy while working on MESSIDOR dataset and the lowest accuracy while working on Magrabi dataset.

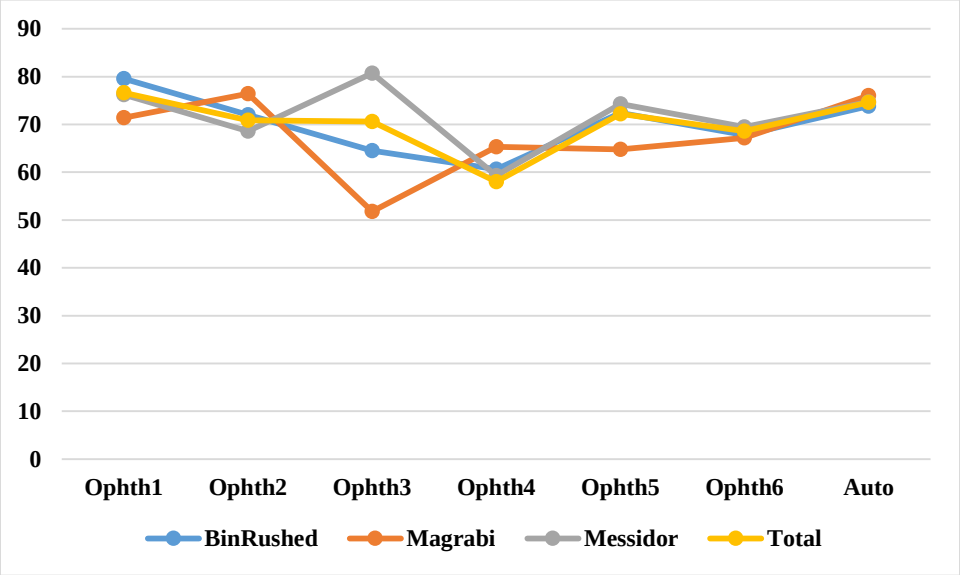

Figure 5.9 The percentage accuracy of the HCDR for the three images set individually. The X axis represents the number of 6 ophthalmologists and the algorithm. The Y axis represents the accuracy (percentage).

5.2.5. Agreement for HCDR

The best agreement was observed between the annotations by ophthalmologist number one and five in 251 of 550 images (45.6%) (Table 5.5). The best agreement for the algorithm was with the annotations by ophthalmologist number one (agreement in 239 images (43.4%)). On the other hand, the lowest agreement was observed between ophthalmologist number four and the algorithm (agreement in 162 images (29.4%)).

In terms of the total number of image agreements, the algorithm was in the sixth place, which does not correspond with its ranking in accuracy. This is similar to what we observed in the previous chapter regarding measurements of disc and cup.

Table 5.5 The number of images agreed for the HCDR between the ophthalmologists as well as the algorithm.

	Ophth1	Ophth2	Ophth3	Ophth4	Ophth5	Ophth6	Auto
Ophth1	550	238	247	192	**251**	234	**239**
Ophth2	238	550	222	173	226	214	212
Ophth3	247	222	550	177	241	224	220
Ophth4	192	173	177	550	177	168	162
Ophth5	251	226	241	177	550	233	223
Ophth6	234	214	224	168	233	550	213
Auto	239	212	220	162	223	213	550
Total	1401	1285	1331	1049	1351	1286	1269

Figure 5.10 clearly illustrates that ophthalmologists number three and five were in best agreement with ophthalmologist number one. Ophthalmologist number two had the best agreement with ophthalmologist number one. Ophthalmologist number three had the best agreement with ophthalmologists number one and five. Ophthalmologist number four had the best agreement with ophthalmologist number one. Ophthalmologist number five had the best agreement with ophthalmologist number one. Ophthalmologist number six had the best agreement with ophthalmologists number one and five. Finally, the algorithm had the best agreement with ophthalmologist number one.

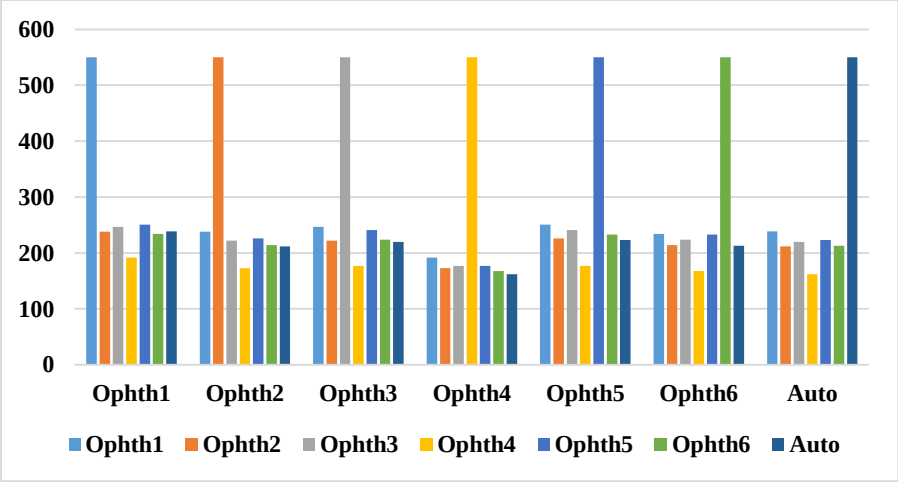

Figure 5.10 The number of images agreed for the HCDR between the ophthalmologists as well as the algorithm. The X axis represents the number of 6 ophthalmologists and the algorithm. The Y axis represents the number of agreed images.

Figure 5.11 clearly shows that the number of images agreed upon for all six ophthalmologists as well as the algorithm ranged between 1250 and 1400 in total, except for ophthalmologist number four. The total number of image agreements for HCDR was less than what we saw for disc and cup separately.

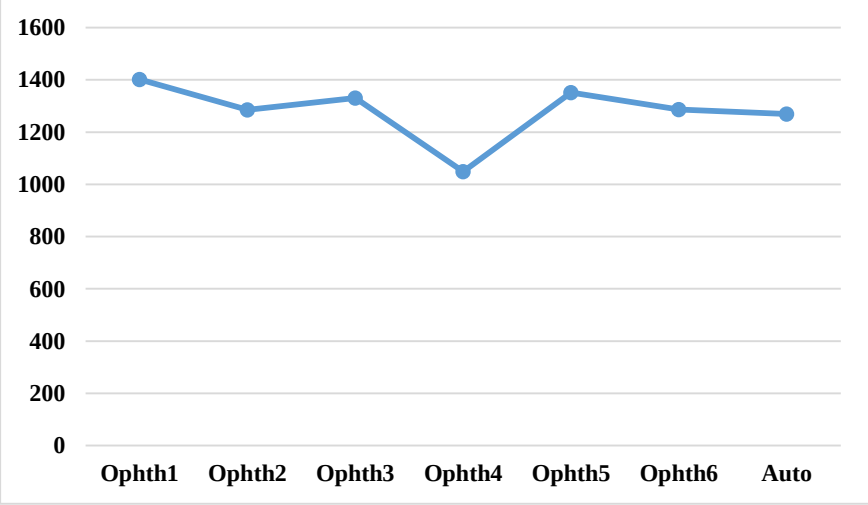

Figure 5.11 The total agreed images for the HCDR between the ophthalmologists as well as the algorithm. The X axis represents the number of 6 ophthalmologists and the algorithm. The Y axis represents the total number of agreed images.

5.3.Vertical Cup to Disc Ratio (VCDR)

The procedures used for calculation of HCDR were repeated to calculate VCDR for the algorithm. Two parameters were considered: disc (area and centroid) and cup (area and centroid). The procedures for eliminating the outliers were the same as those used in HCDR analysis and followed the same steps as shown in Figure 3.17. The same procedures were also conducted for the algorithm in order to decide whether the segmentations are accepted or not as shown in Figure 5.12.

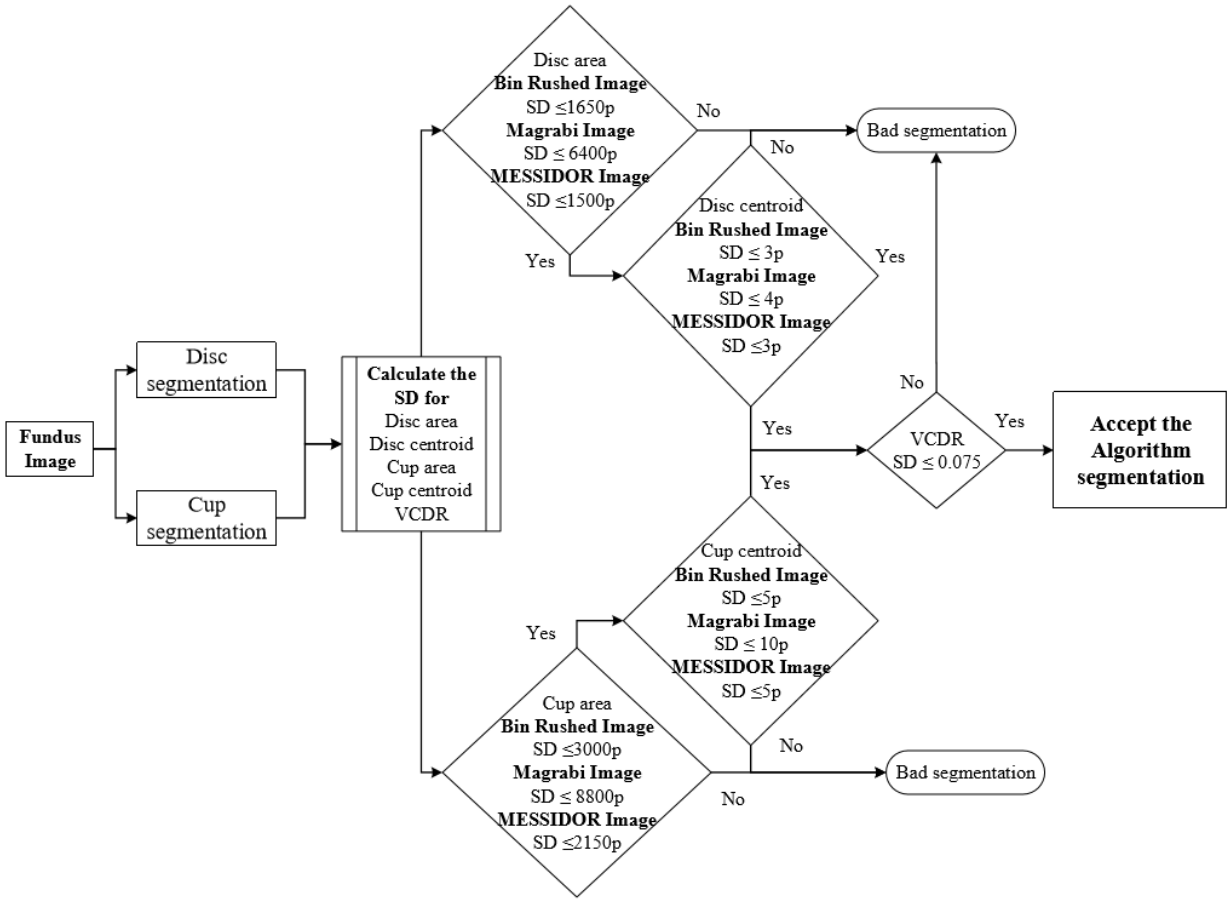

Figure 5.12 Flowchart for the analysis of the VCDR calculation.

Three parameters were considered in this part in order to decide whether an image was eligible to evaluate the algorithm. For each image, if there were at least three outliers each from a different parameter, i.e., all three parameters had an outlier in the disc area, then the image was not used for evaluating the algorithm. However, if the three outliers were from different parameters, for example one for disc centroid, one for cup area and one for VCDR, then the image was not eliminated. On the other hand, if there were four outliers from two different parameters, for example two outliers for the disc area, one outlier for the cup area and another for the VCDR, then the image was eliminated from the evaluation.

In Figure 5.13 different images are presented in the different rows. In the first image, represented in the first row, the annotations by ophthalmologist number one were removed because of the disc area, and the annotations by ophthalmologist number six were removed because of the disc area and cup centroid. The algorithm gave bad results of the VCDR due to bad cup area. In the second image, the annotations by ophthalmologists number two and four were eliminated because of bad cup area, and the algorithm gave bad results due to bad disc segmentation. In the third image, the annotations by ophthalmologists number three and six were removed due to the cup area and centroid. The algorithm gave good results in terms of disc and area. However, the mean SD of VCDR was beyond the 0.075 threshold, and therefore was considered an outlier. Hence, this result was considered inappropriate for calculating the accuracy. In the last image, there is clearly a big variation among the annotations; therefore, this image was not considered a good image for evaluating the algorithm.

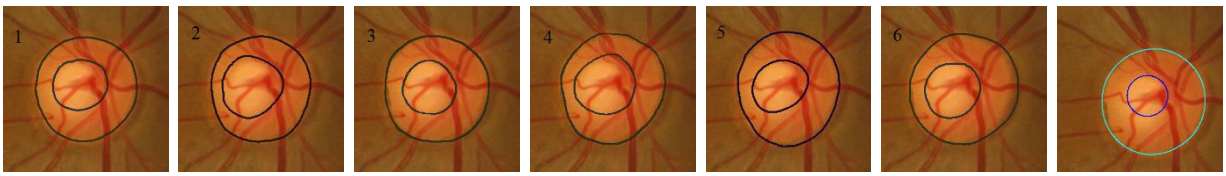

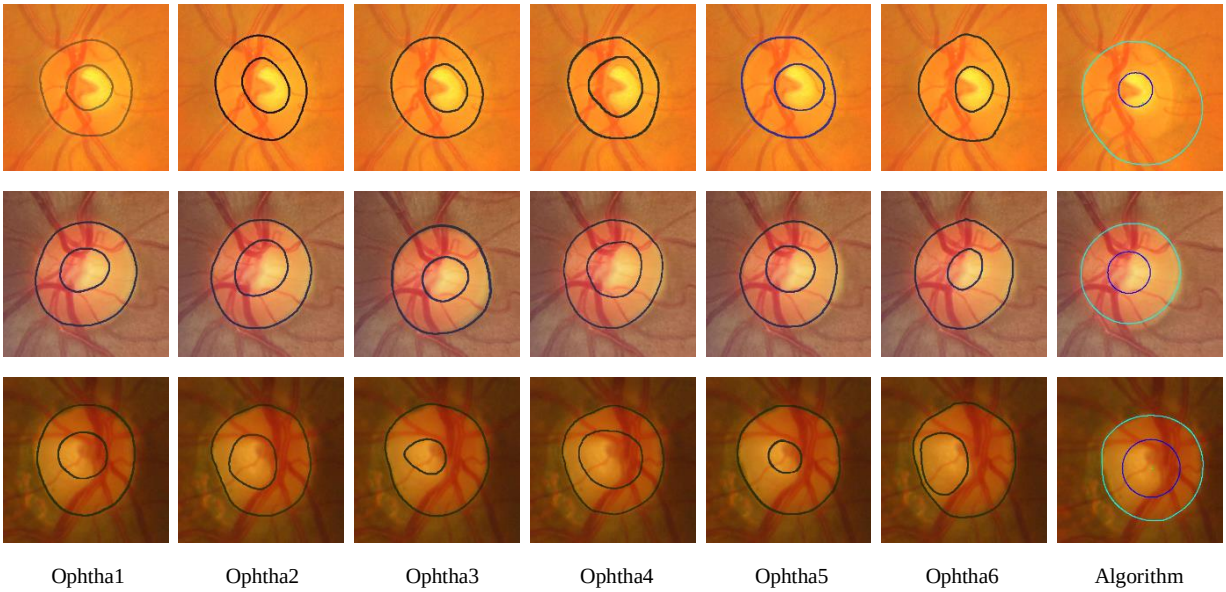

Figure 5.13 The algorithm bad VCDR results.

On the other hand, in Figure 5.14, for the first image (presented in the first row) the SD was 0.03 for the six ophthalmologists, and 0.04 for the algorithm. The algorithm VCDR was 0.45 while it was 0.46, 0.52, 0.54, 0.50, 0.54, and 0.48 for ophthalmologists number one to six, respectively. For the second image, the SD was the same for all manual annotations and the algorithm, and its value was 0.04. Here the VCDR was 0.52 for the algorithm and 0.47, 0.52, 0.41, 0.49, 0.42, and 0.44 for ophthalmologists number one to six, respectively. In the last image, the SD was 0.03 for the six ophthalmologists, and 0.04 for the algorithm. The VCDR was 0.61 for the algorithm and 0.63, 0.63, 0.67, 0.70, 0.64, and 0.62 for ophthalmologists number one to six, respectively.

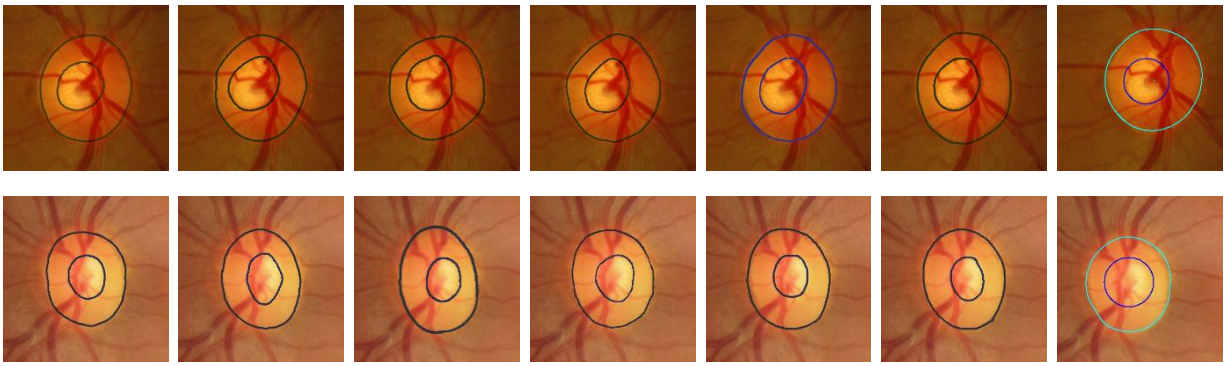

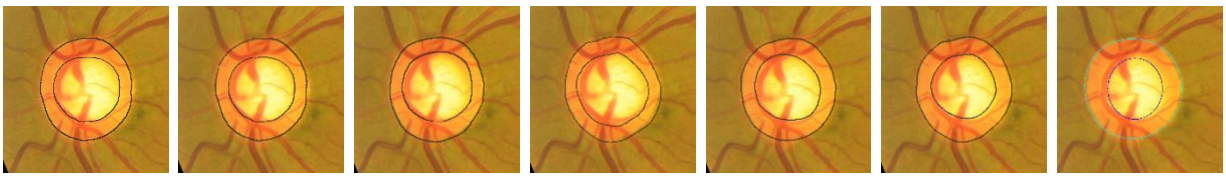

Ophtha1 Ophtha2 Ophtha3 Ophtha4 Ophtha5 Ophtha6 Algorithm

Figure 5.14 The algorithm good VCDR results.

5.3.1. Results of Bin Rushed dataset

The accuracy of the VCDR for all the annotations by the six ophthalmologists as well as the algorithm for Bin Rushed dataset is shown in Table 5.6. About 64 to 80 images were eliminated from the annotations by the ophthalmologists as well as the algorithm due to the many outliers for either disc, cup or the VCDR. Annotations by ophthalmologist number one were the best in terms of the percentage accuracy; the algorithm was the second best followed by ophthalmologist number six. In terms of the number of images accurately annotated, ophthalmologist number one annotated 91 out of 107 images accurately, followed by the algorithm which segmented 82 out of 109 images accurately, and then ophthalmologist number six who accurately annotated 79 out of 105 images.

Table 5.6 The VCDR results for Bin Rushed images set.

	Ophth1	Ophth2	Ophth3	Ophth4	Ophth5	Ophth6	Auto
Total number of images	195	195	195	195	195	195	195
# of images removed due to the lack agreement between the ophthalmologists	78	73	72	64	69	80	76
Images not localized	10	10	10	10	10	10	10
Total number of images tested	107	112	113	121	116	105	109
Accuracy (number of images)	91	76	74	44	76	79	82
Accuracy (percentage)	85	67.8	65.4	36.3	65.5	75.2	75.2

The percentage accuracies for Bin Rushed dataset were between 85% and about 65%, except for ophthalmologist number four who showed the percentage accuracy of about 36% (Figure 5.15). Except for ophthalmologist number four who showed similar percentage accuracies for HCDR

and VCDR, percentage accuracies for VCDR for this dataset were better than the comparable values for HCDR.

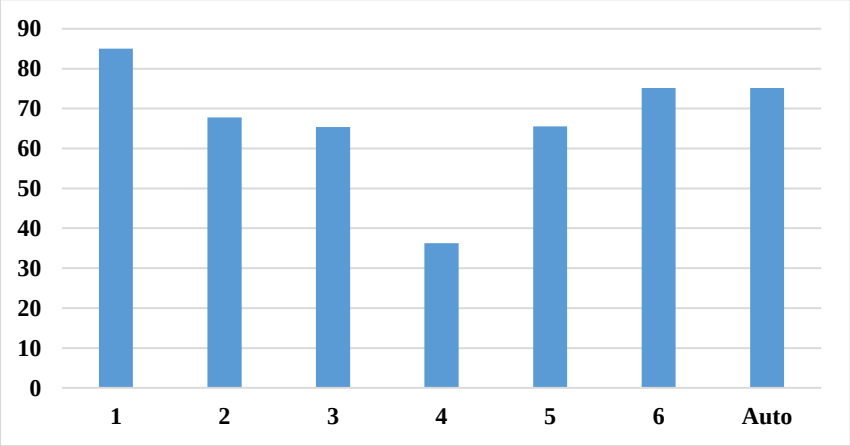

Figure 5.15 The percentage accuracy of the VCDR results for Bin Rushed images set. The X axis represents the number of 6 ophthalmologists and the algorithm. The Y axis represents the accuracy (percentage).

5.3.2. Results of Magrabi dataset

The percentage accuracies for Magrabi dataset are shown in Table 5.7. About 38 to 44 images were eliminated from the work done by the ophthalmologists as well as the algorithm. The best percentage accuracy belonged to the annotations by ophthalmologist number six. The algorithm was the third best in terms of percentage accuracy. In terms of the number of images accurately annotated, ophthalmologists number two and six and the algorithm had the highest performance with 38 out of 49, 48 and 50 images (respectively) annotated accurately.

Table 5.7 The VCDR results for Magrabi images set.

	Ophth1	Ophth2	Ophth3	Ophth4	Ophth5	Ophth6	Auto
Total number of images	95	95	95	95	95	95	95
# of images removed due to the lack agreement between the ophthalmologists	42	40	38	44	39	41	39
Images not localized	6	6	6	6	6	6	6
Total number of images tested	47	49	51	45	50	48	50
Accuracy (number of images)	32	38	29	29	30	38	38
Accuracy (percentage)	68	77.5	56.8	64.4	60	79.1	76

The range of percentage accuracy was between 56% for ophthalmologist number three and 79% for ophthalmologist number six (Figure 5.16); which was better than the range for HCDR. Ophthalmologist number three had the worst results for both HCDR and VCDR for this dataset.

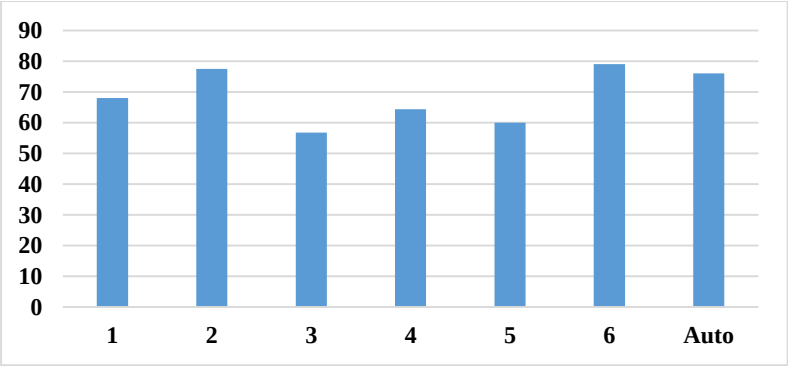

Figure 5.16 The percentage accuracy of the VCDR results for Magrabi images set. The X axis represents the number of 6 ophthalmologists and the algorithm. The Y axis represents the accuracy (percentage).

5.3.3. Results of MESSIDOR dataset

Finally, the percentage accuracy for MESSIDOR dataset is shown in Table 5.8. Sixty to 81 images were eliminated from the work of all six ophthalmologists as well as the algorithm. This number was slightly similar to the number of images eliminated from this dataset for calculation of HCDR which were between 56 to 73 images. Ophthalmologist number three had the best performance in terms of percentage accuracy, while the algorithm was at fifth place. In terms of the number of

images, ophthalmologist number three had 149 out of 169 images annotated accurately, while the algorithm successfully segmented 138 out of 186 images.

Table 5.8 The VCDR results for MESSIDOR images set.

	Ophth1	Ophth2	Ophth3	Ophth4	Ophth5	Ophth6	Auto
Total number of images	260	260	260	260	260	260	260
# of images removed due to the lack agreement between the ophthalmologists	72	60	81	62	73	76	64
Images not localized	10	10	10	10	10	10	10
Total number of images tested	178	190	169	188	177	174	186
Accuracy (number of images)	140	127	149	117	134	131	138
Accuracy (percentage)	78.6	66.8	88.1	62.2	75.7	75.2	74.1

Figure 5.17 shows the accuracy percentage for all six ophthalmologists as well as the algorithm for MESSIDOR dataset. The accuracy percentages ranged from 90% for ophthalmologist number three to about 60% for ophthalmologist number four. For this index, VCDR measurements were better than HCDR.

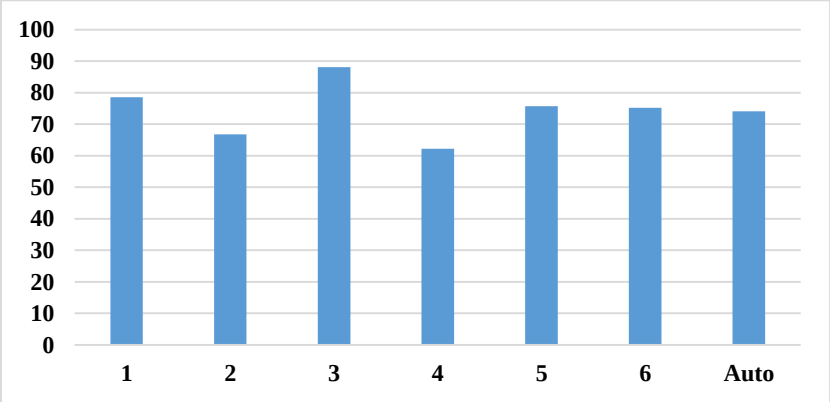

Figure 5.17 The percentage accuracy of the VCDR results for MESSIDOR images set. The X axis represents the number of 6 ophthalmologists and the algorithm. The Y axis represents the accuracy (percentage).

5.3.4. Consolidated results for VCDR

Table 5.9 shows the final results for the VCDR. 170 to 197 images were eliminated due to outliers from the work done by all six ophthalmologists as well as the algorithm (for HCDR, 161 to 181

images were eliminated due to outliers). The best percentage accuracy was 79.2% and belonged to the 332 images tested by ophthalmologist number one. For HCDR the best percentage accuracy was 76.6% and belonged to the 351 images also tested by ophthalmologist number one. The algorithm percentage accuracy was the fourth best with 74.7% of 345 total tested images, while it was the second best for the HCDR with 74.4% of 343 total tested images. In conclusion, for VCDR the annotations by the ophthalmologists and the algorithm had similar results in terms of the total tested images as well as percentage accuracy; while for HCDR the results of the algorithm were better than the annotations by the six ophthalmologists.

Table 5.9 The consolidated results for the VCDR.

	Ophth1	Ophth2	Ophth3	Ophth4	Ophth5	Ophth6	Auto
Total number of images	550	550	550	550	550	550	550
# of images removed due to the lack agreement between the ophthalmologists	192	173	191	170	181	197	179
Images not localized	26	26	26	10	26	26	26
Total number of images tested	332	351	333	370	343	327	345
Accuracy (number of images)	263	241	252	190	240	248	258
Accuracy (percentage)	79.2	68.6	75.6	51.3	69.9	75.8	74.7

Figure 5.18 illustrates that the percentage accuracy for the VCDR was between about 70% and 80%, except for the annotations by ophthalmologist number four. On the other hand, the accuracy range for the HCDR was between about 60% and 75%, which is less than the VCDR accuracy. This was due to the presence of blood vessels which made the annotations, specifically the annotations of the cup, challenging for the ophthalmologists.

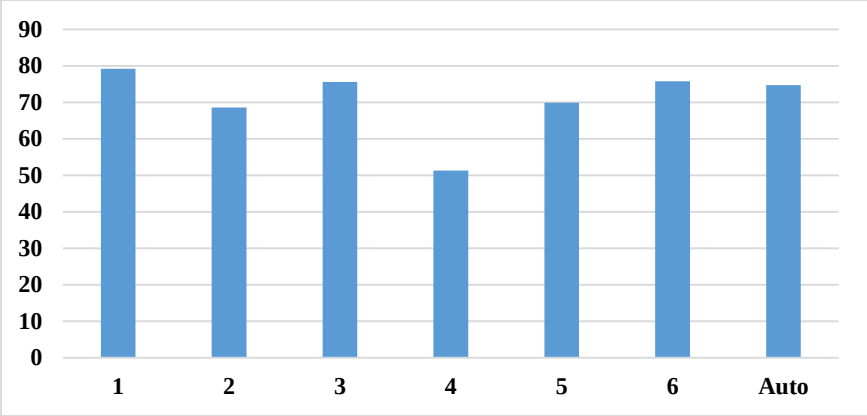

Figure 5.18 The percentage accuracy of the VCDR results for all the three images sets. The X axis represents the number of 6 ophthalmologists and the algorithm. The Y axis represents the accuracy (percentage).

Figure 5.19 shows how the six ophthalmologists as well as the algorithm performed (in terms of VCDR percentage accuracy) on the three datasets. The algorithm had consistent performance regardless of the dataset. This finding was similar to what we observed for the HCDR. The performance of ophthalmologist number six also remained the same across the three datasets. Similar to what was observed for the HCDR, there were small variations in performance of ophthalmologists number one, two and five as they worked on different datasets, with ophthalmologist number three showing the most variable performance for both HCDR and VCDR. Ophthalmologist number four showed a rather consistent performance for HCDR while showing big variation for VCDR.

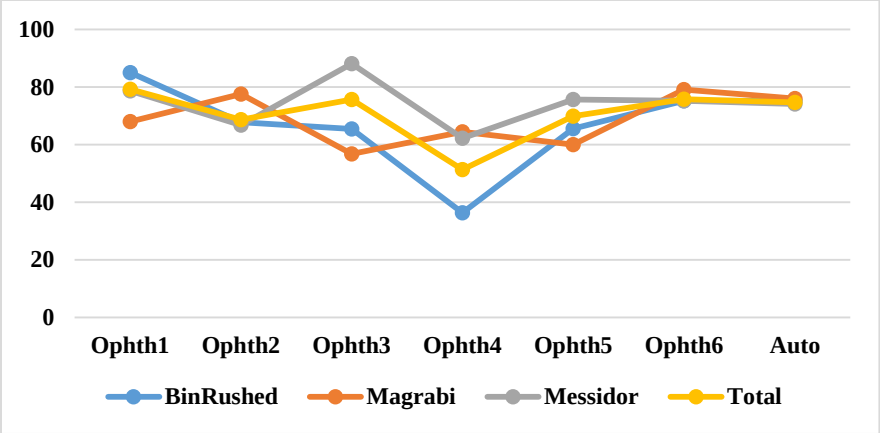

Figure 5.19 The percentage accuracy of the VCDR for the three images set individually. The X axis represents the number of 6 ophthalmologists and the algorithm. The Y axis represents the accuracy (percentage).

5.3.5. Agreement for VCDR

Table 5.10 shows the agreements between the ophthalmologists as well as the algorithm in terms of the number of images. The best agreements were between ophthalmologist number one and ophthalmologist number six in 254 images (46.1%), then between ophthalmologist number one and ophthalmologist number three in 253 images (46%), and between ophthalmologist number one and the algorithm in 252 images (45.8%) of 550 images. The agreements among the ophthalmologists regarding VCDR were almost equal to their agreement regarding HCDR. On the other hand, for the VCDR the algorithm was best agreed in 252 images, while for HCDR the algorithm was best agreed in 239 images (43.4%).

Table 5.10 The number of images agreed for the VCDR between the ophthalmologists as well as the algorithm.

	Ophth1	Ophth2	Ophth3	Ophth4	Ophth5	Ophth6	Auto
Ophth1	550	232	253	186	238	**254**	**252**
Ophth2	232	550	219	172	207	222	218
Ophth3	253	219	550	172	231	239	232
Ophth4	186	172	172	550	162	171	168
Ophth5	238	207	231	162	550	232	221
Ophth6	254	222	239	171	232	550	235
Auto	252	218	232	168	221	235	550
Total	1415	1270	1346	1031	1291	1353	1326

Figure 5.20 shows how the ophthalmologists agreed in the number of images as groups. Five ophthalmologists as well as the algorithm had more than 200 images agreed between each other; only ophthalmologist number four had less than 200 images agreed with the others. Ophthalmologist number one had the best agreement with the others.

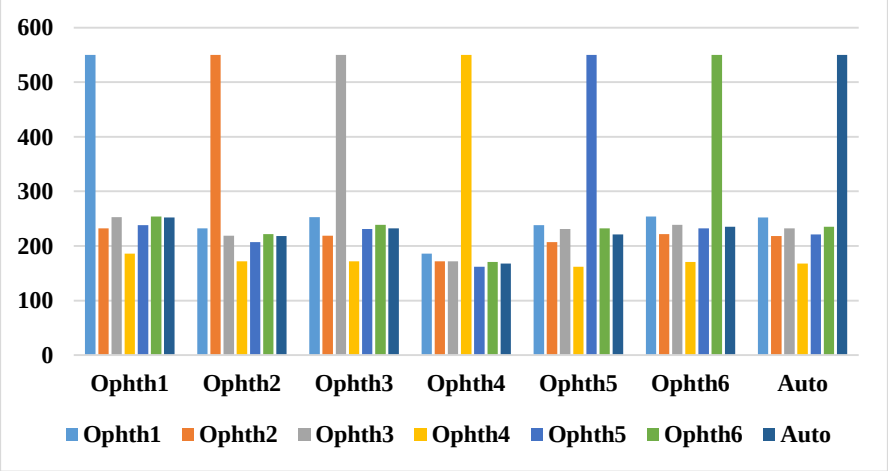

Figure 5.20 The number of images agreed for the HCDR between the ophthalmologists as well as the algorithm. The X axis represents the number of 6 ophthalmologists and the algorithm. The Y axis represents the number of agreed images.

Figure 5.21 shows that in terms of the total images agreed, the range was between 1250 to 1400 images, except for ophthalmologist number four who had only 1000 images. The range of the total images agreed for the VCDR was similar to the results for HCDR.

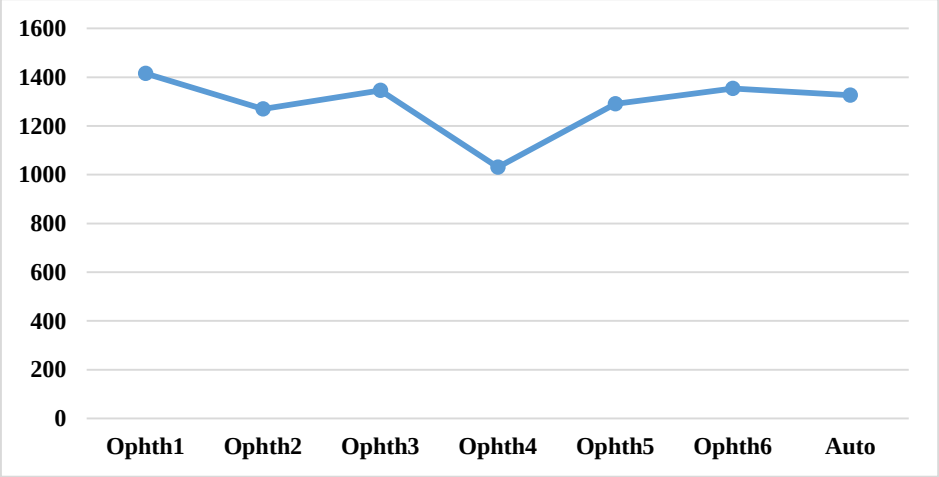

Figure 5.21 The total agreed images for the VCDR between the ophthalmologists as well as the algorithm. The X axis represents the number of 6 ophthalmologists and the algorithm. The Y axis represents the number of total agreed images.

5.4. Final Results (HCDR and VCDR)

In this section the analysis cover all four parameters, i.e., disc (area and centroid), cup (area and centroid), HCDR and VCDR. Therefore, the six annotations had to pass with respect to all four parameters in order to be included in this analysis (Figure 3.21). For each image, if there were at least three outliers for the same parameter, e.g. three outliers in disc area, then the image was eliminated from evaluating the algorithm. If there were three outliers but they were from different parameters, e.g. one for disc centroid, one for cup area and one for HCDR, then the image was not eliminated. However, if there were four outliers with two outliers belonging to the same parameter, e.g. two outliers for the disc area, one outlier for the cup area and one for the VCDR, then the image was eliminated. The same procedures were applied for the results of the algorithm in order to decide whether a segmentation was accepted or not (Figure 4.21).

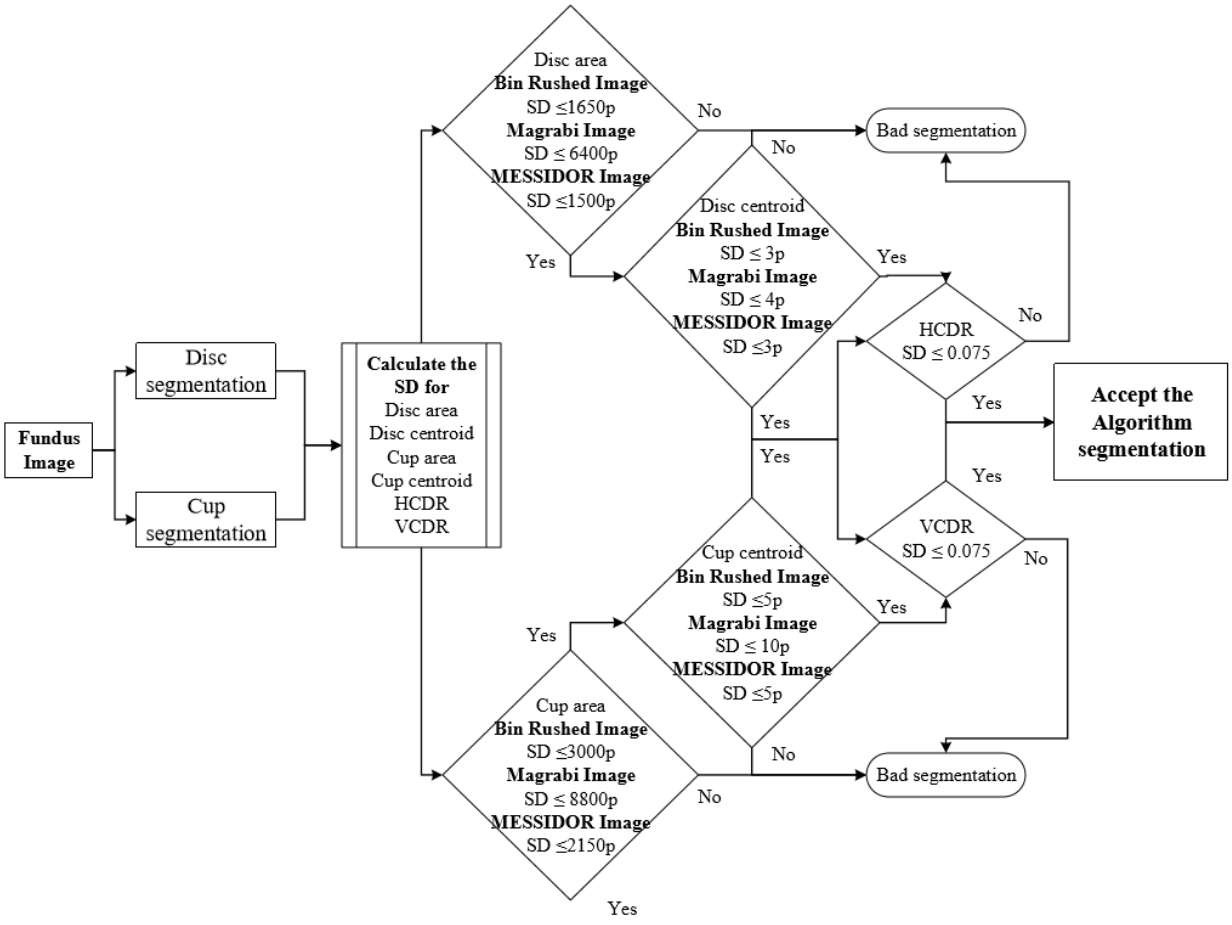

Figure 5.22 Flowchart for the algorithm analysis.

Figure 5.23 shows the results for two images from the MESSIDOR dataset. The HCDRs recorded by ophthalmologists number one to six were 0.67, 0.76, 0.67, 0.73, 0.69, and 0.70, respectively, with SD 0.04. The algorithm's result was 0.67 without any change for the SD. The VCDR recorded by ophthalmologists number one to six were 0.60, 0.61, 0.58, 0.59, 0.67, and 0.60, respectively, with SD 0.03. The algorithm's result was 0.69, again without any change for the SD. In the second image, the HCDRs recorded by ophthalmologists number one to six were 0.47, 0.58, 0.44, 0.56, 0.50, and 0.49, respectively, with SD 0.06. The algorithm's result was 0.55, with SD 0.05. On the other hand, the VCDRs recorded by ophthalmologists number one to six were 0.55, 0.57, 0.54,

0.59, 0.53, and 0.55, respectively, with SD 0.02. The algorithm's result was 0.55 without any change in the SD.

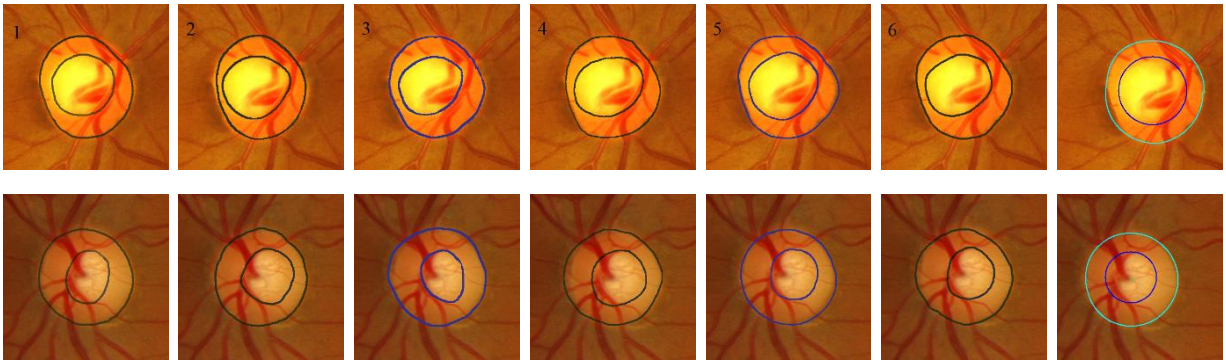

Figure 5.23 The algorithm final results for MESSIDOR images set.

Figure 5.24 shows the results for two images from Bin Rushed dataset. In the first image, the annotations by ophthalmologists number four and five were removed due to the cup size making the SD more than 3000 pixels. The HCDRs recorded by ophthalmologists number one to six were 0.53, 0.54, 0.49, 0.65, 0.43, and 0.45, respectively, with SD 0.05. The algorithm's result was 0.53 without any change in the SD. The VCDRs recorded by ophthalmologists number one to six were 0.48, 0.51, 0.46, 0.61, 0.47, and 0.47, respectively, with SD 0.06. The algorithm's result was 0.5, reducing the SD to 0.05. In the second image, the HCDRs recorded by ophthalmologists number one to six were 0.52, 0.53, 0.53, 0.55, 0.53, and 0.45, respectively, with SD 0.03. The algorithm's result was 0.45, increasing the SD to 0.04. The VCDRs recorded by ophthalmologists number one to six were 0.49, 0.48, 0.45, 0.51, 0.43, and 0.44, respectively, with 0.03 SD. The algorithm's result was 0.045, without any change in the SD.

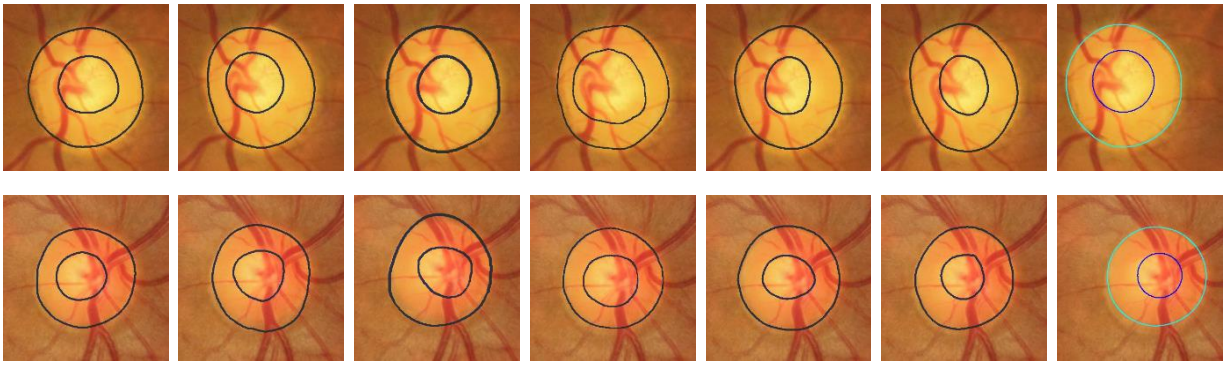

Figure 5.24 The algorithm final results for Bin Rushed images set.

Finally, Figure 5.25 shows the results of Magrabi dataset. For the first image, the top row, the annotations by ophthalmologists number one and three were removed due to the cup area and centroid because the SD was more than 8000 pixels for area and was more than 10 pixels for centroid. The HCDRs recorded by ophthalmologists number one to six were 0.46, 0.52, 0.53, 0.60, 0.51, and 0.47, respectively, with SD 0.05. The algorithm's result was 0.64, while increasing the SD to 0.06. The VCDRs recorded by ophthalmologists number one to six were 0.41, 0.55, 0.46, 0.54, 0.44, and 0.47, respectively, with SD 0.05. The algorithm's result was 0.57, changing the SD to 0.055. In the second image, bottom row, the HCDRs recorded by ophthalmologists number one to six were 0.58, 0.54, 0.50, 0.54, 0.47, and 0.52, respectively, with SD 0.03. The algorithm's result was 0.48, without any change in the SD. The VCDRs recorded by ophthalmologists number one to six were 0.47, 0.45, 0.44, 0.45, 0.39, and 0.45, respectively, with SD 0.03. The algorithm's result was 0.049, increasing the SD to 0.035.

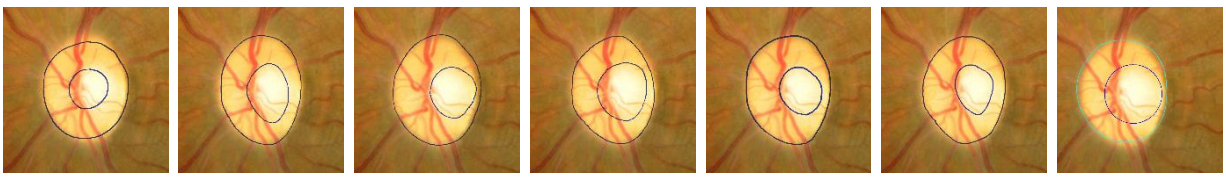

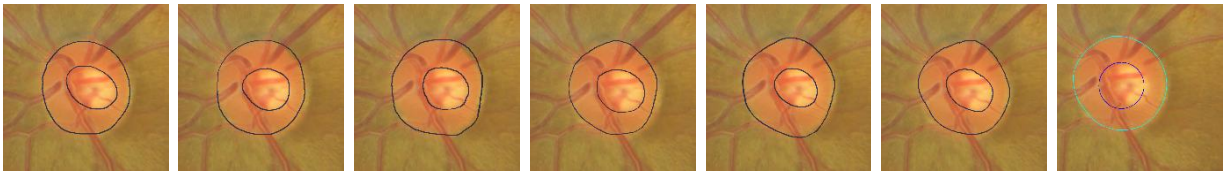

Ophtha1 Ophtha2 Ophtha3 Ophtha4 Ophtha5 Ophtha6 Algorithm

Figure 5.25 The algorithm final results for Magrabi images set.

5.4.1. Results of Bin Rushed dataset

Table 5.11 illustrates the final results for Bin Rushed dataset. 73 to 98 images were eliminated due to the outliers of the aforementioned four parameters between the six ophthalmologists as well as the algorithm which represent 37.4% to %50% of the total number of the images in the dataset. As mentioned before, for all the parameters 10 images were not localized. The best percentage accuracy was for ophthalmologist number one (82.4%) for the total of 97 tested images. The algorithm was the second best, with 70.7% percentage of accuracy for the total of 82 tested images. Ophthalmologist number four had the poorest percentage of accuracy (36.6%) for the total of 112 tested images.

Table 5.11 The final results for Bin Rushed images set.

	Ophth1	Ophth2	Ophth3	Ophth4	Ophth5	Ophth6	Auto
Total number of images	195	195	195	195	195	195	195
# of images removed due to the lack agreement between the ophthalmologists	88	87	79	73	84	87	98
Images not localized	10	10	10	10	10	10	10
Total number of images tested	97	98	106	112	101	98	82
Accuracy (number of images)	80	66	68	41	70	67	58
Accuracy (percentage)	82.4	67.3	64.1	36.6	69.3	68.3	70.7

It is clear from Figure 5.26 that the range of percentage accuracy for all ophthalmologists (except for ophthalmologist number four) as well as the algorithm was from about 65% to 80%.

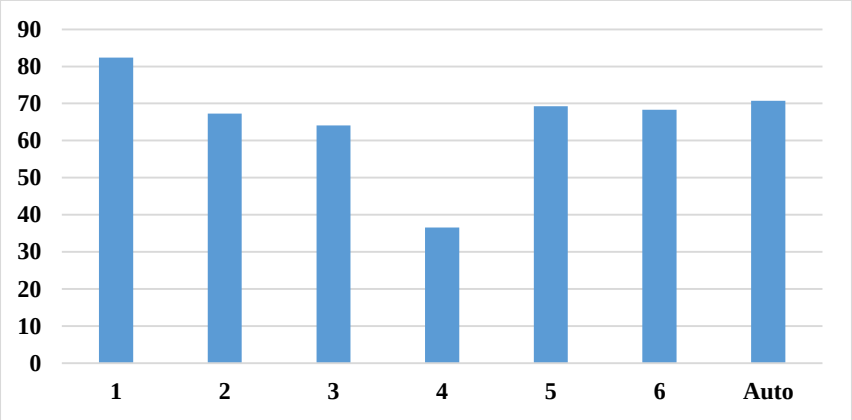

Figure 5.26 The percentage accuracy of the total results for Bin Rushed images set. The X axis represents the number of 6 ophthalmologists and the algorithm. The Y axis represents the accuracy (percentage).

5.4.2. Results of Magrabi dataset

Table 5.12 shows the results of Magrabi dataset. From this dataset 40 to 45 images were eliminated due to the outliers between the six ophthalmologists as well as the algorithm. This accounts for 42 to 50 percent of the images in Magrabi dataset, which was close to the percentage of outliers in Bin Rushed dataset. In addition, 6 images were not localized. The best percentage accuracy was for the algorithm (77.2%) for a total of 44 tested images.

Table 5.12 The final results for Magrabi images set.

	Ophth1	Ophth2	Ophth3	Ophth4	Ophth5	Ophth6	Auto
Total number of images	95	95	95	95	95	95	95
# of images removed due to the lack agreement between the ophthalmologists	43	43	40	44	41	40	45
Images not localized	6	6	6	6	6	6	6
Total number of images tested	46	46	49	45	48	49	44
Accuracy (number of images)	31	35	27	26	29	35	34
Accuracy (percentage)	67.3	76	55.1	57.7	60.4	71.4	77.2

As shown in Figure 5.27, the percentage accuracy range for the work of the six ophthalmologists as well as the algorithm was from 75% to 55%, which was a tighter range than what was observed

for Bin Rushed dataset. For this dataset, ophthalmologist number three showed the poorest performance in terms of the percentage accuracy.

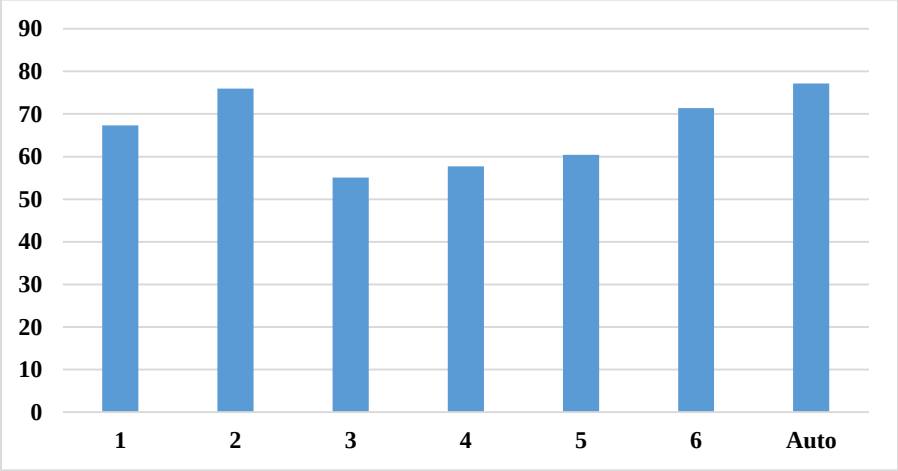

Figure 5.27 The percentage accuracy of the total results for Magrabi images set. The X axis represents the number of 6 ophthalmologists and the algorithm. The Y axis represents the accuracy (percentage).

5.4.3. Results of MESSIDOR dataset

Finally, Table 5.13 shows the results for MESSIDOR dataset. 69 to 86 images were removed due to the outliers of the aforementioned four parameters. This accounts for 26 to 33 percent of images in MESSIDOR dataset which is clearly a smaller percentage in comparison with the other two datasets. In addition, 10 images were not localized. The best percentage accuracy was for ophthalmologist number three (84.7%) for the total of 164 tested images. The algorithm and ophthalmologist number one tied for the second best with 77.3% accuracy when testing a total of 168 and 172 images, respectively.

Table 5.13 The final results for MESSIDOR images set.

	Ophth1	Ophth2	Ophth3	Ophth4	Ophth5	Ophth6	Auto
Total number of images	260	260	260	260	260	260	260
# of images removed due to the lack agreement between the ophthalmologists	78	69	86	70	81	81	82
Images not localized	10	10	10	10	10	10	10
Total number of images tested	172	181	164	180	169	169	168
Accuracy (number of images)	133	118	139	105	128	124	130
Accuracy (percentage)	77.3	65.1	84.7	58.3	75.7	73.3	77.3

Figure 5.28 shows that the percentage accuracy range for all the six ophthalmologists as well as the algorithm was from about 60% to 85%. In this respect, this dataset was better than the other two datasets.

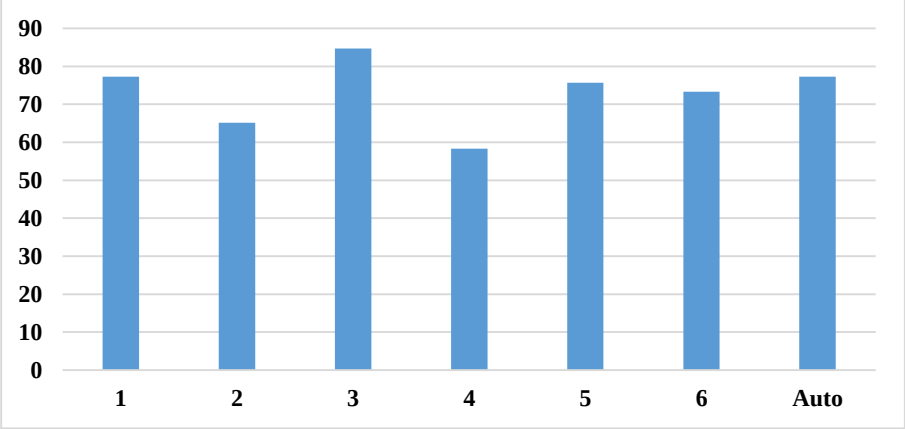

Figure 5.28 The percentage accuracy of the final results for MESSIDOR images set. The X axis represents the number of 6 ophthalmologists and the algorithm. The Y axis represents the accuracy (percentage).

5.4.4. The final consolidated results

As a comprehensive analysis, Table 5.14 illustrates the results for all three datasets together. 187 to 209 images (43 to 38% of the total images) were eliminated from the work of the six ophthalmologists due to their many outliers. On the other hand, 225 images (50% of the total images) were eliminated from testing the algorithm due to the outliers. In addition, 26 images were not localized. The best percentage accuracy was for the annotations by ophthalmologist number

one (77.4% which equals to 244 out of the 315 tested images). The algorithm had the second best percentage accuracy (74.2% which equals to 222 out of 299 tested images). The performance of ophthalmologist number three was the third best in this regard, with percentage accuracy of 73.3% which equals to 234 out of 319 tested images.

Table 5.14 The final consolidated results.

	Ophth1	Ophth2	Ophth3	Ophth4	Ophth5	Ophth6	Auto
Total number of images	550	550	550	550	550	550	550
# of images removed due to the lack agreement between the ophthalmologists	209	199	205	187	206	208	225
Images not localized	26	26	26	10	26	26	26
Total number of images tested	315	325	319	353	318	316	299
Accuracy (number of images)	244	219	234	172	227	226	222
Accuracy (percentage)	77.4	67.3	73.3	48.7	71.3	71.5	74.2

Figure 5.29 shows the percentage accuracy of the annotations by the six ophthalmologists as well as the algorithm. Clearly, the percentage accuracy ranges from 70 to 75%, except for the work of ophthalmologist number four. The percentages of accuracy of the work of five ophthalmologists as well as the algorithm for all three datasets together are relatively close to each other.

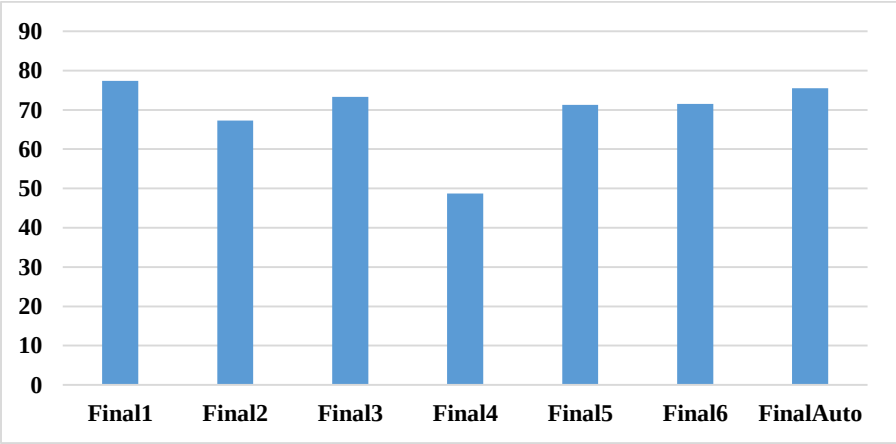

Figure 5.29 The percentage accuracy of the final results including all the three images sets. The X axis represents the number of 6 ophthalmologists and the algorithm. The Y axis represents the accuracy (percentage).

Figure 5.30 illustrates the variation in the performance of the six ophthalmologists as well as the algorithm on the three datasets in terms of percentage accuracy. The algorithm and ophthalmologist number six showed the most consistent performance across all three datasets. The performance of ophthalmologist number two varied slightly; he/she performed slightly better on Magrabi dataset than on the other two datasets. Performances of ophthalmologists number one and five showed larger variations; ophthalmologist number one performed best with Bin Rushed dataset, while ophthalmologist number five performed best with MESSIDOR dataset. Ophthalmologist number three clearly showed a better performance when working on the MESSIDOR dataset. Ophthalmologist number four performed very poorly when working on Bin Rushed dataset. Ophthalmologist number three, four, five and six as well as the algorithm had the best percentage accuracy for MESSIDOR dataset. However, ophthalmologist number two had the lowest percentage accuracy when working with MESSIDOR dataset. The second best performance of three ophthalmologists as well as the algorithm was observed as they worked on Magrabi dataset. The second best performance of only three ophthalmologists was observed as they worked on Bin Rushed dataset. Therefore, we conclude that the assessment of optic nerve by annotating the disc and cup margins was most accurate and consistent in the MESSIDOR dataset, followed by Magrabi dataset in the 2nd place and Bin Rushed dataset in the 3rd place.

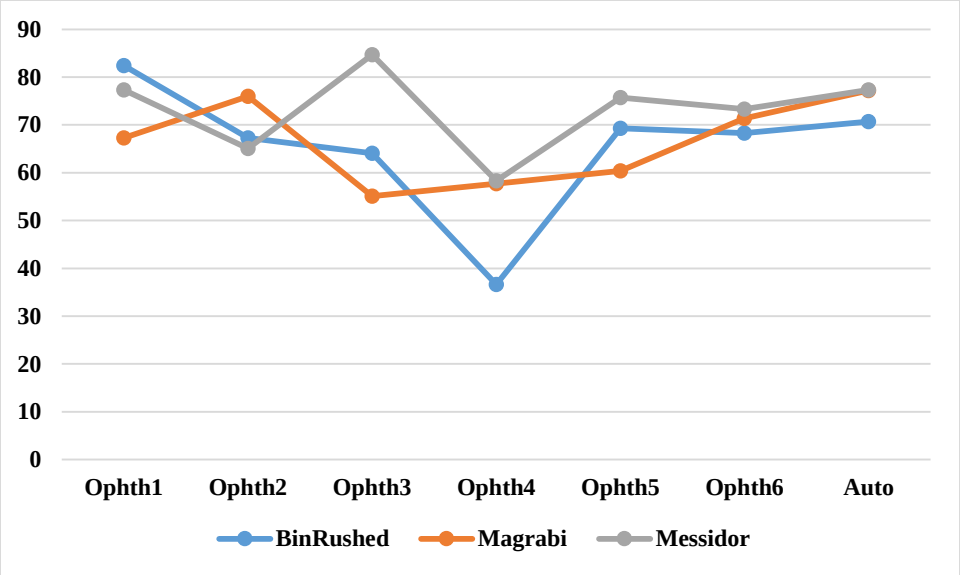

Figure 5.30 The percentage accuracy of the VCDR for the three images set individually. The X axis represents the number of 6 ophthalmologists and the algorithm. The Y axis represents the accuracy (percentage).

5.4.5. Agreement for the final

The best agreement in terms of the number of images was between ophthalmologist number one and three in 242 of the total 550 images (44%) (Table 5.15), while the second best agreement was between ophthalmologist number one and the algorithm as well as ophthalmologist number five in 230 images (41.8%). The agreement among these images was in all the aforementioned four parameters.

Table 5.15 The number of images agreed for the final between the ophthalmologists as well as the algorithm.

	Ophth1	Ophth2	Ophth3	Ophth4	Ophth5	Ophth6	Auto
Ophth1	550	223	**242**	169	**230**	226	**230**
Ophth2	223	550	212	153	198	199	201
Ophth3	242	212	550	155	223	219	216
Ophth4	169	153	155	550	151	148	148
Ophth5	230	198	223	151	550	214	207
Ophth6	226	199	219	148	214	550	207
Auto	230	201	216	148	207	207	550
Total	1320	1186	1267	924	1223	1213	1209

Figure 5.31 shows the number of images agreed between the ophthalmologists as well as the algorithm. Clearly, all the ophthalmologists as well as the algorithm agreements were close to 200 images except for ophthalmologist number four.

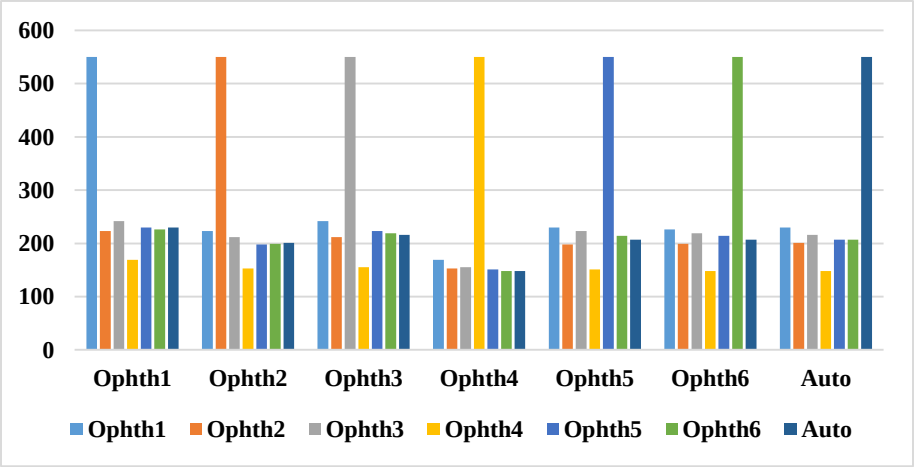

Figure 5.31 The number of images agreed for the HCDR between the ophthalmologists as well as the algorithm. The X axis represents the number of 6 ophthalmologists and the algorithm. The Y axis represents the number of agreed images.

Figure 5.32 shows the total number of agreement for all six ophthalmologists as well as the algorithm. The number of total images agreed ranged from 1200 to 1300 images, except for ophthalmologist number four who in total had less than 1000 images agreed.

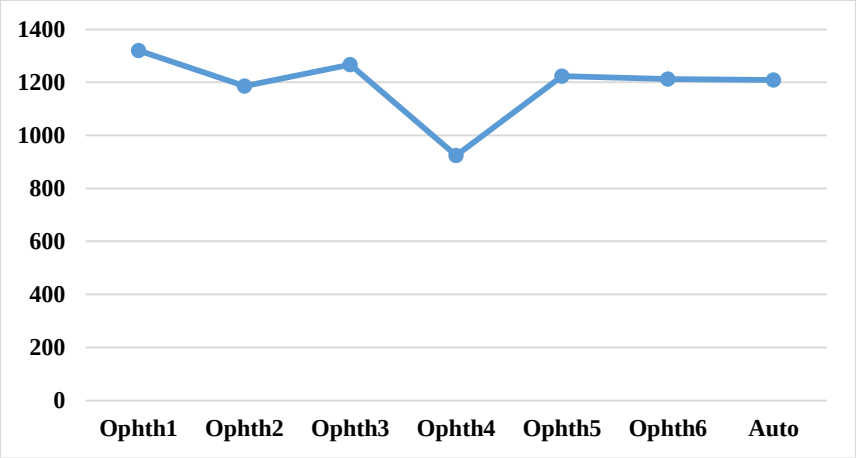

Figure 5.32 The total agreed images for the VCDR between the ophthalmologists as well as the algorithm. The X axis represents the number of 6 ophthalmologists and the algorithm. The Y axis represents the number of total agreed images.

As can be seen in Figure 5.33 the range of the total number of images agreed for HCDR and VCDR was from 1300 to 1400 images, except for ophthalmologist number four. Clearly, the HCDR and VCDR had almost equal number of image agreements. Ophthalmologist number five had more image agreements in HCDR than in VCDR, while ophthalmologist number six and the algorithm had more agreed images in VCDR than in HCDR. In conclusion, the VCDR was better than HCDR in terms of the total images agreed between the six ophthalmologists as well as the algorithm. The range of the final total image agreements (including disc, cup, HCDR and VCDR) was between 1200 and 1300 images, except for ophthalmologist number four who had around 950 image agreements. The highest image agreements were for ophthalmologist number one and then ophthalmologist number three, while ophthalmologist number two, five, six and the algorithm had almost the same number of image agreements.

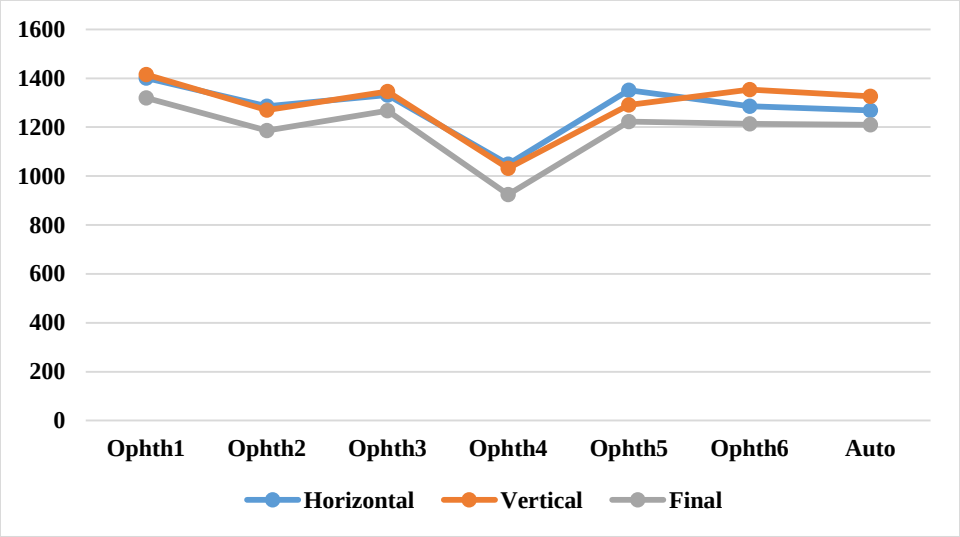

Figure 5.33 The total number of agreement for HCDR, VCDR and final. The X axis represents the number of 6 ophthalmologists and the algorithm. The Y axis represents the number of total agreed images.

Figure 5.34 illustrates the percentage accuracy for all the four parameters as well as the total for the work of all six ophthalmologists and the algorithm. Clearly, the accuracy of disc and cup measurements influences the accuracy of HCDR and VCDR as well as the total. The cup accuracy was the best for three ophthalmologists and the algorithm due to the bigger mean SD for both area and centroid for the cup. There was more constancy for the algorithm performance where the disc had the best accuracy, then the cup, and then the HCDR and VCDR and that was close to the performance of ophthalmologist number six. Ophthalmologist number four was the best in annotating the disc and the worse in annotating the cup; with these measurements clearly affecting the HCDR and VCDR measurements.

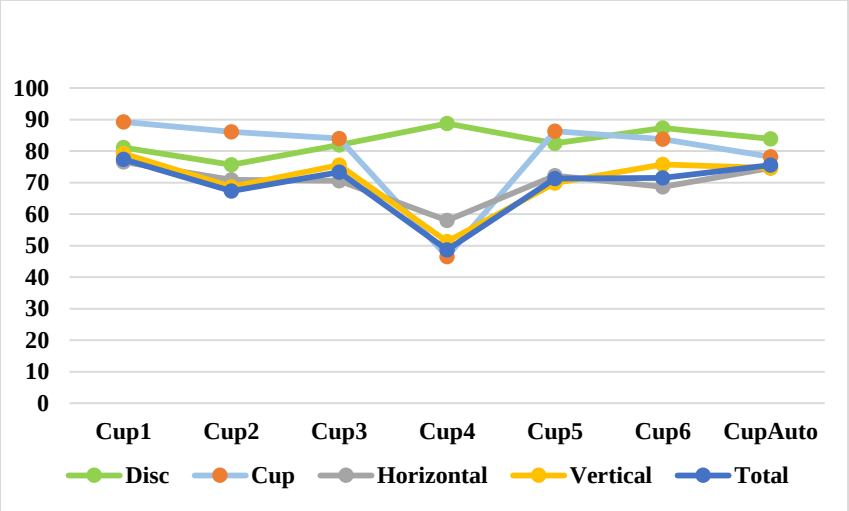

Figure 5.34 The percentage accuracy results for all the four parameters. The X axis represents the number of 6 ophthalmologists and the algorithm. The Y axis represents the accuracy (percentage).

Chapter 6

Conclusions and future works

6.1. Conclusions

With the dramatic increase in the world's population, there is a corresponding increase in the number of patients with glaucoma, or suspected of having glaucoma. Therefore, there is a need to properly diagnose and treat glaucoma and save the vision of those afflicted. Hence, the goal of this thesis was to provide insight on one of the three most important exams for glaucoma, i.e., diagnosing the optic nerve head (ONH) structure, by developing a novel system to detect the disc and cup boundaries which are the diagnostic parameters used in clinics. A literature review was conducted in order to provide a general view of the state of the art and discuss the limitations, weaknesses and strengths of existing approaches for automated determination of cup to disc ratios. Consequently, collecting the images as well as annotating the disc and cup boundaries were the priority to build a reliable system. Most of the previously used image datasets have many limitations. One such limitation is that the diagnosis of the disc and cup differs from one ophthalmologist to another making the created system unreliable if it is based on the opinion of only one ophthalmologist. Therefore, a unique image dataset has to be examined by more than one ophthalmologist in order to have diagnostic value. Indeed, in this thesis I described a new dataset called RIGA dataset consisting of 750 images. RIGA has been collected from three different resources in order to have different image aspects such as quality, size and pathology. Six ophthalmologists annotated the disc and cup manually and independently. The images for which at least four ophthalmologists agreed on the disc and cup boundaries were kept, and those upon which only three ophthalmologists (or fewer) agreed were eliminated. The images for which at least four ophthalmologists agreed upon the measurements of disc and cup boundaries were

suitable for automatic detection, while those with agreement of a maximum of three ophthalmologists were difficult to be automatically detected. This is due to many reasons including bad image quality or bad pathological cases that interfere with detecting the disc and cup boundaries.

A complicated analysis was conducted on RIGA dataset in order to revise the images; keeping the good images (in terms of detectable disc and cup boundaries) and removing the bad ones. The procedure was conducted by calculating the SD of the six annotations for the following four parameters: disc (area and centroid), cup (area and centroid), HCDR and VCDR for every single image. Following this, the mean SD of all 750 images was calculated for every parameter. Subsequently, the mean SDs were used as a standard yardstick to decide whether the annotations were accepted or not. Based on the number of accepted annotations for an image, it was decided whether the image was useful or not (Figure 3.21).

Based on the aforementioned analyses, the number of agreement between the six ophthalmologists as well as the accuracy of annotations by each ophthalmologist were obtained.

The image processing technique was introduced in chapter four. The goal was to have an automatic system capable of segmenting disc and cup boundaries as accurately as the ophthalmologists did. Localizing the ROI was the preprocessing step which was introduced to allow dealing with a small part of the image instead of the whole image. This was done by applying an Interval Type-II fuzzy entropy based thresholding scheme along with Differential Evolution to determine the location of the optic disc. The multi-level image segmentation was a method to segment the image into various objects in order to find the brightest object of the image, which was located in the OC. In terms of the main process, the optic disc segmentation was introduced first by applying the active contour implemented by level set function after inpainting the blood vessels. Inpainting was done to

remove the obstacles that might be present at the level set due to the change in the intensity of the blood vessels. A double level set was applied with more processing for the poor quality images found in the Bin Rushed dataset. The final accuracy of the algorithm was 83.9% for the 441 total tested images. In terms of percentage accuracy, the algorithm was the third best after two ophthalmologists. Every segmented image went through the analysis of only the optic disc area and centroid as shown in Figure 4.10. On the other hand, the cup segmentation was conducted in two stages. In the main stage, the disc segmentation was not considered [88]. The blood vessels were extracted in order to detect the vessel kinks which helped to detect the cup boundaries. The Interval Type-II fuzzy entropy based thresholding scheme along with Differential Evolution were again applied on the localized image to detect the intensity of the optic cup borders. In the localized image, the thresholds were more accurate than the entire image which was used to find the optic disc in the preprocessing. With localized image, the variation in the contrast was more limited since it was applied on a small portion of the image. Then Hough transform was applied in order to approximate the cup. In the second stage, the disc segmentation was involved in order to improve the cup centroid accuracy by developing two more functions for X and Y coordinates. The segmented cup was passed through the procedures shown in Figure 4.23 only for the cup area and centroid parameters in order to decide whether the cup has been successfully segmented.

After revising the images to include only the successfully segmented images in terms of disc and cup, the HCDR was computed based on the conditions shown in Figure 5.22. This enabled further revision of the images to include only those that met the conditions for the three parameters of disc, cup and HCDR. The same procedures were repeated for the VCDR. Thus, in the final analysis only the images that met the conditions of the disc, cup, HCDR and VCDR were considered. As illustrated in Figure 6.1 (A), the algorithm had almost the same number of images segmented

accurately for both HCDR and VCDR as ophthalmologist number three. Four ophthalmologists had more images accepted for the VCDR due to fewer blood vessels in the two sides. However, the accepted images for the HCDR were less accurate due to the existence of blood vessels that covered the cup boundaries. One ophthalmologist had the same number of accepted images for the VCDR and HCDR as the algorithm. Therefore, the algorithm was the second best in terms of HCDR and the fourth best for annotating the VCDR in terms of percentage accuracy (Figure 6.1(B)).

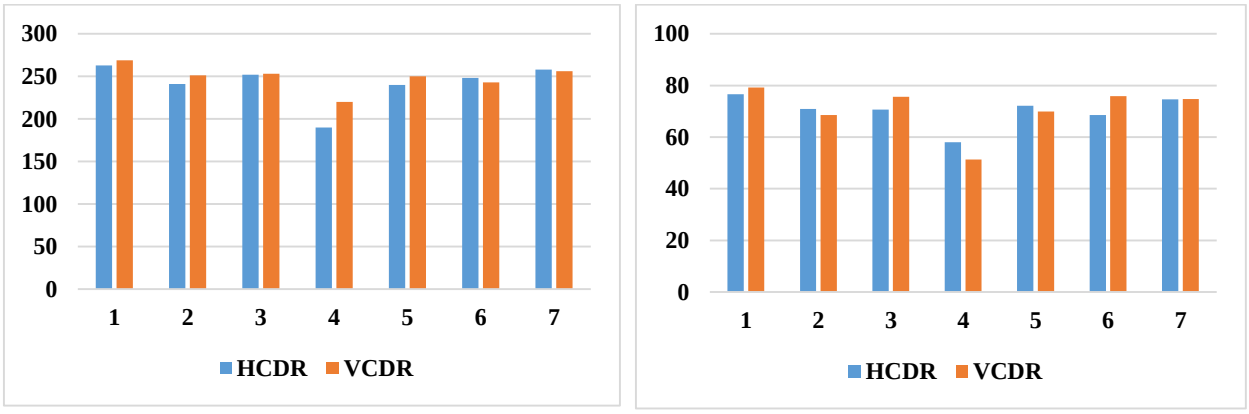

(A) **(B)**

Figure 6.1 The results of HCDR and VCDR: (A) the number of the accepted images; (B) the percentage accuracy. The X axis represents the number of 6 ophthalmologists and the algorithm. The Y axis represents the total agreed images in (B) and the accuracy (percentage) in (B).

Figure 6.2 shows the final results considering the four parameters. In terms of the number of images, the algorithm was the fifth best as illustrated in Figure 6.2 (A). In terms of percentage accuracy however, the algorithm was the second best due to the total number of tested images which varied among the six ophthalmologists as well as the algorithm due to removal of outliers. About 220 to 250 images were accepted for all six ophthalmologists, except for ophthalmologist

number four. The percentages of accuracy were about 70% to 80%, except for ophthalmologist number four (Figure 6.2 (B)).

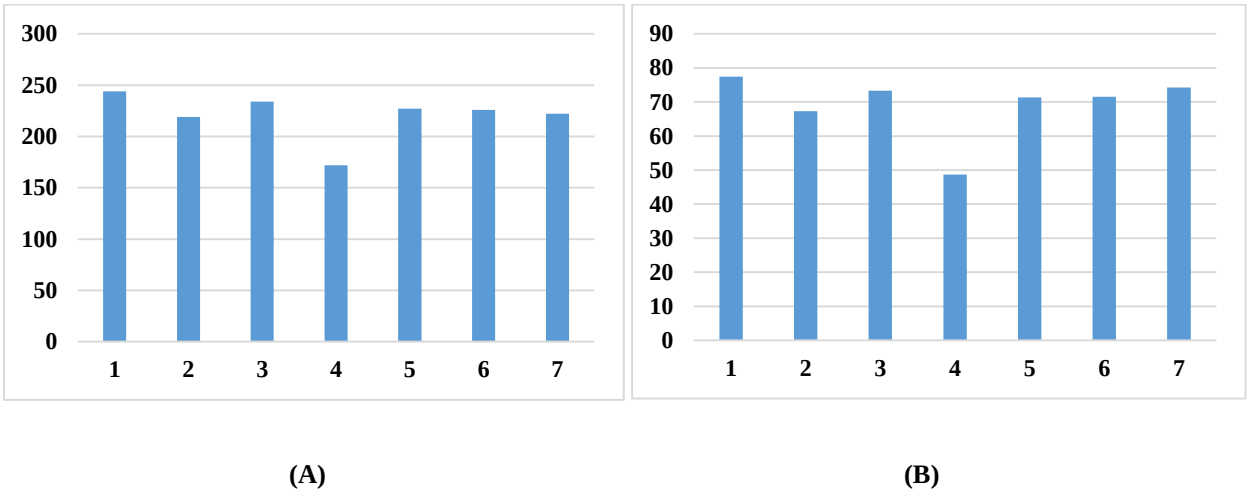

Figure 6.2 The final total results: (A) The number of accepted images; (B) Percentage accuracy. The X axis represents the number of 6 ophthalmologists and the algorithm. The Y axis represents the total agreed images in (B) and the accuracy (percentage) in (B).

Tables 6.1 and 6.2 provide additional details about the best and worst accuracy results, and the highest and lowest number of images agreed among the six ophthalmologists. Ophthalmologist number one was the best for Bin Rushed dataset represented by the final results which considered the cup, HCDR, and VCDR (Table 6.1). Three ophthalmologists as well as the algorithm shared the best rank for Magrabi dataset. Finally, ophthalmologist number three showed the best performance for analyzing MESSIDOR dataset for disc, HCDR and VCDR. In general and considering all three datasets, ophthalmologist number one showed the best performance in analysis of the cup, HCDR and VCDR and had the highest number of image agreements (Table 6.1).

Table 6.1 The best accuracy and agreement for all the four parameters and the three images sets**.**

	Best Accuracy				Most Agreement
	Bin Rushed	Magrabi	MESSIDOR	Total	
Disc	Ophth4	Ophth4	Ophth3	Ophth4	Ophth4
Cup	Ophth1	Ophth2	Ophth5	Ophth1	Ophth1
HCDR	Ophth1	Ophth2	Ophth3	Ophth1	Ophth1
VCDR	Ophth1	Ophth6	Ophth3	Ophth1	Ophth1
Final	Ophth1	Algorithm	Ophth3	**Ophth1**	**Ophth1**

Ophthalmologist number four had the worst accuracy for Bin Rushed and MESSIDOR datasets and ophthalmologist number three had the worst accuracy for Magrabi dataset (Table 6.2). Finally, ophthalmologist number four had the worst percentage accuracy for the final total as well as the lowest number of images agreed with other ophthalmologists as well as the algorithm (Table 6.2).

Table 6.2 The worse accuracy and agreement for all the four parameters and the three images sets.

	Worse Accuracy				Lowest Agreement
	Bin Rushed	Magrabi	MESSIDOR	Total	
Disc	Ophth3	Ophth2	Ophth2	Ophth2	Ophth2
Cup	Ophth4	Ophth4	Ophth4	Ophth4	Ophth4
HCDR	Ophth4	Ophth3	Ophth4	Ophth4	Ophth4
VCDR	Ophth4	Ophth3	Ophth4	Ophth4	Ophth4
Final	Ophth4	Ophth3	Ophth4	**Ophth4**	**Ophth4**

In conclusion, I have developed a large dataset of images including annotations by six ophthalmologists that can be used for testing various image processing algorithms. Then I developed two algorithms for automated disc, cup segmentation and the cup to disc ratios of the automatic segmentations were calculated. The calculated values were then evaluated using the annotations by six ophthalmologists.

6.2.Future work

Developing a smartphone application with a fundus lens attachment that allows taking fundus images and processing them to analyze the ONH structure parameters that help with diagnosis of glaucoma is a priority. Such application will be of great use in the field of optometry especially in developing nations where access to tertiary or specialized centers for glaucoma is difficult. This will enable telemedicine, i.e., if the CDR is indicative of glaucoma the tertiary hospital or specialist will be automatically notified. The smartphone application will also allow the patient to take fundus images at home in order to closely and carefully monitor the progress/remission of the disease.

Developing a graphical user interface (GUI) that allows manual modification of the algorithm (particularly for the cup) should also be considered in the future work. Such feature will allow the ophthalmologist to bring an automatically segmented cup into any position that he/she considers best suited based upon his/her clinical experience.

Validation of the newly developed algorithm is also part of the future work. Fundus images should be taken from patients along with OCT images to correlate OCT images with the fundus annotations.

There is still room for improvement for the disc and cup segmentation algorithm. More functions should be added to solve the disc segmentation errors that occur in some pathological cases such as disc drusen and peripapillary atrophy. Furthermore, different advanced image processing techniques that might address disc segmentation limitations and provide better segmentation results should be applied. On the other hand, RIGA dataset can be improved by annotating more parts such as blood vessels, fovea or some retinal pathologies in order to develop new automated systems to detect and segment the desired part, and thus helping with diagnosis of pathologies.

Therefore, the dataset will be posted online to make it easily accessible to anyone interested in using it without any constraints.

Appendix

```
% This is a program for segmenting the optic disc and cup boundaries from a %fundus image. Written for
%calculating the HCDR and VCDR for diagnosing the glaucoma
% Authors : Ahmed Almazroa, 2016
% email: myh_300@hotmail.com
% Copyright (c) 2014-2016 by Ahmed Almazroa
% U can use an entire fundus image in format of TIFF or JPG
% input - give the image file name as input. eg :- image2prime
clc;
clear all;
close all;
tic
%% Main Input
thLevel =3;% starting with threshold number three
Eye_side = 'R';%can be Left or Right
im_num = 1; %image number


max_pixl_yc = 10; %maximum distance between the disc and cetroid on Yaxis

maxArea = 18000; %maximum cup area
minArea = 2000; %minimum cup area

Extra_side = 0.45;% percentage of extra radius

Radius_up = 0.2;% percentage of extra radius
Radius_down = 0.2;% percentage of extra radius
Radius_right = 0.0;% percentage of extra radius
Radius_left = 0.0;% percentage of extra radius

Level2Set = 1; %if 1 then Level2Set is used to detect the disc (JPG) NONmydriatric retinal camera else (0)
SmoothMuch will be used

% Do not chnage this data
error = 500;
lower_area = 1000;

% Blood Vessel Extraction
L = 45;
Extra_radius = [Radius_up,Radius_down,Radius_right,Radius_left];
Enhanced = 1; %Enable enhance at the beginning
Error = 0; %There is no error

%% CHnage the input images number and name prefix.

   %I=['image',num2str(im_num),'.tif'];
   %I=['image',num2str(im_num),'prime.tif'];
   %I=['image',num2str(im_num),'.jpg'];
   I=['image',num2str(im_num),'prime.jpg'];

   fname = I;
   fprintf('\nWorking on %s\n',I)
   I_temp = ['Localized',fname];
   inImg_temp1 = imread(I);
```

```
    inImg_temp2 = localization(inImg_temp1);
    imwrite(inImg_temp2,I_temp)
    fprintf('\nLocalization is complete and imgae is saved. Now working on threshold and enhancement \n')
    inImg = imread(I_temp);
    [M,N,~] = size(inImg);
    inImg1 = inImg;
    clear inImg_temp1
    clear inImg_temp2


% Start cup extraction with 3 level thresholding to calculate range of area
radiusError = 1;

    while radiusError ==1;
        % Generate 3 level thresholding for estimated cup size
        [~, ThresImg_temp] = Thresholding(inImg,3);
        [M,N,~] = size(inImg);
        Img_temp1 = zeros([M,N]);

        Thres_temp = unique(ThresImg_temp);
        n = length(Thres_temp)+1;
        mean_area = 0;
        while mean_area<lower_area

            n = n-1;
            if n==0;
                mean_area = lower_area;
            else
                Img_temp1(ThresImg_temp>=Thres_temp(n)) = 1;
                mean_area = sum(nonzeros(Img_temp1));
            end
        end

        % Estimate the range of cup size
        max_area = mean_area + error;
        min_area = mean_area - error;

    % Perform main thresholding to detect the cup region
        if Enhanced==1
            [~, thresImg] = Thresholding(inImg,thLevel);

        else
            [~, thresImg] = ThresholdingNE(inImg,thLevel);
        end

        %thresImg = ThresImg_temp;

        Threshold = unique(thresImg);
        Threshold = Threshold';

        % Iterate until the calcualted area falles between the range
        area = 0;
        for i = length(Threshold):-1:1
          area = area +  sum(sum(thresImg==Threshold(i)));

          if area>=min_area
```

```
        if area>max_area
            n = i+1;
        else
            n = i;
        end
        break;
      end
    end

    n = min(n,length(Threshold));

    Img_temp2 = zeros(M,N);
    for i=1:1:M
        for j=1:1:N
            if thresImg(i,j)>= Threshold(n)
                Img_temp2(i,j) = 1;
            end
        end
    end

%% Find tentative circle that covers the cup region

    count = 0;
    r0 = 1;
    try
        while count==0

            [c,rr] = PaintCircle(Img_temp2,r0);
            [count,~] = size(c);

        % Repeat if centre is not found by increasing r0
        if count<=0
            r0=r0+1;
        end
    end
    %% Based on the circle and eye side, find the ellipse that fits the largest number of white pixels
    areaa =[];
    for i=1:1:length(c(:,1))
        % Find the masking filled circle
        [Img_ellipse,~,~,~,~,~] = FillEllipse(c(i,1),c(i,2),rr(i),Extra_radius,M,N,Eye_side,Extra_side);
        ImgCup = Img_ellipse.*Img_temp2;
        areaa = [areaa,nnz(ImgCup)];
    end

    [~,index] = max(areaa);

    cx = round(c(index,1));
    cy = round(c(index,2));
    r = round(rr(index));
    [Img_ellipse,x_ellipse,y_ellipse,a,b,x_set] = FillEllipse(cx,cy,r,Extra_radius,M,N,Eye_side,Extra_side);
    AreaEllipse = nnz(Img_ellipse);

    if AreaEllipse<minArea || AreaEllipse>maxArea
        fprintf('\n Radius out of range. Adjusting threshold and enhancing\n')
        if thLevel == 3 && Enhanced==1
            thLevel = 2;
```

```
            elseif thLevel==2;
                thLevel = 4;
                Enhanced = 0;
            elseif thLevel==4
                thLevel = 3;
                Enhanced = 0;
            else
                Error = 1;
                radiusError =0;
            end
        else
            radiusError =0;
        end

    catch
        fprintf('\n An error occured. Adjusting threshold and enhancing\n')
        if thLevel == 3 && Enhanced==1
            thLevel = 2;
        elseif thLevel==2;
            thLevel = 4;
            Enhanced = 0;
        elseif thLevel==4
            thLevel = 3;
            Enhanced = 0;
        else
            Error = 1;
            radiusError =0;
        end
    end%try


end%radiusError ==1;

if Error ==0
    %% Print Threshold leven and Enhanced

    fprintf('\nThreshold level = %d',thLevel)
    if Enhanced==1
        fprintf('\nEnhancement is enabled')

    else
        fprintf('\nEnhancement is disabled')
    end
    %% Extract the blood vessels
        % Extract blood vessels based on green channel

        if Level2Set ==1
            [filledDisc,edgeDisc,inImg,bloodVessel1,y_disc,x_disc] = discExtractDoubleLevelSet(inImg1);
        else
            [filledDisc,edgeDisc,inImg,bloodVessel1,y_disc,x_disc] = discExtractSmoothMuch(inImg1);
        end

        for i=1:1:M
            for j = 1:1:N

                % paint disc border
```

```
            if edgeDisc(i,j)>=1 %&& i>1 && j>1
                inImg(i,j,:)=[0 255 255];
                inImg(i-1,j,:)=[0 255 255];
                inImg(i,j-1,:)=[0 255 255];
                inImg(i-1,j-1,:)=[0 255 255];
            end
        end
    end

    areaDisc = nnz(filledDisc);
    bloodVessel = bloodVessel1.*filledDisc;
    bloodVessel2 = bloodVessel;

%% Calculate and adjust/set variables
    xc_cup(1) = x_ellipse;

    if abs(y_disc-y_ellipse)>max_pixl_yc
       fprintf('\nY-coordinate is adjusted\n')
       if y_ellipse>y_disc
          y_ellipse = y_disc + 10;
       else
          y_ellipse = y_disc - 10;
       end
    end

    if Eye_side == 'R'
        mul = 1;
        xc_edge = max(x_set);
    else
        mul = -1;
        xc_edge = min(x_set);
    end

%% Find BloodVessel
   [Edges,X,Img_square,max_pixl] = FindBloodVesselPoint2(M,N,bloodVessel,L,cx,cy,Eye_side);

    x_square = cx + mul * round((X-1)*L+L/2);
    bloodVessel1 = bloodVessel.*Img_square;
    border1 = inImg; % This is to show the square box and edge of the ellipse
    edges = edge(Img_ellipse,'sobel');
    for i=1:1:M
        for j = 1:1:N

            % paint ellipse border
            if edges(i,j)>=1
                border1(i,j,:)=[0 0 255];
                border1(i-1,j,:)=[0 0 255];
                border1(i,j-1,:)=[0 0 255];
                border1(i-1,j-1,:)=[0 0 255];
            end
        end
    end

    border1(y_ellipse,xc_cup(1),:) = [255,255,255];
    figure;imshow(border1);title('No adjustment');
%     II = ['EllipseSquare_Cup_NoAdjust', fname];
```

```
%     imwrite(border1,II)


    %Shift to the near edge
    dist_E2NE = round(cx + mul*(X-1)*L)-xc_edge;
    %Shift to the medium edge
    dist_E2M  = round(x_square-xc_edge);
    %Shift to the far edge
    dist_E2FE = round(cx + mul*X*L)-xc_edge;

    Img_ellipseM = MakeFilledEllipse(M,N,x_ellipse,y_ellipse,a,b,dist_E2M ,0);
    Img_ellipseNE = MakeFilledEllipse(M,N,x_ellipse,y_ellipse,a,b,dist_E2NE,0);
    Img_ellipseFE = MakeFilledEllipse(M,N,x_ellipse,y_ellipse,a,b,dist_E2FE,0);

    xc_cup(2:4) = [xc_cup(1) + dist_E2NE, xc_cup(1) + dist_E2M, xc_cup(1) + dist_E2FE];

    overlapped =
[sum(sum(Img_ellipse.*edgeDisc)),sum(sum(Img_ellipseNE.*edgeDisc)),sum(sum(Img_ellipseM.*edgeDisc)),sum
(sum(Img_ellipseFE.*edgeDisc))];

    % below if for the diplay propose
    edgesNE = edge(Img_ellipseNE,'sobel');
    borderNE = inImg;

    for i=1:1:M
       for j = 1:1:N
          if edgesNE(i,j)>=1
             borderNE(i,j,:)=[0 0 255];
             borderNE(i-1,j,:)=[0 0 255];
             borderNE(i,j-1,:)=[0 0 255];
             borderNE(i-1,j-1,:)=[0 0 255];
          end
       end
    end

    borderNE(y_ellipse,xc_cup(2),:) = [255,255,255];
    figure;imshow(borderNE);title('Near-edge Adjustment');

    % below if for the diplay propose
    edgesM = edge(Img_ellipseM,'sobel');
    borderM = inImg;
     for i=1:1:M
       for j = 1:1:N
          if edgesM(i,j)>=1
             borderM(i,j,:)=[0 0 255];
             borderM(i-1,j,:)=[0 0 255];
             borderM(i,j-1,:)=[0 0 255];
             borderM(i-1,j-1,:)=[0 0 255];
          end
       end
    end
    borderM(y_ellipse,xc_cup(3),:) = [255,255,255];
    figure;imshow(borderM);title('Mid-Point Adjustment');


    % below if for the display propose
```

```
edgesFE = edge(Img_ellipseFE,'sobel');
borderFE = inImg;
for i=1:1:M
   for j = 1:1:N
      if edgesFE(i,j)>=1
         borderFE(i,j,:)=[0 0 255];
         borderFE(i-1,j,:)=[0 0 255];
         borderFE(i,j-1,:)=[0 0 255];
         borderFE(i-1,j-1,:)=[0 0 255];
      end
   end
end
borderFE(y_ellipse,xc_cup(4),:) = [255,255,255];
figure;imshow(borderFE);title('Far-edge Adjustment');
%    II = ['EllipseSquare_Cup_FarEdgeAdjust_', fname];
%    imwrite(borderFE,II)

diff_x = abs(x_disc-xc_cup);
cutOff = find(overlapped>0);
diff_x(cutOff) = inf;
[~,ind] = min(diff_x);

% Display Disc statics
areaDisc
x_disc
y_disc

[~,~,~,~,vDist_disc,hDist_disc] = maxminPoints(filledDisc);



II = ['EllipseSquare_Cup_BestAdjust_', fname];

if ind==1
   fprintf('\n No adjustment is needed for x-coordinate\n')
    areaCUP = nnz(Img_ellipse);
    imwrite(border1,II);
    [~,~,~,~,vDist_cup,hDist_cup] = maxminPoints(Img_ellipse);
elseif ind==2
   fprintf('\n Near-edge adjustment is the best for x-coordinate\n')
   areaCUP = nnz(Img_ellipseNE);
   imwrite(borderNE,II);
   [~,~,~,~,vDist_cup,hDist_cup] = maxminPoints(Img_ellipseNE);
elseif ind==3
   fprintf('\n Adjustment to the middle is the best for x-coordinate\n')
   areaCUP = nnz(Img_ellipseM);
   imwrite(borderM,II);
   [~,~,~,~,vDist_cup,hDist_cup] = maxminPoints(Img_ellipseM);
else
   fprintf('\n Far-edge adjustment is the best for x-coordinate\n')
   areaCUP = nnz(Img_ellipseFE);
   imwrite(borderFE,II);
   [~,~,~,~,vDist_cup,hDist_cup] = maxminPoints(Img_ellipseFE);
end
areaCUP
y_cup = y_ellipse
```

```
        x_cup = xc_cup(ind)
        %vDist_cup
        %hDist_cup
        ratioVerticalDistance = vDist_cup/vDist_disc
        ratioHorizontalDistance = hDist_cup/hDist_disc
    else%Error ==0
        fprintf('\n An error occured. This image cannot be processed for cup detection')
    end%Error ==0
toc
h = msgbox({sprintf('Summary for %s',fname) ...
    sprintf('\nDisc:') ...
    sprintf('Area of the disc:\t %d',areaDisc) ...
    sprintf('x-axis of the disc:\t %d',x_disc) ...
    sprintf('y-axis of the disc:\t %d',y_disc) ...
    sprintf('\nCup:') ...
    sprintf('Area of the cup:\t %d',areaCUP) ...
    sprintf('x-axis of the cup:\t %d',x_cup) ...
    sprintf('y-axis of the cup:\t %d',y_cup) ...
    sprintf('\nCup to disc ratio:') ...
    sprintf('Verticle distance:\t %.4f',ratioVerticalDistance) ...
    sprintf('Horizontal distance:\t %.4f',ratioHorizontalDistance)},'Results');
```

Functions

```
function [bw]=better_bloodVesselExtract(gray)

%input parameter:  rgb is a input_imgage;
%output parameter: bw_bloodVessel is a binary image.1 means blood vessel pixel
%Example:
%       rgb=imread('123.tif');
%       [bw_bloodVessel]=bloodVesselExtract(gray_img);
%  I recommendend the green channel of the RGB.

%black top_hat transformation
se= strel('disk',20);
no_blood_vessel = imclose(gray,se);
diff =no_blood_vessel-gray;% diff contains the information of the blood vessel.x
%thresholding segmentation
th=graythresh(diff);
bw=im2bw(diff,th);
%remove the small spot
[L,num] = bwlabel(bw);
for i=1:num
   [x,y]=find(L==i);
   area=size(x);
   if area<10
      bw(x,y)=0;
   end
end
```

```
function [C1,C2]= binaryfit(phi,U,epsilon)
%   [C1,C2]= binaryfit(phi,U,epsilon) computes c1 c2 for optimal binary fitting
%   input:
%       U: input image
%       phi: level set function
%       epsilon: parameter for computing smooth Heaviside and dirac function
%   output:
%       C1: a constant to fit the image U in the region phi>0
%       C2: a constant to fit the image U in the region phi<0
%
%   created on 04/26/2004
%   author: Chunming Li
%   email: li_chunming@hotmail.com
%   Copyright (c) 2004-2006 by Chunming Li

H = Heaviside(phi,epsilon); %compute the Heaveside function values


a= H.*U;
numer_1=sum(a(:));
denom_1=sum(H(:));
C1 = numer_1/denom_1;

b=(1-H).*U;
numer_2=sum(b(:));
c=1-H;
denom_2=sum(c(:));
C2 = numer_2/denom_2;
```

```
function [bdy,bdx]=backward_gradient(f);
% function [bdx,bdy]=backward_gradient(f);
%
%   created on 04/26/2004
%   author: Chunming Li
%   email: li_chunming@hotmail.com
%   Copyright (c) 2004-2006 by Chunming Li
[nr,nc]=size(f);
bdx=zeros(nr,nc);
bdy=zeros(nr,nc);

bdx(2:nr,:)=f(2:nr,:)-f(1:nr-1,:);
bdy(:,2:nc)=f(:,2:nc)-f(:,1:nc-1);
```

```
function B = BoundMirrorEnsure(A)

[m,n] = size(A);

if (m<3 | n<3)
   error('either the number of rows or columns is smaller than 3');
end

yi = 2:m-1;
xi = 2:n-1;
B = A;
B([1 m],[1 n]) = B([3 m-2],[3 n-2]);  % mirror corners
B([1 m],xi) = B([3 m-2],xi);          % mirror left and right boundary
B(yi,[1 n]) = B(yi,[3 n-2]);          % mirror top and bottom boundary
```

```
function B = BoundMirrorExpand(A)

[m,n] = size(A);
yi = 2:m+1;
xi = 2:n+1;
B = zeros(m+2,n+2);
B(yi,xi) = A;
B([1 m+2],[1 n+2]) = B([3 m],[3 n]);  % mirror corners
B([1 m+2],xi) = B([3 m],xi);          % mirror left and right boundary
B(yi,[1 n+2]) = B(yi,[3 n]);          % mirror top and bottom boundary
```

```
function B = BoundMirrorShrink(A)
[m,n] = size(A);
yi = 2:m-1;
xi = 2:n-1;
B = A(yi,xi);
```

```
function onlyDisc = cropDisc(inImg,refMatrix)

[M,N] = size(refMatrix);

if ndims(inImg)>2
    onlyDisc = inImg;
    for i =1:1:M
        for j = 1:1:N

            if refMatrix(i,j)<=0
                onlyDisc(i,j,:) = [0,0,0];
            end
        end
    end
else
   onlyDisc = zeros(M,N);
    for i =1:1:M
        for j = 1:1:N
            if refMatrix(i,j)>0
                onlyDisc(i,j) = inImg(i,j);
            end
        end
    end

end
```

```
function K=curvature(f);
%   K=curvature(f);
% K=div(Df/|Df|)
%  =(fxx*fy^2+fyy*fx^2-2*fx*fy*fxy)/(fx^2+fy^2)^(3/2)
%   created on 04/26/2004
%   author: Chunming Li
%   email: li_chunming@hotmail.com
%   Copyright (c) 2004-2006 by Chunming Li



[f_fx,f_fy]=forward_gradient(f);
[f_bx,f_by]=backward_gradient(f);

mag1=sqrt(f_fx.^2+f_fy.^2+1e-10);
n1x=f_fx./mag1;
n1y=f_fy./mag1;

mag2=sqrt(f_bx.^2+f_fy.^2+1e-10);
n2x=f_bx./mag2;
n2y=f_fy./mag2;

mag3=sqrt(f_fx.^2+f_by.^2+1e-10);
n3x=f_fx./mag3;
n3y=f_by./mag3;

mag4=sqrt(f_bx.^2+f_by.^2+1e-10);
n4x=f_bx./mag4;
n4y=f_by./mag4;

nx=n1x+n2x+n3x+n4x;
ny=n1y+n2y+n3y+n4y;

magn=sqrt(nx.^2+ny.^2);
nx=nx./(magn+1e-10);
ny=ny./(magn+1e-10);

[nxx,nxy]=gradient(nx);
[nyx,nyy]=gradient(ny);

K=nxx+nyy;
```

```
function Delta_h = Delta(phi, epsilon)
%   Delta(phi, epsilon) compute the smooth Dirac function
%
%   created on 04/26/2004
%   author: Chunming Li
%   email: li_chunming@hotmail.com
%   Copyright (c) 2004-2006 by Chunming Li

Delta_h=(epsilon/pi)./(epsilon^2+ phi.^2);
```

```
function [phi,edge_disc2,Img,bloodVessel,xc,yc] = discExtractDoubleLevelSet(inImg)
    U=inImg(:,:,1);
    G=inImg(:,:,2);
    mask=better_bloodVesselExtract(G);
    bloodVessel = mask;
    U(find(U<30))=100;
    hsvImg=rgb2hsv(inImg);
    V=hsvImg(:,:,3);
    V=grayStretch(V);
    V=FastInpaint(V,mask,500);
    U=FastInpaint(U,mask,500);
    G=FastInpaint(G,mask,500);
    % get the size
    [nrow,ncol] =size(U);
    ic=nrow/2;
    jc=ncol/2;
    r=90;
    phi_0 = sdf2circle(nrow,ncol,ic,jc,r);
    delta_t = 0.1;
    lambda_1=1;
    lambda_2=1;
    nu=0;
    h = 1;
    epsilon=8;
    mu = 0.01*255*255;
    I=U;
    % iteration should begin from here
    phi=phi_0;
    numIter = 10;
    for k=1:90,
        phi=evolution_cv(I, phi, mu, nu, lambda_1, lambda_2, delta_t, epsilon, numIter);   % update level set function
    end;
    %%
    phi=im2bw(phi,0);
    phi=bwareaopen(phi,500);
    phi=imcomplement(phi);
    phi=bwareaopen(phi,500);
    edge_disc=edge(phi);
    se=strel('disk',1);
    edge_disc=imclose(edge_disc,se);
    %%
    [m,n]=size(edge_disc);
    cc = bwconncomp(edge_disc);
    numFields = getfield(cc,'NumObjects');
    if(numFields > 1)
    S = regionprops(cc, 'Area');
    P = max([S.Area]);
    L = labelmatrix(cc);
    temp = ismember(L, find([S.Area] >= P));
    for i = 1:m
    for j = 1:n
     if(temp(i,j) == 0)
       edge_disc(i,j) = 0;
     end
      end
    end
```

```
end
%%
[x,y]=find(edge_disc>0);
U2=U(min(x):max(x),min(y):max(y));
%%
[nrow,ncol] =size(U2);
ic=round(nrow/2);
jc=round(ncol/2);
r=90;
phi_0 = sdf2circle(nrow,ncol,ic,jc,r);
%%
edge_disc2=zeros(size(edge_disc));
%left
Uleft=U2(:,1:jc+10);
phi_0left=phi_0(:,1:jc+10);
% I=['C:\Users\weiwei\Desktop\X Y for the localized\Disc\Ibn1\left',num2str(imgNum),'.tif'];
% U3=uint8(Uleft);
% imwrite(U3,I);
I=Uleft;
phi=phi_0left;
for k=1:90,
    phi=evolution_cv(I, phi, mu, nu, lambda_1, lambda_2, delta_t, epsilon, numIter);   % update level set function
end
phi=im2bw(phi,0);
phi=bwareaopen(phi,100);
phi=imcomplement(phi);
phi=bwareaopen(phi,200);
edge_templeft=edge(phi);
edge_disc2(min(x):max(x),min(y):min(y)+jc+9)=edge_templeft;
%%
%right
Uright=U2(:,jc-10:end);
phi_0right=phi_0(:,jc-10:end);
% I=['C:\Users\weiwei\Desktop\X Y for the localized\Disc\Ibn1\right',num2str(imgNum),'.tif'];
% U3=uint8(Uright);
% imwrite(U3,I);
I=Uright;
phi=phi_0right;
for k=1:90,
    phi=evolution_cv(I, phi, mu, nu, lambda_1, lambda_2, delta_t, epsilon, numIter);   % update level set function
end
phi=im2bw(phi,0);
phi=bwareaopen(phi,100);
phi=imcomplement(phi);
phi=bwareaopen(phi,200);
edge_tempright=edge(phi);
edge_disc2(min(x):max(x),min(y)+jc-11:max(y))=edge_tempright;
%%
%%

se=strel('disk',10);
 edge_disc2=imclose(edge_disc2,se);
[m,n]=size(edge_disc2);
cc = bwconncomp(edge_disc2);
numFields = getfield(cc,'NumObjects');
if(numFields > 1)
```

```
S = regionprops(cc, 'Area');
P = max([S.Area]);
L = labelmatrix(cc);
temp = ismember(L, find([S.Area] >= P));
for i = 1:m
for j = 1:n
 if(temp(i,j) == 0)
    edge_disc2(i,j) = 0;
 end
  end
end
end

dif=4;
se=strel('disk',1);
db=0;
recordedx=find(edge_disc2>0);
while(dif>3)
[edge_disc2,dif]=eliminateBlank(edge_disc2);
edge_disc2=imclose(edge_disc2,se);
db=db+1;
if(db==10)
   break;
end
end
recordedx1=find(edge_disc2>0);
edge_disc2=imdilate(edge_disc2,se);
[x3]=find(edge_disc2);
edge_disc2=edgeOptimize(edge_disc2,10);
se=strel('disk',5);
edge_disc2=imclose(edge_disc2,se);
se=strel('disk',2);
edge_disc2=imdilate(edge_disc2,se);
phi=eTp(edge_disc2);
%phi is the final mask of the disc
%figure, imshow(phi)
edge_disc2=edge(phi);
% edge of the final disc image
%figure, imshow(edge_disc2)
[x,y]=find(edge_disc2>0);
xc=round((min(x)+max(x))/2);
yc=round((min(y)+max(y))/2);
num=size(find(phi==1),1);


Img=inImg;
Img1=inImg;
Img2=inImg;
[x]=find(edge_disc>0);
[x2]=find(edge_disc2>0);
r=Img(:,:,1);
g=Img(:,:,2);
b=Img(:,:,3);
% r(x)=0;
% g(x)=255;
% b(x)=0;
```

```
 r(x2)=0;
 g(x2)=0;
 b(x2)=255;
%   r(x3)=0;
%  g(x3)=0;
%  b(x3)=0;
Img(:,:,1)=r;
Img(:,:,2)=g;
Img(:,:,3)=b;
%figure, imshow(Img)
```

```
function [phi,edge_disc,Img,bloodVessel,xc,yc] = discExtractSmoothMuch(inImg)
    U=inImg(:,:,1);
    G=inImg(:,:,2);
    mask=better_bloodVesselExtract(G);
    bloodVessel = mask;
    U(find(U<30))=90;
    hsvImg=rgb2hsv(inImg);
    V=hsvImg(:,:,3);
    V=grayStretch(V);
    V=FastInpaint(V,mask,500);
    U=FastInpaint(U,mask,500);
    G=FastInpaint(G,mask,500);
    % get the size
    [nrow,ncol] =size(U);
    ic=nrow/2;
    jc=ncol/2;
    r=round(nrow/3);
    phi_0 = sdf2circle(nrow,ncol,ic,jc,r);
    delta_t = 5;
    lambda_1=1;
    lambda_2=1;
    nu=0;
    h = 1;
    epsilon=8;
    mu = 0.01*255*255;
    I=U;
    % iteration should begin from here
    phi=phi_0;
    numIter = 10;
    for k=1:70,
        phi=evolution_cv(I, phi, mu, nu, lambda_1, lambda_2, delta_t, epsilon, numIter);   % update level set function
    end;
    %%
    phi=im2bw(phi,0);
    phi=bwareaopen(phi,100);
    phi=imcomplement(phi);
    phi=bwareaopen(phi,200);
    edge_disc=edge(phi);
    area=find(phi==1);
    se= strel('disk',1);
    edge_disc = imdilate(edge_disc,se);
    %%
    [m,n]=size(edge_disc);
    cc = bwconncomp(edge_disc);
    numFields = getfield(cc,'NumObjects');
    if(numFields > 1)
    S = regionprops(cc, 'Area');
    P = max([S.Area]);
    L = labelmatrix(cc);
    temp = ismember(L, find([S.Area] >= P));
    for i = 1:m
    for j = 1:n
     if(temp(i,j) == 0)
       edge_disc(i,j) = 0;
     end
      end
```

```
end
end
%%
dif=4;
se=strel('disk',1);
db=0;
while(dif>3)
[edge_disc,dif]=eliminateBlank(edge_disc);
edge_disc=imclose(edge_disc,se);
db=db+1;
if(db==10)
   break;
end
end
edge_disc=imdilate(edge_disc,se);
edge_disc=edgeOptimize(edge_disc,10);
phi=eTp(edge_disc);
% phi is mask
%figure, imshow(phi)
edge_disc=edge(phi);
% edge of the final disc image
%figure, imshow(edge_disc)

[x,y]=find(edge_disc>0);
xc=round((min(x)+max(x))/2);
yc=round((min(y)+max(y))/2);
num=size(find(phi==1),1);

Img=inImg;
[x]=find(edge_disc>0);
r=Img(:,:,1);
g=Img(:,:,2);
b=Img(:,:,3);
r(x)=0;
g(x)=255;
b(x)=0;
Img(:,:,1)=r;
Img(:,:,2)=g;
Img(:,:,3)=b;
Img(xc-1:xc+1,yc-1:yc+1,1)=0;
Img(xc-1:xc+1,yc-1:yc+1,2)=255;
Img(xc-1:xc+1,yc-1:yc+1,3)=0;

%figure, imshow(Img)
```

```
function [edge_disc]=edgeOptimize(edge_disc,iteration)
[m,n]=size(edge_disc);
[x,y]=find(edge_disc>0);
xc=round((min(x)+max(x))/2);
yc=round((min(y)+max(y))/2);
rad=ones(size(x,1),1);
ang=ones(size(rad));
for l=1:size(x,1)
   delta_x=x(l)-xc;
   delta_y=y(l)-yc;
   rad(l)=sqrt(delta_x*delta_x+delta_y*delta_y);
   cos1=delta_x/rad(l);
   ang(l)=acosd(cos1);
   if(delta_y<0)
      ang(l)=360-ang(l);
   end
end
%%
[sortAng,ind]=sort(ang);
diffang=diff(sortAng);
sortRad=ones(size(sortAng));
for l=1:size(ind,1)
   sortRad(l)=rad(ind(l));
end
sortRad1=sortRad;
for j=1:iteration
[sortRad1]=eliminatePeak1(sortRad1,sortAng);
end
delta_rad=sortRad1-sortRad;
edge_disc(find(edge_disc==1))=0;
delta_x=floor(delta_rad.*cosd(sortAng));
delta_y=floor(delta_rad.*sind(sortAng));
for l=1:size(ind,1)
   x(ind(l))=x(ind(l))+delta_x(l);
end
for l=1:size(ind,1)
   y(ind(l))=y(ind(l))+delta_y(l);
end
  x(find(x<=1))=1;
  y(find(y<=1))=1;
  x(find(x>=m))=m-1;
  y(find(y>=n))=n-1;
for l=1:size(x,1)
   edge_disc(x(l),y(l))=1;
end
end
```

```
function [addedge,dif]=eliminateBlank(edge_disc)
 [x,y]=find(edge_disc>0);
 [m,n]=size(edge_disc);
 xc=round((min(x)+max(x))/2);
 yc=round((min(y)+max(y))/2);
 rad=ones(size(x,1),1);
 ang=ones(size(rad));
 for l=1:size(x,1)
    delta_x=x(l)-xc;
    delta_y=y(l)-yc;
    rad(l)=sqrt(delta_x*delta_x+delta_y*delta_y);
    cos1=delta_x/rad(l);
    ang(l)=acosd(cos1);
    if(delta_y<0)
       ang(l)=360-ang(l);
    end
 end
%%
 [sortAng,ind]=sort(ang);
  sortRad=ones(size(sortAng));
  for l=1:size(ind,1)
    sortRad(l)=rad(ind(l));
  end
  diffAng=abs(diff(sortAng));
  dif1=sortAng(1)+360-sortAng(end);
  mean_diffAng=mean(diffAng);
 [dif,maxInd]=max(diffAng);
if(dif1>dif)
    dif=dif1;
  addNum=floor(dif/mean_diffAng);
  meanDiffRad=(sortRad(1)-sortRad(end))/addNum;
  addAng=zeros(size(ind,1)+addNum,1);
  addRad=zeros(size(addAng));
  addAng(1:size(ind,1),1)=ang;
  addRad(1:size(ind,1),1)=rad;
  or=size(ind,1);
  for count=1:addNum
      tem=(sortAng(end)+mean_diffAng*count);
      if(tem>360)
         tem=tem-360;
      end
      addAng(or+count,1)=tem;
      addRad(or+count,1)=sortRad(end)+meanDiffRad*count;
  end
  addx=zeros(size(ind,1)+addNum,1);
  addy=zeros(size(ind,1)+addNum,1);
  addx(1:size(ind,1),1)=x;
  addy(1:size(ind,1),1)=y;
   for l=or+1:size(addAng,1)
    delta_x=round(addRad(l)*cosd(addAng(l)));
    delta_y=round(addRad(l)*sind(addAng(l)));
    addx(l)=xc+delta_x;
    addy(l)=yc+delta_y;
   end
   addx(find(addx<=1))=1;
   addy(find(addy<=1))=1;
```

```
   addx(find(addx>=m))=m-1;
   addy(find(addy>=n))=n-1;
   addedge=zeros(size(edge_disc));
   for k=1:size(addx,1)
      addedge(addx(k),addy(k))=1;
   end
   %%
else
 if(~isnan(mean_diffAng))
  addNum=floor((sortAng(maxInd+1)-sortAng(maxInd))/mean_diffAng);
  meanDiffRad=(sortRad(maxInd+1)-sortRad(maxInd))/addNum;
  addAng=zeros(size(ind,1)+addNum,1);
  addRad=zeros(size(addAng));
  addAng(1:size(ind,1),1)=ang;
  addRad(1:size(ind,1),1)=rad;
  or=size(ind,1);
  for count=1:addNum
     addAng(or+count,1)=sortAng(maxInd)+mean_diffAng*count;
     addRad(or+count,1)=sortRad(maxInd)+meanDiffRad*count;
  end
  addx=zeros(size(ind,1)+addNum,1);
  addy=zeros(size(ind,1)+addNum,1);
  addx(1:size(ind,1),1)=x;
  addy(1:size(ind,1),1)=y;
   for l=or+1:size(addAng,1)
    delta_x=round(addRad(l)*cosd(addAng(l)));
    delta_y=round(addRad(l)*sind(addAng(l)));
    addx(l)=xc+delta_x;
    addy(l)=yc+delta_y;
   end
   addx(find(addx<=1))=1;
   addy(find(addy<=1))=1;
   addx(find(addx>=m))=m-1;
   addy(find(addy>=n))=n-1;
   addedge=zeros(size(edge_disc));
   for k=1:size(addx,1)
      addedge(addx(k),addy(k))=1;
   end

 else
    addedge=edge_disc;
 end
end
end
```

```
function [y]=eliminatePeak1(y,x)
 numP=zeros(180,1);
 difmean=zeros(180,1);
 sumDif=zeros(180,1);
 count=0;
 for ang=2:2:360
    count=count+1;
   [numP(count,1),difmean(count,1),sumDif(count,1)]=numBy(ang-2,ang,x,y);
 end
%  figure,plot(1:180,numP);
 [maxNum,inMax]=max(difmean);
 for i=15:-1:1
    ran=-i:1:i;
    ran=ran+inMax;
    tem=find(ran<1);
    ran(tem)=ran(tem)+count;
    tem=find(ran>180);
    ran(tem)=ran(tem)-count;
    numRan=2*i+1;
    meanNum=sum(numP(ran))/numRan;
    meandif=sum(difmean(ran))/numRan;
    if(meanNum>4&meandif>0.7)
       ind1=ran(1)*2;
       [~,ind1]=min(abs(x-ind1));
       ind2=ran(2*i+1)*2;
       [~,ind2]=min(abs(x-ind2));
       rad1=y(ind1);
       rad2=y(ind2);
       increase=(rad2-rad1)/(numRan-1);
       for j=2:size(ran,2)
          if ran(j)==1
             changeInd=find(x>=(ran(j)*2-2)&x<=(ran(j)*2));
          else
             changeInd=find(x>(ran(j)*2-2)&x<=(ran(j)*2));
          end

          y(changeInd)=increase*(j-1)+rad1;
       end
       break;
    end

 end
end
function [numP,difMean,sumDif]=numBy(ang1,ang2,x,y)
  n=size(x,1);
  dif=diff(y);
  dif=abs(dif);
  if ang1==0
     ind=find(x>=ang1&x<=ang2);
  else
     ind=find(x>ang1&x<=ang2);
  end

  numP=size(ind,1);
  sumDif=0;
  for k=1:size(ind,1)
```

```
    in=ind(k);
    if in==k
       sumDif=sumDif+abs(y(end)-y(1));
    else
       sumDif=sumDif+dif(in-1);
    end
  end
  difMean=sumDif/numP;
end
```

```
function [phi]=eTp(edge_disc)
 phi=zeros(size(edge_disc));
 [x,y]=find(edge_disc>0);
 for i=min(x):1:max(x)
    indx=find(x==i);
    y1=min(y(indx));
    y2=max(y(indx));
    for j=y1:1:y2
       phi(i,j)=1;
    end
 end
 se=strel('disk',2);
 phi=imclose(phi,se);
end
```

```
function u = EVOLUTION(u0, g, lambda, mu, alf, epsilon, delt, numIter)
%  EVOLUTION(u0, g, lambda, mu, alf, epsilon, delt, numIter) updates the level set function
%  according to the level set evolution equation in Chunming Li et al's paper:
%      "Level Set Evolution Without Reinitialization: A New Variational Formulation"
%       in Proceedings CVPR'2005,
%  Usage:
%   u0: level set function to be updated
%   g: edge indicator function
%   lambda: coefficient of the weighted length term L(\phi)
%   mu: coefficient of the internal (penalizing) energy term P(\phi)
%   alf: coefficient of the weighted area term A(\phi), choose smaller alf
%   epsilon: the papramater in the definition of smooth Dirac function, default value 1.5
%   delt: time step of iteration, see the paper for the selection of time step and mu
%   numIter: number of iterations.
%
% Author: Chunming Li, all rights reserved.
% e-mail: li_chunming@hotmail.com
% http://vuiis.vanderbilt.edu/~licm/

u=u0;
[vx,vy]=gradient(g);

for k=1:numIter
   u=NeumannBoundCond(u);
   [ux,uy]=gradient(u);
   normDu=sqrt(ux.^2 + uy.^2 + 1e-10);
   Nx=ux./normDu;
   Ny=uy./normDu;
   diracU=Dirac(u,epsilon);
   K=curvature_central(Nx,Ny);
   weightedLengthTerm=lambda*diracU.*(vx.*Nx + vy.*Ny + g.*K);
   penalizingTerm=mu*(4*del2(u)-K);
   weightedAreaTerm=alf.*diracU.*g;
   u=u+delt*(weightedLengthTerm + weightedAreaTerm + penalizingTerm);  % update the level set function
end

% the following functions are called by the main function EVOLUTION
function f = Dirac(x, sigma)
f=(1/2/sigma)*(1+cos(pi*x/sigma));
b = (x<=sigma) & (x>=-sigma);
f = f.*b;

function K = curvature_central(nx,ny);
[nxx,junk]=gradient(nx);
[junk,nyy]=gradient(ny);
K=nxx+nyy;

function g = NeumannBoundCond(f)
% Make a function satisfy Neumann boundary condition
[nrow,ncol] = size(f);
g = f;
g([1 nrow],[1 ncol]) = g([3 nrow-2],[3 ncol-2]);
g([1 nrow],2:end-1) = g([3 nrow-2],2:end-1);
g(2:end-1,[1 ncol]) = g(2:end-1,[3 ncol-2]);
```

```
function phi = EVOLUTION_CV(I, phi0, mu, nu, lambda_1, lambda_2, delta_t, epsilon, numIter);
%   evolution_withoutedge(I, phi0, mu, nu, lambda_1, lambda_2, delta_t, delta_h, epsilon, numIter);
%   input:
%       I: input image
%       phi0: level set function to be updated
%       mu: weight for length term
%       nu: weight for area term, default value 0
%       lambda_1:  weight for c1 fitting term
%       lambda_2:  weight for c2 fitting term
%       delta_t: time step
%       epsilon: parameter for computing smooth Heaviside and dirac function
%       numIter: number of iterations
%   output:
%       phi: updated level set function
%
%   created on 04/26/2004
%   author: Chunming Li
%   email: li_chunming@hotmail.com
%   Copyright (c) 2004-2006 by Chunming Li


I=BoundMirrorExpand(I);
phi=BoundMirrorExpand(phi0);

for k=1:numIter
    phi=BoundMirrorEnsure(phi);
    delta_h=Delta(phi,epsilon);
    Curv = curvature(phi);
    [C1,C2]=binaryfit(phi,I,epsilon);
    % updating the phi function
    phi=phi+delta_t*delta_h.*(mu*Curv-nu-lambda_1*(I-C1).^2+lambda_2*(I-C2).^2);
end
phi=BoundMirrorShrink(phi);
```

```
function [filledDisc,edge_disc,edge_disc1,bloodVessel,xc,yc] = extractDisc(inImg,pixl)
      % example that CV model works well
   G=inImg(:,:,2);
   G(find(G<30))=60;
   mask=better_bloodVesselExtract(G);
   bloodVessel = mask;
   U=inImg(:,:,1);
   U(find(U<30))=90;
   U=FastInpaint(U,mask,500);
   se=strel('disk',10);
   % U=imopen(U,se);
   %I=['inpaintV',num2str(imgNum),'.tif'];
   th=graythresh(U);
   bw_th=im2bw(U,th);
   edge_bw=edge(bw_th);
   U=grayStretch(U);
   %imwrite(U,I);
   % get the size
   [nrow,ncol] =size(U);
   ic=nrow/2;
   jc=ncol/2;
   r=100;
   phi_0 = sdf2circle(nrow,ncol,ic,jc,r);

   delta_t = 0.1;
   lambda_1=1;
   lambda_2=1;
   nu=0;
   h = 1;
   epsilon=8;
   mu = 0.01*255*255;
   I=U;
   % iteration should begin from here
   phi=phi_0;
   numIter = 10;
   for k=1:70,
      phi=evolution_cv(I, phi, mu, nu, lambda_1, lambda_2, delta_t, epsilon, numIter);   % update level set function
   end
   %%
   phi=im2bw(phi,0);
   phi=bwareaopen(phi,100);
   phi=imcomplement(phi);
   phi=bwareaopen(phi,200);
   edge_disc=edge(phi);
   area=find(phi==1);
   se= strel('disk',1);
   edge_disc = imdilate(edge_disc,se);
   %%
   [m,n]=size(edge_disc);
   cc = bwconncomp(edge_disc);
   numFields = getfield(cc,'NumObjects');
   if(numFields > 1)
      S = regionprops(cc, 'Area');
      P = max([S.Area]);
      L = labelmatrix(cc);
      temp = ismember(L, find([S.Area] >= P));
```

```
        for i = 1:m
            for j = 1:n
                if(temp(i,j) == 0)
                  edge_disc(i,j) = 0;
                end
            end
        end
    end
    %%
    [edge_disc,edge_disc1]=edgeOptimize(edge_disc,pixl);


    [edge_disc1,~]=edgeOptimize(edge_disc1,0);
    [x,y]=find(edge_disc>0);
    xc=round(mean(x));
    yc=round(mean(y));

    filledDisc = FillDisc(edge_disc1);
end
```

```
function k=FastInpaint(I,mask,liter)%(I,mask,liter,bar)
%Image inpainting by Manuel M. Oliveira's method Fast Digital Image
%Inpainting
% 09-10-2007

%parameters:
%     I------image to be inpainted
%  mask------the noise mask which is a binary image
% liter------literation times
%   bar_____diffusion barrier
%timer start
I=im2double(I);
     if islogical(mask)
       mask=mask;
    else
        mask=im2bw(mask);
    end
diffker=[0.073235 0.176765 0.0732325; 0.17675 0 0.17675; 0.073235 0.176775 0.073235];
%There are two kinds of diffusion kernels in Olivera's article I use the
%first one[0.073235 0.176765 0.0732325; 0.17675 0 0.17675; 0.073235 0.176775 0.073235].
%Another is [0.125 0.125 0.125; 0.125 0 0.125; 0.125 0.125 0.125].
[r,c]=find(mask);
if (size(I, 3) == 3)  %Color image process
    r=FInpaintGray(I(:,:,1),mask,liter,diffker);
    g=FInpaintGray(I(:,:,2),mask,liter,diffker);
    b=FInpaintGray(I(:,:,3),mask,liter,diffker);
    k=cat(3,r,g,b);
else                %Gray image process
    k=FInpaintGray(I,mask,liter,diffker);
end
k=uint8(k.*255);
%show the elapsed time.
%-------------------------------------------------------------------------%
function g=FInpaintGray(I,mask,liter,diffker)
[r,c]=find(mask);
f=incrSize(I);
for n=1:liter
   for i=1:length(r)
        x=r(i)+1;%+1
        y=c(i)+1;%+1
        f(x,y)=f(x-1,y-1)*0.073235 + f(x-1,y)*0.176765 + f(x-1,y+1)*0.073235 + f(x,y-1)*0.176765
+f(x,y+1)*0.176765 + f(x+1,y-1)*0.073235 + f(x+1,y)*0.176765 + f(x+1,y+1)*0.073235;
        %f(x,y)=f(x-1,y-1)*diffker(1,1)+f(x-1,y)*diffker(1,2)+f(x-1,y+1)*diffker(1,3)+f(x,y-
1)*diffker(2,1)+f(x,y+1)*diffker(2,3)+f(x+1,y-1)*diffker(3,1)+f(x+1,y)*diffker(3,2)+f(x+1,y+1)*diffker(3,3);
    end
end
g=mat2gray(f(2:end-1,2:end-1));
%-------------------------------------------------------------------------%
function u=incrSize(f)
A=im2double(zeros(size(f,1)+2,size(f,2)+2));
A(2:end-1,2:end-1)=f;
A(1:1,2:end-1)=f(1:1,1:end);
A(2:end-1,1:1)=f(1:end,1:1);
A(2:end-1,end:end)=f(1:end,end:end);
A(end:end,2:end-1)=f(end:end,1:end);
u=A;
```

```
function [Img_ellipse,h,k,a,b,x_set] = FillEllipse(cx,cy,r,C,M,N,Eye_side,e)

%C = correction on up, down, right and left
%e = correction on the side where there is the blood vessels

Img_ellipse = zeros(M,N);

p_up = max(0,round(cy-r-C(1)*r));
p_down  = min(M,round(cy+r+C(2)*r));

p_left = max(0,round(cx-r-C(4)*r));
p_right = min(N,round(cx+r+C(3)*r));



if Eye_side=='R'
   p_right = min(N,p_right+round(r*e));
else
   p_left = max(0,round(p_left-e*r));
end



a = round(abs(p_right - p_left)/2);
b = round(abs(p_down - p_up)/2);

h = round(p_left + (p_right - p_left)/2);

k = round(p_up + (p_down - p_up)/2);

x_set = h-a:1:h+a;

[x,y]=meshgrid(-(h-1):(N-h),-(k-1):(M-k));

Img_ellipse =((x.^2/a^2+y.^2/b^2)<=1);

%figure(),imshow(Img_ellipse);
```

```
function [Edges,I,opt_square,max_pixl] = FindBloodVesselPoint2(M,N,BloodVessel,L,cx,cy,Eye_side)

Edges = zeros(M,N);
[x,y]=meshgrid(1:N,1:M);

uperHalfL = round(L/2);
downHalfL = L - uperHalfL;
flag = 0;
x1 = cx;
y1 = max(0,cy-uperHalfL);
y2 = y1+L;

if Eye_side == 'R'
   a = 1;
else
   a = -1;
end
max_pixl = zeros(1,0);
while(flag==0)
      Img_square = zeros(M,N);

      x2 = x1+a*L;
      if x2>N || x2<0
         flag = 1;
      else
         xx1 = min(x1,x2);
         xx2 = max(x1,x2);

         for i=1:1:M
            for j=1:1:N
               if x(i,j)>=xx1 && x(i,j)<=xx2 && y(i,j)>=y1 && y(i,j)<=y2
                  %Img_square(j,i) = 1;
                  Img_square(i,j) = 1;
               end
            end
         end
         Edges = Edges + edge(Img_square,'sobel');
         point = BloodVessel.*Img_square;
         max_pixl = [max_pixl,nnz(point)];
         x1 = x2;
      end
end

[~,I] = max(max_pixl);


opt_square = zeros(M,N);

x1 = cx+a*L*(I-1);
x2 = x1+a*L;

xx1 = min(x1,x2);
xx2 = max(x1,x2);
for i=1:1:M
   for j=1:1:N
      if x(i,j)>=xx1 && x(i,j)<=xx2 && y(i,j)>=y1 && y(i,j)<=y2
```

```
            opt_square(i,j) = 1;
        end
    end
end
```

```
function [fdy,fdx]=forward_gradient(f);
% function [fdx,fdy]=forward_gradient(f);
%
%   created on 04/26/2004
%   author: Chunming Li
%   email: li_chunming@hotmail.com
%   Copyright (c) 2004-2006 by Chunming Li
[nr,nc]=size(f);
fdx=zeros(nr,nc);
fdy=zeros(nr,nc);

a=f(2:nr,:)-f(1:nr-1,:);
fdx(1:nr-1,:)=a;
b=f(:,2:nc)-f(:,1:nc-1);
fdy(:,1:nc-1)=b;
```

```
%this function computes the phi required initially  */
function [xcontour, ycontour] = get_phi(I, nrow, ncol,margin)
% I is the image matrix
% nrow is the no of rows
% ncol is the no of columns


count=1;
x=margin;
for y=margin:nrow-margin+1,
   xcontour(count) = x;
   ycontour(count) = y;
   count=count+1;
end;
y=nrow-margin+1;
for x=margin+1:ncol-margin+1,
   xcontour(count) = x;
   ycontour(count) = y;
   count=count+1;
end;

x=ncol-margin+1;
for y=nrow-margin:-1:margin,
   xcontour(count) = x;
   ycontour(count) = y;
   count=count+1;
end;

y=margin;
for x=ncol-margin:-1:margin+1,
   xcontour(count) = x;
   ycontour(count) = y;
   count=count+1;
end;
```

```
function[B]= grayStretch(Ac)
M=max(max(Ac));
m=min(min(Ac));
B=double(Ac-m);
B=B/double(M-m)*double(255-0);
B=uint8(B);
end
```

```
function H = Heaviside(phi,epsilon)
%   Heaviside(phi,epsilon)  compute the smooth Heaviside function
%
%   created on 04/26/2004
%   author: Chunming Li
%   email: li_chunming@hotmail.com
%   Copyright (c) 2004-2006 by Chunming Li
H = 0.5*(1+ (2/pi)*atan(phi./epsilon));
```

```
function Xcol_seg = localization(I)
   trim_pxl = 100;
   inputpixel=175;
   I_red=I(:,:,1);
   if length(size(I))==3
     I_bw = rgb2gray(I);
   end
   [M, N, O] =size(I);
%    global p;
%    global L;
%    global Th;
%    global alpha;
%
%    global max_val;
%    global min_val;

   L = 256;
   H=imhist(I_bw);
   %figure,imhist(I)
   p = H / (M * N);

   %figure(2); plot(h)

   max_val=double(max(max(I_red)));
   min_val=double(min(min(I_red))+1);

   %************************************************************************
   % 1. Define problem hyperspace and plot in 2D
   %************************************************************************
   Th =2;
   % No of thresholds
   D = Th*2;   %   no of dimensions
   range_min = min_val*ones(1,D);
   range_max = max_val*ones(1,D);% minimum & maximum range;
   alpha=1.5;
   %************************************************************************
   % 2. initialize the population
   %************************************************************************
   NP = 10*D ;            %   population size
   maxgen =100;           %   no of generations
   F = 0.5;
   CR = 0.9;

   max_runs = 2;

   globalbest1 = [];

   statistics_f = [];
   statistics_x = [];
%    tstart = tic;
   for runn = 1:max_runs
      x=[];
      for i = 1 : NP
         for j = 1:D
            x(i, j) =  round(range_min(j) + ((range_max(j)-range_min(j))*(rand)));
         end
```

```
        x(i,:)=sort(x(i,:));

        fitness_parent(i,1) = ultrafuzziness([0 0 x(i,:) 255 255],p,alpha);
    end

    v = zeros(size(x));
    u = zeros(size(x));

    %**************************************************************************
    % 4. start iteration
    %**************************************************************************
%     tStart = tic;

    for gen = 2:maxgen
%       [o-2]
        %**************************************************************************
        % 3. find mutation population
        %**************************************************************************
        for i = 1:NP
            r = ceil(rand(1,3)*NP);
            while r(1)==r(2) || r(2)== r(3) || min(r)==0 || max(r)>NP
                r = ceil(rand(1,3)*NP);
            end

            v(i,:) = x(r(1),:) + F*(x(r(2),:) - x(r(3),:));

            for j = 1:D
                if rand > CR
                    u(i,j) = x(i,j);
                else
                    u(i,j) = v(i,j);
                end
            end
            u(i,:)= round(u(i,:));
            u(i,:)=sort(u(i,:));
        end

        for i = 1:NP
            for jj = 1:D
                u(i,jj) = max(u(i,jj), range_min(jj));
                u(i,jj) = min(u(i,jj), range_max(jj));
            end
            u(i,:)=sort(u(i,:));
            fitness_child(i,1) = ultrafuzziness([0 0  u(i,:) 255 255],p,alpha);
        end

        for i = 1:NP
            if fitness_parent(i) < fitness_child(i)
                fitness_parent(i) = fitness_child(i);
                x(i,:) = u(i,:);
            end
        end

        [globalbest,globalbest_index] = max(fitness_parent);
        global_xbest = sort(x(globalbest_index,:));
```

```
%       clc
%       runn
%       fprintf('Optimisation through Differential Evolution\n')
%       fprintf('Generation: %0.5g\nGlobalbest: %2.7g\n', gen, globalbest)
%       fprintf('Best particle position : %0.11g\n', global_xbest)

        globalbest1 = [globalbest1, globalbest];


    end

%    tElapsed = toc(tStart);
%    tElapsed

    globalbest1 = [globalbest1, globalbest];

    statistics_f = [statistics_f, globalbest];
    statistics_x = [statistics_x; (global_xbest)];

end

%plot(1:NP:NP*50,globalbest1(1:50),'-bs','MarkerFaceColor','b');
%hold on

f_mean = mean(statistics_f);
f_stddev = std(statistics_f);

best_fitness = max(statistics_f);
worst_fitness = min(statistics_f);

x_median = median(statistics_x);

%% select the threshold points
% T = [min_val round(x_median) max_val];
% Thres=T(2:2:2*Th)

t1=x_median(1:2:D);
t2=x_median(2:2:D);
Thres=round((t1+t2)/2);
X=grayslice(I_bw,[Thres]);
X1=uint8(255*mat2gray(X));
%    timestop=toc(tstart);
%    tstop1(im_num)=timestop/2;
%figure,imshow(X1);

%% Trimp the image first
XX1 = trimp(X1,trim_pxl);
%XX1 = X1;
%% New Code cup is the largest spot
X3 = XX1==255;

% Find all the connected components
CC = bwconncomp(X3);

% Number of pixels in each connected components
numPixels = cellfun(@numel,CC.PixelIdxList);
```

```
    % Largest connected compnent
    [biggest,idx] = max(numPixels);

    %     if(aaaa)
    %         %% Additional code to remove Fringe
    %         numPixels_temp = sort(numPixels,'descend');
    %         idx = find(numPixels==numPixels_temp(2));
    %     end

    %Calculating the cetroid of the largest component
    S = regionprops(CC,'Centroid'); % Calculate centroids for connected components in the image using regionprops.
    cntr = cat(1, S.Centroid); %Concatenate structure array containing centroids into a single matrix.
    centroid_x=round(cntr(idx,1));
    centroid_y=round(cntr(idx,2));


    %figure, imshow(I)
    % hold on
    % plot(centroid_x,centroid_y, 'b*')
    % hold off

    % Calculating region
    newx_up=centroid_y-inputpixel;
    newx_down=min(M,centroid_y+inputpixel);
    newy_left=centroid_x-inputpixel;
    newy_right=min(N,centroid_x+inputpixel);
%     tstop2(im_num)=toc(tstart);


    %% Extract image
    for i = newx_up :newx_down
        for j = newy_left : newy_right
            Xcol_seg(i - newx_up + 1, j - newy_left + 1,:)=I(i,j,:);
        end
    end

%     clear p;
%     clear L;
%     clear Th;
%     clear alpha;
%
%     clear max_val;
%     clear min_val;
```

```
function [Img_ellipse] = MakeFilledEllipse2(M,N,h,k,a,b,ch,ck)

Img_ellipse = zeros(M,N);

h = h+ch;

k = k+ck;

[x,y]=meshgrid(-(h-1):(N-h),-(k-1):(M-k));

Img_ellipse =((x.^2/a^2+y.^2/b^2)<=1);
```

```
function  T  =   maxFilter(inImg , w)


%%%%%%%%%%%%%%%%%%%%%%%%%%%%%%%%%%%%%%%%%%%%%%%%%%%%%%%%%%%%
%%%%%%%
%
%  Computes the maximum 'local' dynamic range
%
%  inImg       : grayscale image
%  [-w, w]^2   : search window (w must be odd)
%  T           : maximum local dynamic range
%
%  Author: Kunal N. Chaudhury
%  Date:   March 1, 2012
%
% Reference:
%
% K.N. Chaudhury, "Acceleration of the shiftable O(1) algorithm for
% bilateral filtering and non-local means," arXiv:1203.5128v1.
%
%%%%%%%%%%%%%%%%%%%%%%%%%%%%%%%%%%%%%%%%%%%%%%%%%%%%%%%%%%%%
%%%%%%%

T = -1;

sym    = (w - 1)/2;

[m, n] = size(inImg);

pad1 =  w*ceil(m/w) - m;
pad2 =  w*ceil(n/w) - n;

inImg = padarray(inImg, [pad1 pad2], 'symmetric', 'post');

template = inImg;

m = m + pad1;
n = n + pad2;

% scan along row
for ii = 1 : m
    L     = zeros(n, 1);
    R     = zeros(n, 1);
    L(1)  = template(ii, 1);
    R(n)  = template(ii, n);

    for k = 2 : n
        if  mod(k - 1, w) == 0
            L(k)          = template(ii ,  k);
            R(n - k + 1)  = template(ii ,  n - k + 1);
        else
            L(k)          = max( L(k-1) , template(ii, k) );
            R(n - k + 1)  = max( R(n - k + 2), template(ii, n - k + 1) );
        end
    end
```

```
    for k = 1 : n
     p = k - sym;
     q = k + sym;
     if p < 1
        r = -1;
     else
        r = R(p);
     end
     if q > n
        l = -1;
     else
        l = L(q);
     end
       template(ii, k) = max(r,l);
    end

end

% scan along column
for jj = 1 : n

    L    = zeros(m, 1);
    R    = zeros(m, 1);
    L(1) = template(1, jj);
    R(m) = template(m, jj);

    for k = 2 : m
       if  mod(k - 1, w) == 0
          L(k)         = template(k, jj);
          R(m - k + 1)  = template(m - k + 1, jj);
       else
          L(k)         = max( L(k - 1), template(k, jj) );
          R(m - k + 1)  = max( R(m - k + 2), template(m - k + 1, jj));
       end
    end

    for k = 1 : m
     p = k - sym;
     q = k + sym;
     if p < 1
        r = -1;
     else
        r = R(p);
     end
     if q > m
        l = -1;
     else
        l = L(q);
     end
       temp = max(r,l) - inImg(k, jj);
       if temp > T
          T = temp;
       end
    end

end
```

```
function [xMin,yMin,xMax,yMax,vDistance,hDistance] = maxminPoints(inImg)

%figure, imshow(inImg)
[y,x] = find(inImg>=1);
xMax = max(x);
xMin = min(x);
yMax = max(y);
yMin = min(y);

vDistance = yMax - yMin;

hDistance = xMax - xMin;

inImg(yMax,:)=1;
inImg(yMin,:)=1;
inImg(:,xMax) = 1;
inImg(:,xMin) = 1;

%figure,imshow(inImg)
```

```
function [centers, radii] = PaintCircle(in,e)
[M,N] = size(in);

% edges = edge(in,'sobel');
% spot_size = 25;
% edges = bwareaopen(edges,spot_size);%figure;imshow(x)

spot_size = 50;
in = bwareaopen(in,spot_size);%figure;imshow(x)
se = strel('disk',10);
in = imclose(in,se);
edges = edge(in,'sobel');

in = [];
in = edges;
M1 = 0;
M2 = 0;
for i=1:1:M
   for j = 1:1:N
      if in(i,j)>0
         M1 = i;
         j = N;
         i = M;
      end
   end
end

for i=M:-1:1
   for j = 1:1:N
      if in(i,j)>0
         M2 = i;
         j = N;
         i = M;
      end
   end
end

if M1*M2>0
   r = round(abs(M1-M2)/2);
else
   r = 60;
end

edges = edge(in,'sobel');
[centers, radii, ~] = imfindcircles(edges,[r-e,r+e],'Sensitivity',0.9775,'Method','twostage');
%hold on
%figure, imshow(edges);
%hold off
%h = viscircles(centers,radii);
% hold on
%h = viscircles([centers(1,1),centers(1,2)],radii(1));
% hold off
% hold on
% h = viscircles([centers(2,1),centers(2,2)],radii(2));
% hold off
function [gray]=PCA_rgb2gray(rgb)
```

```
[row,col,dim]=size(rgb);
   A=zeros(dim,row*col);
   count=1;
   for i=1:row
      for j=1:col
         A(:,count)=rgb(i,j,:);
         count=count+1;
      end
   end
   [x,~,la]=pca(A');
   eV=[x(:,3),x(:,2),x(:,1)];
   %PC1
   P_e=eV(:,3);
   AI=P_e'*A;
   count=1;
   for i=1:row
      for j=1:col
         I(i,j)=AI(:,count);
         count=count+1;
      end
   end
Ac=I;
M=max(max(Ac));
m=min(min(Ac));
B=double(Ac-m);
B=B/double(M-m)*double(255-0);
B=uint8(B);
gray=B;
end
```

```
function [c,h]=plotLevelSet(u,zLevel, style)
%   plotLevelSet(u,zLevel, style) plot the level contour of function u at
%   the zLevel.
%   created on 04/26/2004
%   author: Chunming Li
%   email: li_chunming@hotmail.com
%   Copyright (c) 2004-2006 by Chunming Li
% hold on;
[c,h] = contour(u,[zLevel zLevel],style);
% hold off;
```

```
function f = sdf2circle(nrow,ncol, ic,jc,r)
%   sdf2circle(nrow,ncol, ic,jc,r) computes the signed distance to a circle
%   input:
%       nrow: number of rows
%       ncol: number of columns
%       (ic,jc): center of the circle
%       r: radius of the circle
%   output:
%       f: signed distance to the circle
%
%   created on 04/26/2004
%   author: Chunming Li
%   email: li_chunming@hotmail.com
%   Copyright (c) 2004-2006 by Chunming Li


[X,Y] = meshgrid(1:ncol, 1:nrow);

f = sqrt((X-jc).^2+(Y-ic).^2)-r;
% figure;
% imagesc(f)
end
```

```
function u = signed_distance(I,xcontour, ycontour,margin)
% I is the image matrix
% nrow is the no of rows
% ncol is the no of columns

[nrow, ncol] = size(I);
[temp, contsize] = size(xcontour);

Mark = zeros(nrow, ncol);

for y=1:nrow,
   for x=1:ncol
      if  (x > ncol-margin+1) | (x < margin) | (y < margin) | (y > nrow-margin+1)
         Mark(y,x) = -1;
      end;
   end;
end;

for y = 1:nrow,
   for x =1: ncol,
      u(y,x) = sqrt(min((x-xcontour).^2+(y-ycontour).^2));
      if Mark(y,x) == -1
         u(y,x) = -u(y,x);
      end;
   end;
end;
```

```
function [Thres,X1] = Thresholding(I1,Th)

%figure, imshow(I1)
I=I1(:,:,1:3);
I_red=I(:,:,1);
%%%%%%%
A=I_red;
M=max(max(A));
m=min(min(A));
B=double(A-m);
B=B/double(M-m)*double(255-0);
B=uint8(B);
I_red=B;
%%%%%%%%%%%
if length(size(I))==3
  I_bw = rgb2gray(I);
end
[M, N, O] =size(I);

L = 256;
%H=imhist(I_bw);
H=imhist(I(:,:,2));
%figure,imhist(I)
p = H / (M * N);

%figure(2); plot(h)

max_val=double(max(max(I_red)));
min_val=double(min(min(I_red))+1);

%************************************************************************
% 1. Define problem hyperspace and plot in 2D
%************************************************************************
%Th =7;
% No of thresholds
D = Th*2;   %   no of dimensions
range_min = min_val*ones(1,D);
range_max = max_val*ones(1,D);% minimum & maximum range;
alpha=1.5;
%************************************************************************
% 2. initialize the population
%************************************************************************
NP = 10*D ;            %   population size
maxgen =100;           %   no of generations
F = 0.5;
CR = 0.9;

max_runs = 2;

globalbest1 = [];

statistics_f = [];
statistics_x = [];
tstart = tic;
for runn = 1:max_runs
    x=[];
```

```
    for i = 1 : NP
        for j = 1:D
            x(i, j) =  round(range_min(j) + ((range_max(j)-range_min(j))*(rand)));
        end
        x(i,:)=sort(x(i,:));

        fitness_parent(i,1) = ultrafuzziness([0 0 x(i,:) 255 255],p,alpha);
    end

    v = zeros(size(x));
    u = zeros(size(x));

    %*************************************************************************
    % 4. start iteration
    %*************************************************************************
    tStart = tic;

    for gen = 2:maxgen
%       [o-2]
        %*************************************************************************
        % 3. find mutation population
        %*************************************************************************
        for i = 1:NP
            r = ceil(rand(1,3)*NP);
            while r(1)==r(2) || r(2)== r(3) || min(r)==0 || max(r)>NP
                r = ceil(rand(1,3)*NP);
            end

            v(i,:) = x(r(1),:) + F*(x(r(2),:) - x(r(3),:));

            for j = 1:D
                if rand > CR
                    u(i,j) = x(i,j);
                else
                    u(i,j) = v(i,j);
                end
            end
            u(i,:)= round(u(i,:));
            u(i,:)=sort(u(i,:));
        end

        for i = 1:NP
            for jj = 1:D
                u(i,jj) = max(u(i,jj), range_min(jj));
                u(i,jj) = min(u(i,jj), range_max(jj));
            end
            u(i,:)=sort(u(i,:));
            fitness_child(i,1) = ultrafuzziness([0 0  u(i,:) 255 255],p,alpha);
        end

        for i = 1:NP
            if fitness_parent(i) < fitness_child(i)
                fitness_parent(i) = fitness_child(i);
```

```
            x(i,:) = u(i,:);
          end
        end

        [globalbest,globalbest_index] = max(fitness_parent);
        global_xbest = sort(x(globalbest_index,:));

%         clc
%         runn
%         fprintf('Optimisation through Differential Evolution\n')
%         fprintf('Generation: %0.5g\nGlobalbest: %2.7g\n', gen, globalbest)
%         fprintf('Best particle position : %0.11g\n', global_xbest)
%
        globalbest1 = [globalbest1, globalbest];


    end

    tElapsed = toc(tStart);
%     tElapsed

    globalbest1 = [globalbest1, globalbest];

    statistics_f = [statistics_f, globalbest];
    statistics_x = [statistics_x; (global_xbest)];

end

% plot(1:NP:NP*50,globalbest1(1:50),'-bs','MarkerFaceColor','b');
% hold on
f_mean = mean(statistics_f);
f_stddev = std(statistics_f);

best_fitness = max(statistics_f);
worst_fitness = min(statistics_f);

x_median = median(statistics_x);

%% select the threshold points
% T = [min_val round(x_median) max_val];
% Thres=T(2:2:2*Th)
t1=x_median(1:2:D);
t2=x_median(2:2:D);
Thres=round((t1+t2)/2);
X=grayslice(I_bw,[Thres]);
X1=uint8(255*mat2gray(X));
timestop=toc(tstart);
 function [Thres,X1] = Thresholding(I1,Th)

%figure, imshow(I1)
I=I1(:,:,1:3);
I_red=I(:,:,1);
if length(size(I))==3
  I_bw = rgb2gray(I);
end
[M, N, O] =size(I);
```

```
L = 256;
% H=imhist(I_bw);
H=imhist(I(:,:,2));
%figure,imhist(I)
p = H / (M * N);

%figure(2); plot(h)

max_val=double(max(max(I_red)));
min_val=double(min(min(I_red))+1);

%*************************************************************************
% 1. Define problem hyperspace and plot in 2D
%*************************************************************************
%Th =7;
% No of thresholds
D = Th*2;   %   no of dimensions
range_min = min_val*ones(1,D);
range_max = max_val*ones(1,D);% minimum & maximum range;
alpha=1.5;
%*************************************************************************
% 2. initialize the population
%*************************************************************************
NP = 10*D ;            %   population size
maxgen =100;           %   no of generations
F = 0.5;
CR = 0.9;

max_runs = 2;

globalbest1 = [];

statistics_f = [];
statistics_x = [];
tstart = tic;
for runn = 1:max_runs
   x=[];



   for i = 1 : NP
      for j = 1:D
         x(i, j) =  round(range_min(j) + ((range_max(j)-range_min(j))*(rand)));
      end
      x(i,:)=sort(x(i,:));

      fitness_parent(i,1) = ultrafuzziness([0 0 x(i,:) 255 255],p,alpha);
   end

   v = zeros(size(x));
   u = zeros(size(x));

   %*************************************************************************
   % 4. start iteration
   %*************************************************************************
```

```
    tStart = tic;

    for gen = 2:maxgen
%     [o-2]
      %**************************************************************************
      % 3. find mutation population
      %**************************************************************************
      for i = 1:NP
         r = ceil(rand(1,3)*NP);
         while r(1)==r(2) || r(2)== r(3) || min(r)==0 || max(r)>NP
            r = ceil(rand(1,3)*NP);
         end

         v(i,:) = x(r(1),:) + F*(x(r(2),:) - x(r(3),:));

         for j = 1:D
            if rand > CR
               u(i,j) = x(i,j);
            else
               u(i,j) = v(i,j);
            end
         end
         u(i,:)= round(u(i,:));
         u(i,:)=sort(u(i,:));
      end

      for i = 1:NP
         for jj = 1:D
            u(i,jj) = max(u(i,jj), range_min(jj));
            u(i,jj) = min(u(i,jj), range_max(jj));
         end
         u(i,:)=sort(u(i,:));
         fitness_child(i,1) = ultrafuzziness([0 0  u(i,:) 255 255],p,alpha);
      end

      for i = 1:NP
         if fitness_parent(i) < fitness_child(i)
            fitness_parent(i) = fitness_child(i);
            x(i,:) = u(i,:);
         end
      end

      [globalbest,globalbest_index] = max(fitness_parent);
      global_xbest = sort(x(globalbest_index,:));

%        clc
%        runn
%        fprintf('Optimisation through Differential Evolution\n')
%        fprintf('Generation: %0.5g\nGlobalbest: %2.7g\n', gen, globalbest)
%        fprintf('Best particle position : %0.11g\n', global_xbest)
%
      globalbest1 = [globalbest1, globalbest];


    end
```

```
    tElapsed = toc(tStart);
%     tElapsed

    globalbest1 = [globalbest1, globalbest];

    statistics_f = [statistics_f, globalbest];
    statistics_x = [statistics_x; (global_xbest)];

end

% plot(1:NP:NP*50,globalbest1(1:50),'-bs','MarkerFaceColor','b');
% hold on
f_mean = mean(statistics_f);
f_stddev = std(statistics_f);

best_fitness = max(statistics_f);
worst_fitness = min(statistics_f);

x_median = median(statistics_x);

%% select the threshold points
% T = [min_val round(x_median) max_val];
% Thres=T(2:2:2*Th)

t1=x_median(1:2:D);
t2=x_median(2:2:D);
Thres=round((t1+t2)/2);
X=grayslice(I_bw,[Thres]);
X1=uint8(255*mat2gray(X));
timestop=toc(tstart);
```

```
function BW2 = Trimp2(BW,pixl)

[M,N] = size(BW);
% figure, imshow(BW);
BW2 = BW;
for i=1:1:M
   for j=1:1:N
      if BW(i,j)>0
         BW(i,j) = 255;
      end
   end
end

% figure,imshow(BW);
BW1 = BW;


CC = bwconncomp(BW);
numPixels = cellfun(@numel,CC.PixelIdxList);

% Largest connected compnent
numPixels_temp = sort(numPixels,'descend');
idx = find(numPixels==numPixels_temp(1));

%figure, imshow(CC.PixelIdxList{idx})
BW1(CC.PixelIdxList{idx}) = 0;

% figure, imshow(BW1);

BW3 = BW-BW1;

% figure, imshow(BW3);
CC = bwconncomp(BW3);

% Number of pixels in each connected components
numPixels = cellfun(@numel,CC.PixelIdxList);

% Largest connected compnent
[biggest,idx] = max(numPixels);


S = regionprops(CC,'Centroid'); % Calculate centroids for connected components in the image using regionprops.
cntr = cat(1, S.Centroid); %Concatenate structure array containing centroids into a single matrix.
centroid_x=round(cntr(idx,1));
centroid_y=round(cntr(idx,2));



% hold on
% plot(centroid_x,centroid_y, 'b*')
% hold off
x_left = [];
x_right = [];
y_left = [];
y_right = [];
```

```
count = 1;
for i=1:1:M
   for j=1:1:centroid_x
      if BW(i,j)==255
         BW2(i,j:j+pixl) = 0;
         break;
      end
   end
end



count = 1;
y_down = 0;
for i=1:1:M
   for j=N:-1:centroid_x-1
      if BW(i,j)==255
         BW2(i,j:-1:j-pixl) = 0;
         y_down = i;
         break;
      end
   end
end


for i=y_down:-1:y_down-pixl
   BW2(i,:) = 0;
end

% figure();plot(x_left,y_left,'b*',x_right,y_right,'r*')

% figure();imshow(BW2)
```

```
function f=ultrafuzziness(v,p,alpha)


% if(length(v)==3)
%     u=trimf(1:256,v);
%     uL=u.^(alpha);
%     uU=u.^(1/alpha);
%     f=sum((uU-uL).*p');
% else
%     f=ultrafuzziness(v(1:3))*ultrafuzziness(v(3:length(v)));
% end

if(length(v)==4)
    v=v+1;
    u=trapmf(1:256,v);
    uL=u.^(alpha);
    uU=u.^(1/alpha);
    y=(uU-uL).*p';
    x=sum(y);
    f=0;
    if x~=0
        for i=v(1):v(4)
            if y(i)~=0
                f=f+(y(i)/x)*log(y(i)/x);
            end
        end
        f=-f;
    end
else
    f=ultrafuzziness(v(1:4),p,alpha)+ultrafuzziness(v(3:length(v)),p,alpha);
end
```

References

1. H. A., & Broman, A. T. (2006). The number of people with glaucoma worldwide in 2010 and 2020. *The British Journal of Ophthalmology*, *90*(3), 262-267.

2. Costagliola, C., dell'Omo, R., Romano, M. R., Rinaldi, M., Zeppa, L., & Parmeggiani, F. (2009). Pharmacotherapy of intraocular pressure: part I. Parasympathomimetic, sympathomimetic and sympatholytics. *Expert Opinion on Pharmacotherapy*, *10*(16), 2663-2677.

3. Costagliola, C., dell'Omo, R., Romano, M. R., Rinaldi, M., Zeppa, L., & Parmeggiani, F. (2009). Pharmacotherapy of intraocular pressure-part II. Carbonic anhydrase inhibitors, prostaglandin analogues and prostamides. *Expert Opinion on Pharmacotherapy*, *10*(17), 2859-2870.

4. European Glaucoma Society. (2014), *Terminology and Guidelines for Glaucoma*, PubliComm, Savona, Italy, 4th edition, pp 63-63

5. Stewart, W. C. (1990). *Clinical practice of glaucoma* Slack Inc, pp 1-1.

6. Cheng, J., Liu, J., Xu, Y., Yin, F., Wong, D. W. K., Tan, N., Wong, T. Y. (2013). Superpixel classification based optic disc and optic cup segmentation for glaucoma screening. , *IEEE Transactions on Medical Imaging*, *32*(6), 1019-1032.

7. Toprak, I., Yaylalı, V., & Yildirim, C. (2015). Diagnostic consistency and relation between optical coherence tomography and standard automated perimetry in primary open-angle glaucoma. *Seminars in Ophthalmology*, 1-6.

8. Nicolela, M. T. (2010). Optic nerve: clinical examination. *Pearls of Glaucoma Management* (pp. 15-21) Springer.

9. hrástek, R., Wolf, M., Donath, K., Niemann, H., Paulus, D., Hothorn, T., Michelson, G. (2005). Automated segmentation of the optic nerve head for diagnosis of glaucoma. *Medical Image Analysis*, *9*(4), 297-314.

10. Damms, T., & Dannheim, F. (1993). Sensitivity and specificity of optic disc parameters in chronic glaucoma. *Investigative Ophthalmology & Visual Science, 34*(7), 2246-2250.

11. Cassin, B., & Solomon, S. (1990). *Dictionary of Eye Terminology.*

12. Bouma, B. (2001). *Handbook of optical coherence tomography.* Informa Health Care.

13. Brezinski, M. E., Tearney, G. J., Bouma, B. E., Boppart, S. A., Hee, M. R., Swanson, E. A., Fujimoto, J. G. (1996). Imaging of coronary artery microstructure (in vitro) with optical coherence tomography. *The American Journal of Cardiology, 77*(1), 92-93.

14. Sinthanayothin, C., Boyce, J. F., Cook, H. L., & Williamson, T. H. (1999). Automated localisation of the optic disc, fovea, and retinal blood vessels from digital colour fundus images. *The British Journal of Ophthalmology*, *83*(8), 902-910.

15. Gagnon, L., Lalonde, M., Beaulieu, M., & Boucher, M. (2001). Procedure to detect anatomical structures in optical fundus images. *International Society for Optics and Photonics,* 1218-1225.

16. Youssif, A. A. A., Ghalwash, A. Z., & Ghoneim, Amr Ahmed Sabry Abdel-Rahman. (2008). Optic disc detection from normalized digital fundus images by means of a vessels' direction matched filter. *IEEE Transactions on Medical Imaging, 27*(1), 11-18.

17. Ophthalmic Photographers Society. (2011).
http://www.opsweb.org/?page=Monochromatic.

18. Li, H., & Chutatape, O. (2003). A model-based approach for automated feature extraction in fundus images. *Ninth IEEE International Conference on Computer Vision*, 394-399.

19. Li, H., & Chutatape, O. (2001). Automatic location of optic disk in retinal images. *IEEE International Conference on Image Processing, 2* 837-840.

20. Abdel-Ghafar, R., Morris, T., Ritchings, T., & Wood, I. (2004). Detection and characterisation of the optic disk in glaucoma and diabetic retinopathy. *Proceedings of Medical Image Understanding and Analysis.*

21. Niemeijer, M., Staal, J., Ginneken, B., Loog, M., & Abramoff, M. (2004). *DRIVE: Digital Retinal Images for Vessel Extraction.*
http://www.isi.uu.nl/Research/Databases/DRIVE/.

22. Hoover, A., Kouznetsova, V., & Goldbaum, M. (2000). Locating blood vessels in retinal images by piecewise threshold probing of a matched filter response. , *IEEE Transactions on Medical Imaging*, *19*(3), 203-210.
http://www.ces.clemson.edu/~ahoover/stare/probing/index.html

23. MESSIDOR: Methods for Evaluating Segmentation and Indexing technique Dedicated to Retinal Ophthalmology.(2004).
http://messidor.crihan.fr/index-en.php.

24. Zhang, Z., Yin, F. S., Liu, J., Wong, W. K., Tan, N. M., Lee, B. H., Wong, T. Y. (2010). Origa-light: An online retinal fundus image database for glaucoma analysis and research. *Annual International Conference of the IEEE Engineering in Medicine and Biology Society*, 3065-3068.

25. The Singapore Eye Research Institute (SERI), (2013).
http://www.seri.com.sg/.

26. Kauppi, T., Kalesnykiene, V., Kamarainen, J., Lensu, L., Sorri, I., Uusitalo, H., Pietilä, J. (2006). DIARETDB0: Evaluation database and methodology for diabetic retinopathy algorithms. *Machine Vision and Pattern Recognition Research Group.*

27. Kauppi, T., Kalesnykiene, V., Kamarainen, J., Lensu, L., Sorri, I., Raninen, A., Pietilä, J. (2007). The DIARETDB1 Diabetic Retinopathy Database and Evaluation Protocol. *Bmvc*, pp 1-10.

28. Kumar, V., & Sinha, N. (2013). Automatic Optic Disc segmentation using maximum intensity variation. *IEEE TENCON Spring Conference*, 29-33.

29. Gloster, J., & Parry, D. G. (1974). Use of photographs for measuring cupping in the optic disc. *The British Journal of Ophthalmology, 58*(10), 850-862.

30. Muramatsu, C., Nakagawa, T., Sawada, A., Hatanaka, Y., Yamamoto, T., & Fujita, H. (2011). Automated determination of cup-to-disc ratio for classification of glaucomatous and normal eyes on stereo retinal fundus images. *Journal of Biomedical Optics, 16*(9), 096009-1-096009-7.

31. Harizman, N., Oliveira, C., Chiang, A., Tello, C., Marmor, M., Ritch, R., & Liebmann, J. M. (2006). The ISNT rule and differentiation of normal from glaucomatous eyes. *Archives of Ophthalmology, 124*(11), 1579-1583.

32. Annu, N., & Justin, J. (2013). Automated Classification of Glaucoma Images by Wavelet Energy Features. *International Journal of Engineering and Technology (IJET), 5*(2), 1716-1721.

33. Glasbey, C. A., & Horgan, G. W. (1995). *Image analysis for the biological sciences* Wiley Chichester, pp 93-93.

34. Aquino, A., Gegúndez-Arias, M. E., & Marín, D. (2010). Detecting the optic disc boundary in digital fundus images using morphological, edge detection, and feature extraction techniques. *IEEE Transactions on Medical Imaging, 29*(11), 1860-1869.

35. Lu, S. (2011). Accurate and efficient optic disc detection and segmentation by a circular transformation. *IEEE Transactions on Medical Imaging, 30*(12), 2126-2133.

36. Lupascu, C. A., Tegolo, D., & Rosa, L. D. (2008). Automated detection of optic disc location in retinal images. *21st IEEE International Symposium on Computer-Based Medical Systems,* 17-22.

37. Zhu, X., & Rangayyan, R. M. (2008). Detection of the optic disc in images of the retina using the Hough transform. *30th Annual International Conference of the IEEE Engineering in Medicine and Biology Society,* 3546-3549.

38. Welfer, D., Scharcanski, J., Kitamura, C. M., Dal Pizzol, M. M., Ludwig, L. W., & Marinho, D. R. (2010). Segmentation of the optic disk in color eye fundus images using an adaptive morphological approach. *Computers in Biology and Medicine, 40*(2), 124-137.

39. Tjandrasa, H., Wijayanti, A., & Suciati, N. (2012). Optic nerve head segmentation using Hough transform and active contours. *TELKOMNIKA (Telecommunication Computing Electronics and Control, 10*(3), 531-536.

40. Yin, F., Liu, J., Ong, S. H., Sun, Y., Wong, D. W., Tan, N. M., Wong, T. Y. (2011). Model-based optic nerve head segmentation on retinal fundus images. *Annual International Conference of the IEEE Engineering in Medicine and Biology Society,* 2626-2629.

41. Cheng, J., Liu, J., Wong, D. W. K., Yin, F., Cheung, C., Baskaran, M., Wong, T. Y. (2011). Automatic optic disc segmentation with peripapillary atrophy elimination. *2011 Annual*

International Conference of the IEEE Engineering in Medicine and Biology Society, 6224-6227.

42. Dehghani, A., Moghaddam, H. A., & Moin, M. (2012). Optic disc localization in retinal images using histogram matching. *EURASIP Journal on Image and Video Processing*, (1), 1-11.

43. Zhang, D., Yi, Y., Shang, X., & Peng, Y. (2012). Optic disc localization by projection with vessel distribution and appearance characteristics. *International Conference on Pattern Recognition*, pp 3176-3179.

44. Fraga, A., Barreira, N., Ortega, M., Penedo, M. G., & Carreira, M. J. (2012). Precise segmentation of the optic disc in retinal fundus images. *Computer Aided Systems Theory* (pp. 584-591) Springer.

45. Sinha, N., & Babu, R. V. (2012). Optic disk localization using L 1 minimization. *IEEE International Conference on Image Processing*, 2829-2832.

46. Land, E. H., & McCann, J. (1971). Lightness and retinex theory. *Josa*, *61*(1), 1-11.

47. Hoover, A., & Goldbaum, M. (2003). Locating the optic nerve in a retinal image using the fuzzy convergence of the blood vessels. *IEEE Transactions on Medical Imaging*, *22*(8), 951-958.

48. Blanco, M., Penedo, M. G., Barreira, N., Penas, M., & Carreira, M. J. (2006). Localization and extraction of the optic disc using the fuzzy circular Hough transform. *Artificial Intelligence and Soft Computing* (pp. 712-721) Springer.

49. Otsu, N. (1975). A threshold selection method from gray-level histograms. *Automatica*, *11*(285-296), 23-27.

50. Zhang, K., Zhang, L., Song, H., & Zhou, W. (2010). Active contours with selective local or global segmentation: a new formulation and level set method. *Image and Vision Computing, 28*(4), 668-676.

51. Gonzalez, R. C., & Woods, R. E. (2002). Digital image processing. *2Ed: Prentice Hall Press, ISBN 0-201-18075-8*, pp 134-137, 88-89, 395-395.

52. Canny, J. (1986). A computational approach to edge detection. *IEEE Transactions on Pattern Analysis and Machine Intelligence*, (6), 679-698.

53. Shang, X., & Zhang, D. (2012). Blood skeleton extraction approach for retinopathy images. *Measuring Technology and Mechatronics Automation in Electrical Engineering* (pp. 145-150) Springer.

54. Mahfouz, A. E., & Fahmy, A. S. (2009). Ultrafast localization of the optic disc using dimensionality reduction of the search space. *Medical Image Computing and Computer-Assisted Intervention* (pp. 985-992) Springer.

55. Youssif, A. A., Ghalwash, A. Z., & Ghoneim, A. S. (2007). A comparative evaluation of preprocessing methods for automatic detection of retinal anatomy. *Proceedings of the Fifth International Conference on Informatics and Systems*, pp 24- 30.

56. Chaudhuri, S., Chatterjee, S., Katz, N., Nelson, M., & Goldbaum, M. (1989). Detection of blood vessels in retinal images using two-dimensional matched filters. *IEEE Transactions on Medical Imaging, 8*(3), 263-269.

57. Wong, D., Liu, J., Lim, J., Jia, X., Yin, F., Li, H., & Wong, T. (2008). Level-set based automatic cup-to-disc ratio determination using retinal fundus images in ARGALI. *30th Annual International Conference of the IEEE Engineering in Medicine and Biology Society,* pp 2266-2269.

58. Wong, D., Liu, J., Lim, J., Li, H., & Wong, T. (2009). Automated detection of kinks from blood vessels for optic cup segmentation in retinal images. *SPIE Medical Imaging*, 72601J-1-72601J-8.

59. Narasimhan, K., & Vijayarekha, K. (2011). An efficient automated system for glaucoma detection using fundus image. *Journal of Theoretical and Applied Information Technology*, *33*(1), 104-110.

60. Ho, C., Pai, T., Chang, H., & Chen, H. (2011). An automatic fundus image analysis system for clinical diagnosis of glaucoma. *International Conference on Systems Complex, Intelligent and Software Intensive*, pp 559-564.

61. Mishra, M., Nath, M. K., & Dandapat, S. (2011). Glaucoma detection from color fundus images. *International Journal of Computer & Communication Technology*, *2*(6), 7-10.

62. Yin, F., Liu, J., Wong, D. W. K., Tan, N. M., Cheung, C., Baskaran, M., Wong, T. Y. (2012). Automated segmentation of optic disc and optic cup in fundus images for glaucoma diagnosis. *25th International Symposium on Computer-Based Medical Systems*, pp 1-6.

63. Narasimhan, K., Vijayarekha, K., JogiNarayana, K., SivaPrasad, P., & Kumar, V. S. (2012). Glaucoma Detection From Fundus Image Using Opencv. *Research Journal of Applied Sciences, Engineering and Technology*, pp 5459-5463.

64. Chandrika, S., & Nirmala, K. Analysis of CDR Detection for Glaucoma Diagnosis. *International Journal of Engineering Research and Application*, pp 2248-9622.

65. Damon, W. W. K., Liu, J., Meng, T. N., Fengshou, Y., & Yin, W. T. (2012). Automatic detection of the optic cup using vessel kinking in digital retinal fundus images. *9th IEEE International Symposium on Biomedical Imaging*, pp 1647-1650.

66. Ingle, R., & Mishra, P. (2013). Cup Segmentation by Gradient Method for the Assessment of Glaucoma from Retinal Image. *International Journal of Engineering Trends and Technology, 4(6), 2540*–2543.

67. Zuiderveld, K. (1994). Contrast limited adaptive histogram equalization. *Graphics Gems IV*, pp 474-485.

68. Weinreb, R. N., Aung, T., & Medeiros, F. A. (2014). The pathophysiology and treatment of glaucoma: a review. *Jama*, 311(18), 1901-1911.

69. Jonas, J. B., Fernández, M. C., & Stürmer, J. (1993). Pattern of glaucomatous neuroretinal rim loss. *Ophthalmology*, 100(1), 63-68.

70. Li, H., & Chutatape, O. (2003). Boundary detection of optic disk by a modified ASM method. *Pattern Recognition, 36*(9), 2093-2104.

71. Itzgibbon, A., Pilu, M., & Fisher, R. B. (1999). Direct least square fitting of ellipses. *IEEE Transactions on Pattern Analysis and Machine Intelligence, 21*(5), 476-480.

72. Achanta, R., Shaji, A., Smith, K., Lucchi, A., Fua, P., & Susstrunk, S. (2012). SLIC superpixels compared to state-of-the-art superpixel methods. *IEEE Transactions on Pattern Analysis and Machine Intelligence, 34*(11), 2274-2282.

73. Chang, C., & Lin, C. (2011). LIBSVM: A library for support vector machines. *ACM Transactions on Intelligent Systems and Technology, 2*(3), 27. https://www.csie.ntu.edu.tw/∼cjlin/libsvm/.

74. Fraz, M., Javed, M., & Basit, A. (2008). Evaluation of retinal vessel segmentation methodologies based on combination of vessel centerlines and morphological processing. *4th International Conference on Emerging Technologies*, pp 232-236.

75. Duan, L., Tsang, I. W., & Xu, D. (2012). Domain transfer multiple kernel learning. *IEEE Transactions on Pattern Analysis and Machine Intelligence, 34*(3), 465-479.

76. Fraz, M. M., Remagnino, P., Hoppe, A., Uyyanonvara, B., Rudnicka, A. R., Owen, C. G., & Barman, S. A. (2012). Blood vessel segmentation methodologies in retinal images–a survey. *Computer Methods and Programs in Biomedicine, 108*(1), 407-433.

77. Russ, J. C. (2011). *The image processing handbook* CRC press, pp. 274-275, 395-396.

78. Zadeh, L. A. (1965). Fuzzy sets. *Information and Control, 8*(3), 338-353.

79. Tizhoosh, H. R. (2005). Image thresholding using type II fuzzy sets. *Pattern Recognition, 38*(12), 2363-2372.

80. Mendel, J. M., & John, R. I. B. (2002). Type-2 fuzzy sets made simple. *IEEE Transactions on Fuzzy Systems, 10*(2), 117-127.

81. Kass, M., Witkin, A., & Terzopoulos, D. (1988). Snakes: Active contour models. *International Journal of Computer Vision, 1*(4), 321-331.

82. Osher, S., & Sethian, J. A. (1988). Fronts propagating with curvature-dependent speed: algorithms based on Hamilton-Jacobi formulations. *Journal of Computational Physics, 79*(1), 12-49.

83. Osher, S., & Paragios, N. (2003). *Geometric level set methods in imaging, vision, and graphics* Springer Science & Business Media, pp 43-43.

84. Sonka, M., Hlavac, V., & Boyle, R. (2014). *Image processing, analysis, and machine vision* Cengage Learning, pp 273-273.

85. Li, C., Xu, C., Gui, C., & Fox, M. D. (2005). Level set evolution without re-initialization: a new variational formulation. *IEEE Computer Society Conference on Computer Vision and Pattern Recognition*, pp 430-436.

86. Burman, R., Almazroa, A., Raahemifar, K., & Lakshminarayanan, V. (2015). Automated Detection of Optic Disc in Fundus Images. *Advances in Optical Science and Engineering* (pp. 327-334) Springer.

87. Richard, Manuel M Oliveira Brian Bowen, & Chang, M. Y. (2001). Fast digital image inpainting. *Appeared in the Proceedings of the International Conference on Visualization, Imaging and Image Processing*, pp 106-107.

88. Almazroa, A., Alodhayb, S., Burman, R., Sun, W., Raahemifar, K., & Lakshminarayanan, V. (2015). Optic cup segmentation based on extracting blood vessel kinks and cup thresholding using Type-II fuzzy approach. *2nd International Conference on Opto-Electronics and Applied Optics*, pp 1-3.